REPORT DOCUMENTATION PAGE

Form Approved OMB NO. 0704-0188

1. REPORT DATE (DD-MM-YYYY)	2. REPORT TYPE	3. DATES COVERED (From - To)
26-11-2014	Ph.D. Dissertation	-

4. TITLE AND SUBTITLE

THE ROLE OF MOLECULAR MOTORS IN THE MECHANICS OF ACTIVE GELS AND THE EFFECTS OF INERTIA, HYDRODYNAMIC INTERACTION AND COMPRESSIBILITY IN PASSIVE MICRORHEOLOGY

5a. CONTRACT NUMBER
W911NF-09-1-0378

5b. GRANT NUMBER

5c. PROGRAM ELEMENT NUMBER
8D10AZ

6. AUTHORS
Andres Cordoba

5d. PROJECT NUMBER

5e. TASK NUMBER

5f. WORK UNIT NUMBER

7. PERFORMING ORGANIZATION NAMES AND ADDRESSES
Illinois Institute of Technology
3300 South Federal Street
Room 301 Main Bldg
Chicago, IL 60616 -3793

8. PERFORMING ORGANIZATION REPORT NUMBER

9. SPONSORING/MONITORING AGENCY NAME(S) AND ADDRESS (ES)

U.S. Army Research Office
P.O. Box 12211
Research Triangle Park, NC 27709-2211

10. SPONSOR/MONITOR'S ACRONYM(S)
ARO

11. SPONSOR/MONITOR'S REPORT NUMBER(S)
56388-EG-DRP.41

12. DISTRIBUTION AVAILIBILITY STATEMENT

Approved for public release; distribution is unlimited.

13. SUPPLEMENTARY NOTES

The views, opinions and/or findings contained in this report are those of the author(s) and should not contrued as an official Department of the Army position, policy or decision, unless so designated by other documentation.

14. ABSTRACT

The mechanical properties of soft biological materials are essential to their physiological function and cannot easily be duplicated by synthetic materials. The study of the mechanical properties of biological materials has lead to the development of new rheological characterization techniques. In the technique called passive microbead rheology, the positional autocorrelation function of a micron-sized bead embedded in a viscoelastic fluid is used to infer the dynamic modulus of the fluid.

15. SUBJECT TERMS

microrheology, high frequency response, tissue, active matter

16. SECURITY CLASSIFICATION OF:			17. LIMITATION OF ABSTRACT	15. NUMBER OF PAGES	19a. NAME OF RESPONSIBLE PERSON
a. REPORT	b. ABSTRACT	c. THIS PAGE			Jay Schieber
UU	UU	UU	UU		19b. TELEPHONE NUMBER 312-567-3046

Report Title

THE ROLE OF MOLECULAR MOTORS IN THE MECHANICS OF ACTIVE GELS AND THE EFFECTS OF INERTIA, HYDRODYNAMIC INTERACTION AND COMPRESSIBILITY IN PASSIVE MICRORHEOLOGY

ABSTRACT

The mechanical properties of soft biological materials are essential to their physiological function and cannot easily be duplicated by synthetic materials. The study of the mechanical properties of biological materials has lead to the development of new rheological characterization techniques. In the technique called passive microbead rheology, the positional autocorrelation function of a micron-sized bead embedded in a viscoelastic fluid is used to infer the dynamic modulus of the fluid. Single particle microrheology is limited to fluids were the microstructure is much smaller than the size of the probe bead. To overcome this limitation in two-bead microrheology the cross-correlated thermal motion of pairs of tracer particles is used to determine the dynamic modulus. Here we present a time-domain data analysis methodology and generalized Brownian dynamics simulations to examine the effects of inertia, hydrodynamic interaction, compressibility and non-conservative forces in passive microrheology. A type of biological material that has proven specially challenging to characterize are active gels. They are formed by semiflexible polymer filaments driven by motor proteins that convert chemical energy from the hydrolysis of adenosine triphosphate (ATP) to mechanical work and motion. Active gels perform essential functions in living tissue. Here we introduce a single-chain mean-field model to describe the mechanical properties of active gels. We model the semiflexible filaments as bead-spring chains and the molecular motors are accounted for by using a mean-field approach. The level of description of the model includes the end-to-end length and attachment state of the filaments, and the motor-generated forces, as stochastic state variables which evolve according to a proposed differential Chapman-Kolmogorov equation. The model allows accounting for physics that are not available in models that have been postulated on coarser levels of description. Moreover it allows the prediction of observables at time scales that will be too difficult to achieve in multi-chain simulations.

THE ROLE OF MOLECULAR MOTORS IN THE MECHANICS OF ACTIVE GELS AND THE EFFECTS OF INERTIA, HYDRODYNAMIC INTERACTION AND COMPRESSIBILITY IN PASSIVE MICRORHEOLOGY

BY

ANDRÉS CÓRDOBA URIBE

Submitted in partial fulfillment of the
requirements for the degree of
Doctor of Philosophy in Chemical Engineering
in the Graduate College of the
Illinois Institute of Technology

Approved _____
Advisor

Chicago, Illinois
July 2014

ACKNOWLEDGMENT

I would like to thank Prof. Jay Schieber for his valuable guidance. I also appreciate the prompt and fair feedback on my writings. I am also grateful to Dr. Tsutomu Indei for useful discussions and feedback on my writings.

I would also like to thank the thesis committee members, Professors David Venerus, Juan de Pablo, Vijay Ramani and Xiaofan Li for taking the time to review my thesis and listen to my presentations and for their valuable comments.

I am also grateful to my parents Cristina Uribe and Luis F. Córdoba for all their love and emotional support during these years.

I also thank Maria Katzarova and my other fellow research group members for their friendship and insightful discussions.

Finally, for the financial support of this work the Army Research Office (grants W911NF-09-2-0071 and W911NF-09-1-0378) is gratefully acknowledged.

TABLE OF CONTENTS

LIST OF TABLES

LIST OF FIGURES

LIST OF SYMBOLS

Symbol	Definition
k_B	Boltzmann constant
T	temperature
t	time
ω	frequency
$\bar{\mathcal{F}}\{...\}$	one-sided Fourier transform
$\mathcal{F}\{...\}$	two-sided Fourier transform
$G^*(\omega)$	dynamic modulus
$G'(\omega)$	storage modulus
$G''(\omega)$	loss modulus
$G(t)$	relaxation modulus
$J(t)$	creep compliance
$J^*(\omega)$	complex creep compliance
$K^*(\omega)$	complex bulk modulus
$\nu^*(\omega)$	complex Poisson ratio
$\delta\boldsymbol{r}_\mathrm{b}$	bead displacement
$\boldsymbol{v}_\mathrm{b}$	bead velocity
$\boldsymbol{p}_\mathrm{b}$	bead momentum
g_j	elastic modulus of the j-th Maxwell element
H_j	strength of the j-th element of the memory function
c_j	strength of the j-th element of the inertia-less memory function

$\boldsymbol{Q}_j$	end-to-end vector of the j-th virtual spring
λ_j	relaxation time of the j-th Maxwell element
Λ_j	retardation time of the j-th Maxwell element
η_0	viscosity of the purely viscous element
$\langle \Delta\delta r_{\mathrm{b}}^2(t) \rangle_{\mathrm{eq}}$	mean-squared displacement of the bead
$\langle \overline{\Delta\delta r_{\mathrm{b}}^2}[\omega] \rangle$	one-sided Fourier transform of $\langle \Delta\delta r_{\mathrm{b}}^2(t) \rangle_{\mathrm{eq}}$
$\langle \Delta\delta r_{\mathrm{b}(1,2)}^2(t) \rangle_{\mathrm{eq}}$	cross-correlation of bead displacements
$\langle \overline{\Delta\delta r_{\mathrm{b}(1,2}^2}[\omega] \rangle$	one-sided Fourier transform of $\langle \Delta\delta r_{\mathrm{b}(1,2)}^2(t) \rangle_{\mathrm{eq}}$
m	bead mass
R	bead radius
ρ	medium density
L	distance between bead centers
Q	R/L
H_{e}	trap stiffness
$\zeta(t)$	memory function
$\bar{\zeta}[\omega]$	one-side Fourier transform of $\zeta(t)$
$\mu(t)$	inertia-less memory function
$\bar{\mu}[\omega]$	one-side Fourier transform of $\mu(t)$
$\langle ... \rangle_{\mathrm{eq}}$	ensemble average at equilibrium
$\langle ... \rangle_{\mathrm{st}}$	ensemble average at non-equilibrium steady state
$\Delta(\omega)$	wavelength
$\Lambda(\omega)$	penetration length

$c(\omega)$	speed of sound
$d\boldsymbol{W}(t)$	Wiener increment
$\alpha(\omega)$	complex compliance
$\boldsymbol{f}_{\mathrm{B}}$	Brownian force
$\boldsymbol{\delta}$	identity matrix
$\delta(...)$	Dirac delta function
$\delta_{i,j}$	Kronecker delta
$A_{\perp}$	hydrodynamic interaction function in the direction perpendicular to the line of centers of the beads
$A_{\parallel}$	hydrodynamic interaction function in the direction parallel to the line of centers of the beads
Ω	filament conformation
$\hat{\omega}$	subset of Ω, $\{s, \boldsymbol{F}\}$
$\psi(\Omega; t)$	probability density function
$\psi_{\mathrm{eq}}(\Omega)$	equilibrium probability density function
$\phi(s, r; t)$	marginal probability density function
N	number of beads
F_j	force generated by a motor attached to bead j
$\boldsymbol{F}$	$\{F_1, F_2, ...F_j, ...F_N\}$
s	attachment state
r_j	change in the end-to-end length of a strand j
$\boldsymbol{r}$	$\{r_1, r_2, ...r_j, ...r_N\}$
k_{b}	spring constant for the filaments (Fraenkel springs)
f	tension on a strand

$p(F)$	motor force distribution
F_m	mean motor stall force
δF_m	standard deviation of the motor force distribution
ℓ_0	rest length of a strand
ℓ_p	persistence length of a filament
ℓ_f	end-to-end length of a filament
ℓ_c	contour length
F_{B}	buckling force
k_{WLC}	spring constant for the filaments (worm-like chain)
τ_d	average time a motor spends attached before detaching
τ_a	average time a motor spends detached before reattaching
ζ_a	friction coefficient for a bead when a motor is attached to it
ζ_a	friction coefficient for a bead with no motor attached to it
$\tau_{r,a}$	ζ_a/k_{b}
$\tau_{r,d}$	ζ_d/k_{b}
$\mathbb{W}(\hat{\omega}\|\hat{\omega}')$	transition rate matrix
$\phi_{\mathrm{B}}(t)$	fraction of buckled filaments
n_c	number of filaments per unit volume
ϵ	strain
ϵ_0	strain magnitude
$\dot{\epsilon}$	strain rate
σ	stress in the direction of filament orientation

$\langle \Delta R_c^2(t) \rangle_{\mathrm{st}}$	mean-squared displacement of the filament center
$\boldsymbol{\tau}(t)$	stress tensor
$\hat{\boldsymbol{\tau}}(t)$	microscopic stress tensor
$\boldsymbol{\gamma}$	deformation tensor
$\mathcal{H}(\boldsymbol{x})$	Hamiltonian or free energy

ABSTRACT

The mechanical properties of soft biological materials are essential to their physiological function and cannot easily be duplicated by synthetic materials. The study of the mechanical properties of biological materials has lead to the development of new rheological characterization techniques. In the technique called passive microbead rheology, the positional autocorrelation function of a micron-sized bead embedded in a viscoelastic fluid is used to infer the dynamic modulus of the fluid. Single particle microrheology is limited to fluids were the microstructure is much smaller than the size of the probe bead. To overcome this limitation in two-bead microrheology the cross-correlated thermal motion of pairs of tracer particles is used to determine the dynamic modulus. Here we present a time-domain data analysis methodology and generalized Brownian dynamics simulations to examine the effects of inertia, hydrodynamic interaction, compressibility and non-conservative forces in passive microrheology. A type of biological material that has proven specially challenging to characterize are active gels. They are formed by semiflexible polymer filaments driven by motor proteins that convert chemical energy from the hydrolysis of adenosine triphosphate (ATP) to mechanical work and motion. Active gels perform essential functions in living tissue. Here we introduce a single-chain mean-field model to describe the mechanical properties of active gels. We model the semiflexible filaments as bead-spring chains and the molecular motors are accounted for by using a mean-field approach. The level of description of the model includes the end-to-end length and attachment state of the filaments, and the motor-generated forces, as stochastic state variables which evolve according to a proposed differential Chapman-Kolmogorov equation. The model allows accounting for physics that are not available in models that have been postulated on coarser levels of description. Moreover it allows the prediction of observables at time scales that will be too difficult to achieve in multi-chain simulations.

CHAPTER 1

INTRODUCTION

The mechanical properties of soft biological materials are essential to their physiological function and cannot easily be duplicated by synthetic materials. A better understanding of the relations between molecular composition and mechanical properties of biological materials will increase our understanding of the processes that sustain life. This, in turn, will allow a more rational design of biomimetic materials and suggest strategies to counteract defects when they arise. Therefore the relation between molecular composition and the mechanical and rheological properties of biological materials is a highly active and growing filed of scientific study. The study of the mechanical properties of biological materials has lead to the development of new rheological characterization techniques. For instance, in the technique called passive microbead rheology, a tracer bead of radius R sufficiently small to be subjected to Brownian motion ($R < 1\mu$m), but larger than the microstructure of the medium, is placed in a viscoelastic medium, and the trajectory or displacement of the bead is measured by some optical technique [86, 1, 128, 59, 112]. The positional autocorrelation function of the trajectory is used to infer the dynamic modulus of the fluid. Unlike bulk rheometers, microbead rheology requires only very small samples (pico- to microliter order) and elastic modulus as small as 10-500 Pa can be measured [59]. These advantages make the technique especially useful for the analysis of biological samples [1, 128].

An especially relevant type of biological material are active gels. Active gels are networks of semiflexible polymer filaments driven by motor proteins that can convert chemical energy from the hydrolysis of adenosine triphosphate (ATP) to mechanical work and motion. Active gels perform essential functions in living tissue including motions, generation of forces and sensing of external forces. The cell cy-

toskeleton is an active gel composed of many different types of filaments and motors that performs most of the mechanical functions of cells. Moreover, active gels play a central role in driving cell division and cell motility [23, 118, 94] and have also been successfully prepared *in vitro* to study their mechanical and rheological properties [117, 8, 91]. Recent advances in experimental techniques have allowed the characterization of mechanical and rheological properties of active gels. For instance an important mechanical feature of active gels that has been extensively studied experimentally, is their capacity of self-contraction and self-organization [71, 119, 23, 65, 63]. These recent findings suggest a strategy for creating a new class of active materials whose rheological properties are controlled by enzymatic activity.

1.1 Passive microbead rheology

In the original one-point passive microrheology technique introduced by Mason and Weitz [86], the positional autocorrelation function of a micron-sized bead embedded in a viscoelastic fluid is used to infer the dynamic modulus, $G^*(\omega)$, of the fluid. Analysis is typically made in the frequency domain via the generalized Stokes-Einstein relation (GSER). Inertia of both bead and medium are neglected in the GSER so that the analysis based on the GSER is not valid at high frequency where inertia is important. Moreover since the analysis of microbead rheology data relies on a generalized Stokes relation [108] it is limited to fluids were the microstructure is much smaller than the size of the probe bead. If this condition is not satisfied the continuum mechanics assumptions used in the data analysis [52, 72, 124, 87] can become invalid. To overcome this limitation Crocker et al. [19] proposed a modification of the original one-point passive microbead rheology technique based on measuring the cross-correlated thermal motion of pairs of tracer particles to determine $G^*(\omega)$. Optical traps are often used in passive microrheology to hold the probe beads near their equilibrium position and as part of the technique to track their position. How-

ever optical traps have been shown to exert non-conservative, non-linear forces on the particles [104, 103]. Also particles can be trapped by aharmonic potentials generated by a surrounding solid network [25, 116]. Such complications prevent analytic analysis of the data.

The dynamics of a bead embedded in a viscoelastic medium are described by the generalized Langevin equation (GLE) [86]. A memory function accounts for the frictional resistance experienced by a micron-sized particle in the GLE description. The GLE description predicts ballistic behavior in the autocorrelation function of bead displacements at short time scales [52, 89, 28, 124]. In real systems the bead mass is very small and therefore the ballistic regime is usually not observed experimentally, not even in the highest-frequency measurements available [125, 124]. Therefore, eliminating the inertia-related fast variable from the GLE to obtain equations that can correctly describe the bead displacements inside the experimentally observable window provides a more efficient way of modeling and simulating passive microbead rheology. There are however subtle physical and mathematical issues that arise in the elimination of inertia from the GLE. McKinley et al. [89] were the first to discuss the singular nature of the zero mass limit, however they did not solve it. Later Indei et al. [52] addressed this issue in detail and concluded that to eliminate bead inertia in a self-consistent way, one must have a high-frequency purely dissipative element in the memory kernel. This purely dissipative element can be introduced as a purely viscous element arising from say solvent viscosity, but it can also come from the fluid inertia.

Data analysis of passive microbead rheology is usually based on formulas that relate bead displacement statistics to the dynamic modulus of the material in the frequency-domain. Therefore methods of analysis require conversion of the data to the frequency-domain using numerical Fourier transform routines. These methods are

known to introduce errors associated with frequency discretization and finite window size. Time-domain data analysis methods based on a single bead trajectory were introduced by Fricks et al. [28] as an alternative to the frequency-domain formulas. In that work, the time-domain data analysis algorithm was evaluated using synthetic bead paths generated using a generalized Langevin equation. However their method relies on an analytic solution of the GLE to simulate the sample bead trajectories and therefore can not be extended to include non-linear effects such as those generated by non-linear traps.

As stated above, in two-point passive microrheology the cross-correlations of two micron-sized beads embedded in a viscoelastic fluid are used to estimate the dynamic modulus of a material. The two-point technique allows for sampling of larger length scales which means that it can be used in materials with a coarser microstructure. An optimal separation between the beads exists at which the desired length and time scales are sampled while keeping a desired signal-to-noise-ratio in the cross-correlations. A large separation can reduce the effect of higher order reflections, but will increase the effects of medium inertia and reduce the signal-to-noise-ratio. The modeling formalisms [19, 73, 113, 48] commonly used to relate two-bead cross-correlations to $G^*(\omega)$ neglect inertia effects and underestimate the effect of reflections. A simple dimensional analysis presented here suggests for a model viscoelastic fluid that there exists a very narrow window of bead separation and frequency range where these effects can be neglected.

There has also been a recent interest to use the two-point microrheology technique to measure the complex compressibility of biopolymers and cell components such as filamentous actin and microtubules [99, 20]. This would seem at first glance an excellent benchmark application for the two-point microrheology technique. Microrheology methods are specially suitable to test the often scarce and expensive

biological samples. Moreover the linkage of Poisson ratio to specific microstructural characteristics of a great variety of materials has been studied extensively. For example it is well known that the Poisson ratio is intimately connected with the way structural elements are packed [38]. However a rigorous analysis of the sensitivity of the technique to the static and dynamic properties of the Poisson ratio was still lacking.

1.2 Active gels

Microrheology experiments in active polymeric networks have revealed fundamental differences from their passive counterparts. Some of the differences are not surprising given that these are materials in which molecular motors continuously convert chemical energy into mechanical work. For instance, recent microrheology experiments [8, 117, 91] on active gels have shown that the fluctuation-dissipation theorem (FDT) and the generalized Stokes-Einstein relation (GSER) are violated in active gels. The FDT is a central part of data analysis of passive microrheology experiments, where it is used to relate the position fluctuations of the probe bead to a frequency-dependent friction coefficient, from which, using a generalized Stokes relation rheological properties can be extracted [51, 15, 108]. The violation of FDT is observed as frequency-dependent discrepancy between the material response function obtained from active and passive microrheology experiments. Moreover other microrheology experiments in active gels [117, 91] have shown that motor-activity induces significant strain hardening of the semiflexible network. It has also been observed that the mass transport of probe beads in active gels often exhibits super-diffusive behavior [68, 105]. This is different from passive polymeric networks where the mass transport of probe beads exhibits sub-diffusive behavior due to the viscoelasticity of the medium.

In the recent past several models have been proposed to describe active gels. A

common approach is to use simple generalizations or extensions of the FDT for out-of-equilibrium systems. In general, these extensions of FDT to out-of-equilibrium systems model the non-equilibrium forces as effective Brownian forces, with an effective temperature [78, 79, 80], which is higher than the real temperature and is meant to account for the larger magnitude of the non-equilibrium fluctuations. These type of models are usually postulated on a continuum level of description and are inspired by hydrodynamic theories of liquid crystals [65, 63]. This kind of approach can not explain the observations in the microrheology experiments in active gels [91] since Brownian forces alone can not produce a frequency-dependent discrepancy between the material response obtained from the material's spontaneous stress fluctuations, and the material response obtained by applying a small external perturbation and observing the material response. Other works [74, 43] have modeled the attachment/detachment dynamics of motor forces as a stochastic jump process. This approach has been successful in describing some of the features observed in the microrheology experiments of active gels, such as the super-diffusive behavior of tracer beads. However these models assume that motors can be described as force dipoles inside a continuum, which is an assumption that can easily break down for semiflexible networks, where the mesh size is smaller than the persistence length of the filaments. They also assume that the motors do not interact through the strain field in the network and neglect strain hardening. Given the level of description of such models, removal of these assumptions is difficult; therefore more microscopic models are required to elucidate the specific effect that these physical features have on the rheology of active gels.

More microscopic models have described active gels using a master equation for interacting polar rods; Aranson and Tsimring [2] presented analytic and numerical results for rigid rods, later Head et al. [42] presented more detailed numerical simulations that account for filament semiflexibility. These models have been suc-

cessful in describing large-scale phenomena such as the formation and dynamics of cytoskeletal patterns (eg.: asters, vortices). However, the precise microscopic mechanisms underlying these processes are still the subject of considerable experimental and theoretical investigation. Moreover these multi-chain simulations are notoriously expensive and calculation of observables at time scales of practical interest is often not possible. Recently, a microscopic single-filament mean-field model to describe myosin-induced contraction of non-sarcomeric F-actin bundles was postulated by Lenz et al. [71]. Sarcomeres are highly organized structures from which striaded muscle is made. In sarcomeres, myosin motors are restricted to one end of filamentous actin, while passive permanent cross-linkers are present at the other end of the actin filaments. This structure is crucial to the contraction mechanism in sarcomeric actomyosin gels. However many contractile active gels found *in vivo* such as the contractile ring in the cytoplasm and smooth muscle fibers lack sarcomeric organization. In those systems contractility has been shown to arise from more microscopic mechanisms that originate at the single filament level [94, 119]. In this work we use a similar description of active gels to the one proposed by Lenz et al. [71]. However there are several issues in the level of description and mathematical formulation of the model of Lenz et al. [71] that we discuss and reformulate here.

1.3 Outline

In Chapter 2, published in the Journal of Rheology [16], we present a time-domain data analysis formalism and Brownian dynamics (BD) simulations for passive single-particle microbead rheology. Using these we perform Monte-Carlo simulations on synthetic data to evaluate and compare analysis algorithms for systems in which particles are trapped in linear or non-linear traps. We show that by including a small purely dissipative element in the memory function of the GLE we can eliminate inertia-related fast variables directly from the GLE to find an inertia-less GLE,

avoiding the singularity reported by McKinley et al. [89]. Using the inertia-less GLE the computational cost of the BD simulations are reduced by nearly five orders of magnitude. We also show that, in real systems, this purely dissipative element can arise from fluid inertia, since the Basset force acts dissipative at high frequencies.

In Chapter 3, published in Physics of Fluids [18], we use generalized data analysis and generalized Brownian dynamics simulations to examine the effects of higher order reflections and medium inertia in two-point passive microrheology. Our proposed analysis relies on recent analytic results of Ardekani and Rangel [3] for a purely viscous fluid, which are generalized to linear viscoelastic fluids. Implementation requires approximations to estimate Laplace transforms efficiently. These approximations are then used to create generalized BD simulation algorithms. The data analysis formalism presented here can expand the region of separation between the beads and frequencies at which rheological properties can be accurately measured using two-point passive microrheology. Moreover the additional physics introduced in the data analysis formalisms do not add additional significant computational costs.

In Chapter 4, published in Soft Matter [15], we extend our analysis for two-point passive microrheology to compressible viscoelastic solids. We show that the cross-correlations in the direction parallel to the line of centers is insensitive to compressibility, so may reliably be used to determine G^* alone. Although, the cross-correlation in the perpendicular direction may then be used to extract a constant Poisson ratio, it is relatively insensitive to its frequency dependence. We consider the example of a composite actin/microtubule network.

In Chapters 5 and 6 we introduce a single-chain mean-field mathematical model to describe the role of molecular motors in the mechanical properties of active gels. We model the semiflexible filaments that compose the active gel as bead-spring chains; the active interactions between filaments generated by molecular motors are

accounted for using a mean-field approach, in which filaments have prescribed probabilities to undergo a transition from one motor attachment state into the other depending on the state of the probe filament. The model allows physics that are not available in models postulated on coarser levels of description. Moreover it proposes a level of description that allows the prediction of observables at time scales too difficult to achieve in multi-chain simulations for realistic filament lengths and densities. In Chapter 5, published in RSC advances [17], we make several assumptions to simplify the mathematics and obtain analytical results. In Chapter 6 we relax some of the assumptions and apply the model introduced in Chapter 5 to describe the role of molecular motors in the mechanical properties of active gels.

CHAPTER 2

ELIMINATION OF INERTIA FROM A GENERALIZED LANGEVIN EQUATION: APPLICATIONS TO MICROBEAD RHEOLOGY MODELING AND DATA ANALYSIS

This Chapter previously appeared in the Journal of Rheology (The Society of Rheology), volume 56, issue 1, pages 185-212, year 2012.

2.1 Introduction

There are a variety of physical systems in which a well-defined separation of time scales exists; that is, a class of variables fluctuates on a time scale that is characteristically more rapid than the time scale of the remaining variables [31]. A well known and widely studied system is Brownian motion of micron-sized particles in suspension. Here one follows the position of the Brownian particles, since momentum fluctuates too rapidly to be observed.

In the technique called passive microbead rheology, a tracer bead of radius R sufficiently small to be subjected to Brownian motion ($R < 1\mu$m), but larger than the microstructure of the medium, is placed in a viscoelastic medium, and the trajectory or displacement of the bead is measured by some optical technique [86, 1, 128, 59, 112]. Unlike bulk rheometers, microbead rheology requires only very small samples (pico- to microliter order) and elastic modulus as small as 10-500 Pa can be measured [59]. These advantages make the technique especially useful for the analysis of biological samples [1, 128].

One-bead microrheology is limited to systems where the microstructure of the medium is smaller than the size of the bead. If this condition is not satisfied the continuum mechanics assumptions used in the analysis may become invalid. Two-bead microrheology is used to overcome this issue. In that technique the cross-correlation of two beads is used to estimate the rheological properties [73]. The

distance between the two beads is chosen to be larger than the characteristic length-scale of the material. In the present work our models are blind to the microstructure of the medium and the bead-medium interactions and we assume that continuum mechanics hold throughout. Extension of our methods to two bead microrheology is treated in Chapters 3 and 4.

The dynamics of a bead embedded in a viscoelastic medium are described by the generalized Langevin equation (GLE) [86]. A memory function accounts for the frictional resistance experienced by a diffusing particle in the GLE description. Because of the viscoelasticity, this frictional resistance is nonlocal in time and the frictional force experienced by a diffusing particle is influenced by its velocity at earlier times. The GLE description predicts ballistic behavior in the autocorrelation function of bead displacements at short time scales [52, 89, 28, 124]. In real systems the bead mass is very small and therefore the ballistic regime is usually not observed experimentally, not even in the highest-frequency measurements available [125, 124]. Therefore, eliminating the inertia-related fast variables from the GLE to obtain fundamental equations that can correctly describe the bead displacements inside the experimentally observable window provides a more efficient and simpler way of modeling and simulating passive microbead rheology.

There are however subtle physical and mathematical issues that arise in the elimination of inertia from the GLE. McKinley et al. [89] were the first to discuss the singular nature of the zero mass limit, by pointing out that there is an anomalous gap between the MSD derived by taking the zero-mass limit in the equation of motion and the MSD for finite bead mass. In a separate work [52] we address this issue in detail. For purposes of the present work the main conclusion is that, to eliminate bead inertia in a self-consistent way, one must have a high-frequency purely dissipative element in the memory kernel. This purely dissipative element can be introduced as a purely

viscous element arising from say solvent viscosity, but it can also come from the fluid inertia, since the Basset forces act as a purely dissipative element at high frequency damping the oscillations that arise from bead inertia. We have previously shown the occurrence of this inertia-driven damping in a one-mode Maxwell fluid [52], in this work we show that the results can be extended to multi-mode fluids.

The elimination of particle inertia from the Langevin Equation, used to describe the motions of colloidal particles suspended in Newtonian fluids, is a common, well-documented, practice [31, 47]. This procedure has been widely exploited in BD simulations to increase computational efficiency [47, 37]. The elimination of particle inertia from the GLE poses a more difficult mathematical problem that has not been fully explored and exploited. A method called adiabatic elimination is often used to eliminate fast or irrelevant degrees of freedom from the description of a system, resulting in a reduced and simpler description in terms of the remaining slow degrees of freedom [31, 107]. The method can be directly applied if the model describing the system is expressed in terms of Markovian equations (*i.e.*, Langevin equations). If the governing equations are non-Markovian (*e.g.*, the GLE), the elimination of fast variables might still be accomplished by the adiabatic elimination method, but the equations must first be reduced to Markovian equations [28, 107, 22, 92]. This means that before eliminating inertia one must specify a memory kernel, which must be discrete for the GLE to be written as a discrete system of Markovian equations. In this work we present an alternative method to eliminate inertia from the GLE in the frequency domain. Our approach to eliminate inertia from the GLE, produces results equivalent to the adiabatic elimination method but is mathematically simpler and does not require a discrete memory kernel to be specified before eliminating inertia. This means that the derived GLE is not limited to discrete memory kernels, but can be used with continuous memory kernels. Of course BD simulations of the GLE still requires discretization, but this may be accomplished after inertia elimination, using

either a generalized Maxwell or a continuous fraction approximation [22] of the memory function. This allows for a somewhat more general approach and avoids having to apply the method of adiabatic elimination for a high-dimensional system of stochastic differential equations.

Fricks et al. [28] have recently introduced direct GLE simulation and data analysis algorithms for microbead rheology. They developed an exact algorithm to generate particle trajectories efficiently from a GLE with a Prony series memory kernel with an arbitrary number of modes N, which corresponds to the generalized Maxwell model. They have also shown that the time-domain analysis of microbead rheology data is a valuable complement to formulas based on bead displacement statistics in the frequency domain [87, 110]. A very common approach to microbead rheology data analysis is to calculate the one-sided Fourier transform of the MSD from the trajectory data using fast Fourier transform (FFT) algorithms. These methods are known to introduce errors associated with frequency discretization and finite size windowing. In the method developed by Fricks et al. [28] a single trajectory of the bead is analyzed in the time-domain using the maximum likelihood estimators via the Kalman filter.

Following on those ideas we have developed a similar simulation and data analysis toolkit for microbead rheology. Our aim is to develop time-domain methods that can be extended to trapped particles. Traps can introduce non-linear terms in the GLE, and therefore the methods introduced and developed by Fricks et al. [28], which are highly efficient and exact for linear GLEs can not be applied. In microbead rheology there are various scenarios where particles might be trapped. For instance, some microbead rheology techniques use optical tweezers, which have been shown to exert non-conservative, non-linear forces on the particles [104, 103]. Also particles can be trapped by anharmonic potentials generated by a surrounding solid network

(*e.g.,* gel) [25, 116].

Simulations of the microbead rheology experiment have been shown to be useful for testing data analysis algorithms and data acquisition errors inherent to specific particle tracking techniques. For instance Brownian dynamics (BD) simulations have been used in Reference [106] to study dynamic and static errors in video-microscopy microrheology measurements. In that work, trajectories of a particle embedded in a purely viscous fluid were generated, with the aim of quantifying the effects of sampling time in the signal-to-noise ratio.

This Chapter is organized as follows. In Section 2.2 we describe how to eliminate inertia from a GLE in the frequency domain. In Section 2.3 we use the generalized Stokes relation (GSR) to relate the memory functions in the inertial and inertia-less GLEs to $G(t)$ and $J(t)$. We show that methods used to inter-convert between discrete forms of these material functions can be applied directly to the memory functions. In Section 2.4 the non-Markovian GLEs are lifted to higher-dimensional Markovian SDEs. The results of the synthetic MSD data generated with BD simulations, for beads embedded in viscoelastic fluids, are shown in section 2.5. Using our simulation toolkit we illustrate the synergistic effects of medium and particle inertia in in a multimode Maxwell fluid in Section 2.6. In Section 2.7, we show how to analyze the MSD data in the time domain to obtain J^* and G^*. In Section 2.8 we illustrate the elimination of inertia for particles trapped in anharmonic potentials and present BD simulations results for the case of a cubic trap.

2.2 Elimination of Inertia in the Generalized Langevin Equation

Neglecting particle inertia in the Langevin equation is a common, well documented practice in the modeling and simulation of colloidal particles suspended in Newtonian fluids [32, 47, 37]. If the particle and the media are isotropic, elimination

of particle inertia from the Langevin equation can be done simply, setting the particle mass equal to zero [37].

In GLEs, neglecting particle inertia is a more complicated and not fully explored problem. It was first addressed by Schaink et al. [107] using the method of adiabatic elimination. That approach requires the GLE to be made Markovian at the onset; the authors accomplish this by specifying a one-mode exponential memory kernel and using the method proposed by Dygas et al. [22] to rewrite the GLE as a higher dimensional Markovian system. This method was generalized to N-mode exponential memory kernels by McKinley et al. [89]. There are two limitations with that approach. The first one is that it limits *a priori* the memory kernels that can be used in the inetia-less GLE. The second problem is that unless $N \to \infty$ the inertia-less GLE does not produce bead displacement autocorrelations consistent with the complete GLE [89]. In this work we eliminate inertia directly from the GLE in the frequency domain and derive an inertia-less GLE that is not limited to discrete or exponential memory kernels. Additionally we show that for discrete exponential memory kernels, introducing a very small but purely dissipative element makes the autocorrelations derived from the inertia-less GLE consistent with the ones derived from the complete GLE, even for a small number of modes.

The dynamics of a bead embedded in a viscoelastic fluid are known to be described by a GLE [45, 13].

$$\frac{d\boldsymbol{p}_{\mathrm{b}}(t)}{dt} = -H_{\mathrm{e}}\delta\boldsymbol{r}_{\mathrm{b}}(t) - \int_{-\infty}^{t} \zeta(t-t')\frac{\boldsymbol{p}_{\mathrm{b}}(t')}{m}dt' + \boldsymbol{f}_{\mathrm{B}}(t), \tag{2.1}$$

Where k_{B} is the Boltzmann constant and T is the temperature. If fluid inertia is not considered, m is purely bead mass, but in the presence of fluid inertia, the mass of fluid dragged around with the bead should be included in m. $\zeta(t)$ is the memory function, which has been written as a scalar, implying that we consider only isotropic particles and materials. The models presented in this work can be extended to non-

spherical particles or anisotropic materials by using an appropriate tensorial form for $\zeta(t)$. The external force to trap the particle around a fixed position is assumed to be linear with restoring constant H_{e}. The trapping force is often produced by an optical tweezer in experimental systems. Although recent work has shown that optical traps can exert nonlinear nonconservative forces on particles [104, 103], the linear approximation is commonly used for the trapping force for laser tweezers and small bead displacement [36, 95]. The microbead rheology simulation toolkit presented in this work is generalized to nonlinear traps in Section 2.8. $\delta\boldsymbol{r}_{\mathrm{b}}$ is the displacement of the bead from the equilibrium position of the trap and $\boldsymbol{p}_{\mathrm{b}}$ is the momentum. The random force on the bead satisfies the fluctuation dissipation theorem

$$\langle \boldsymbol{f}_{\mathrm{B}}(t)\boldsymbol{f}_{\mathrm{B}}(t')\rangle_{\mathrm{eq}} = k_{\mathrm{B}}T\zeta(t-t')\boldsymbol{\delta}. \tag{2.2}$$

Because of the integral that appears in the GLE, the elimination of the inertia-related fast variable, $\boldsymbol{p}_{\mathrm{b}}$, may not seem simple, at first sight. However, the elimination of the momentum is straightforward in the frequency domain. By taking the two-sided Fourier transform of the GLE, eq.(2.1), we obtain

$$-m\omega^2\delta\boldsymbol{r}_{\mathrm{b}}[\omega] = -H_{\mathrm{e}}\delta\boldsymbol{r}_{\mathrm{b}}[\omega] - i\omega\bar{\zeta}[\omega]\delta\boldsymbol{r}_{\mathrm{b}}[\omega] + \boldsymbol{f}_{\mathrm{B}}[\omega] \tag{2.3}$$

where $\delta\boldsymbol{r}_{\mathrm{b}}[\omega] = \mathcal{F}\{\delta\boldsymbol{r}_{\mathrm{b}}(t)\} := \int_{-\infty}^{\infty}\delta\boldsymbol{r}_{\mathrm{b}}(t)e^{-i\omega t}dt$ is the two-sided Fourier transform of the bead displacement and $\bar{\zeta}[\omega]$ is the one-sided Fourier transform of the memory kernel (*i.e.,* $\bar{\zeta}[\omega] \equiv \bar{\mathcal{F}}\{\zeta(t)\} := \int_0^{\infty}\zeta(t)e^{-i\omega t}dt$). We indicate the Fourier transform by frequency argument with square brackets, and one-sided transform by an over-bar. In the frequency domain, eq. (2.2) can be written as

$$\langle \boldsymbol{f}_{\mathrm{B}}[\omega]\boldsymbol{f}_{\mathrm{B}}[\omega']\rangle_{\mathrm{eq}} = 2\pi k_{\mathrm{B}}T\delta(\omega+\omega')\zeta[\omega]\boldsymbol{\delta}. \tag{2.4}$$

Note that it is the two-sided Fourier transform of $\zeta(t)$ that arises here. The presence of $\delta(\omega+\omega')$ in eq.(2.4) indicates that $\boldsymbol{f}_{\mathrm{B}}$ is a stationary process. Now making the left

side of eq. (2.3) zero and solving for $\delta \boldsymbol{r}_{\mathrm{b}}$, we obtain the GLE without inertia for the bead displacement

$$i\omega \delta \boldsymbol{r}_{\mathrm{b}}[\omega] = -H_{\mathrm{e}} \bar{\mu}[\omega] \delta \boldsymbol{r}_{\mathrm{b}}[\omega] + \boldsymbol{g}_{\mathrm{B}}[\omega] \tag{2.5}$$

where $\bar{\mu}[\omega]$ is the one-sided Fourier transform of the memory function with respect to the inertia-less bead motion. This is given as unity divided by the one-sided Fourier transform of the original memory function,

$$\bar{\mu}[\omega] := \frac{1}{\bar{\zeta}[\omega]}. \tag{2.6}$$

For non-spherical particles or anisotropic materials the inertia-less memory function is defined by $\bar{\boldsymbol{\zeta}}[\omega] \cdot \bar{\boldsymbol{\mu}}[\omega] = \boldsymbol{\delta}$. The second term in the right side of eq.(2.5) is the colored noise defined by

$$\boldsymbol{g}_{\mathrm{B}}[\omega] := \bar{\mu}[\omega] \boldsymbol{f}_{\mathrm{B}}[\omega]. \tag{2.7}$$

Using eqs. (2.6) and (2.4), it can be proven that it satisfies the FDT

$$\begin{aligned} \langle \boldsymbol{g}_{\mathrm{B}}[\omega] \boldsymbol{g}_{\mathrm{B}}[\omega'] \rangle_{\mathrm{eq}} &= \langle \bar{\mu}[\omega] \boldsymbol{f}_{\mathrm{B}}[\omega] \bar{\mu}[\omega'] \boldsymbol{f}_{\mathrm{B}}[\omega'] \rangle_{\mathrm{eq}} \\ &= 2\pi k_{\mathrm{B}} T \delta(\omega + \omega') \frac{|\bar{\mu}[\omega]|^2}{2\mathcal{R}\{\bar{\mu}[\omega]\}} \boldsymbol{\delta} \\ &= 2\pi k_{\mathrm{B}} T \delta(\omega + \omega') \mu[\omega] \boldsymbol{\delta} \end{aligned} \tag{2.8}$$

where $\mu[\omega]$ is the two-sided Fourier transform of $\mu(t)$ $\left(= \bar{\mathcal{F}}^{-1}\{\bar{\mu}[\omega]\}\right)$. By taking the two-sided inverse Fourier transform of eq. (2.5), the general form of the inertia-less GLE in the time domain can be obtained as

$$\frac{d\delta \boldsymbol{r}_{\mathrm{b}}(t)}{dt} = -H_{\mathrm{e}} \int_{-\infty}^{t} \mu(t - t') \delta \boldsymbol{r}_{\mathrm{b}}(t') dt' + \boldsymbol{g}_{\mathrm{B}}(t), \tag{2.9a}$$

$$\langle \boldsymbol{g}_{\mathrm{B}}(t) \boldsymbol{g}_{\mathrm{B}}(t') \rangle_{\mathrm{eq}} = k_{\mathrm{B}} T \mu(t - t') \boldsymbol{\delta}. \tag{2.9b}$$

Equation (2.9) describes the bead motion except at the short-time regime $t \leq \sqrt{m/H_{\mathrm{e}}}$ where inertial effects are not negligible. The simplicity of the mathematical procedure

presented to eliminate particle inertia from the GLE does not imply that the effects of particle inertia should be treated as irrelevant in the analysis of microbead rheology. The procedure presented to eliminate inertia from the GLE is effectively equivalent to applying an optimal low pass filter in the frequency domain to the Brownian force to eliminate the high frequencies where inertial effects are present. This is clear in eq.(2.7), where the inertia-less Brownian force is defined; the memory function is acting as a low pass filter. In recent microrheology experiments where high-frequency measurements (up to 10^6 rad/s) are made of wormlike micelle solutions oscillations are not observed in the MSD. This indicates that in real measurements, the high frequency inertial components of the Brownian force are being filtered out by dissipative elements in the medium.

The GLEs derived in this section can be solved to obtain relations between positional autocorrelation functions of the bead (*e.g.*, MSD, power spectral density) and the memory functions ζ or μ. The positional autocorrelation functions of the bead are observable quantities, while the memory functions contain combined information about the rheological properties of the medium, and size of the probe bead.

One widely used equation in the analysis of microbead rheology is the GSER, which relates the G^* to the MSD in the frequency domain. The GSER is comprised of two important relations. The Einstein component of the GSER, which relates the MSD to the memory function ζ in the frequency domain, is a solution to eq.(2.1). Additional assumptions and equations are required to extract rheological properties from the memory functions, which comprise the Stokes component of the GSER.

2.3 Spectral Decomposition of the memory function

Eqs. (2.1) and (2.9) can be used to relate an observable quantity (positional autocorrelations of a probe bead) with the response of the fluid to the bead. However

we usually seek a material property of the fluid, *i.e.*, G^* or J^*. If the the probe size is much larger than the microstructure of the material, constitutive equations from continuum mechanics can be used to find a relation between the memory function and the material property. To obtain the so-called generalized Stokes relation (GSR) for viscoelastic fluids, we make use of the correspondence principle between the equation of motion for a Newtonian fluid (creeping flow) and for a linear viscoelastic material in the frequency domain [69, 129, 126]. According to the correspondence principle, we make the substitution $\eta \to G^*/(i\omega)$ in the Stokes relation for Newtonian fluid to obtain the GSR

$$\bar{\zeta}[\omega] = \frac{6\pi G^*(\omega) R}{i\omega}. \tag{2.10}$$

In the last equation, the terms corresponding to fluid inertia are neglected. This simplification is justified at frequencies much smaller than the characteristic frequency of fluid inertia determined from the penetration length around the bead [67, 126, 77, 52]. We consider the effects of fluid inertia in Section 2.6.

Since the creep compliance and the dynamic modulus are related by $G^*(\omega)J^*(\omega) = 1$, the GSR can be expressed in terms of the creep compliance and the memory function for the GLE with no particle inertia as

$$\bar{\mu}[\omega] = \frac{J^*(\omega) i\omega}{6\pi R}. \tag{2.11}$$

Equations (2.10) and (2.11) indicate that efficient methods for conversion between the dynamic modulus and the creep compliance may be directly adapted to obtain $\mu(t)$ from $\zeta(t)$. We use here a procedure introduced by Baumgaertel and Winter [6] for a discrete relaxation spectrum.

A specific functional form for $G(t)$ and $J(t)$ must now be prescribed to obtain a final, useful form of the memory functions. These functions are defined through the relaxation spectrum $H(\lambda)$ of the fluid and can be obtained by a simple integral

transformation, *e.g.*,

$$G(t) = \int_0^\infty H(\lambda) e^{-t/\lambda} \frac{d\lambda}{\lambda}. \tag{2.12}$$

The relaxation spectrum $H(\lambda)$ can be continuous or discrete (*i.e.*, a sum of Dirac delta functions). One continuous relaxation spectrum that has been widely used for describing material functions obtained from molecular models is the BSW spectrum [7]. However, for convenience in data analysis and modeling of viscoelastic materials, discrete representations of the relaxation or retardation spectrum are often used. Moreover, a continuous spectrum can be approximated to arbitrary accuracy by a discrete spectrum [5, 7]. Note that eq. (2.9) can be used with any type of memory kernel, discrete or continuous, in contrast to previous works where a discrete memory kernel is specified [107] before eliminating particle momentum from the GLE. Therefore, continuous spectra such as the BSW spectrum can be used with this equation.

In what follows, we consider a discrete relaxation spectrum. We assume that its dynamic modulus is described in terms of the generalized N-mode Maxwell model plus a purely viscous element which takes into account the presence of a solvent or of faster, unresolvable viscoelastic modes. The inclusion of a purely dissipative element in the dynamic modulus of the medium is a novel idea that allows us to eliminate particle inertia avoiding the singularity observed in the inertia-less MSD by McKinley et al. [89]. Details of the physical origins of this purely dissipative term and its relation to inertial effects are given elsewhere [52].

$$G^*(\omega) = i\omega\eta_0 + \sum_{j=1}^{N} \frac{g_j \lambda_j i\omega}{1 + \lambda_j i\omega}, \tag{2.13}$$

where g_j and λ_j are the elastic modulus and the relaxation time of the j-th Maxwell element respectively, and η_0 is the viscosity of the purely viscous element. This viscosity can be very small, even experimentally undetectable, but it should be finite

to avoid the inertia-less singularity. Inserting eq. (2.13) into eq. (2.10) we obtain

$$\bar{\zeta}[\omega] = \zeta_0 + \sum_{j=1}^{N} \frac{H_j \lambda_j}{1 + \lambda_j i\omega}. \tag{2.14}$$

where $H_j := 6\pi R g_j$ and $\zeta_0 = 6\pi R \eta_0$. Taking the inverse one- sided Fourier transform of eq. (2.14), we obtain the expression for the memory function in the time domain as

$$\zeta(t) = 2\zeta_0 \delta(t) + \sum_{j=1}^{N} H_j e^{-t/\lambda_j}. \tag{2.15}$$

Now that the memory function for the complete GLE (eq.(2.6)) has been specified, we seek an efficient procedure to find the spectrally decomposed memory function for the inertia-less GLE. Since the one-sided Fourier transforms of $\zeta(t)$ and $\mu(t)$ are directly proportional to G^* and J^* respectively, methods for calculating the retardation spectrum from a relaxation spectrum can be directly used to solve the problem. The memory function for the inertia-less GLE in the time domain is found to be,

$$\mu(t) = 2\mu_0 \delta(t) - \sum_{j=1}^{N} c_j e^{-t/\Lambda_j} \tag{2.16}$$

where the parameters μ_0, $\{c_j\}$ and $\{\Lambda_j\}$, which specify J^* and $\mu(t)$ using the procedure described in Reference [5] after setting the values for ζ_0, $\{H_j\}$ and $\{\lambda_j\}$. The cited procedure reduces to finding the roots of a polynomial to obtain $\{\Lambda_j\}$ and solving a linear system of equations to obtain μ_0 and $\{c_j\}$.

All the elements necessary to relate bead displacement autocorrelations to the rheological properties of the viscoelastic medium have now been presented. In what follows, we use these models to create computer simulations of passive microbead rheology experiments. To that end, a discrete G^* is specified and using eqs.(2.15) and (2.16) memory functions for the inertia and inertia-less GLEs calculated. We consider two different viscoelastic fluids, whose relaxation spectra are shown in Tables 2.1-2.2. Using the procedure described in the next section simulations can then be used to produce autocorrelation functions of the bead displacements.

Table 2.1. Parameters that define the discrete modulus and creep compliance of a fluid with 4 closely spaced Maxwell modes (M4C). Parameters are made dimensionless using $\sqrt{k_{\mathrm{B}}T/H_{\mathrm{e}}}$ as the characteristic length scale and the smallest $\lambda(=\lambda_1)$ as characteristic time scale. ($\zeta_0^* = 0.1$, $\mu_0^* = 10$).

Input				
j	H_j^*	λ_j^*	c_j^*	Λ_j^*
1	4.0	1.0	1.0×10^{2}	1.0×10^{-2}
2	3.0	5	1.7×10^{-2}	1.5
3	2.0	10	4.7×10^{-4}	7.0
4	1.0	18	5×10^{-6}	16
Output				
1	2.8	8.5×10^{-1}	9.8×10^{1}	1.0×10^{-2}
2	4.5	3.5	1.9×10^{-3}	1.1
3	2.7	16	1.6×10^{-4}	7.1
4	$--$	$--$	$--$	$--$

Table 2.2. Parameters that define the discrete modulus and creep compliance of a fluid with 4 widely spaced Maxwell modes (M4W). Parameters are made dimensionless using $\sqrt{k_B T/H_e}$ as the characteristic length scale and the smallest λ as characteristic time scale. ($\zeta_0^* = 0.1$, $\mu_0^* = 10$).

Input				
j	H_j^*	λ_j^*	c_j^*	Λ_j^*
1	4.0	1.0	1.0×10^{2}	1.0×10^{-2}
2	3.0	1.0×10^{1}	2.1×10^{-2}	1.6
3	2.0	1.0×10^{2}	3.5×10^{-4}	1.9×10^{1}
4	1.0	1.0×10^{3}	5.6×10^{-6}	2.6×10^{2}
Output				
1	3.8	9.7×10^{-1}	9.9×10^{1}	1.0×10^{-2}
2	3.3	8.8	2.2×10^{-2}	1.5
3	2.1	1.2×10^{2}	4.6×10^{-5}	18
4	8.4×10^{-1}	1.2×10^{3}	3.5×10^{-7}	3.5×10^{2}

The relations derived in this section are also the starting point for constructing data analysis algorithms for microbead rheology. In that case the goal is to obtain rheological properties of the host medium from the bead displacement autocorrelation (*i.e.*, MSD) data obtained from an experiment. As discussed in section 2.2, the memory functions can be related to the MSD from solutions to eq.(2.1) for the complete GLE or eq.(2.9) for the inertia-less GLE. Then eq.(2.10) or eq.(2.11) can be used to obtain a relation between the probe motion and G^* or J^* respectively. In the next section we discuss in detail how to obtain G^* from MSD data.

As a consistency check we perform computer simulated experiments in which G^* is specified *a priori*. We then use the simulated MSD to calculate an output G^*. The input and output G^* should be equivalent.

2.4 Markovian Stochastic Differential Equations

Lower-dimensional non-Markovian SDEs can be written as equivalent higher-dimensional Markovian SDEs. In this section the non-Markovian GLEs (2.1) and (2.9) with memory functions (2.15) and (2.16), respectively, are written as Markovian SDEs by introducing new stochastic variables with white noise spectra. In this particular case, the complete GLE eq.(2.1) is a 6-dimensional system, comprised of 3-dimensional equations for momentum and displacement. The Markovian SDEs are necessary for performing the Brownian dynamics simulations presented in the next section. We follow the methodology presented by Fricks et al. [28] for GLEs for exponential multi-mode memory kernels, in which only one additional stochastic variable is introduced per mode. Dygas et al. [22] had previously presented the same procedure for a 2-mode memory kernel. The Markovian SDE for particle momentum is given by,

$$d\boldsymbol{p}_b(t) = -\left(H_e \delta \boldsymbol{r}_\mathrm{b}(t) + \sum_{j=1}^{N} H_j \boldsymbol{Q}_j(t) + \frac{\zeta_0}{m}\boldsymbol{p}_\mathrm{b}(t) \right) dt + \sqrt{2k_\mathrm{B}T\zeta_0}\, d\boldsymbol{W}_0(t) \tag{2.17}$$

where $\boldsymbol{Q}_j$ are the new stochastic variables introduced to make the system Markovian. The SDEs for $\boldsymbol{Q}_j$ are found to be

$$d\boldsymbol{Q}_j(t) = \frac{\boldsymbol{p}_\mathrm{b}}{m}dt - \frac{\boldsymbol{Q}_j(t)}{\lambda_j}dt + \sqrt{\frac{2k_\mathrm{B}T}{\lambda_j H_j}}\, d\boldsymbol{W}_j(t), \qquad (j = 1, 2, ..., N) \tag{2.18}$$

where the N+1 Wiener processes $\{\boldsymbol{W}_j\}$ $(j = 0, 1, 2, ..., N)$ have white-noise properties, *i.e.*,

$$\langle d\boldsymbol{W}_j(t)\rangle_\mathrm{eq} = 0, \qquad \langle d\boldsymbol{W}_i(t) d\boldsymbol{W}_j(t')\rangle_\mathrm{eq} = \delta(t-t')\delta_{ij}\boldsymbol{\delta} dt dt'. \tag{2.19}$$

The resulting Markovian system of SDEs is a set of $6 + 3N$ equations, which includes the 3D equations for momentum, displacement and $3N$ additional stochastic variables. It is possible to prove that eqs.(2.17-2.18) are equivalent to eq.(2.1) by integrating eq.(2.18) by parts and inserting the solution for $\boldsymbol{Q}_j$ into eq.(2.17). The remaining statistics follow from eq.(2.19).

The derivation of eqs.(2.17) and (2.18) is purely mathematical. However there is a mathematical isomorphism between the evolution equations for the simple physical system shown in Figure 2.1A and the Markovian SDEs that describe the motion of a bead embedded in a viscoelastic fluid. In the physical system depicted in Figure 2.1A a labeled Brownian bead trapped by an elastic spring of strength H_{e} is embedded in a purely viscous fluid. A viscous drag force and a delta correlated Brownian force act directly on it. Additionally the labeled bead is connected to N other virtual Brownian beads by virtual springs with strengths H_1, H_2, ...H_N. $\boldsymbol{Q}_j$ is a vector connecting the real bead to the virtual beads and gives the deformation of the virtual springs.

Similarly, the particle motion described by the GLE without inertia (eq. (2.9)) with memory function (eq.(2.16)) can be written as an equivalent higher-dimensional Markovian system of SDEs. In this case, the complete GLE is comprised of a 3-dimensional equation for the particle displacement. The procedure for reducing the non-Markovian inertia-less GLE to Markovian SDEs is similar to the one used for the GLE with inertia. However, since the memory functions have slightly different forms, the results are different. The SDE for the particle displacement in this case is,

$$\begin{aligned} d\delta\boldsymbol{r}_{\mathrm{b}}(t) &= -\left(H_{\mathrm{e}}\mu_0\delta\boldsymbol{r}_{\mathrm{b}}(t) + \sum_{j=1}^{N}\frac{c_j\boldsymbol{Q}_j(t)}{\mu_0}\right)dt + \\ &\sqrt{2k_{\mathrm{B}}T\left(\mu_0 - \sum_{j=1}^{N}c_j\Lambda_j\right)}d\boldsymbol{W}_0(t) + \sum_{j=1}^{N}\sqrt{2k_{\mathrm{B}}Tc_j\Lambda_j}d\boldsymbol{W}_j(t) \quad (2.20) \end{aligned}$$

where here again $\boldsymbol{Q}_j$ are the new stochastic variables introduced to make the system Markovian. Baumgaertel and Winter [5] have shown that the term $\mu_0 - \sum_{j=1}^{N} c_j\Lambda_j$ is guaranteed to be positive according to the constraints.

The SDEs for $\boldsymbol{Q}_j$ can be written as

$$d\boldsymbol{Q}_j(t) = -\left(H_{\mathrm{e}}\mu_0\delta\boldsymbol{r}_{\mathrm{b}}(t) + \frac{\boldsymbol{Q}_j(t)}{\Lambda_j}\right)dt + \sqrt{\frac{2k_{\mathrm{B}}T\mu_0^2}{c_j\Lambda_j}}d\boldsymbol{W}_j(t), \quad (j = 1, 2, ..., N) \tag{2.21}$$

where the $N+1$ Wiener processes $\{\boldsymbol{W}_j\}$ $(j = 0, 1, 2, ..., N)$ satisfy eq. (2.19)

Here again a mathematical isomorphism exists between eqs.(2.20) and (2.21) and the simple physical system depicted in Figure 2.1B. In this case, $N+1$ delta-correlated Brownian forces are acting directly on the labeled Brownian bead, which again is trapped by an elastic spring. However the spring constant has been modified with respect to the system with inertia. Here too, the labeled bead is connected by springs to N virtual Brownian beads and the stochastic variables $\boldsymbol{Q}_j$ can be interpreted as the displacement of the virtual Brownian beads.

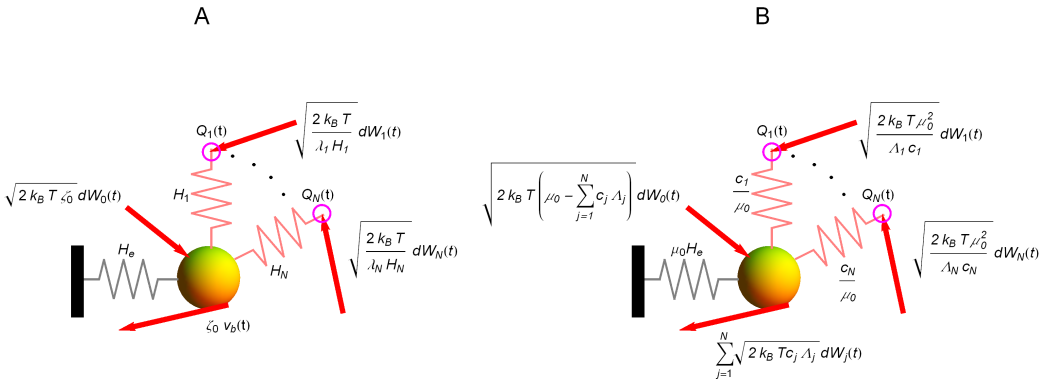

Figure 2.1. Diagram of a physical system whose evolution equations are mathematically isomorphic to A: GLE with particle inertia eq.(2.1) and B: inertia-less GLE eq.(2.9)

It is illustrative to consider an example where the inertia-less model can be expressed analytically in terms of the original material parameters. We consider a three-parameter model comprised of a single Maxwell element and a purely viscous element originating from the solvent viscosity. The viscoelastic parameters are H, λ

and ζ_0. The original memory function for the three element model is

$$\zeta(t) = 2\zeta_0\delta(t) + He^{-t/\lambda}. \tag{2.22}$$

By setting $N = 1$ we obtain $\mu_0 = 1/\zeta_0$, $c = H/\zeta_0^2$, and $\Lambda = \zeta_0\lambda/(H\lambda + \zeta_0)$. Thus, the memory function for the inertia-less GLE becomes

$$\mu(t) = \frac{2}{\zeta_0}\delta(t) - \frac{H}{\zeta_0^2}e^{-t\left(\frac{H}{\zeta_0}+\frac{1}{\lambda}\right)}. \tag{2.23}$$

In the next section, materials with multi-mode relaxation spectra are considered.

2.5 Brownian Dynamics simulations

Fricks et al. [28] have proposed an efficient algorithm to generate sample paths from a GLE with a memory kernel given by the generalized Maxwell model. Their method takes advantage of the fact that the GLE to be simulated has no non-linear elements. Therefore they can use the quadrature solution of the higher dimensional Markovian process that is derived from the GLE after specifying the generalized Maxwell model kernel. Since the method uses the analytical solution, the simulated sample paths are guaranteed not to be polluted with time-discretization errors. Additionally they have established appropriate sampling rates of the quadrature solution to properly resolve the bead position autocorrelations.

However for GLEs that contain non-linear elements (*i.e.*, particles trapped in anharmonic potentials) analytical quadrature solutions can not be written for eqs. (2.17) and (2.18) or for eqs. (2.20) and (2.21), and a discrete numerical method must be used to generate the bead displacement trajectories. Additionally, since the physics of external particle traps or purely elastic elements of the medium appear at long time scales, it becomes necessary to simulate longer bead trajectories. These longer trajectories, in turn, require an appropriate method for processing long bead-displacement trajectories. To observe all the relevant time scales of the materials

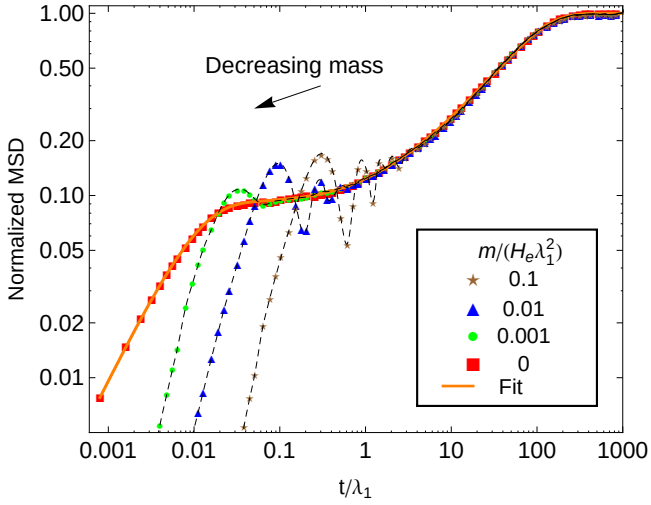

Figure 2.2. Simulated MSD for different values of bead mass in a 4-mode fluid (M4C). Corresponding input parameters for this simulation are shown in Table 2.1. The continuous line is the fit of eq. (2.27) to the inertia-less MSD.

considered here we have developed our simulation toolkit by adapting widely used algorithms for BD dynamics simulations [31] and time-domain correlators [84].

We start by making the Markovian stochastic differential equations with and without inertia, eqs. (2.17), (2.18), (2.20) and (2.21) dimensionless by using $\sqrt{k_{\rm B}T/H_{\rm e}}$ as the characteristic length scale and the smallest relaxation time, λ =min$\{\lambda_j\}$, as the characteristic time scale (dimensionless parameters are denoted by an asterisk). We have used either an explicit vector Euler algorithm or the more stable, weak vector semi-implicit algorithm [32, 96] for discretization of the SDEs. The choice of algorithm, for a specific simulation, depends on the stiffness of the memory function and the particle trap. Time steps of $10^{-5} \leq \Delta t/\lambda \leq 10^{-3}$ were used. The simulation results presented here were convergent and stable in this range of time-step sizes. To observe all the characteristic relaxation time scales of the synthetic fluids introduced in Tables 2.1-2.2 a long-time trajectory for the probe particle is simulated. A typical trajectory consists of 10^9 time steps, and storage of these trajectories is computationally impractical. Therefore an adaptation of a multi-tau photon correlation

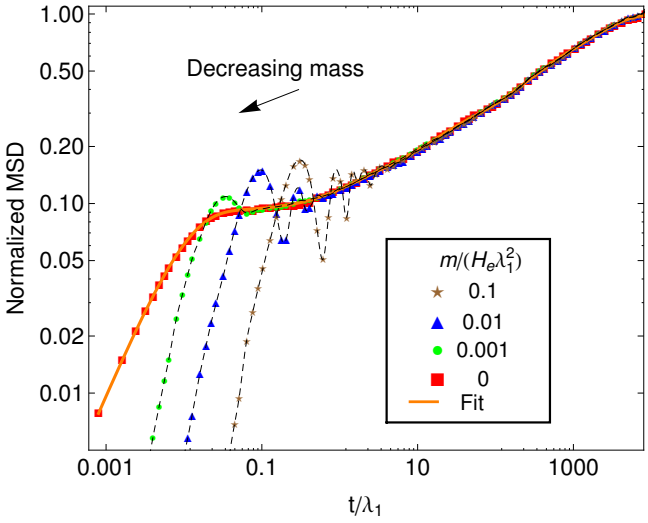

Figure 2.3. Simulated MSD for different values of bead mass in a 4-mode fluid with widely spaced modes (M4W). Corresponding input parameters for this simulation are shown in Table 2.2. The continuous line is the fit of eq. (2.27) to the inertia-less MSD.

spectroscopy (PCS) algorithm [27, 84, 76] was used to calculate the MSD during the simulations. Instead of storing the complete trajectory and calculating the MSD in post-processing, the MSD at specified lag times (on the order of 10^2) is calculated in real time during the simulations. The PCS algorithm makes use of correlators with adjustable size and sample rate. Each correlator is used to calculate the MSD in a different range of lag times. The results from all the correlators are assembled to obtain the MSD over a wide range of time scales. Between six and seven correlators, fed with 10^4 trajectory points, were used to obtain each of the MSDs presented in this work, which span over six decades of lag times. The PCS method allows us to calculate positional autocorrelation functions of very long trajectories, using 5 orders of magnitude smaller storage [76]. An extensive study of the effect of sample rate and its associated errors induced by this in the calculation of autocorrelation functions by the PCS has been presented by Magatti and Ferri [84]

Figure 2.2 shows the MSD calculated with the BD simulations for a particle

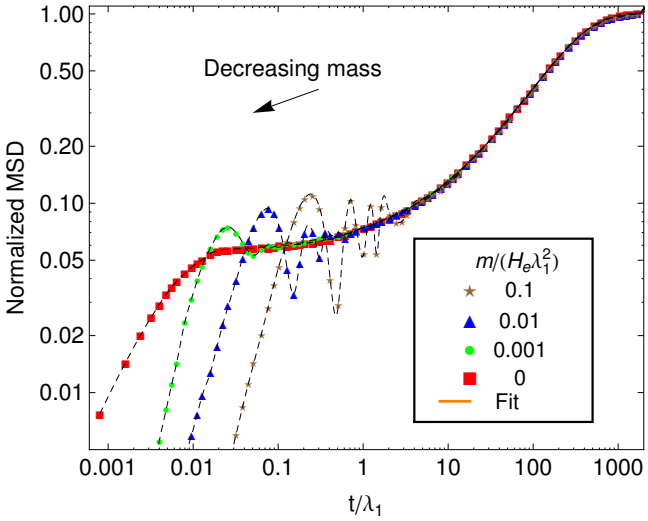

Figure 2.4. Simulated MSD for different values of bead mass in a 10-mode fluid (M10). Input parameters: $H_j/H_e = \{5, 4, 3, 2, 1, 0.5, 0.4, 0.3, 0.2, 0.1\}$, $\lambda_j/\lambda_1 = \{1, 7, 12, 17, 34, 52, 63, 75, 86, 94\}$ and $\zeta_0 = 0.1$

embedded in a fluid described by 4, closely spaced, Maxwell modes. We have performed simulations using the SDEs which include inertia for three different values of particle mass, eqs.(2.17) and (2.18). In the simulations that include particle inertia, the mass was set to artificially large values, to illustrate inertial effects. Oscillations can be observed in the MSD of simulations performed with equations where particle mass is retained. This behavior has also been previously discussed and observed in theoretical constructions of the MSD [124, 89, 52]. The time range during which the oscillations occur is determined by the particle mass and the trap stiffness; more precisely the characteristic time of the oscillation is $\lambda_m = \sqrt{m/H_e}$. The oscillations in the MSD stem from the resonance between the elastic component and the inertia of the bead. For time scales large compared to λ_m, the fluctuations in particle momentum relax to zero and the effects of particle inertia become negligible. As mass is made smaller, the MSD obtained from the simulations that include particle inertia approach the MSD obtained with the inertia-less SDEs. This shows that the results from the complete GLE converge to our derived inertia-less GLE, thus providing an

independent confirmation for our derivation.

Figure 2.3 corresponds to the MSD of a bead embedded in a fluid with 4 Maxwell modes but in this case the modes are widely spaced and therefore the spectrum is broader. To illustrate that the simulation is not limited by the number of modes in the material Figure 2.4 shows the MSD of a particle embedded in a fluid with 10 Maxwell modes. Again as the mass is progressively made smaller the results from the simulations performed with the SDEs that include bead inertia approach the inertia-less results.

A feature that is common to all the MSD curves plotted in Figs.2.2-2.4 is the plateau reached at long time scales. This plateau in the MSD appears because the particle is trapped; if the particle were not trapped, it would behave in a purely diffusive way at long time scales. The value of the MSD at this plateau depends on the trap stiffness and is $\langle \Delta\delta r_{\mathrm{b}}^2(t=\infty)\rangle_{\mathrm{eq}} = 6k_{\mathrm{B}}T/H_{\mathrm{e}}$. The continuous lines in Figs. 2.3 and 2.4 are the least-squares fits of $6k_{\mathrm{B}}T/H_{\mathrm{e}}$ minus a sum of exponentials to the MSD generated by the BD simulation. We explain below what the exact form of this fitted function is and how it can be used to calculate G^* or J^*.

The main motivation to eliminate particle inertia from the complete GLE for particle momentum was to obtain a simpler, more efficient model, that could describe correctly the observable trajectory of a particle embedded in a viscoelastic medium. In real systems, where the particle mass is very small and the solvent viscosity is small but finite, effects of particle inertia appear only in the high frequency regime. In a typical system, $\omega_{\mathrm{m}} := 1/\lambda_{\mathrm{m}}$ is of the order of 10 MHz [113]. In the simulations performed with eqs.(2.17) and (2.18), the small particle mass limit is hard to approach numerically since as mass is made smaller the bead position fluctuates faster making it necessary to use very small time steps $\Delta t \ll \lambda_m$ to achieve convergent and stable solutions. If the zero particle mass limit is to be approached numerically, the time-

step size must be reduced proportionally to keep the BD simulations stable. These issues can be avoided simply by using the inertia-less SDEs, eqs.(2.20) and (2.21). With these equations the experimentally observable MSD can be simulated using BD with much less computational cost. This implies the computation time for simulating the observable frequency window for a typical real system can be reduced by a factor as high as 10^4. Additionally there is a less significant reduction in the computation time of the inertia-less simulations caused by the elimination of one variable (*i.e.*, momentum) from the description of the system.

In a recent work [52], we discussed in detail the importance of the purely viscous element in the dynamic modulus of the fluid for safely eliminating inertia. If the zero-particle-mass limit is taken without the presence of a purely viscous element, the frequency of oscillation ω_{m} diverges and the correct long-time plateau in the MSD, *i.e.*, $\langle \Delta\delta r_{\mathrm{b}}^2(t=\infty)\rangle_{\mathrm{eq}} = 6k_{\mathrm{B}}T/H_{\mathrm{e}}$ is not produced. However, in the presence of a (very small) purely viscous element, particle inertia can be eliminated safely and the inertia-less model reproduces correctly the MSD of the model with inertia at time scales larger than λ_{m}. At short time scales, the inertia-less model produces a MSD in which inertial effects do not appear and the behavior changes from ballistic ($\sim t^2$) to diffusive ($\sim t$). In real fluids the purely viscous element can be interpreted as the presence of a solvent or as the diffusive part of a faster viscoelastic mode of the fluid that is outside the experimentally observable window. The purely viscous element can also come from the the fluid inertia, which at high frequencies acts dissipative, as shown in the next section.

2.6 Medium Inertia

When writing eq.(2.10) we neglected the terms corresponding to medium inertia. These inertial contributions from the fluid are comprised of the fluid mass dragged by the bead and the viscoelastic Basset force. This last term can be ne-

glected if $\omega \ll \omega_{\mathrm{M}}$ where ω_{M} is determined by

$$\sqrt{\frac{|G^*(\omega_{\mathrm{M}})|}{\rho R^2}} = \omega_{\mathrm{M}}. \tag{2.24}$$

If the Basset force is taken into account, eq. (2.10) becomes [52]

$$\bar{\zeta}[\omega] = \frac{6\pi R G^*(\omega)}{i\omega} + 6\pi R^2 \sqrt{\rho G^*(\omega)}. \tag{2.25}$$

Where ρ is the medium density. And m in eq.(2.1) should now be taken as an effective mass which includes the mass of fluid dragged by the bead. In Figure 2.5, BD simulation results that include both bead inertia and fluid inertia are shown. The input dynamic modulus used for these simulations corresponds to a fluid with 4 Maxwell modes (M4C, Table 2.1). For these simulations the purely viscous element was not included in the memory functions.

To perform BD simulations that include fluid inertia, the inverse one-sided Fourier transform of eq.(2.25) has to be calculated. The Basset-force term, which includes the square root of G^* can not be inverted to the time-domain analytically. We have therefore used a rational minimax approximation [40] of the Basset force term, which is valid in the frequency range at which the simulations are performed. The rational approximation can easily be transformed to the time-domain. Putting the spectrally decomposed dynamic modulus for the M4C fluid (Table 2.1) and the rational approximation for the Basset force in eq.(2.25) and taking the inverse one-sided Fourier transform, an 8-mode exponential memory kernel is obtained, with the 4 Maxwell modes coming from the Stokes component and 4 additional modes coming from the Basset force.

The main effect of introducing fluid inertia is that the oscillations in the MSD are damped. For time scales smaller than λ_{m} the MSD assumes a ballistic behavior ($\sim t^2$). For the red squares in Figure 2.5 bead inertia has been eliminated, but keeping a small value of fluid density. Note that no gap is observed between this result and

the results that include bead inertia. The only difference being that a purely diffusive regime is observed at short time scales. In this case the Basset force is effectively acting as the purely viscous element that allows elimination of bead inertia, without observing the anomalous gap pointed out by McKinley et al. [89]. These results are in agreement with what is observed experimentally for the MSD of Brownian particles in viscous and viscoelastic fluids. Only under extremely low pressures, in air, have oscillations been observed in the MSD of a Brownian particle [75].

For a single-mode Maxwell fluid we pointed out in a previous work [52] that the Basset forces generated by the medium inertia effectively become a purely dissipative element at high frequencies, damping the oscillations produced by particle inertia. The results presented in Figure 2.5 illustrate a generalization of this observation to multi-mode Maxwell fluids.

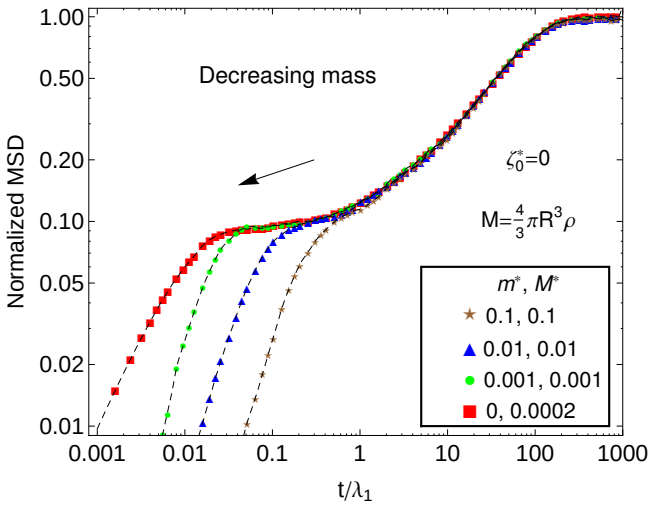

Figure 2.5. Simulated MSD for different values of bead mass in a 4-mode fluid (M4C) including particle and medium inertia. Corresponding input parameters for this simulation are shown in Table 2.1. $\zeta_0 = 0$ for the simulations that include particle and bead inertia. The time step size used in the simulation was $\Delta t = 10^{-5}$, a trajectory of 10^{10} time steps was simulated.

2.7 Analysis of the Synthetic MSD data

In what follows, we present an efficient way to recover the material parameters from the simulated MSD. Most relations between the MSD of the bead and the rheological properties of the host fluid have very general and simple forms in the frequency domain. On the other hand the MSD data are usually taken in the time domain. A common approach to analyze microbead rheology data is to calculate the power spectral-density (PSD) by applying FFT directly to the raw bead position data and squaring the absolute value of the result, then the imaginary part of the one-sided Fourier transform of the MSD is obtained from the Kramers-Kronig relation [110].

Fricks et al. [28] recently developed a time-domain data analysis algorithm for passive microbead rheology. Their method is based on the analysis of a single short bead path using a maximum likelihood function derived using a Kalman filter. The autocorrelation functions of the bead velocity are used as an exploratory tool to determine appropriate sample rate for the path and the initial values of the parameters to be found by maximizing the maximum likelihood function.

In this work we also use a time-domain data analysis strategy. However our methods have been chosen with the purpose of analyzing long bead displacement paths. The PCS method allows us to calculate the MSD at specified lag times chosen in a convenient logarithmic scale. This is a significant data reduction step that makes it computationally feasible to analyze materials with a wide range of relaxation times, including time scales spanning from particle and material inertia effects to particle traps or purely elastic elements. Our approach is therefore to derive analytical functions that can be fitted to the MSD data in the time domain. We show how $J(t)$ and $G(t)$ can be obtained from the fitted parameters.

The continuous line in Figure 2.6, labeled as input, shows the PSD calculated analytically using the inertia-less GLE eq.(2.5) and the GSR eq.(2.10) corresponding to the dynamic modulus specified in Table 2.1. The finely dashed lines show the

PSD obtained by analyzing the trajectories obtained from the BD simulations using the FFT routine. This technique reproduces the input PSD well at the intermediate frequency range but fails at the high and low frequency ends. The errors in the PSD calculated using FFT are due to a well-known aliasing, an issue inherent to discrete Fourier transforms [101]. As can be observed in Figure 2.6 these errors are particularly problematic for the study of inertial effects, which occur at high frequencies. The discrepancies observed at low frequencies will also be problematic if, for example, the effects of non-linear traps, which will be observable at long time scales, are to be analyzed. Additionally the PCS method allows the calculation of autocorrelation functions with less error, and less computational resources, than the FFT-based PSD estimators [76, 84].

The starting point for our data analysis procedure is the GSER written in terms of the inertia-less memory function

$$\langle \overline{\Delta\delta r_{\mathrm{b}}^2}[\omega] \rangle_{\mathrm{eq}} = \frac{6k_{\mathrm{B}}T\bar{\mu}[\omega]}{i\omega\left(i\omega + H_{\mathrm{e}}\bar{\mu}[\omega]\right)}. \tag{2.26}$$

Since we are seeking an analytic expression that we can fit to the time-domain data, we need to take the inverse one-sided Fourier transform of both sides of this relation.

By putting the one-sided Fourier transformed expression for the spectrally decomposed inertialess memory function, eq.(2.16) into eq.(2.26) and taking the inverse one-sided inverse Fourier transform we obtain

$$\langle \Delta\delta r_{\mathrm{b}}^2(t) \rangle_{\mathrm{eq}} = \frac{6k_{\mathrm{B}}T}{H_{\mathrm{e}}} - \sum_{j=1}^{N+1} c_j'(\{c_j\}, H_{\mathrm{e}}, \mu_0) e^{-t/\Lambda_j'(\{c_j\}, H_{\mathrm{e}}, \mu_0)} \tag{2.27}$$

where we have introduced the modified retardation times $\{\Lambda_j'\}$ and the modified $\{c_j'\}$ which, as indicated by the parentheses, are functions of the original parameters that determine $J(t)$ that is, $\{\Lambda_j\}$, $\{c_j\}$, μ_0 and of the trap stiffness H_{e}. The relation between the modified and the original parameters are found numerically for a spectrum with more than 2 Maxwell modes. After finding the modified parameters $\{\Lambda_j'\}$

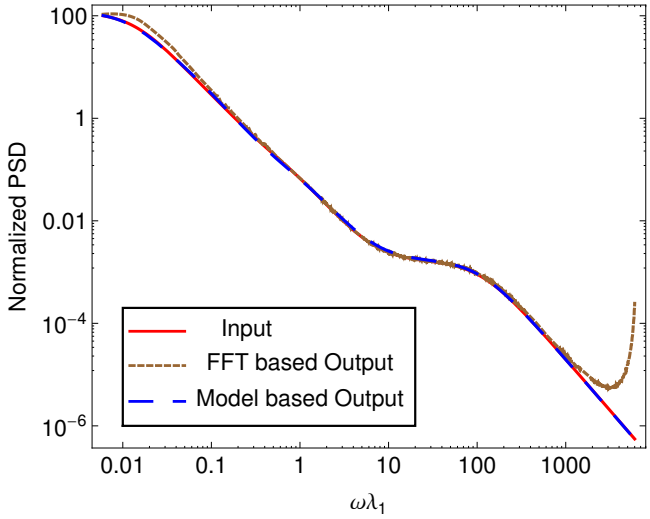

Figure 2.6. Comparison between the PSD obtained by analyzing the simulated trajectory data of the 4-mode fluid M4C by two different approaches, the time domain model-based analysis presented in this work and the common numerical FFT analysis.

and $\{c'_j\}$ by fitting eq.(2.27) to the time-domain MSD data the the parameters $\{c_j\}$, $\{\Lambda_j\}$ and μ_0 are found by putting the one-sided Fourier transformed expression for the spectrally decomposed inertialess memory function, eq.(2.16), into eq.(2.26) and equating the result to the one-sided Fourier transform of eq.(2.27). This results in an equation with rational functions on both sides of the equal sign, which gives the following equation for the numerators

$$\sum_{j=1}^{N+1}\left[c'_j\prod_{k=1,k\neq j}^{N+1}(i\omega+1/\Lambda'_k)\right]=\prod_{k=1}^{N}(i\omega+1/\Lambda_k)\,. \tag{2.28}$$

Therefore the retardation times $\{\Lambda_j\}$ can found from the inverse of the real roots of the polynomial with respect to $i\omega$, that appears on the left hand side of eq.(2.28).

On the other hand the denominators must satisfy

$$H_{\mathrm{e}} i\omega \prod_{k=1}^{N} (i\omega + 1/\Lambda_k) + H_{\mathrm{e}}^2 \left[\mu_0 \prod_{k=1}^{N} (i\omega + 1/\Lambda_k) - \sum_{j=1}^{N} \left(c_j \prod_{k=1, k\neq j}^{N} (i\omega + 1/\Lambda_k) \right) \right] = \prod_{k=1}^{N+1} (i\omega + 1/\Lambda'_k) \tag{2.29}$$

therefore $\{c_j\}$ and μ_0 can be found by solving the $N+1$ linear equations that result from pairing the corresponding frequency terms in eq.(2.29) Once the parameters that determine $J(t)$ (*i.e.*, $\{c_j\}$, $\{\Lambda_j\}$ and μ_0) have been found, the parameters that determine $G(t)$, (*i.e.*, $\{H_j\}$, $\{\lambda_j\}$ and ζ_0), can be calculated using the method described in Reference [7]. The set of parameters that was initially inputed into the simulations, and the ones that are obtained from analyzing the BD simulation results are compared to evaluate the efficacy of the data analysis procedure. The continuous lines shown in Figs. 2.2 and 2.3 are the fits of eq.(2.27) to the MSD obtained with the inertia-less BD simulations.

To perform a blind test of the data analysis algorithm we have used only the MSD data produced with the inertia-less BD simulations. Since the functional form of the MSD becomes more complex and the fitting to the more noisy data more challenging, analyzing the MSD data with oscillations will be a harder task. This however does not constitute a limitation of our analysis methodology since, as has been pointed out in Section 2.6, oscillations are not observed in the MSD of particles embedded in real fluids, where the medium inertia acts as a purely dissipative element at high frequencies.

In this work the MSD data used are synthetic. Hence the number of Maxwell modes in the input spectrum used to generate the MSD is known. Consequently the number of parameters necessary to fit the MSD is also known. However in the analysis of actual experimental data the number of modes necessary to fit the MSD

is not known *a priori*. To make the analysis more realistic we have allowed the fitting parameters $\{c'_j\}$ to become equal to zero during the fitting procedure. This means that modes that do not improve the fit can be eliminated by the algorithm. For the fluid that was originally specified as having a dynamic modulus with 4 closely spaced Maxwell modes (Table 2.1), the analysis produces an output modulus with only 3 modes. For the fluid with a broader relaxation spectrum M4W (Table 2.2) the analysis produces a spectrum with the same number of modes as the input spectrum.

For the three-element model discussed in section 2.4, eq. (2.27) reduces to a very simple analytical expression in terms of the parameters that determine the dynamic modulus of the fluid

$$\left\langle \Delta\delta r_{\mathrm{b}}^2(t) \right\rangle_{\mathrm{eq}} = \frac{6k_{\mathrm{b}}T}{H_{\mathrm{e}}} - \frac{6k_{\mathrm{b}}TH}{H_{\mathrm{e}}\left(H+H_{\mathrm{e}}\right)}\left[e^{-\frac{H_{\mathrm{e}}t}{(H_{\mathrm{e}}+H)\lambda}} + \frac{H_{\mathrm{e}}}{H}e^{-\frac{(H+H_{\mathrm{e}})t}{\zeta_0}}\right]. \tag{2.30}$$

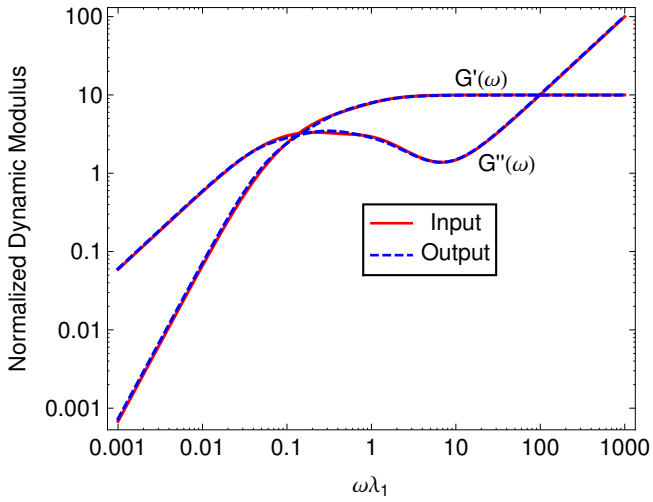

Figure 2.7. Comparison between the dynamic modulus used as input in the inertialess simulations and the dynamic modulus recovered by fitting eq. (2.27) to the simulation results for synthetic material M4C. The time step size used in the simulation was $\Delta t = 10^{-4}$, a trajectory of 10^8 time steps was simulated.

The continuous line plotted in Figure 2.7 is the dynamic modulus that was input into the BD simulations for the fluid with 4 closely spaced Maxwell modes

(M4C, Table 2.1). The dynamic modulus that results from analyzing the MSD data produced with the inertia-less BD simulations is plotted with a dashed line. A very good agreement between the input and output functions is obtained. Figure 2.8 shows the same comparison but for the material with 4 widely spaced Maxwell modes (M4W, Table 2.2). Again good agreement between the input and output dynamic modulus is obtained, confirming the robustness of the proposed analysis.

In Figure 2.6, the PSD obtained using FFT was compared to the PSD obtained using the time-domain model-based analysis used in this work. Both methods reproduce equally well the input PSD in the intermediate frequency range, but the time-domain analysis reproduces significantly more accurately the input PSD at the lower and higher frequency ranges. A similar comparison between time-domain analysis and the traditional numerical frequency-domain calculation of rheological properties from MSD data has previously been done by Fricks et al. [28], who also find the time-domain analysis to be more accurate.

To illustrate that their simulation methods are not mode limited Fricks et al. [28] presented the MSD obtained from simulations for a GLE with a 22-mode memory kernel. The performance of their time-domain maximum likelihood method in recovering the dynamic modulus, from a simulated bead trajectory, was illustrated with a 4-mode Maxwell fluid. The number of degrees of freedom in the maximum likelihood function scales linearly with the number of modes in the memory kernel. Therefore its maximization becomes harder as the number of modes increases. Our methods suffer from the same limitation. Since the number of parameters to be fitted scales linearly with the number of modes, the minimization of the sum of squared residuals becomes a harder problem as the number of modes increases. Note that μ_0, $\{c'_j\}$ and $\{\Lambda'_j\}$ are all fitting parameters and therefore we are performing non-linear fits. This constitutes a limitation when the number of modes increases, since the convergence

of the fits becomes harder to achieve and the uncertainty in the fitted parameters becomes larger. Both in our data analysis methodology and in the maximum likelihood method proposed by Fricks et al. [28], the limitation is associated with the convergence of the numerical optimization algorithm (minimization or maximization respectively), as the number of modes increases.

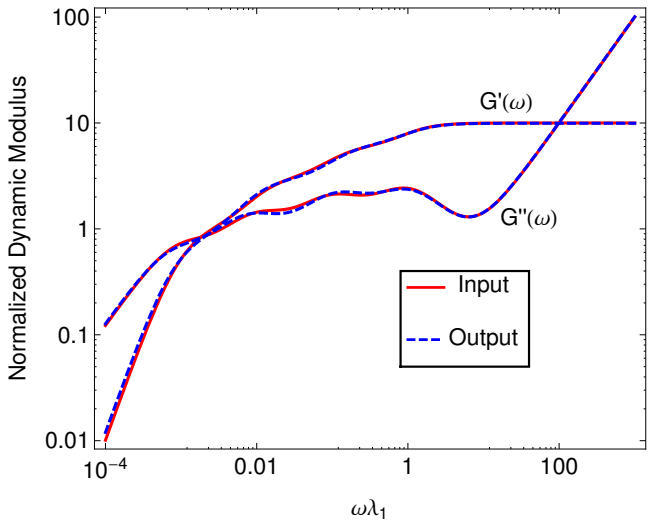

Figure 2.8. Comparison between the dynamic modulus used as input in the inertialess simulations and the dynamic modulus recovered by fitting eq. (2.27) to the simulation results for synthetic material M4W. The time step size used in the simulation was $\Delta t = 10^{-4}$, a trajectory of 10^9 time steps was simulated.

The differences between the input and output G^* are generated by the numerical errors introduced by the numerical techniques used for generating and analyzing the synthetic data. The synthetic trajectory data is exempt of static and dynamic errors inherent to experimental tracking setups, and in this work we have not attempted to include tracking noise in our model. However, the simulated MSD does contain statistical errors associated with the finite size of the bead trajectory used to calculate it. Increasing the size of the trajectory or performing ensemble averages can reduce these errors, but will also increase the computational cost of the simulation. Details about the statistical error in the PCS method can be found in Reference [84]. The

statistical errors propagate through the fitting to G^*, which gives rise to the small differences observed between the input and output moduli. A useful application of the simulations of passive microbead rheology presented here would be to study how the capacity of the microrheology technique to resolve the relaxation modes of the fluid, is affected by different types of measurement noise. For example, by including equations in the model to describe the experimental noise of specific techniques one can predict the resolution of the experimental technique [106].

We have used an efficient method for data analysis in which an explicit function of time is fitted to the MSD. In our procedure, no numerical transformation of the raw data from the time to the frequency domain is necessary. We have derived analytical expressions for all the quantities involved, and therefore transformations between time and frequency domain are performed very efficiently.

2.8 Non-linear traps

Some of the most common microbead rheology experimental set-ups use optical tweezers and laser interferometry to trap and track the displacement of the probe beads. The forces generated by these optical traps are usually assumed to depend linearly on bead displacement and to be conservative. However, recent work has shown that radiation pressure exerted by laser tweezers on spherical beads can be non-linear and non-conservative. This produces an accumulation of circulation in the trajectory of the particle. [104, 103]. Additionally recent experimental evidence [25, 116] indicates that biological networks and gels exhibit non-linear elasticity even at very small deformations. This means that even in passive microbead rheology a non-linear response of the elastic elements of the material might be observed. Therefore, the analytic tools used to date cannot be applied to such systems. The tools developed here are applicable, however.

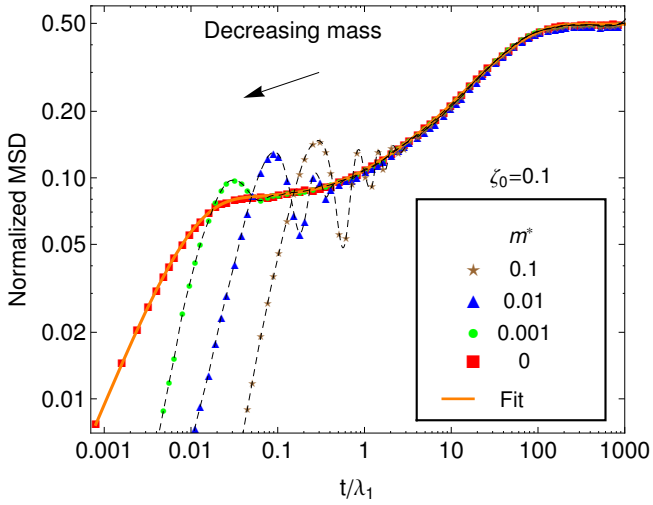

Figure 2.9. Simulated MSD for a bead embedded in synthetic material M4C (Table 2.1) bead and trapped by a quartic potential.

In Section 2.2 we assumed that the trapping force acting on the bead is produced by a harmonic potential. However, the procedure for eliminating inertia from the GLE in the frequency domain is also valid for anharmonic potentials. For that general case, we can rewrite eq. (2.1) as

$$\frac{d\boldsymbol{p}_{\rm b}(t)}{dt} = -\frac{\partial\Phi(\delta\boldsymbol{r}_{\rm b}(t))}{\partial\delta\boldsymbol{r}_{\rm b}(t)} - \int_{-\infty}^{t}\zeta(t-t')\frac{\boldsymbol{p}_{\rm b}(t')}{m}dt' + \boldsymbol{f}_{\rm B}(t), \tag{2.31}$$

where $\Phi(\delta\boldsymbol{r}_{\rm b}(t))$ is an external potential field acting on the bead. It is important to note that we are considering non-linearities of the purely elastic element only. The memory function $\zeta(t)$ remains linear and can therefore still be determined from the GSR.

The same procedure to derive the inertia-less GLE in the frequency domain, described in Section 2.2 can be used to eliminate the particle momentum from eq.(2.31) to obtain

$$\frac{d\delta\boldsymbol{r}_{\rm b}(t)}{dt} = -\int_{-\infty}^{t}\frac{\partial\Phi(\delta\boldsymbol{r}_{\rm b}(t'))}{\partial\delta\boldsymbol{r}_{\rm b}(t')}\mu(t-t')dt' + \boldsymbol{g}_{\rm B}(t), \tag{2.32}$$

Note that eq.(2.5) can be recovered simply by setting $\Phi(\delta\boldsymbol{r}_{\rm b}(t)) = \frac{H_{\rm e}}{2}\left|\delta\boldsymbol{r}_{\rm b}(t)\right|^2$.

Equations (2.31) and (2.32) can be written as a set of equivalent higher-dimensional Markovian SDEs by the procedure described in Section 2.4. The elimination of inertia for an anharmonic quartic potential was checked numerically by performing BD simulations for a trapped bead embedded in material M4C (Table 2.1), the length scale to make the material parameters dimensionless in this case is $\sqrt[4]{k_{\mathrm{B}}T/H_{\mathrm{e}}}$. The external potential field used was isotropic and quartic; therefore the trapping force becomes $-H_{\mathrm{e}}\left|\delta\boldsymbol{r}_{\mathrm{b}}(t)\right|^{2}\delta\boldsymbol{r}_{\mathrm{b}}(t)$. The MSD for the particle embedded in material M4C and trapped in the quartic potential is shown in Figure 2.9. It can be observed that, as the particle mass is progressively decreased, the MSDs obtained with the complete model, eq.(2.31), converge to the simulations performed with the inertia-less model, eq.(2.32).

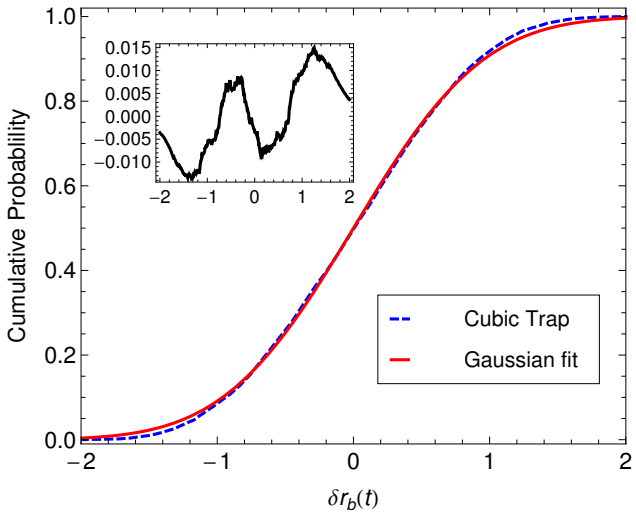

Figure 2.10. Equilibrium distribution of bead positions for a trapped bead embedded in fluid M4C (Table 2.1) and trapped in a quartic potential. The inset shows the residuals between the actual distribution that comes out from a BD simulation and a fit of that distribution to a Gaussian curve.

In Figure 2.10 we show the equilibrium distribution of bead positions when the bead is trapped in the quartic potential, the continuous line is a Gaussian fit to this distribution. It can be observed that the fit becomes worst at the edges of the distribution. To illustrate the effect of the nonlinear elastic element in the analysis

of microbead rheology data we now proceed with the analysis as if the trap were harmonic. The continuous orange line in Figure 2.9 shows a fit of eq. (2.27) to the inertia-less MSD obtained for the particle trapped in the quartic potential. We use this fit to obtain G^* using the procedure described in Section 2.7.

The comparison between the dynamic modulus used as input in the simulation and the output modulus that results from treating the trap as if it were linear is shown in Figure 2.11. Note that we have included the purely elastic element (the trap), in G^* since our goal here is to show the effect of nonlinearities in the analysis of materials that can be modeled as a purely elastic mesh embedded in a viscoelastic fluid. Figure 2.11(A) shows that there is a small discrepancy between the input and output G^* at low frequencies. This discrepancy becomes more significant if the trapping potential is stiffer (sextic potential) as can be observed in 2.11(B), where the error propagates through most of the frequency range. In the analysis shown the trap stiffness (elastic constant) was obtained from the MSD fit and not from the Gaussian fit to the distribution of bead positions. If the Gaussian fit to the distribution is used to obtain the trap stiffness the errors in the estimated G^* become larger. These results indicate that for materials that strain harden at very small strains, using the traditional microbead rheology data analysis techniques may introduce small errors in the estimated rheological properties.

New experimental and theoretical evidence presented by References [104] and [100] shows that a colloidal particle immersed in a fluid and trapped by an optical tweezer does not come to equilibrium, but rather circulates in steady-state motion. This has been shown to be caused by non-conservative forces exerted on the particles by the optical trap. The non-conservative force comes from radiation pressure that acts in the direction of the propagating laser beam. Roichman et al. [104] modeled the trap as a radially symmetric harmonic well with radiation pressure directed along

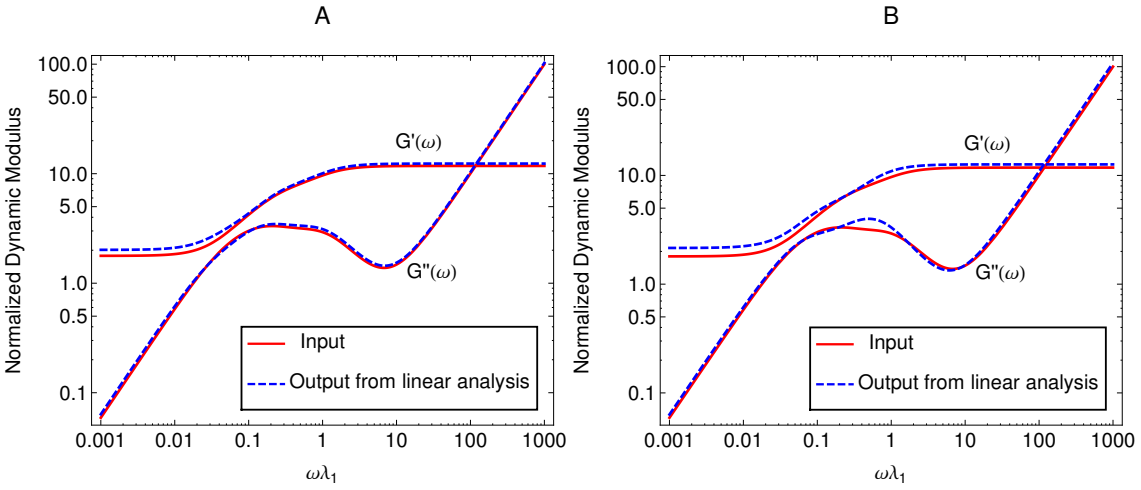

Figure 2.11. A: Dynamic modulus that includes a quartic potential and 4 Maxwell modes. B: Dynamic modulus that includes a sextic potential and 4 Maxwell modes. The continuous lines are obtained with the parameters used as input in the simulations. The dashed lines result from analyzing the synthetic data as if the purely elastic element were linear.

the optical axis,

$$\boldsymbol{F}(\delta \boldsymbol{r}_{\mathrm{b}}) = -H_{\mathrm{e}}\delta \boldsymbol{r}_{\mathrm{b}} + f_1 \exp\left(-\frac{|\delta \boldsymbol{r}_{\mathrm{b}}(t')|^2}{2\sigma^2}\right)\boldsymbol{\delta}_z. \tag{2.33}$$

Where the trap stiffness H_{e} and the scale of radiation pressure f_1, are proportional to the laser's power. And σ is the effective width of the trap, $\boldsymbol{\delta}_z$ is the unit vector in the direction of the optical axis. [104]. They consider only viscous fluids.

The non-conservative force exerted by the trap causes the particle to wind clockwise in a plane parallel to the beam direction [104, 100]. The amount of clockwise circulation can be quantified using the accumulated circulation $\chi(t)$ defined by

$$\begin{aligned} \chi(t) &:= \int_0^t \langle \delta \boldsymbol{r}_{\mathrm{b}}(t') \times \delta \boldsymbol{r}_{\mathrm{b}}(0)\rangle \cdot \boldsymbol{\delta}_\theta dt' \\ &= \int_0^t \langle \delta z_{\mathrm{b}}(0)\delta r_{\mathrm{b}}(t')\rangle - \langle \delta z_{\mathrm{b}}(t')\delta r_{\mathrm{b}}(0)\rangle \, dt'. \end{aligned} \tag{2.34}$$

Where δr and δz are the first and third components of the displacement vector $\delta \boldsymbol{r}_{\mathrm{b}}$ in cylindrical coordinates, and $\boldsymbol{\delta}_\theta$ is the unit vector in the θ direction. The angle brackets denote taking an average at steady state.

Exploring the effect of such non-conservative forces on a particle immersed in a viscoelastic fluid is a non-linear problem with a wide spectrum of relevant time scales, where the use of our microbead rheology simulation toolkit is useful. Figure 2.12 shows the accumulated circulation results obtained from BD simulations for a purely viscous fluid ($\zeta_0^* = 0.1$), a 1-mode Maxwell fluid and for the 4-mode Maxwell fluid specified in Table 2.2. It can be observed that in the viscoelastic fluid the bead also circulates. However the more complex spectrum of time scales is clearly reflected in the circulation rate. In real systems, the quantity $f_1/(\sigma H_e)$ is a small number around 0.1 [104]. However to emphasize the effects of the non-conservative force in the simulations we have set $f_1/(\sigma H_e) = 1$. This allows the particle to explore regions far away from the trap center. Thus the particle motion is more influenced by the non-conservative force [100].

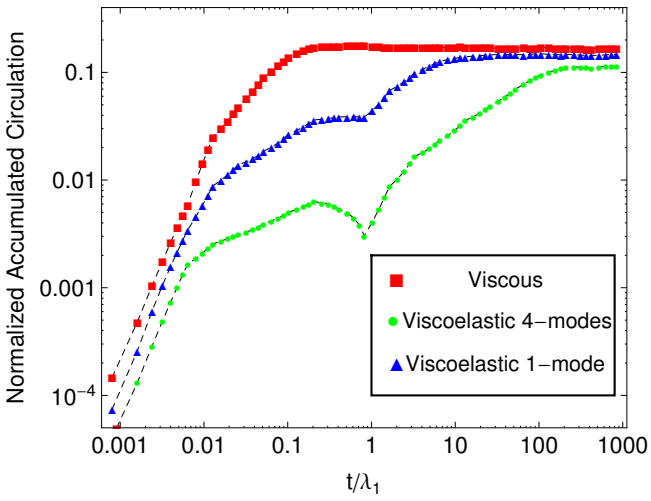

Figure 2.12. Accumulated circulation for a bead trapped in an optical tweezer with non-conservative forces along the optical axis. For the purely viscous fluid $\zeta_0^* = 0.1$, the parameters used for the simulations with the viscoelastic fluid are shown in Table 2.1.

A relevant question to microbead rheology is if the circulation of the bead produced by the radiation pressure has an effect in the rheological properties obtained from the bead displacement data. From a simple inspection of eq.(2.33) one

notices that the radiation pressure can affect only the z-component of the bead displacement, therefore we consider the data analysis of that component. Here we wish to see if a naive analysis that ignores the non-Gaussian shape of the trap and the non-equilibrium circulation still gives a good estimate of G^*. One might expect that the fluid memory could couple with the circulation to modify the relationship between MSD and G^*. Pesce et al. [100] have already shown that bead displacement autocorrelations are not affected by these forces for a viscous fluid.

To analyze the bead displacement data we simply treat the displaced center of the non-conservative trap as the origin of an effective harmonic trap. Figure 2.13 shows a comparison between the MSDs, of three different fluids, obtained from simulations that include radiation pressure (symbols) and analytical solutions that do not include radiation pressure (continuous lines). The absolute residuals between the MSDs that include radiation pressure and the ones that do not, are shown in the inset. No pattern is observed in this residuals, and their magnitude is what is expected from the finite size of the ensemble used to calculate the MSDs obtained from simulations. We can therefore conclude that the radiation pressure will not have any effect in the rheological properties estimated from the MSD of a trapped particle.

These results are not surprising in light of the fact that the angular velocities of the circulation made dimensionless by the longest relaxation time of the fluid is approximately 10^{-2} , which means that the circulation is effectively Newtonian. Considering that we have made the radiation pressure unrealistically large in our simulations, this suggests that the circulatory motion is probably always too slow to have any effect in the estimates of the rheological properties of an homogeneous fluid obtained from microbead rheology.

2.9 Conclusions

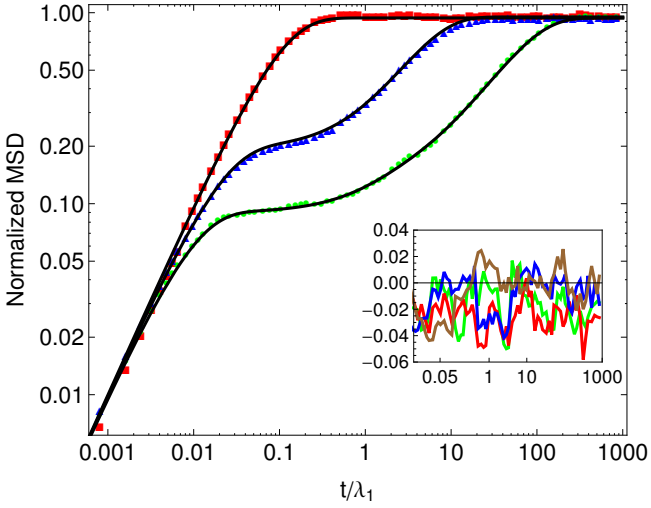

Figure 2.13. Comparison between the MSDs that include radiation pressure (symbols, obtained from BD simulations) and the ones that do not include radiation pressure (continuous lines, obtained from analytical solutions). For the purely viscous fluid $\zeta_0^* = 0.1$, the parameters used for the simulations with the viscoelastic fluid are shown in Table 2.1. The modulus for the 1-mode viscoelastic is the first mode of the 4-mode fluid. Plot markers as in Figure 2.12. Inset: Relative residuals between the MSDs that include the effect of radiation pressure and the ones that do not. Brown line shows the residuals for a BD simulation without radiation pressure.

Simulations of the motion of micron-sized particles embedded in viscoelastic fluids can be useful for developing and testing data analysis algorithms for passive microbead rheology. However these simulations become computationally cumbersome if high-frequency inertial effects are taken into account explicitly. The elimination of particle momentum from the Langevin description of colloidal particles suspended in viscous fluids is a wide-spread practice used to increase the computational efficiency of BD simulations. The elimination of particle inertia from the generalized Langevin equation (GLE) with a multi-mode exponential memory kernel has been addressed by McKinley et al. [89] and previously by Schaink et al. [107] for a one-mode exponential memory kernel.

In this work we have presented a method to derive an inertia-less GLE, by eliminating particle inertia in the frequency domain. Our method does not require a

specific type of memory function to be specified before eliminating inertia, therefore the derived inertia-less GLE can be used either with continuous or discrete memory functions. For the case of discrete exponential memory functions McKinley et al. [89] have shown that the inertia-less limit is singular and that an infinite number of modes are required to obtain self-consistent results. By adding a very small (possibly undetectable) purely viscous element to the exponential multi-mode memory function we have shown that the inertia-less GLE produces MSDs consistent with the numerical zero-particle-mass limit of the inertial GLE simulations, even for a small number of modes. Additionally we have previously shown that this purely dissipative element can arise entirely from fluid inertia, since the Basset force acts dissipative at high frequency. Therefore we conclude that the presence of the purely dissipative element in the memory function is not limited to special cases, such as dilute polymer solutions, where important viscous dissipation arises from the solvent, but is rather a general feature for any system where the particle and medium density are similar.

Time-domain simulation and data analysis strategies for passive microbead rheology were recently developed and introduced by Fricks et al. [28]. Their simulation strategy exploits the linearity of the GLE and therefore is exact and highly efficient. Their methodology to extract rheological properties from bead trajectories is based on the analysis of a single path using the maximum likelihood function. We have developed an alternative time-domain strategy that extends the applicability of the time-domain methods to include medium inertia effects and linear and non-linear particle traps. Our approach was to adapt traditional BD simulation algorithms to the simulation of the GLE. Analogous to the common practice of BD simulations of Langevin equations we have made use of the inertia-less GLE to make the simulation of the non-linear GLEs more computationally efficient. By making use of the photon correlation spectroscopy algorithm (PCS), Our methodology has been made especially suitable and efficient for the analysis of data with a broad distribution of

timescales spanning from high frequency inertial effects to purely elastic responses (over six decades of frequency). As a relevant example of the specific applicability of our microrheology simulation toolkit we have shown that, the radiation pressure of optical traps [104] do not affect passive microbead rheology data analysis.

Having all the necessary elements to simulate the microbead rheology experiment by BD and the explicit time-domain analytical expressions to fit the MSD data, we performed Monte Carlo simulations to test the data analysis algorithm. The correspondence between the dynamic modulus inputed into the simulations and the dynamic modulus that is obtained after analyzing the MSD data obtained from the BD simulations was very good. We have shown that a small purely dissipative element in the memory function of the GLE allows one to simulate the passive rheology correctly with zero-mass, avoiding the singularity. As has been demonstrated here and in other works [28, 106], BD simulations are useful for testing data analysis or error handling algorithms in microbead rheology.

CHAPTER 3

THE EFFECTS OF HYDRODYNAMIC INTERACTION AND INERTIA IN DETERMINING THE HIGH-FREQUENCY DYNAMIC MODULUS OF A VISCOELASTIC FLUID WITH TWO-POINT PASSIVE MICRORHEOLOGY

This Chapter previously appeared in Physics of Fluids (The American Institute of Physics), volume 24, issue 7, page 073103, year 2012.

3.1 Introduction

In the original one-point passive microrheology technique introduced by Mason and Weitz [87] the positional autocorrelation function of micron-sized beads ($R < 1\mu$m) embedded in a viscoelastic fluid is used to infer the dynamic modulus of the fluid [86, 1, 128, 59, 112]. Unlike bulk rheometers, microbead rheology requires only very small samples (pico- to microliter order) and elastic modulus as small as 10-500 Pa can be measured [59]. These advantages make the technique especially useful for the analysis of biological samples [1, 128]. However since the analysis of microbead rheology data relies on a generalized Stokes relation [52, 87] it is limited to fluids where the microstructure is much smaller than the size of the probe bead. If this condition is not satisfied the continuum mechanics assumptions used in the data analysis formalisms [52, 72, 124, 87] can become invalid.

To overcome this limitation Crocker et al. [19] proposed a modification of the original one-point passive microbead rheology technique based on measuring the cross-correlated thermal motion of pairs of tracer particles to determine $G^*(\omega)$. The pair of particles of radius R is separated by a distance L larger than the microstructure of the fluid. It has been shown that two-point microrheology can correctly reproduce results obtained with a mechanical rheometer, in systems where single-particle microrheology gives erroneous results [73, 19]. In the passive two-point microrheology experiment the motion of the beads is driven by Brownian forces. The motion of the beads creates

a velocity field in the otherwise undisturbed fluid. This velocity field is characterized by waves that originate at the bead-fluid interface, and then reflect back and forth between the beads. The cross-correlations of the two tracer beads will therefore be determined by the nature of those waves. The waves produced at the bead-fluid boundary can be characterized by a wavelength and a penetration depth. At a given frequency the wavelength indicates the velocity at which the waves propagate while the penetration length indicates a characteristic distance the wave propagates before dissipating significantly from the medium.

Data analysis formalisms for two-point microrheology usually make two important approximations (i) that the waves produced at the bead-boundary interface decay before producing reflections, (ii) and that the waves propagate through the fluid instantaneously, in other words that the inertia of the medium is negligible. For a given material to satisfy those assumptions only data gathered with beads placed at a distance $2L$ at which the reflections produced by one bead will significantly decay before reaching the other bead should be used. Similarly, the methods are only applicable to data gathered at frequencies where the waves can be assumed to be propagating much faster than the relaxation times being measured. However finding the experimental conditions where all these assumptions are met might not be possible for a viscoelastic fluid, especially if a wide spectrum of relaxation times is to be measured.

Levine and Lubensky [73] have demonstrated theoretically the validity of the Crocker hypothesis by solving the elastic problem of two spheres embedded in an inhomogeneous compressible viscoelastic medium. They calculated the mutual response function for these beads and showed that in the limit that the bead-bead separation (L) is large compared to the radius of the beads (R), this response function measures the bulk rheological properties of the medium independently of the

rheological properties of the regions immediately surrounding the two beads. This conclusion was reached when the response functions were derived with lowest-order reflections. The corrections due to higher-order reflections were estimated and shown to be small for a large bead-bead separation (L). Their analysis however was based on the steady Stokes equation and therefore the effects of fluid inertia in the mutual response functions were not considered in that work.

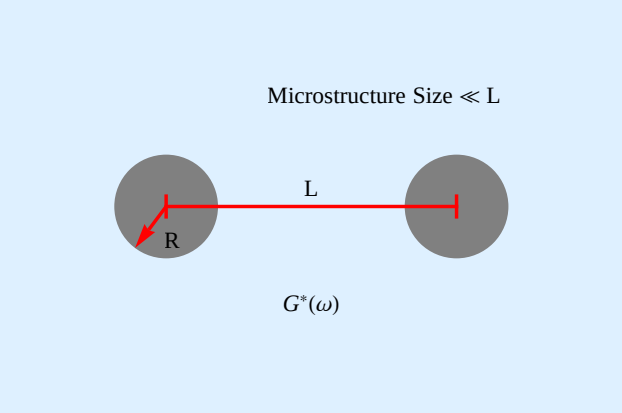

Figure 3.1. Schematic of the two-point microrheology experiment

Following Levine and Lubensky [73], Hohenegger and Forest [48] generalized an elastic problem to include both inner and outer moduli as well as the thickness of a chemically modified layer around each bead. They considered the case where the second probe bead is a passive point source of force. They presented inverse characterization tools for the two-point passive microrheology experiment for the determination of the local and non-local $G^*(\omega)$, as well as the thickness of the chemically modified layer. While Levine and Lubensky [73], Crocker et al. [19] and Starrs and Barlett [113] considered response functions with only first-order terms in the (R/L) ratio. Hohenegger and Forest [48] considered second-order reflections of the waves generated at the bead-fluid interface, but assumed that the waves travel much faster than the shortest relaxation time of the fluid to derive response functions with errors of order $(L/R)^3$.

The main effect of inertia in the response of viscoelastic liquids is the finite propagation time of stress. Therefore the combined effect of inertia and reflected waves is expected to be different from the effect of reflections alone. This is more precisely characterized by the penetration depth and the wavelength of the waves generated at the bead-fluid interface [50, 77]. Microscopically, the manifestation of inertia is the vortex-like flow or displacement field, which appears both in the equilibrium response at a distance, as well as in the correlations of fluctuations about thermal equilibrium [77]. It has been shown that medium inertia can affect the cross-correlations of two neighboring Brownian particles and that the effect becomes more pronounced for more elastic materials.

In a two-point microrheology experiment an optimal distance between the two beads exists at which the desired length scales are sampled while a good signal-to-noise ratio is maintained in the cross-correlations. However this optimal distance might not be large enough for higher-order reflections to be neglected from the analysis of two-point cross-correlations. Additionally if the dynamic modulus of a fluid is going to be measured at high frequencies, inertial effects can become important. Moreover increasing the distance between the beads will attenuate the effect of reflections, but will increase the effect of inertia and reduce the signal-to-noise ratio in the two-point cross-correlations. It therefore seems that having to choose experimental conditions under which both reflections and inertia effects are negligible, while sampling the desired length scales and maintaining a good signal-to-noise ratio reduces the versatility of the two-point microrheology technique.

To our knowledge the combined effect of medium inertia and an infinite number of wave reflections in the analysis of microbead rheology data, has not been previously considered. A data analysis formalism for two-point microrheology that can account for both the finite velocity at which the waves propagate and for the effects

of reflected waves will significantly broaden the applicability of the technique. We have recently introduced a one-point passive microrheology formalism that takes into account bead and medium inertia and can therefore be used to infer high-frequency linear viscoelastic properties from bead position autocorrelations [52]. In this work we introduce methods to analyze two-point cross correlations that take into account the combined effects of bead and medium inertia as well as reflections. The methods introduced here are expected to be useful for inferring high-frequency relaxation modes in $G^*(\omega)$ from two-point cross-correlations.

Hydrodynamic interactions of micron-sized particles suspended in Newtonian fluids have been extensively studied theoretically and experimentally. The most common theoretical approach has been to solve the Stokes equations using approximate methods such as the method of reflections [4, 39, 66] or the method of induced forces [88]. These results have been extensively exploited to construct simulation algorithms for predicting the behavior of suspensions of Brownian particles in Newtonian fluids [26, 11]. Most theoretical work has been done using the steady Stokes equation as the starting point, for which fluid inertia effects are neglected. Mazur et al. [123] were the first to calculate the hydrodynamic interactions for suspended micron-sized spherical particles resulting from the time-dependent linearized Navier-Stokes equation. In that work the time-dependent mobilities for the particles were calculated using the method of induced forces. In general, hydrodynamic interactions in dilute suspensions of particles can be obtained by taking only hydrodynamic pair interactions into account. However this approximation has proven to fail for more concentrated suspensions. The method of induced forces introduced by Mazur et al. [123] is specially suitable to treat the many sphere problem. More recently Ardekani and Rangel [3] used the method of reflections to solve the unsteady creeping flow field produced by two hydrodynamically interacting spheres suspended in a Newtonian fluid. The correspondence that exists between the creeping flow equations for Newtonian fluids and

viscoelastic fluids in the frequency domain [52, 126, 129], allows one to use solutions found for Newtonian fluids to study equivalent problems in linear viscoelasticity. The main problem that remains is to perform the transformations of the creeping flow solutions from the frequency to the time-domain, which can be a non-trivial mathematical problem *per se*.

A very common approach to microbead rheology data analysis is to calculate the one-sided Fourier transform of the bead auto or cross-correlations from the trajectory data using fast Fourier transform (FFT) algorithms. These methods are known to introduce errors associated with frequency discretization and finite size windowing [28]. Time-domain methods that avoid the use of FFT have been recently proposed for the analysis of one-point passive microbead rheology data [16, 28]. For the analysis of two-point passive microrheology data Starrs and Barlett [113] used a time-domain method based on fitting the two-bead cross-correlations to cubic-splines. Their analysis however does not include inertia or reflections. In Chapter 2 we introduced a simulation and data analysis toolkit for microbead rheology [16]. We derived a generalized Brownian dynamics (GBD) algorithm that can account for inertial effects, nonlinear and nonconservative effects in particle traps. We also introduced a regularization for the limit with zero-mass of the bead, This limit as has been previously shown to be a singular limit [52, 89]. By including a small purely dissipative element in the memory function of the GLE, ζ_0, one can eliminate bead inertia from the GLE avoiding the singularity [52, 16]. It can be shown that the purely dissipative element can arise entirely from medium inertia, since the Basset force arising from medium inertia plays the same role as a frictional force at high frequencies [50].

In this Chapter we show how our methods can be extended to simulate the two-point passive microrheology experiment. The generalized Brownian dynamics simulations are then used to perform Monte-Carlo evaluations of our time-domain data

analysis formalism for inferring the high-frequency of $G^*(\omega)$ from cross-correlations of beads embedded in viscoelastic fluids. The Chapter is organized as follows. In Section 3.2 we derive generalized Stokes tensors with medium inertia and an infinite number of reflections for viscoelastic fluids by making use of a solution for the unsteady creeping flow field produced by two hydrodynamically interacting spheres suspended in a Newtonian fluid [3] and the correspondence principle. In Section 3.3 a generalized Langevin equation for two hydrodynamically interacting trapped beads embedded in a viscoelastic fluid is presented. The equation is solved in the frequency domain to obtain relations between the beads auto- and cross-correlations and the components of the generalized Stokes tensor derived in Section 3.2. In Section 3.4 we use simple dimensional arguments to construct a phase diagram for two-point passive microrheology, which can serve as a guide to indicate experimental conditions under which inertia and reflections may become important. In Section 3.5 we present a time-domain data analysis strategy for inferring high-frequency $G^*(\omega)$ from two-point cross-correlations. The time-domain strategy is evaluated using Monte-Carlo simulations. In Section 3.6 we show that the formalism presented here converges to the commonly used formalism introduced by Crocker et al. [19] in the limit of zero inertia and lowest order reflections. In Section 3.7 we show that this simplified data analysis formalism can generate errors in estimating $G^*(\omega)$ when used to analyze data gathered outside the range of experimental conditions where inertia and reflections are negligible. Moreover the region of experimental conditions where these assumptions are valid can be very small for viscoelastic fluids.

3.2 High-frequency generalized Stokes tensors

In this section we begin by deriving a generalized Stokes tensor for two-point microrheology that accounts for inertial effects and an infinite number of reflected waves. We make use of previously derived unsteady Stokes tensors [3] for Newto-

nian fluids and use the correspondence principle [52, 126] to obtain the frequency-dependent friction tensors for beads suspended in viscoelastic fluids. Previous analyses of two-point microbead rheology are based on solutions obtained from the steady Stokes equation [48, 113, 73, 19], which neglects the effects of medium inertia.

The correspondence principle allows one to replace the viscosity of simple viscous liquids, η, by the complex viscosity of linear viscoelastic materials, after the equations have been transformed from the time domain to frequency space. This identification is possible because linear viscoelasticity presumes a convolution integral for the stress tensor, whose Fourier transform yields the Stokes relation with complex (frequency-dependent) viscosity. Therefore in the frequency domain, the creeping flow equations (steady or unsteady) for a viscoelastic fluid are equivalent to the creeping flow equations for a viscous fluid. Whenever the creeping viscous flow problem can be solved, the analogous solution of the viscoelastic flow problem follows [126]. In this work we make use of the unsteady creeping flow solution derived by Ardekani and Rangel [3] and the correspondence principle to derive a generalized Stokes relation for two-point microrheology that includes inertial effects and infinite reflections.

Ardekani and Rangel [3] used the method of reflections, which is an approximate method for calculating the force exerted on two small spheres moving in Stokes flow to solve the unsteady problem. The particles are assumed to be sufficiently close to each other to interact hydrodynamically but sufficiently distant from boundary walls so that the surrounding fluid is regarded as infinite. Solutions for a single time-dependent point-force or for an isolated sphere are used in combination with the method of reflections. The velocity field that satisfies boundary conditions on two spheres is constructed by a linear superposition of an infinite number of velocity fields that satisfy boundary conditions on one sphere, each velocity field representing a reflection of the wave generated at the bead-fluid interface. Because of symmetry of

the geometry the problem is axisymmetric about the line of centers between the two beads. The method of reflections gives the solution as an infinite series. Calculating all the terms in this geometric series, one can analytically find the summation of all the terms.

Consider two particles of radius R located at a distance L from each other and moving with velocities $\boldsymbol{v}_{b(1)}(t)$ and $\boldsymbol{v}_{b(2)}(t)$ in an unbounded viscoelastic fluid (Figure 3.1). In the absence of the particles the fluid is at rest; the motion of the the particles produces a velocity field in the medium $\boldsymbol{v}(\boldsymbol{r},t)$. The particles are at least a few diameters apart. We assume following References [48, 113, 73, 19] that L is independent of the motion of the beads, which implies that the displacements of the beads are small compared to L. The correspondence principle is used by making the substitution $\eta \Rightarrow G^*(\omega)/i\omega$, in the Fourier transform of the unsteady Stokes solutions introduced by Ardekani and Rangel [3] to obtain the frequency-dependent friction tensor for a viscoelastic fluid. The following relation between the motion of the two beads and the force exerted by the viscoelastic fluid on one of the particles is obtained,

$$\boldsymbol{F}_{(1)}[\omega] = -\bar{\zeta}[\omega]\left(\frac{\boldsymbol{v}_{b(1)\perp}[\omega]-\boldsymbol{v}_{b(2)\perp}[\omega]A_{\perp}(\omega)}{1-A_{\perp}(\omega)^2}\boldsymbol{\delta}_{\perp}+\frac{\boldsymbol{v}_{b(1)\parallel}[\omega]-\boldsymbol{v}_{b(2)\parallel}[\omega]A_{\parallel}(\omega)}{1-A_{\parallel}(\omega)^2}\boldsymbol{\delta}_{\parallel}\right). \quad (3.1)$$

Where,

$$\bar{\zeta}[\omega] = \frac{6\pi R G^*(\omega)}{i\omega} + 6\pi R^2\sqrt{\rho G^*(\omega)} + \frac{2}{3}\pi R^3 \rho i\omega \quad (3.2)$$

is the one-sided Fourier transform of the single-bead memory kernel including the "Stokes-Basset" force term and the fluid mass dragged by the bead (*i.e.,* $\bar{\zeta}[\omega] \equiv \bar{\mathcal{F}}\{\zeta(t)\} := \int_0^\infty \zeta(t)e^{-i\omega t}dt$). We indicate the Fourier transform by frequency argument with square brackets, and one-sided transform by an over-bar. The first subindex indicates the bead number, and the symbols $\perp$ and $\parallel$ indicate the directions perpendicular and parallel to the line of centers of the two beads, respectively. Eq.(3.1) is the geometric series that results from adding an infinite number of re-

flected waves. The necessary conditions for the convergence of the geometric series to eq.(3.1) are that $(A_\perp(\omega)/8\pi)^2 < 1$ and $(A_\parallel(\omega)/8\pi)^2 < 1$.

We now consider two different approximations for reflections. In this first calculation we assume that particle 1 is located at a relatively large distance (several diameters) from particle 2. We then compute the translational effect of particle 1 by assuming that: (i) it generates the same force as that produced by a point force located at the center of the particle; (ii) the drag resulting from the field reflected at a given particle can be approximated by considering the field to be equivalent to a uniform velocity field with the same magnitude and direction as would actually exist at the location of the particle center if it were not present [39]. As long as L/R is sufficiently large the assumptions should be safe. Then the functions $A_\parallel(Q,\omega)$ and $A_\perp(Q,\omega)$ are given by

$$A_\parallel(\omega) = \frac{i\omega Q\bar{\zeta}[\omega]}{4\pi G^*(\omega)}\left\{\frac{2}{ik(\omega)L}e^{ik(\omega)L} - \frac{2}{(ik(\omega)L)^2}\left[e^{ik(\omega)L}-1\right]\right\}. \tag{3.3}$$

$$A_\perp(\omega) = -\frac{A_\parallel(\omega)}{2} + \frac{i\omega Q\bar{\zeta}[\omega]}{4\pi G^*(\omega)}e^{ik(\omega)L}, \tag{3.4}$$

where $Q = R/L$. It is important to note that in viscoelastic media, unlike purely viscous or purely elastic media, the waves produced at the bead-fluid interface have a frequency-dependent, complex wave-number $k(\omega) = -\omega\sqrt{\rho/G^*(\omega)}$. It is useful to define the wavelength of the wave penetrating into the fluid from the bead surface [50],

$$\Lambda(\omega) := 1/|k'(\omega)| \tag{3.5}$$

where $k'(\omega)$ is the real part of the frequency-dependent wave number. We may also define the penetration depth of the wave as,

$$\Delta(\omega) := 1/k''(\omega) \tag{3.6}$$

where $k''(\omega)$ is the imaginary part of the frequency-dependent complex wave number. From eqs.(3.5-3.6) we can see that,

$$ik(\omega)L = -\frac{L}{\Delta(\omega)} + \frac{iL}{\Lambda(\omega)}. \tag{3.7}$$

The first term on the right hand side of eq.(3.7), which involves the penetration length, determines how fast the wave decays. The second term, which involves the wavelength, characterizes the oscillatory part of the memory function tensor. If the distance L between the two beads is much larger than the penetration depth, $\Delta(\omega)$, then the reflected waves decay significantly before reaching the other bead and therefore the effect of reflections is small. However if the distance between the beads is comparable to the penetration depth the reflected waves from bead 2 will have an important effect in the motion of bead 1 and vice-versa. For viscoelastic fluids, the penetration depth increases with decreasing frequency, so that reflections are expected to have a larger effect at lower frequencies. On the other hand, the wavelength $\Lambda(\omega)$ can be a good indicator whether medium inertia is effective at a given frequency; if the frequency is high and therefore the wave length is smaller than the distance between the beads $L \gg \Lambda(\omega)$, the contributions of fluid inertia to the memory functions become effective. The penetration depth of viscoelastic materials is often below 1 μm in the MHz range [125]. On the other hand, medium inertia may be important in the high frequency regime since the wavelength is always smaller than the penetration depth and therefore $\Lambda(\omega)$ can be smaller than L. For micron-sized beads only a few diameters apart (*e.g.*, $Q = 0.2$), both fluid inertia and reflected waves can have an effect in determining the response function.

In deriving eqs. (3.4) and (3.3) we have made use of the solutions for a point-force. The finite size of the beads can be accounted for approximately by instead using a solution to the solitary sphere in unsteady Stokes flow and then again applying the method of reflections to satisfy the boundary conditions on two spheres. Here again

we have generalized the solutions presented by Ardekani and Rangel [3] to viscoelastic fluids, by making use of the correspondence principle,

$$A_{\parallel}(\omega) = \frac{3Q}{(ik(\omega)L)^2} - \frac{3Q^2}{ik(\omega)L} + Q^3 i\omega - 3Qe^{(1-Q)ik(\omega)L}\left[\frac{1}{(ik(\omega)L)^2} - \frac{1}{ik(\omega)L}\right] \quad (3.8)$$

and

$$A_{\perp}(\omega) = -\frac{A_{\parallel}(\omega)}{2} + \frac{3Q}{2}e^{(1-Q)ik(\omega)L} \quad (3.9)$$

Eqs.(3.9) and (3.8) can be used together with eq.(3.1) and eq.(3.2) to write response functions that will account for inertial effects and reflections, and that will be suitable for use when the probe beads are only a few diameters apart. Again, it is important to note that the error in eq.(3.1) used with eqs.(3.2), (3.9) and (3.8) is of order Q^3. This error is due to the fact that the drag resulting from the reflected field is approximated by considering it to be equivalent to a uniform velocity field whose magnitude and direction are the same as what would exit at the center of the particle if it were not present.

3.3 Two-point high-frequency generalized Langevin Equation

In this section we write the equations of motion for the two probe beads of radius R and separated by a distance L. The dynamics of micron-sized beads embedded in a viscoelastic fluid are known to be described by a generalized Langevin Equation (GLE) [45, 13],

$$\frac{d\boldsymbol{p}_{\mathrm{b}}(t)}{dt} = -\boldsymbol{H}_{\mathrm{e}} \cdot \delta\boldsymbol{r}_{\mathrm{b}}(t) - \int_{-\infty}^{t} \boldsymbol{\zeta}(t-t') \cdot \frac{\boldsymbol{p}_{\mathrm{b}}(t')}{m} dt' + \boldsymbol{f}_{\mathrm{B}}(t). \quad (3.10)$$

Where,

$$\delta\boldsymbol{r}_{\mathrm{b}} = \begin{pmatrix} \delta r_{\mathrm{b}(1)\perp} \\ \delta r_{\mathrm{b}(1)\parallel} \\ \delta r_{\mathrm{b}(2)\perp} \\ \delta r_{\mathrm{b}(2)\parallel} \end{pmatrix} \quad (3.11)$$

is the bead displacement vector and $\boldsymbol{p}_{\mathrm{b}} = m\frac{d\delta\boldsymbol{r}_{\mathrm{b}}(t)}{dt}$ are the beads momenta, with m the bead mass. The Brownian forces satisfy the fluctuation-dissipation theorem (FDT),

$$\langle \boldsymbol{f}_{\mathrm{B}}(t)\boldsymbol{f}_{\mathrm{B}}(t')\rangle_{\mathrm{eq}} = k_{\mathrm{B}}T\boldsymbol{\zeta}(t-t'). \tag{3.12}$$

If the distance L between the two probe beads is assumed to be constant, the equation of motion of the beads can be decoupled from the unsteady Stokes equation. This is a reasonable assumption if the fluctuations of the beads' positions are small compared to L. In that case solutions to the unsteady Stokes equation such as eq.(3.1) can be used to write a GLE with a bead-position-independent memory kernel, We can use eqs.(3.1) and (3.2) to write the components of the memory function tensor, $\boldsymbol{\zeta}(t) = \bar{\mathcal{F}}^{-1}\left\{\bar{\boldsymbol{\zeta}}[\omega]\right\}$ (where $\bar{\mathcal{F}}^{-1}\{\bar{f}[\omega]\}$ is the inverse one-sided Fourier transform),

$$\bar{\boldsymbol{\zeta}}[\omega] = \bar{\zeta}[\omega]\begin{pmatrix} \frac{1}{1-A_{\perp}(\omega)^2} & 0 & -\frac{A_{\perp}(\omega)}{1-A_{\perp}(\omega)^2} & 0 \\ 0 & \frac{1}{1-A_{\parallel}(\omega)^2} & 0 & -\frac{A_{\parallel}(\omega)}{1+A_{\parallel}(\omega)^2} \\ -\frac{A_{\perp}(\omega)}{1-A_{\perp}(\omega)^2} & 0 & \frac{1}{1-A_{\perp}(\omega)^2} & 0 \\ 0 & -\frac{A_{\parallel}(\omega)}{1-A_{\parallel}(\omega)^2} & 0 & \frac{1}{1+A_{\parallel}(\omega)^2} \end{pmatrix} \tag{3.13}$$

Note that, although the two beads are correlated, the $\perp$ and $\parallel$ directions are decoupled.

These expressions for the components of the memory function tensor are general and can be used with either the expression for $A_{\perp}(\omega)$ and $A_{\parallel}(\omega)$ derived with the point-force approximation (eqs.(3.4) and 3.3) or with the expressions that take some account of the finite size of the bead (eqs.(3.9) and (3.8)). In what follows we show how the two solutions compare when predicting the mean-squared displacement and cross-correlations of probe particles in a viscoelastic fluid.

The external force to trap the particle near a fixed position is initially assumed to be linear and isotropic with restoring constant H_{e}, therefore $\boldsymbol{H}_{\mathrm{e}} = H_{\mathrm{e}}\boldsymbol{\delta}$.

The trapping force is often produced by an optical tweezer in experimental systems. Although recent work has suggested that optical traps can exert nonlinear, nonconservative forces on particles [104, 103], the linear approximation is commonly used for the trapping force for laser tweezers and small bead displacement [36, 95]. We have recently shown that nonconservative forces in optical traps can be neglected in one-point microbead rheology data analysis [16]. The particles may also be trapped by purely elastic elements of the medium; recent experimental evidence [25, 116] indicates that biological networks and gels exhibit non-linear elasticity even at very small deformations. Our methods can be extended to analyze systems with non-linear traps by making use of generalized Brownian dynamics simulations (GBDS) [16].

Since eq.(3.10) is linear in $\delta \boldsymbol{r}_{\rm b}(t)$ it can be Fourier transformed and solved. By making use of the FDT (eq.(3.12)) we can obtain analytical expressions for all the components of the one-sided Fourier transform of the mean-squared displacement tensor ($\langle \overline{\delta \boldsymbol{r}_{\rm b}[\omega] \delta \boldsymbol{r}_{\rm b}[\omega]} \rangle_{\rm eq}$). Since the process is stationary, we can utilize $\langle \delta \boldsymbol{r}_{\rm b}(0) \delta \boldsymbol{r}_{\rm b}(0) \rangle_{\rm eq} = \langle \delta \boldsymbol{r}_{\rm b}(t) \delta \boldsymbol{r}_{\rm b}(t) \rangle_{\rm eq}$ to write

$$\langle \Delta \delta \boldsymbol{r}_{\rm b}(t) \Delta \delta \boldsymbol{r}_{\rm b}(0) \rangle_{\rm eq} = 2 \left(\langle \Delta \delta \boldsymbol{r}_{\rm b}(0) \Delta \delta \boldsymbol{r}_{\rm b}(0) \rangle_{\rm eq} - \langle \Delta \delta \boldsymbol{r}_{\rm b}(t) \Delta \delta \boldsymbol{r}_{\rm b}(0) \rangle_{\rm eq} \right) \tag{3.14}$$

where the angular brackets $\langle ... \rangle_{\rm eq}$ mean an ensemble average taken at equilibrium.

For a homogeneous isotropic medium the mean-squared displacement tensor will be symmetric with four distinct components. A diagonal component involving only autocorrelations in the direction perpendicular to the line of centers,

$$\langle \Delta \delta r_{\rm b}^2(t) \rangle_{\perp} \;\; := \;\; 2 \left(\langle \delta r_{\rm b(1)\perp}(0)^2 \rangle - \langle \delta r_{\rm b(1)\perp}(t) \delta r_{\rm b(1))\perp}(0) \rangle \right), \tag{3.15}$$

and a similar definition for the mean-squared displacement (MSD) in the direction parallel to the line of centers. The off-diagonal components of the mean-squared displacement tensor involve only cross-correlations, one of them in the direction per-

pendicular to the line of centers,

$$\langle \Delta\delta r^2_{\mathrm{b}(1,2)}(t)\rangle_\perp \;:=\; -2\langle \delta r_{\mathrm{b}(1)\perp}(t)\delta r_{\mathrm{b}(2))\perp}(0)\rangle \tag{3.16}$$

and an equivalent cross-mean-squared displacement (CMSD) in the direction perpendicular to the line of centers.

The following relationship between the one-sided Fourier transform of the mean-squared displacement in the direction perpendicular to the line of centers and the memory function tensor can be found by using the the FDT eq.(3.12) and the solution of the GLE eq.(3.10) in the frequency domain,

$$\langle \overline{\Delta\delta r^2_{\mathrm{b}}}[\omega]\rangle_\perp = \frac{2k_{\mathrm{B}}T\left(H_{\mathrm{e}} - m\omega^2 + i\omega\bar{\zeta}_{1,1}[\omega]\right) i\omega}{-\omega^2\left(H_{\mathrm{e}} - m\omega^2 + i\omega\bar{\zeta}_{1,1}[\omega]\right)^2 - \omega^4\bar{\zeta}_{1,3}[\omega]^2}. \tag{3.17}$$

An equivalent relation can be written for the direction parallel to the line of centers with the replacements $\bar{\zeta}_{1,1}[\omega] \to \bar{\zeta}_{2,2}[\omega]$ and $\bar{\zeta}_{1,3}[\omega] \to \bar{\zeta}_{2,4}[\omega]$. The following relation between the CMSD and the components of the memory tensor, can also be obtained from the solution of the GLE and the FDT in the frequency domain,

$$\langle \overline{\Delta\delta r^2_{\mathrm{b}(1,2)}}[\omega]\rangle_\perp = \frac{2k_{\mathrm{B}}T\bar{\zeta}_{1,3}[\omega]\omega^2}{-\omega^2\left(H_{\mathrm{e}} - m\omega^2 + i\omega\bar{\zeta}_{1,1}[\omega]\right)^2 - \omega^4\bar{\zeta}_{1,3}[\omega]^2}. \tag{3.18}$$

Here again an equivalent equation can be written for the direction parallel to the line of centers with the replacements $\bar{\zeta}_{1,1}[\omega] \to \bar{\zeta}_{2,2}[\omega]$ and $\bar{\zeta}_{1,3}[\omega] \to \bar{\zeta}_{2,4}[\omega]$.

Eqs.(3.17) and (3.18) and their equivalent equations in the direction parallel to the line of centers, used together with eq.(3.13) and a set of definitions for the functions $A_\perp(\omega)$ and $A_\parallel(\omega)$, either eqs. (3.4) and (3.3) for the point force approximation, or eqs.(3.9) and (3.8) for the finite-sized beads, relate observable two-bead statistics to linear viscoelastic properties of the fluid. These relations include bead and medium inertia as well as an infinite number of reflections.

For the sample calculations that follow we consider a discrete relaxation spec-

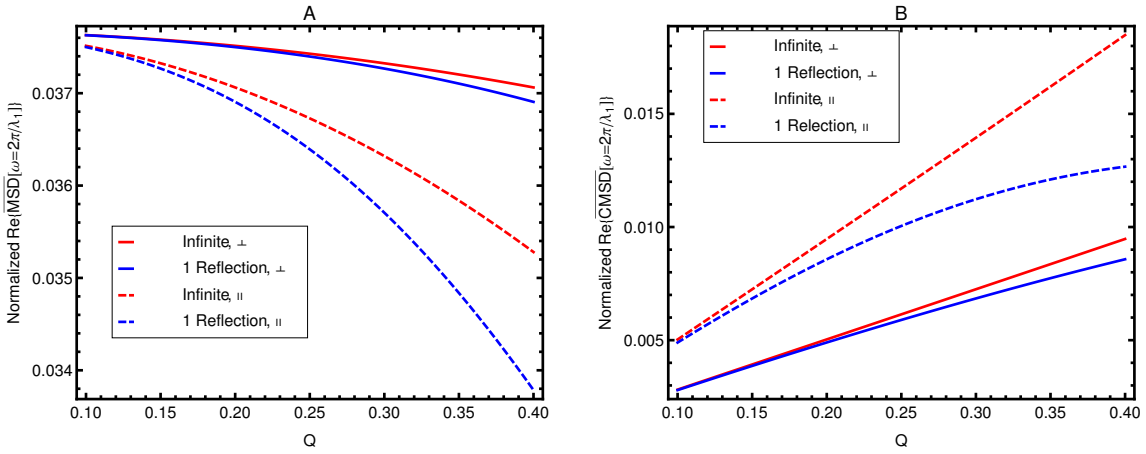

Figure 3.2. Real part of the one-side Fourier transform of the mean-squared displacements (MSD) and cross-mean-squared displacement (CMSD) evaluated at the frequency corresponding to the smallest relaxation time ($\omega = 2\pi/\lambda_1$), for beads embedded in a 4-mode fluid as a function of the bead radius to bead separation ratio. Comparisons between curves obtained with memory tensors with one reflection and infinite reflections are shown. A:Real part of the MSD. B:Real part of the CMSD.

trum, which gives the following form for the dynamic modulus of the medium

$$G^*(\omega) = \sum_{j=1}^{N} \frac{g_j \lambda_j i\omega}{1 + \lambda_j i\omega}, \tag{3.19}$$

To illustrate the effect of reflections and finite bead size on the solutions derived above, we consider the 4-mode relaxation spectrum, $\boldsymbol{H}^* = \{4, 3, 2, 1\}$ and $\boldsymbol{\lambda}^* = \{1, 3, 9, 27\}$ where $H_j := 6\pi R g_j$ and the asterisk indicates the they have been made dimensionless by using $\sqrt{k_B T / H_e}$ as the characteristic length scale and the smallest relaxation time, $\lambda = \min\{\lambda_j\}$, as the characteristic time scale. For the following illustrations the dimensionless bead mass is set to $m^* = m/(\lambda_1^2 H_e) = 0.0001$ and the mass of fluid per bead volume ($M = \frac{4}{3}\pi R^3 \rho$) is set to the same value. Therefore $\sqrt{m^*} = \sqrt{M^*} = 0.01$ is the ratio between the smallest inertial time scale of the system and the shortest relaxation time of this fluid. For micron-size beads suspended in water and trapped by optical tweezers ($H_e \approx 7 \times 10^{-4} N/m$) there is a single characteristic time scale which is defined by the viscosity of the fluid and the strength of the trap ($\lambda = 6\pi R\eta / H_e$). In that system the ratio between the inertial time scale λ_m and the viscous characteristic

time scale is approximately 0.07. For example, when performing microrheology of biopolymers, which usually contain water as solvent, it is reasonable to assume that viscoelastic relaxation time scales will start to be observable shortly after the viscous characteristic time for water. Therefore a ratio $\lambda_m/\lambda_1 = 0.01$ will be typical in this type of system.

Figure 3.2 shows the real part of the one-sided Fourier transform of the MSD and CMSD, evaluated at the frequency corresponding to the smallest relaxation time ($\omega = 2\pi/\lambda_1$), as a function of Q. We first consider the effect of including an infinite number of reflections in the memory function tensors, for the plots in Figure 3.2 the point-force expressions for $A_\perp(\omega)$ and $A_\parallel(\omega)$ were used. It can be observed that the memory functions with only one reflection systematically underestimate the MSD and the CMSD at timescales where viscoelasticity dominates. Not surprisingly, the closer the beads are placed (larger Q), the more important the number of reflections. As a reference, when the beads are placed one bead diameter apart, $Q = 0.25$. As expected, both solutions converge to the same estimates of the MSD and CMSD as Q decreases.

In Figure 3.3 the real part of the one-sided Fourier transform of the MSD and CMSD generated using the memory tensors with the point-force approximation, eqs.(3.4) and (3.3), are compared with the MSD and CMSD generated using the memory function tensors that were derived using the the finite-size solutions, eqs.(3.9) and (3.8). The point-force approximation slightly overestimates the MSD in the direction perpendicular to the line of centers, but significantly underestimates the MSD in the direction parallel to the line of centers for $Q \geq 0.25$. Ordinarily this difference at $Q > 0.25$ would be unimportant in two-point microrheology, where length scales larger than the bead size are sampled and therefore Q is always chosen to be smaller than 0.25. On the other hand the point-force approximation slightly

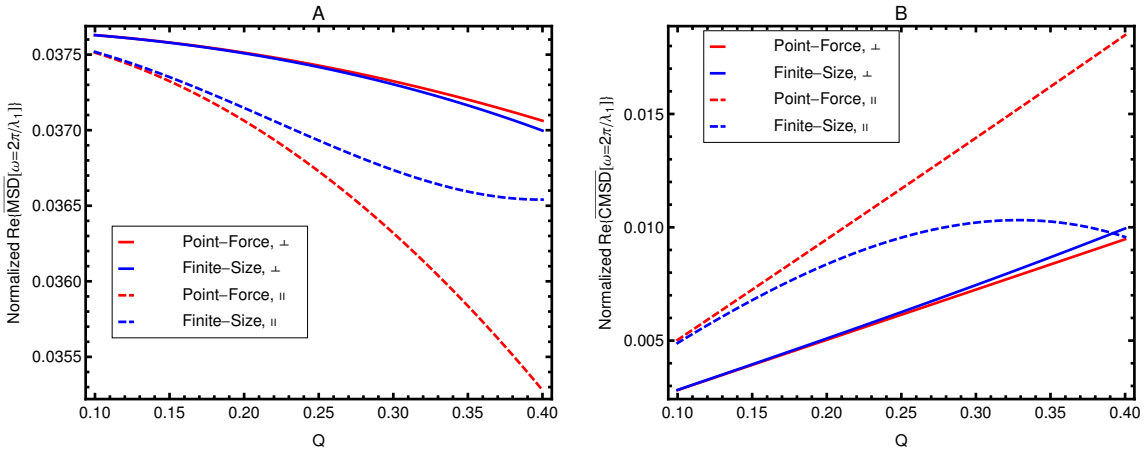

Figure 3.3. Real part of the one-side Fourier transform of the mean-squared displacements (MSD) and cross-mean-squared displacement (CMSD) evaluated at the frequency corresponding to the smallest relaxation time ($\omega = 2\pi/\lambda_1$), for beads embedded in a 4-mode fluid as a function of the bead radius to bead separation ratio. Comparisons between curves obtained with memory tensors with one reflection and an infinite number of reflections are shown. A:Real part of the MSD. B:Real part of the CMSD.

underestimates the CMSD in the direction perpendicular to the line of centers but significantly overestimates it in the direction parallel to the line of centers for $Q \geq 0.25$.

At frequencies higher than that corresponding to the fastest relaxation time of the fluid the discrepancies between the MSD predicted by the point-force approximation and the finite-size sphere become larger. Figure 3.4 shows comparisons between the real part of the one-sided Fourier transform of the MSD generated by the point-force approximation and the finite-size solutions. In the direction parallel to the line of centers both methods predict the same high-frequency plateau followed by a ballistic region. The relative residuals between the two solutions increase as frequency increases, but are evenly distributed around zero and do not increase beyond 5%. On the other hand, for the direction parallel to the line of centers the memory tensor calculated with the finite-bead-size solution produces an MSD with a much longer

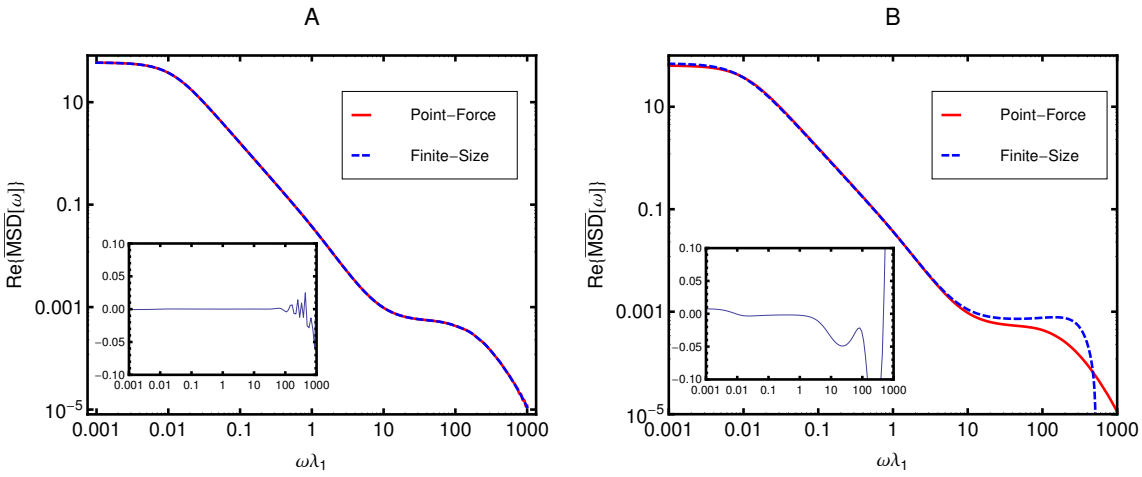

Figure 3.4. Real part of the one-sided Fourier transform of the mean-squared displacement (MSD) for a 4-mode fluid as a function of frequency. The bead radius to bead separation ratio was set to 0.2 for these figures. A: In the direction perpendicular to the line of centers. B: In the direction perpendicular to the line of centers. The insets show the relative residuals between the two curves.

high-frequency plateau and no ballistic region, while the point-force approximation produces a much smaller high-frequency plateau followed by a ballistic region.

3.4 Phase diagram for two-point microrheology

We address here when the data analysis formalism that includes inertia and infinite reflections should be used, and when the inertia-less one, with only the lowest-order reflections gives correct results. We consider two simple dimensional arguments that can serve as guides to choose the proper data analysis strategy for a given fluid and set of experimental conditions. As was shown in Section 3.2, for the wave that forms in the bead-fluid interface to decay before producing multiple reflections it is required that $\frac{2L}{\Delta(\omega)} \gg 1$. For a viscoelastic fluid the ratio $\frac{2L}{\Delta(\omega)}$ increases as $\sim \omega^{1/2}$ at low frequencies. Whereas for a purely viscous fluid the ratio $\frac{L}{\Delta(\omega)}$ always increases with increasing frequency as $\sim \omega^{1/2}$, for a viscoelastic fluid it reaches a plateau at high frequencies, where elasticity dominates in the response, and becomes frequency independent. Figure 3.5 shows a phase diagram for the two-point microrheology

experiment done by Crocker et al. [19] on 0.25 % guar solutions with 0.20 μm diameter beads. The dashed line represent $\frac{2L}{\Delta(\omega)} = 1$, which means that, in region II, below this line it is safe to neglect higher order reflections in the analysis of the CMSD. The line stops at a $\omega = 0.2\lambda_1$ because for larger values of Q the ratio $\frac{2L}{\Delta(\omega)}$ never becomes greater than one. Again this is due to the elasticity of the fluid which dominates at high frequencies, making $\Delta(\omega)$ frequency independent.

We turn now to the effects of medium inertia. The main effect of medium inertia is that it can significantly affect the velocity at which the waves generated at the bead-fluid interface propagate through the fluid. Therefore to analyze these effects it is useful to define the speed at which the wave produced at the bead-fluid interface propagates through the fluid,

$$c(\omega) = \omega\Lambda(\omega). \tag{3.20}$$

Where $\Lambda(\omega)$ is the wavelength of the wave, that was defined in eq.(3.5). Therefore the time it takes for the wave to travel from one bead to the other is $\frac{L}{c(\omega)}$. At time scales much longer than this the propagation of stress through the medium can be assumed to be instantaneous and therefore inertia can be safely neglected from the analysis. Therefore for medium inertia to be negligible $\frac{\omega L}{c(\omega)} \ll 1$. At high frequencies inertia becomes important because the time the wave takes to travel between the beads becomes comparable to the relaxation time of the fluid being measured at a frequency ω. At low frequencies the waves behave as they would in a purely viscous fluid, $\frac{\omega L}{c(\omega)} \sim \omega^{1/2}$. With increasing frequency the response becomes more elastic and the effects of medium inertia more pronounced, $\frac{\omega L}{c(\omega)} \sim \omega$. Opposite to what is required to reduce the effect of reflections, to reduce the effect of inertia a large Q is required. This is because the shorter the distance between the beads, the shorter the time it takes for the waves to propagate between them and therefore the assumption that the propagation occurs instantaneously is more easily approached. The continuous line in

the phase diagram shown Figure 3.5 represents $\frac{\omega L}{c(\omega)} = 1$. In region III, above this line, the effects of inertia can be neglected when inferring $G^*(\omega)$ from the CMSD. Region I in the phase diagram is the intersection of regions II and III and therefore both higher order reflections and inertia can be neglected when inferring $G^*(\omega)$ in that region. When inferring $G^*(\omega)$ from a two-point microrheology experiment, carried under conditions that fall inside region IV a data analysis formalism that accounts for inertia and reflections is more appropriate.

The phase diagram shown in Figure 3.5 corresponds to a specific ratio between the smallest characteristic time for inertia and the shortest relaxation time of the fluid, $\sqrt{M/(H_e\lambda_1^2)}$. If only a low-frequency range of the dynamic modulus is to be measured then the $\sqrt{M/(H_e\lambda_1^2)}$ ratio will have a smaller value and the continuous line (inertial boundary) will move to the right (towards higher frequencies). The main result being that region III will be expanded while region IV will shrink. On the other hand if one wishes to measure viscoelastic properties at smaller time scales, then the ratio $\sqrt{M/(H_e\lambda_1^2)}$ will become larger and the inertial boundary will move to the left that is, towards lower dimensionless frequencies, making region III smaller.

We now check more precisely the ability of this simple dimensional analysis to predict the importance of inertia and reflections. We calculate the MSD for a model viscoelastic fluid using generalized Brownian dynamics simulations and compare the performance in recovering the input $G^*(\omega)$ of data analysis algorithms that do not include inertia and high order reflections with the data analysis formalisms that includes inertia and all reflections.

3.5 Time-domain data-analysis strategy

A common approach to analyze microbead rheology data is to calculate the power spectral-density (PSD) by applying FFT directly to the raw bead position data

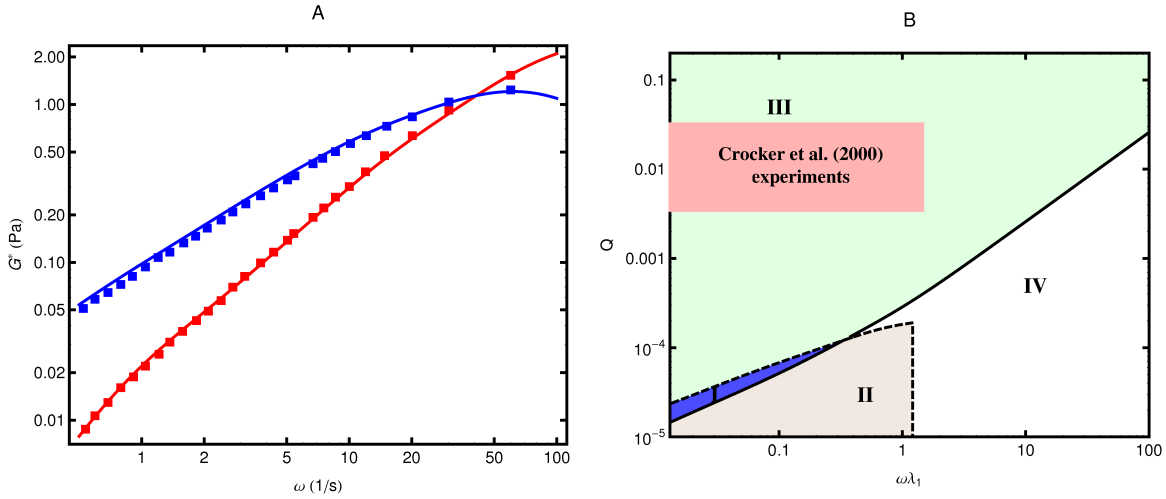

Figure 3.5. A: Data points correspond to G' (filled symbols) and G" (empty symbols) data for 0.25 % guar solutions obtained by passive two-point microrheology presented by Crocker et al. [19]; the continuous lines is a fit of a multimode Maxwell model to the experimental data. B: The phase diagram for the two-point microrheology experiment of the 0.25 % guar solutions [19] using dimensional analysis. The continuous line represents $\frac{\omega L}{c(\omega)} = 1$, and the dashed line is $\frac{2L}{\Delta(\omega)} = 1$. In region II, $\frac{2L}{\Delta(\omega)} \gg 1$, higher order reflections can be neglected. In region III, $\frac{\omega L}{c(\omega)} \ll 1$, fluid inertia can be neglected. In region I both inertia and reflections can be neglected. In region IV neither reflection nor inertia should be neglected when inferring $G^*(\omega)$ from the CMSD. For this fluid λ_1 is equal to 0.014 seconds.

and squaring the absolute value of the result to obtain the real part of the one-sided Fourier transform of the MSD. The imaginary part of the one-sided Fourier transform of the MSD is obtained from the Kramers-Kronig relation [110]. These methods however are known to introduce errors associated with frequency discretization and finite-size windowing. Recently time-domain data analysis strategies that overcome these issues were proposed [16, 28] for one-point microrheology. However, to derive time-domain methods for high-frequency two-point passive microrheology the inverse one-sided Fourier transform of eqs.(3.17) and (3.18) must be calculated. We next propose an efficient method to approximate these integrals.

3.5.1 Rational approximations of the memory function tensors. For a

purely viscous fluid the one-sided Fourier transform of eq.(3.13) can be performed analytically using the contour integration technique [3]. However for viscoelastic fluids the inverse one-sided Fourier transform of eq.(3.13) can not be taken analytically since it involves terms that contain the square root of $G^*(\omega)$ or the inverse of the square root of $G^*(\omega)$ in an exponent. Even for the simplest model to describe $G^*(\omega)$ for a viscoelastic fluid, the one-mode Maxwell model, the one-sided Fourier transforms of eq.(3.13) can not be performed analytically. We therefore seek rational function approximations in the frequency domain for the non-zero components of the memory tensor eq.(3.13) which will allow us to take the inverse one-sided Fourier transforms in a straightforward and computationally efficient way. To construct the approximations we start by specifying a functional form for $G^*(\omega)$ given by an N-mode discrete relaxation spectrum, eq.(3.19). Moreover, a continuous spectrum can be approximated to arbitrary accuracy by a discrete spectrum [5, 7]. We find that the memory function tensor that includes infinite reflections and medium inertia effects can be well approximated by,

$$\boldsymbol{\zeta}(t) \approx \bar{\mathcal{F}}^{-1}\left\{\boldsymbol{a} + \boldsymbol{b}i\omega + \sum_{i=1}^{N}\frac{\boldsymbol{c}_i}{i\omega+\lambda_i}\right\} = \boldsymbol{a}\delta(t) + \boldsymbol{b}\frac{d\delta(t)}{dt} + \sum_{i=1}^{N}\boldsymbol{c}_i e^{-t/\lambda_i}. \qquad (3.21)$$

The non-zero components of the tensors $\boldsymbol{a}$, $\boldsymbol{b}$, $\boldsymbol{c}_1$, ... $\boldsymbol{c}_N$ are found by sampling the components of eq.(3.13) and fitting rational functions to them. We find that $\boldsymbol{b} = M_{\text{eff}}\boldsymbol{\delta}$ is always a diagonal tensor that contains the effective mass of fluid dragged by each individual bead accounting for the effect of reflections. $\boldsymbol{a}$ is an effective coefficient for the dissipation of energy from the bead caused by fluid inertia and the $\{\boldsymbol{c_i}\}$ tensors contain the strengths of each Maxwell mode modified by fluid inertia and reflections.

To illustrate the performance of the rational approximation for the memory function tensor, Figure 3.6 shows a comparison between the MSD generated with the exact solutions and with the rational approximations for the 4-mode Maxwell fluid introduced in the previous section, $\boldsymbol{H}^* = \{4, 3, 2, 1\}$ and $\boldsymbol{\lambda}^* = \{1, 3, 9, 27\}$. The insets

show the absolute residuals between the exact solutions generated with the point force method and those generated using the rational approximations. The approximations reproduce the exact MSD well in the entire frequency range. At higher frequencies, in the ballistic region, the relative residuals become larger but they usually stay below 5% and are distributed around zero without a systematic error. Moreover at those high frequencies, where ballistic motion dominates, rheological properties can not be extracted from the MSD or CMSD so these small errors are not expected to be important. This type of approximation for the memory function tensor can in principle be used for discrete relaxation spectra with arbitrary number of modes, since the computational cost of generating the approximations scales linearly with the number of modes.

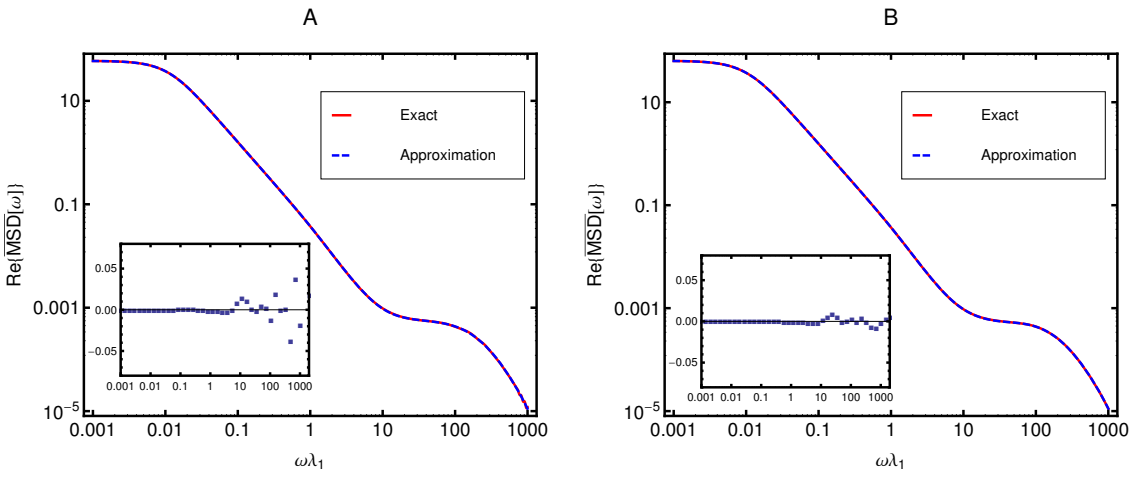

Figure 3.6. Comparison between the real part of the one-sided Fourier transform of the mean-squared displacement (MSD) for beads embedded in a 4-mode fluid generated by using exact solutions of the memory tensor or by using rational approximations. Insets show the relative residuals between the curves. A: In the direction perpendicular to the line of centers. B: In the direction parallel to the line of centers. The insets show the relative residuals between the two curves.

Figure 3.7 shows the effect that the radius-to-separation ratio, Q, has on the capacity of the rational approximations to reproduce the MSD and CMSD generated by the exact solution at frequencies corresponding to the fastest relaxation time of

the fluid. The rational approximations reproduce the exact solutions very well for all values of Q. Note that for $Q = 0.5$ the beads are touching and for $Q = 0.25$ exactly one bead would fit in the space between the two beads. For two point microrheology experiments, where the objective is primarily to sample length scales larger than with one point microrheology, Q is usually smaller than 0.25. The agreement seen for $Q < 0.25$ provides some justification for the approximation usually used in data analysis.

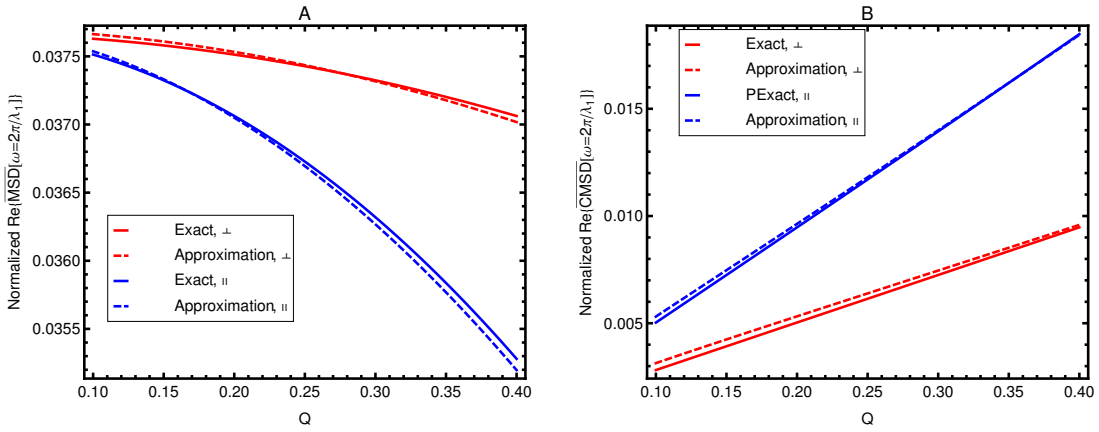

Figure 3.7. Effect of the radius-to-distance ratio, Q, on the quality of the rational approximation of the memory tensor. A: On reproducing the mean-squared-displacement (MSD) evaluated at the frequency corresponding to the fastest relaxation time. B: On reproducing the cross-mean-squared-displacement (CMSD) at the frequency corresponding to the fastest relaxation time.

Using the rational approximation for the memory function tensor, eqs.(3.17) and (3.18) can be transformed to the time domain using well-known methods for calculating the inverse one-sided Fourier transform of rational functions. These methods involve a one-dimensional root finding, and the solution of a linear system of equations [5]. The time-domain expressions, which are sums of exponentials, can be fitted to MSD and CMSD data in the time domain. $G^*(\omega)$ is inferred using the fitted parameters.

3.5.2 Generalized Brownian dynamics simulations. The rational approx-

imation of the memory function tensor also allows us to extend our one-point microrheology simulation tools [16] to two-point microrheology. The GLE, eq.(3.10), with a memory function tensor given by eq.(3.21) can be written as an equivalent higher-dimensional Markovian system of SDEs. We can therefore perform Brownian dynamics (BD) simulations of the two-point microrheology experiment, and use these simulations to perform Monte-Carlo evaluations of our time-domain data analysis strategy.

Lower-dimensional non-Markovian stochastic differential equations SDEs can be written as equivalent higher-dimensional Markovian SDEs. The non-Markovian GLE eq.(3.10) with memory tensor (3.21) can be written as a system of Markovian SDEs by introducing new stochastic variables with white noise spectra [16, 28, 22]. The SDE for the momentum of bead 1 in the direction perpendicular to the line of centers is,

$$\begin{aligned} dp_{\mathrm{b}(1)\perp}(t) &= -H_{\mathrm{e}}\delta r_{\mathrm{b}(1)\perp}(t)dt - \left(\sum_{j=1}^{N} c_{1,1,j}Q_{(1)\perp,j}(t) - \sum_{j=1}^{N} c_{1,3,j}Q_{(2)\perp,j}(t)\right)dt \\ &\quad - \left(\frac{a_{1,1}p_{\mathrm{b}(1)\perp}(t)}{m_{\mathrm{eff}}} + \frac{a_{1,3}p_{\mathrm{b}(2)}(t)}{m_{\mathrm{eff}}}\right)dt \\ &\quad + \sqrt{\frac{k_{\mathrm{B}}T}{2}}\left(\sqrt{a_{1,1}-a_{1,3}} + \sqrt{a_{1,1}+a_{1,3}}\right)dW_{1,\perp}(t) \\ &\quad + \sqrt{\frac{k_{\mathrm{B}}T}{2}}\left(\sqrt{a_{1,1}-a_{1,3}} - \sqrt{a_{1,1}+a_{1,3}}\right)dW_{2,\perp}(t) \end{aligned} \tag{3.22}$$

where $m_{\mathrm{eff}} = m + M_{\mathrm{eff}}/2$, and $Q_{(1)\perp,j}$ and $Q_{(2)\perp,j}$ are the new stochastic variables introduced to make the system Markovian. The SDEs for $\{Q_{(1)\perp,j}\}$ are,

$$\begin{aligned} dQ_{(1)\perp,j}(t) &= \left(\frac{p_{\mathrm{b}(1)\perp}}{m_{\mathrm{eff}}} - \frac{Q_{(1)\perp,j}(t)}{\lambda_j}\right)dt \\ &\quad + \sqrt{\frac{k_{\mathrm{B}}T}{2}}\left(\sqrt{\frac{1}{\lambda_j\left(c_{1,1,j}-c_{1,3,j}\right)}} + \sqrt{\frac{1}{\lambda_j\left(c_{1,1,j}+c_{1,3,j}\right)}}\right)dW_{1,\perp,j}(t) \\ &\quad + \sqrt{\frac{k_{\mathrm{B}}T}{2}}\left(\sqrt{\frac{1}{\lambda_j\left(c_{1,1,j}-c_{1,3,j}\right)}} - \sqrt{\frac{1}{\lambda_j\left(c_{1,1,j}+c_{1,3,j}\right)}}\right)dW_{2,\perp,j}(t), \end{aligned} \tag{3.23}$$

Where the vector of Wiener processes $d\boldsymbol{W} = \{dW_{1,\perp}, dW_{2,\perp}, dW_{1,\perp,1}, dW_{2,\perp,1}, ...dW_{1,\perp,j}, dW_{2,\perp,j}, ...\}$ has white-noise properties, *i.e.*,

$$\langle d\boldsymbol{W}(t)\rangle_{\text{eq}} = 0, \qquad \langle d\boldsymbol{W}(t)d\boldsymbol{W}(t')\rangle_{\text{eq}} = \delta(t-t')\boldsymbol{\delta}dtdt'. \tag{3.24}$$

Equivalent equations for bead number 2 are coupled to eqs.(3.22) and (3.23). The resulting system of coupled SDEs has $2+2N$ equations, the vector of Wiener processes for the system has $4+4N$ components. A similar system, but involving different components of the memory function tensor can be written for the direction parallel to the line of centers. We simulate these systems of Markovian SDEs using Brownian dynamics [16, 32, 96]. A multi-tau photon correlation spectroscopy (PCS) algorithm [27, 84, 76] is used to calculate the MSDs and CMSDs on the fly, during the simulations [16].

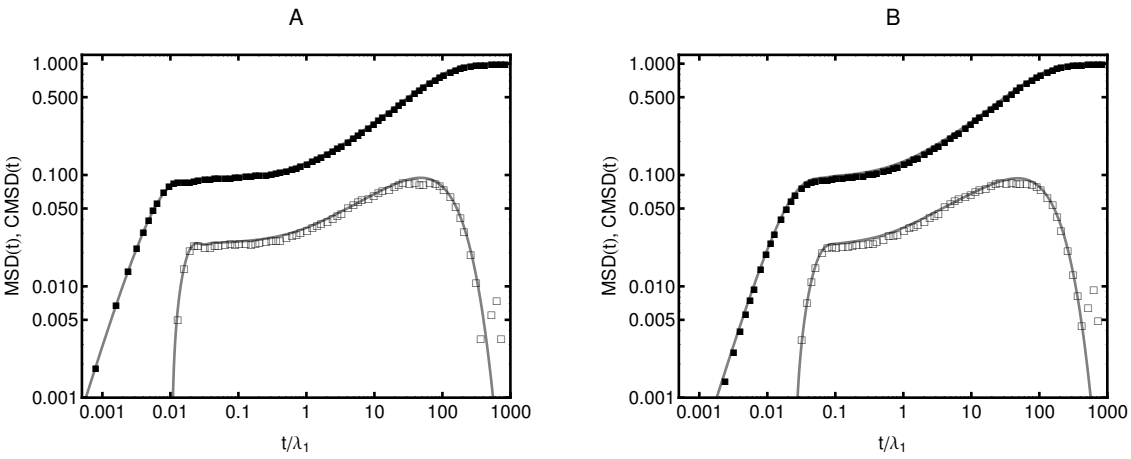

Figure 3.8. Normalized mean-squared-displacement (filled squares) and cross-mean-squared-displacement (empty squares), in the direction parallel to the line of centers, generated by generalized Brownian dynamics simulations for beads embedded in a 4-mode Maxwell fluid, including inertia and infinite reflections. A: $\sqrt{M/(H_e\lambda_1^2)} = 0.01$, $Q = 0.2$. B: $\sqrt{M/(H_e\lambda_1^2)} = 0.032$, $Q = 0.2$. The lines are fits used to transform the data to the frequency domain.

Figure 3.8 shows the MSD (filled squares) and CMSD (empty squares), in the direction parallel to the line of centers, obtained with BD simulations of the two-point passive microrheology experiment for beads embedded in the 4-mode Maxwell

fluid introduced earlier. The generalized Brownian dynamics simulations are not limited however to a small number of modes in the discrete relaxation spectrum, as we have previously illustrated [16]. At very short time scales ($t \leq 0.002\lambda_1$) the MSD is characterized by a ballistic region ($\sim t^2$) caused by particle inertia. This is followed by a small diffusive ($\sim t$) region ($0.005\lambda_1 \leq t \leq 0.01\lambda_1$) caused by the medium inertia, which at these high frequencies plays the same role as a purely viscous element, and therefore damps the oscillations that would otherwise be produced by particle inertia [52, 16]. A plateau caused by the elastic elements of the fluid can be observed for $0.01\lambda_1 \leq t \leq \lambda_1$. For time scales longer than the shortest relaxation time of the fluid ($t > \lambda_1$) an anomalous diffusion region ($\sim t^{1/2}$) can be observed. This is followed by the elastic plateau caused by the trap. In the CMSD the high-frequency ballistic and diffusive slopes are not observed, the cross-correlations becomes zero for $t \leq 0.01\lambda_1$. The high-frequency viscoelastic plateau and the anomalous diffusion regions can be observed in the CMSD. However no elastic plateau is observed at long time scales since the traps are uncorrelated.

In the simulation that gives the results shown in Figure 3.8A Q was set to 0.2 and the ratio between the smallest inertial characteristic time scale and the shortest relaxation time of the fluid, $\sqrt{M^*} = \sqrt{M/(H_e\lambda_1^2)}$ was set to 0.01. The results shown in Figure 3.8B correspond to a simulation where Q was also set to 0.2, but the ratio of time scales $\sqrt{M^*}$ was set to 0.032, which means that there is a less pronounced separation of inertial and viscoelastic time scales in the system. Recall that for micron-sized beads suspended in water and trapped by optical tweezers the ratio between the inertial time scale and the characteristic viscous time scale is approximately 0.07. Therefore a value of $\sqrt{M^*}$ of 0.032 is still a reasonable value at which high-frequency viscoelastic response may be observed in biopolymers that contain water as solvent.

Since we have assumed that the fluid is a continuum, which implies that the radius of the beads is much larger than the microstructure of the medium, the dynamic modulus obtained from both the MSD and the CMSD, obtained from the BD simulations, should be the same. We have previously performed Monte-Carlo evaluations for the time-domain data analysis of MSDs [16], therefore in this work we focus on analyzing the CMSDs in the time domain to obtain $G^*(\omega)$. The lower gray line in Figure 3.8A is a fit of the inverse one-sided Fourier transform of eq.(3.18) to the CMSD generated with the BD simulations. The fitted parameters are the strengths $\{H_j\}$ and the relaxation times $\{\lambda_j\}$ of the 4-mode Maxwell model. To check self consistency we have also plotted (in Figure 3.8) the one-sided inverse Fourier transform of eq.(3.17) using the parameters obtained from fitting the CMSD. As expected, since we have assumed a continuum, this line falls on top of the MSD generated by the BD simulations. In cases were the size of the bead is smaller than the microstructure of the medium the rheological properties inferred from the CMSD can differ from the ones obtained from analyzing the MSD. It has been shown experimentally [19] and theoretically [73] that the CMSD is less contaminated by local inhomogeneities surrounding the beads, and is therefore a better estimator for the bulk rheological properties of the medium. Note however that the signal-to-noise ratio in the CMSD will alway be smaller than in the MSD. Therefore in experiments an optimal distance L between the beads exists at which the desired length scales are sampled with the CMSD, while keeping a desired signal-to-noise-ratio. If the data analysis method being used can not account for the effects of inertia and reflections one has to add yet another restriction to the choice of Q, since it must be large enough to make such effects negligible.

3.6 The inertia-less limit

In this section we consider the inertia-less and zero-reflections limit of the com-

ponents of the memory function tensor eq.(3.13) and the GLE eq.(3.10). We consider this limit because the expressions that result from it are those most commonly used to analyze two-point passive microrheology experiments. We then compare a time-domain method based on the inertia-less zero-reflections versions of eqs.(3.17) and (3.18) to the time domain method described in the previous section which includes medium and bead inertia as well as infinite reflections.

For small $Q = R/L$ ratio (only first-order terms of a Taylor series expansion) and in the limit $\rho \to 0$, the memory functions take the well known inertia-less forms [113, 19, 4],

$$\zeta_{1,1}(t) = \zeta_{3,3}(t) = \zeta_{2,2}(t) = \zeta_{4,4}(t) = \bar{\mathcal{F}}^{-1}\left\{\frac{6\pi R G^*(\omega)}{i\omega}\right\} \tag{3.25}$$

$$\zeta_{2,4}(t) = \zeta_{4,2}(t) = -\frac{3Q}{2}\zeta_{1,1}(t) = \bar{\mathcal{F}}^{-1}\left\{-\frac{9Q\pi R G^*(\omega)}{i\omega}\right\} \tag{3.26}$$

$$\zeta_{1,3}(t) = \zeta_{3,1}(t) = \frac{\zeta_{2,4}(t)}{2} = \frac{\zeta_{4,2}(t)}{2} \tag{3.27}$$

Note that the one-sided inverse Fourier transforms in eqs.(3.25-3.27) can be taken analytically if a generalized Maxwell model is specified for $G^*(\omega)$, since all the integrands can be written as rational functions.

By using the simplified memory functions eqs.(3.25-3.27) and by setting the bead mass equal to zero in eq.(3.17) we obtain the following expression for the MSD of the two beads,

$$\langle\overline{\Delta\delta r_{\mathrm{b}}^2}[\omega]\rangle = \frac{6k_{\mathrm{B}}T}{i\omega\left(H_{\mathrm{e}} + i\omega\bar{\zeta}_{1,1}[\omega]\right)}. \tag{3.28}$$

Similarly, by using eqs.(3.25-3.27) together with eq.(3.18) we obtain the following simplified expression for the CMSD between the two beads,

$$\langle\overline{\Delta\delta r_{\mathrm{b}(1,2)}^2}[\omega]\rangle = \frac{9Qk_{\mathrm{B}}T\bar{\zeta}_{1,1}[\omega]}{2\left(H_{\mathrm{e}} + i\omega\bar{\zeta}_{1,1}[\omega]\right)^2}. \tag{3.29}$$

Eqs.(3.28) and (3.29) or their analogs for free particles are well known, and widely used to analyze two-point passive microrheology experiments. However one must be careful when taking this inertia-less limit since it is singular [52, 89]. We have previously shown that by including a small, purely dissipative element in the memory function of the GLE, ζ_0, one can eliminate inertia from the GLE avoiding the singularity [52, 16]. In the memory functions that include medium inertia the purely dissipative element arises naturally at high frequencies from the Basset force terms. However once these terms are neglected a small purely dissipative element must be introduced in the memory functions of the inertia-less GLE to avoid the inertia-less singular limit [52].

The inverse one-sided Fourier transforms of Eqs.(3.28) and (3.29) can also be taken analytically if a generalized Maxwell model is used for $G^*(\omega)$, since the right sides involve only rational functions. Similar to Reference [16], the following expression results from taking the one-sided Fourier transform of eq.(3.29), after specifying a generalized Maxwell model for $G^*(\omega)$.

$$\langle \Delta\delta r^2_{\mathrm{b}(1,2)}(t)\rangle \;=\; \sum_{j=1}^{N+1}\left[c'_j(\{c_j\},H_{\mathrm{e}},\zeta_0)+c''_j(\{c_j\},H_{\mathrm{e}},\zeta_0)t\right]e^{-t/\lambda'_j(\{c_j\},H_{\mathrm{e}},\zeta_0)} \quad (3.30)$$

where the relations between H_j, λ_j, ζ_0 and H_{e} with c'_j, c''_j, and Λ'_j are found numerically when performing the transform.

3.7 Monte-Carlo evaluation of the data analysis algorithms

In this section we use the synthetic data generated with the simulations that include all reflections and medium inertia to test the data analysis algorithms presented in Sections 3.5 and 3.6. Figure 3.9 shows a comparison between the $G^*(\omega)$ used as input in the simulations and the $G^*(\omega)$ that is obtained from the time-domain data analysis of the CMSD generated with the BD simulations (Figure 3.8). Output 1 was obtained including inertia effects and an infinite number of reflections, Output

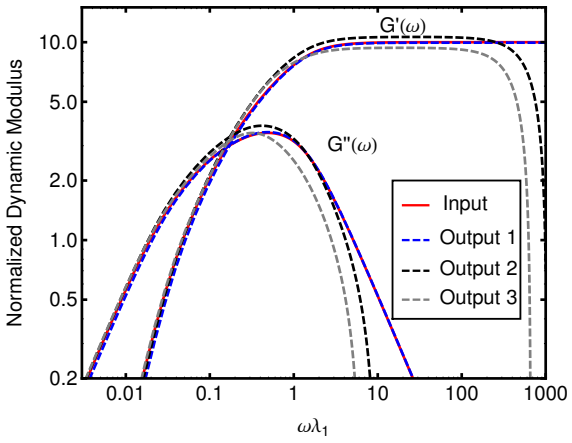

Figure 3.9. Monte-Carlo evaluation of the time-domain data analysis algorithms using the synthetic CMSD data generated with the BD simulations. Output 1: Obtained with the data analysis algorithm that include inertia and infinite reflections, eq. (3.18). Output 2: Obtained with the data analysis algorithm that neglects inertia and accounts only for first order reflections eq. (3.29). The ratio between the smallest inertial time scale and the shortest relaxation time of the fluid is 0.01 for this case. Output 3: Obtained with the data analysis algorithm that neglects inertia and accounts only for first order reflections eq. (3.29). The ratio between the smallest inertial time scale and the shortest relaxation time of the fluid is 0.032 for this case.

2 was inferred using the data analysis formalism that neglects fluid inertia and high order reflections, that is eq.(3.29). Both data analysis algorithms were applied to the same time-domain CMSD fit, therefore the errors observed in output 2 are entirely due to neglecting inertia and higher-order reflections when inferring $G^*(\omega)$. Output 2 was obtained from analyzing the CMSD obtained from a simulation in which the ratio between the smallest inertial time scale and the shortest relaxation time of the fluid, $\sqrt{M/(H_e\lambda_1^2)}$, was set to 0.01 while Output 3 was obtained from analyzing a CMSD in which this ratio was 0.032. It can be observed that in Output 3 the errors caused by neglecting inertia in the data analysis start corrupting the inferred $G^*(\omega)$ at lower frequencies than in output 2. On the other hand, the time-domain data analysis, that includes inertia and all reflections, performs equally well in inferring the dynamic modulus from the synthetic CMSD data for both values of $\sqrt{M/(H_e\lambda_1^2)}$.

We can now analyze the results presented in Figure 3.9 in the light of the phase diagram for two-point microrheology that was presented in Figure 3.5. The CMSD from which the $G^*(\omega)$ of Output 1 and Output 2 was inferred corresponds to a system at the top of region III of the phase diagram. At frequencies near the cross-over between G' and G'' the errors in Output 2 can be attributed entirely to neglecting higher-order reflections in the analysis. At frequencies close to $2\pi/\lambda_1$ there is a cancellation of the errors produced by neglecting higher-order reflections and the errors produced by neglecting inertia. At higher frequencies (region IV) inertia becomes important and the observed discrepancies from the input are due to inertial effects. When the separation between the smallest inertial time scale and the shortest relaxation time of the fluid is smaller (Output 3, in Figure 3.9), region III in the phase diagram shrinks and inertial effects become important at lower frequencies.

3.8 Conclusions

We have derived a generalized Stokes tensor for two hydrodynamically interacting beads embedded in a viscoelastic fluid. The tensors include the effects of medium inertia and consider an infinite number of reflections of the velocity waves caused by the motions of the beads. A generalized Langevin equation for two hydrodynamically interacting trapped beads embedded in a viscoelastic fluid was presented. Using the memory function tensor obtained from the generalized Stokes relation the GLE was solved in the frequency domain to obtain relations between the beads' auto- and cross-correlations and the components of the generalized Stokes tensor. We have analyzed the effects of including one reflection or an infinite number of reflections of velocity waves, in the generalized Stokes tensor. The memory functions with only one reflection systematically underestimate the MSD and the CMSD of particles embedded in a viscoelastic fluid. The effect of using point-force solutions or solutions for finite-size spheres, when constructing the tensors has also been addressed. MSDs

and CMSDs generated with both solutions agree for values of the radius-to-separation ratio below 0.25, but deviate significantly for values larger than that. However it is important to note that experiments are typically made with a radius-to-separation ratio below 0.25.

To derive a time-domain data analysis strategy for inferring high-frequency linear viscoelastic properties from two-point cross correlations, we have proposed rational function approximations for the components of the memory function tensor. The approximations allow one to perform efficiently the inverse one-sided Fourier transform of the expressions obtained for the MSD and CMSD from solutions of the GLE in the frequency domain. The rational approximation of the memory function tensor was also used to construct generalized Brownian dynamics (BD) simulations of the two-point passive microrheology experiment. The time-domain data analysis strategy for the two-point cross correlations was evaluated using synthetic data produced with the simulations.

We have taken the zero-inertia and lowest order reflections limit of the generalized Stokes tensor and the GLE and shown that in this limit our methods converge to the formulas most commonly used in the literature to analyze passive two-point microrheology. There is a considerably large region of values for the radius-to-distance ratio and frequency, relevant to microbead rheology experiments, where the data analysis formalism that neglects medium inertia and higher order reflections produces noticeable errors in the dynamic modulus inferred from two-point cross-correlations. At high frequencies the wavelength of the waves propagating trough the viscoelastic fluid becomes small compared to the distance between the beads and therefore the assumption that stress propagates instantaneously becomes invalid. Additionally reflected waves can be important at low frequencies, where the penetration depth of the waves can become larger than the distance between the beads. In experiments

an optimal distance L between the beads exists at which the desired length and time scales are sampled while keeping a desired signal-to-noise-ratio in the CMSD. A large L can reduce the effect of higher-order reflections, but will increase the effects of medium inertia and reduce the signal-to-noise-ratio in the CMSD. The data analysis formalism presented in this work significantly expands the region of distances between the beads and frequencies at which rheological properties can be accurately measured using two-point passive microrheology. Moreover the additional physics introduced in the data analysis formalisms do not add additional significant computational costs.

CHAPTER 4

THE EFFECTS OF COMPRESSIBILITY, HYDRODYNAMIC INTERACTION AND INERTIA ON TWO-POINT, PASSIVE MICRORHEOLOGY OF VISCOELASTIC MATERIALS

This Chapter previously appeared in Soft Matter (The Royal Society of Chemistry) volume 9, issue 13, page 3521-3534, year 2013.

4.1 Introduction

The two-point passive microrheology technique is based on measuring the cross-correlated thermal motion of pairs of tracer micron-sized beads ($R < 1\mu$m) to determine $G^*(\omega)$ [19, 73, 48]. Unlike bulk rheometers, microbead rheology requires only very small samples (pico- to microliter order) and elastic modulus as small as 10-500 Pa can be measured [59]. These advantages make the technique especially useful for the analysis of biological samples [1, 128]. The pair of particles of radius R is separated by a distance L larger than the microstructure of the medium. In the passive two-point microrheology experiment the beads are driven by Brownian forces. The motion of the beads creates a velocity field in the otherwise undisturbed medium. This velocity field is characterized by waves that originate at the bead-medium interface, and then reflect back and forth between the beads. The cross-correlations of the two tracer beads will therefore be determined by the nature of those waves. The waves produced at the bead-medium boundary can be characterized by a wavelength and a penetration depth. At a given frequency the wavelength indicates the velocity at which the waves propagate while the penetration length indicates a characteristic distance the wave propagates before dissipating significantly from the medium. If the medium is compressible, then there are two kinds of waves, each of which has two such length scales.

There has been a recent interest to use the two-point microrheology technique

to measure the complex compressibility of biopolymers and cell components such as F-actin and microtubules [99]. This would seem at first glance an excellent benchmark application for the two-point microrheology technique. As stated above microrheology methods are specially suitable to test the often scarce and expensive biological samples. Moreover the linkage of Poisson ratio to specific microstructural characteristics of a great variety of materials has been studied extensively. For example it is well known that the Poisson ratio is intimately connected with the way structural elements are packed [38]. Measurements of the Poisson ratio might be appropriate for testing or fitting microscopic models of cell mechanics. This approach has already proven successful in the understanding and molecular-based design of other type of materials [38]. A rigorous theoretical study of the sensitivity of the passive two-point microrheology technique is still lacking however. Therefore the reliability of compressible data obtained using two-point microrheology has not been well established.

Data analysis for two-point microrheology usually makes two important approximations: (i) that the waves produced at the bead-boundary interface decay before producing reflections, (ii) and that the waves propagate through the medium instantaneously, in other words that the inertia of the medium is negligible. For a given material to satisfy those assumptions only data gathered with beads placed at a distance $2L$ at which the reflections produced by one bead will significantly decay before reaching the other bead should be used. Similarly, the methods are only applicable to data gathered at frequencies where the waves can be assumed to be propagating much faster than the relaxation times being measured. However finding the experimental conditions where all these assumptions are met might not be possible for a viscoelastic material, especially if a wide spectrum of relaxation times is to be measured.

The compressibility of the medium adds another factor to consider in the

analysis of the two-point microrheology data. [72] have previously pointed out there are two basic reasons to question the validity of the traditional microrheology data analysis (generalized Stokes-Einstein relation) in compressible viscoelastic solids. A probe particle moving at a given frequency will excite modes other than simple shear modes, and its response to external forces will, in general, depend on all of these modes in a way not simply described by the shear modulus. To model the effect of medium compressibility in the two-point microrheology experiment they considered a model viscoelastic medium consisting of a viscoelastic network that is viscously coupled to an incompressible, Newtonian fluid. They calculated an approximate mutual response function for their two-fluid medium and showed that in the limit that the bead-bead separation (L) is large compared to the radius of the beads (R), this response function measures the bulk rheological properties of the medium independently of the rheological properties of the regions immediately surrounding the two beads [73]. This conclusion was reached when the response functions were derived with lowest-order reflections only. The corrections due to higher-order reflections were estimated and shown to be small for a large bead-bead separation (L). Their analysis however was based on the steady Stokes equation and therefore the effects of medium inertia in the mutual response functions were not considered.

In Chapter 3 we presented a data analysis algorithm for the two-point microrheology technique that accounts for medium inertia and high-order hydrodynamic reflections and therefore expands the versatility of the technique. We have shown that the waves produced by two micron-sized beads trapped close together inside a viscoelastic fluid travel through the medium at a frequency-dependent speed. This is unlike purely viscous or elastic media. In a purely viscous medium the penetration length is identical to the wavelength, therefore there is only one relevant length scale. On the other hand in a purely elastic solid the waves travel back and forth between the beads without ever dissipating. Therefore the only relevant length scale is the

wavelength of this oscillatory wave. In a viscoelastic material the waves created at the bead-medium interfaces will display two different length scales, the penetration length and the wavelength. Moreover these two length scales will have a frequency dependence determined by the dynamic modulus of the material. In the two-point microrheology technique rheological properties are inferred from the particular characteristics of these waves. However it is usually assumed that the waves travel infinitely fast between the two beads and that they decay significantly before wave reflections can return to the beads. The first of these assumptions is usually valid at low frequencies, but can break down at high frequencies where the time scales being measured become comparable to the time it takes the waves to travel between the beads. The second of these assumptions is expected to be valid when the beads are separated by a distance at much larger than the penetration length of the wave. We have shown that if these assumptions are used outside this range then observable errors can be introduced in the inferred rheological properties. However due a cancellation of the errors produced by neglecting higher-order reflections and the errors produced by neglecting inertia these simplified techniques can sometimes work outside the expected domain. In this Chapter we extend our data analysis formalism to viscoelastic compressible solids. In contrast to incompressible materials, two types of waves can propagate through a compressible medium, namely shear waves and longitudinal waves. Characterizing the velocity at which these two types of waves travel and the distance they travel before significantly dissipating from the medium is important for the correct analysis of two-bead microrheology data of compressible materials. We address these issues here.

In Section 4.2 we derive generalized Stokes tensors with medium inertia and an infinite number of reflections for compressible viscoelastic solids. We make use of well-known analytic solutions for an isolated sphere in a compressible elastic medium [129, 90], the method of reflections [18, 3], and exploit the correspondence principle. Simple

dimensional arguments are then used to construct a phase diagram for the shear and longitudinal waves propagating through a viscoelastic solid, which can serve as a guide to indicate experimental conditions under which inertia and reflections may become important for compressible materials. In Section 4.3 a generalized Langevin equation is given for two hydrodynamically interacting beads embedded in a viscoelastic solid. The equation is solved in the frequency domain to obtain relations between the beads auto- and cross- correlations and the components of the generalized Stokes tensor derived in Section 4.2. In Section 4.4 we present a detailed analysis of the sensitivity of the two-point microrheology technique to changes in the complex compressibility of viscoelastic solids. We consider the sensitivity of two-bead cross-correlations to dynamic and static properties of the Poisson ratio. Finally in Section 4.5 we make use of generalized Brownian dynamics (GBD) [16] and a microscopic model which relates the Poisson ratio to the microstructure of the medium [20] to simulate the two-bead passive microrheology experiment in F-actin and microtubule composites. We use the simulated two-point cross-correlations to test the traditional data analysis formalism which neglects inertia and high order hydrodynamic interactions, and show the errors that can be generated in the inferred Poisson ratio. As comparison, we use the data analysis formalism which is obtained from the equations derived in Section 4.3 and show that a better estimation of the Poisson ratio, and therefore of microstructural characteristics of the actin-microtubules composites, can be obtained.

4.2 High-frequency generalized compressible Stokes tensors

We begin this section by deriving a generalized Stokes tensor for the two-point microrheology of compressible materials that accounts for inertial effects and an infinite number of reflected waves. To construct the Stokes tensors for compressible media we make use of two components: (i) the well known response function for a sphere in a compressible viscoelastic fluid [129, 90] and (ii) the method of reflections

for unsteady Stokes flows introduced by Ardekani and Rangel [3], and previously generalized by us to viscoelastic incompressible fluids [18]. Previous analyses of two-point microbead rheology are based on solutions obtained from the steady Stokes equation [48, 113, 73, 19], which neglects the effects of medium inertia and higher-order hydrodynamic reflections.

Zwanzig and Bixon [129] were the first to derive the unsteady response function for an isolated sphere in a compressible 1-mode viscoelastic medium. However as Metiu et al. [90] later pointed out their derivation contains a minor error which causes an additional erroneous term to appear in their expression for the response function. The correct unsteady response function for the isolated sphere was first derived by Metiu et al. [90].

Ardekani and Rangel [3] used the method of reflections [39], which is an approximate method for calculating the force exerted on two small spheres moving in Stokes flow to solve the unsteady problem. The particles are assumed to be sufficiently close to each other to interact hydrodynamically but sufficiently distant from boundary walls so that the surrounding medium is regarded as an infinite sea. Solutions for a single time-dependent point-force or for an isolated sphere are used in combination with the method of reflections. The velocity field that satisfies boundary conditions on two spheres is constructed by a linear superposition of an infinite number of velocity fields that satisfy boundary conditions on one sphere, each velocity field representing a reflection of the wave generated at the bead-medium interface.The problem is axisymmetric about the line of centers between the two beads, and can therefore be reduced to a two-dimensional problem. The method of reflections gives the solution as an infinite series. Calculating all the terms in this geometric series, one can analytically find the summation of all terms.

The correspondence principle allows one to replace the frequency-independent

shear modulus and Poisson ratio of simple elastic materials by the complex shear modulus and complex Poisson ratio of linear viscoelastic materials, after the equations have been transformed from the time domain to frequency space. This identification is possible because linear viscoelasticity presumes a convolution integral for the stress tensor, whose Fourier transform yields the Stokes relation with complex (frequency-dependent) modulus. Therefore in the frequency domain, the linearized Cauchy equations (steady or unsteady) for a compressible viscoelastic material are equivalent to the linearized Cauchy equations for a compressible purely elastic solid. Whenever the linear elastic deformation problem can be solved, the analogous solution of the linear viscoelastic deformation problem follows [126, 120, 69].

Consider two particles of radius R located a distance L apart and moving with velocities $\boldsymbol{v}_{b(1)}(t)$ and $\boldsymbol{v}_{b(2)}(t)$ in an unbounded viscoelastic solid. In the absence of the particles the medium is not deformed; the motion of the particles produces a velocity field in the medium $\boldsymbol{v}(\boldsymbol{r},t)$. The particles are at least a few diameters apart. We assume following References [48, 113, 73, 19] that L is independent of the motion of the beads, which implies that the displacements of the beads are small compared to L. The relation between the motion of the two beads and the force exerted by the viscoelastic solid on one of the particles is,

$$\boldsymbol{F}_{(1)}[\omega] = -\bar{\zeta}[\omega]\left(\frac{\boldsymbol{v}_{b(1)\perp}[\omega]-\boldsymbol{v}_{b(2)\perp}[\omega]A_{\perp}(\omega)}{1-A_{\perp}(\omega)^2}\boldsymbol{\delta}_{\perp}+\frac{\boldsymbol{v}_{b(1)\parallel}[\omega]-\boldsymbol{v}_{b(2)\parallel}[\omega]A_{\parallel}(\omega)}{1-A_{\parallel}(\omega)^2}\boldsymbol{\delta}_{\parallel}\right), \quad (4.1)$$

where,

$$\bar{\zeta}[\omega] := \frac{4\pi G^*(\omega)}{i\omega}R\left(ik_{\mathrm{t}}(\omega)R\right)^2\left\{\frac{\left[1-ik_l(\omega)R\right]A_{\mathrm{t}}-2\left[ik_{\mathrm{t}}(\omega)R-1\right]A_l}{2\left(ik_{\mathrm{t}}(\omega)R\right)^2A_l+\left(ik_l(\omega)R\right)^2A_{\mathrm{t}}}\right\}, \quad (4.2)$$

is the one-sided Fourier transform (*i.e.*, $\bar{\zeta}[\omega] \equiv \bar{\mathcal{F}}\{\zeta(t)\} := \int_0^\infty \zeta(t)e^{-i\omega t}dt$) of the frequency-dependent friction coefficient including the Basset force term and the mass of material dragged by a single bead embedded in a viscoelastic compressible medium. We indicate the Fourier transform by frequency argument with square brackets, and

one-sided transform by an over-bar. The first subindex indicates the bead number, and the symbols $\perp$ and $\parallel$ indicate the direction perpendicular and parallel to the line of centers of the two beads, respectively. A_{t} and A_l are defined by,

$$A_{\mathrm{t}} = 3 - 3ik_{\mathrm{t}}(\omega)R + (ik_{\mathrm{t}}(\omega)R)^2 \tag{4.3}$$

$$A_l = 3 - 3ik_l(\omega)R + (ik_l(\omega)R)^2 . \tag{4.4}$$

$k_{\mathrm{t}}(\omega)$ and $k_l(\omega)$ are frequency-dependent, complex wave-numbers for the shear and longitudinal waves respectively,

$$\begin{aligned} k_{\mathrm{t}}(\omega) = -\omega\sqrt{\frac{\rho}{G^*(\omega)}}, \qquad k_l(\omega) &= -\omega\sqrt{\frac{\rho\,(2\nu^*(\omega)-1)}{2G^*(\omega)\,(\nu^*(\omega)-1)}} \\ &= -\omega\sqrt{\frac{\rho}{K^*(\omega)+\frac{4}{3}G^*(\omega)}} \end{aligned} \tag{4.5}$$

The complex Poisson ratio, $\nu^*(\omega)$, is defined as

$$\nu^*(\omega) = \frac{3K^*(\omega) - 2G^*(\omega)}{6K^*(\omega) + 2G^*(\omega)} = \frac{\lambda^*(\omega)}{2(G^*(\omega) + \lambda^*(\omega))} \tag{4.6}$$

where $K^*(\omega)$ is the bulk modulus, $G^*(\omega)$ is the dynamic modulus, and $\lambda^*(\omega) = K^*(\omega) - \frac{2}{3}G^*(\omega)$ is the first Lamé coefficient. Note that the real part of the complex Poisson, $\nu'(\omega)$, ratio is always bounded between -1 and $1/2$ and its imaginary part, $\nu''(\omega)$, between 0 and $1/2$ [120]. These inherent bounds of the Poisson ratio make it specially convenient to characterize the compressibility of a material by significantly reducing the parameter space to be explored during data analysis.

To calculate the reflections we assume that particle 1 is located at a relatively large distance (several diameters) from particle 2. We then compute the translational effect of particle 1 by assuming that: (i) it generates the same force as that produced by a point force located at the center of the particle; (ii) the drag resulting from the field reflected at a given particle can be approximated by considering the field to be equivalent to a uniform velocity field with the same magnitude and direction as would

exist at the location of the particle center if it were not present [39]. As long as L/R is sufficiently large the assumptions should be safe. Then the functions $A_{\parallel}(Q,\omega)$ and $A_{\perp}(Q,\omega)$ are given by

$$\begin{aligned} A_{\parallel}(\omega) &= \frac{i\omega Q\bar{\zeta}[\omega]}{4\pi G^*(\omega)}\left\{\frac{2}{ik_{\mathrm{t}}(\omega)L}e^{ik_{\mathrm{t}}(\omega)L}-\frac{2}{(ik_{\mathrm{t}}(\omega)L)^2}\left[e^{ik_{\mathrm{t}}(\omega)L}-1\right]\right\} \\ &\quad+\frac{i\omega Q\bar{\zeta}[\omega]}{4\pi G^*(\omega)}\left(\frac{1-2\nu^*(\omega)}{2-2\nu^*(\omega)}\right) \\ &\quad\times\left\{e^{ik_l(\omega)L}-\frac{2}{ik_l(\omega)L}e^{ik_l(\omega)L}+\frac{2}{(ik_l(\omega)L)^2}\left[e^{ik_l(\omega)L}-1\right]\right\}, \end{aligned} \tag{4.7}$$

$$A_{\perp}(\omega)=-\frac{A_{\parallel}(\omega)}{2}+\frac{i\omega Q\bar{\zeta}[\omega]}{4\pi G^*(\omega)}\left\{e^{ik_{\mathrm{t}}(\omega)L}+\left(\frac{1-2\nu^*(\omega)}{2-2\nu^*(\omega)}\right)\frac{e^{ik_l(\omega)L}}{2}\right\}, \tag{4.8}$$

where $Q=R/L$ is the bead radius to bead separation ratio. The detailed derivation of eqs.(4.7) and (4.8) is given in Appendix A.

It is important to note that in viscoelastic media, unlike purely viscous or purely elastic media, the waves produced at the bead-medium interface have frequency-dependent, complex wave-numbers $k_{\mathrm{t}}(\omega)$ and $k_l(\omega)$, for the waves propagating in the transverse and longitudinal directions, respectively. We previously considered incompressible fluids where only shear waves are produced [18]; a detailed characterization and dimensional analysis for the shear waves propagating through a viscoelastic medium has already been presented in Chapter 3. Although the characterization and dimensional analysis is analogous in this work we restate it for the longitudinal waves propagating through a compressible viscoelastic solid. The wavelength of the longitudinal wave penetrating into the viscoelastic solid from the bead surface is defined as,

$$\Lambda_l(\omega):=1/|k_l'(\omega)| \tag{4.9}$$

where $k_l'(\omega)$ is the real part of the frequency-dependent wave number. We may also define the penetration depth of the wave as,

$$\Delta_l(\omega):=1/k_l''(\omega) \tag{4.10}$$

where $k_l''(\omega)$ is the imaginary part of the frequency-dependent complex wave number. From eqs.(4.9-4.10) we can see that,

$$-ik_l(\omega)L = \frac{L}{\Delta_l(\omega)} + \frac{iL}{\Lambda_l(\omega)}. \tag{4.11}$$

The first term on the right hand side of eq.(4.11), which involves the penetration length, determines how fast the wave decays. The second term, which involves the wavelength, characterizes the oscillatory part of the memory function tensor. If the distance L between the two beads is much larger than half the penetration depth, $\Delta_l(\omega)/2$, then the reflected waves decay significantly before reaching the other bead and therefore the effect of reflections is small. However if the distance between the beads is comparable to the penetration depth the reflected waves from bead 2 will have an important effect in the motion of bead 1 and vice-versa.

Based on eq.(4.11) we propose two simple dimensional arguments that can serve as guides to determine whether or not medium inertia and high order hydrodynamic reflections should be taken into account when determining the compressibility of a viscoelastic solid with the two-point microrheology technique. The Brownian motion of two micron-sized near each other in a viscoelastic medium produce waves at the bead-medium interfaces. These waves will travel a distance equal to their penetration length before dissipating significantly. If the distance between the two beads is comparable to, or smaller than, the penetration length, then bead 1 will feel the presence of bead 2, and vice versa. This effect is called "hydrodynamic interaction", and its observable manifestation is the appearance of cross-correlations in the statistics of the beads' displacements. Additionally, when the wave produced by bead 1 reaches bead 2 it gets reflected, bouncing back towards bead 1. This reflection is the so-called "first-order reflection" of the hydrodynamic waves. If the distance between the beads is sufficiently small, then these first-order reflections will return to bead 1 before dissipating; the same holds for bead 2. Therefore in such a situation

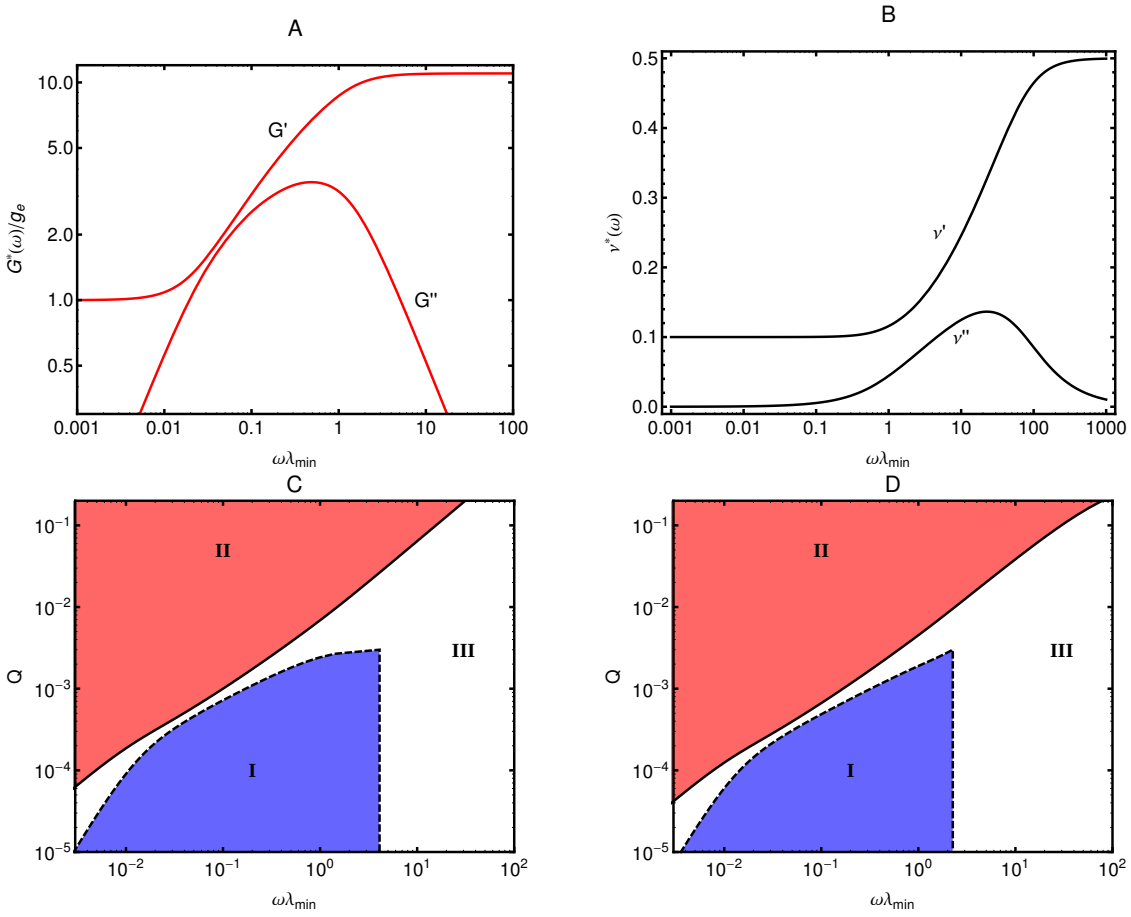

Figure 4.1. A: Dynamic modulus, eq.(4.25) normalized by the equilibrium modulus g_e, and B: complex Poisson ratio, eq.(4.26), of the viscoelastic solid for which the dimensional-analysis phase diagrams in parts C and D were constructed. C: Phase diagram for the shear waves propagating through the medium. D: Phase diagram for the longitudinal waves propagating through the medium. In both phase diagrams the continuous line represents $\frac{\omega L}{c_l(\omega)} = 1$, and the dashed line is $\frac{2L}{\Delta_l(\omega)} = 1$. In region I where $\frac{2L}{\Delta_l(\omega)} \gg 1$ higher order reflections should be negligible. In region II where $\frac{\omega L}{c_l(\omega)} \ll 1$ it is safe to neglect medium inertia. In region III both inertia and high order hydrodynamic reflections may have a measurable effect in the dynamics of the shear and longitudinal waves propagating through the viscoelastic medium. Frequency is made dimensionless by the shortest relaxation time of the material, $\lambda_{\min}$.

the beads feel the first-order reflections. These in turn, have an observable effect on the cross-correlations of the beads' displacements. Moreover if the beads are brought closer together, then higher-order reflections are felt by the beads before dissipating.

Figure 4.1 shows a dimensional-analysis phase diagram for the waves propagating through a 4-mode Maxwell viscoelastic solid during a two-bead microrheology experiment. For the wave that forms in the bead-medium interface to decay before producing multiple reflections it is required that $\frac{2L}{\Delta_l(\omega)} \gg 1$. The dashed line in parts C and D represent $\frac{2L}{\Delta_l(\omega)} = 1$, which means that, in region I, below this line higher-order reflections are not relevant for the analysis of the waves propagating through the compressible viscoelastic medium.

We turn now to the effects of medium inertia. Inertia causes a vortex-like flow surrounding a localized disturbance at short times which leads to enhanced correlations in the thermal velocity fluctuations in liquids. A well-studied consequence of these correlations is the slow, decay of velocity correlations, known as the long-time tail [129, 90]. In viscoelastic media the velocity autocorrelation functions, specifically their oscillatory character, becomes much more pronounced with increasing elastic component of the shear modulus [77]. At a more microscopic level the main effect of medium inertia is that it can significantly affect the velocity at which the waves generated at the bead-medium interface propagate through the medium. In traditional microrheology analysis one assumes that hydrodynamic waves propagate instantaneously between the beads. However, for sufficiently large bead separation, or sufficiently high frequencies, the lag time for wave propagation can be important. Therefore to analyze these effects it is useful to define the propagation speed of the longitudinal wave (speed of sound) produced at the bead-medium interface as,

$$c_l(\omega) = \omega \Lambda_l(\omega). \tag{4.12}$$

Where $\Lambda_l(\omega)$ is the wavelength of the wave, that was defined in eq.(4.9). Therefore the time it takes for the wave to travel from one bead to the other is $\frac{L}{c_l(\omega)}$. At time scales much longer than this the propagation of longitudinal stress through the medium can be assumed to be instantaneous and therefore inertia can be safely neglected from

the analysis of the longitudinal waves. Therefore for medium inertia is negligible if $\frac{\omega L}{c_l(\omega)} \ll 1$. At high frequencies inertia becomes important because the time the wave takes to travel between the beads becomes comparable to the relaxation or delay time of the fluid being measured at a frequency ω. Opposite to what is required to reduce the effect of reflections, to reduce the effect of inertia a large separation between the beads is required. This is because the shorter the distance between the beads, the shorter the time it takes for the waves to propagate between them and therefore the assumption that the propagation occurs instantaneously is more easily approached. The solid lines in the phase diagrams shown in Figure 4.1 represents $\frac{\omega L}{c_l(\omega)} = 1$. In region II, above this line, the waves can be assumed to be traveling infinitely fast. In region III the magnitude of the effect of both inertia and reflections on the motion of the waves propagating through the viscoelastic medium becomes important.

Note that the phase diagrams shown in Figure 4.1 differ from the phase diagrams we have presented before [18] for viscoelastic fluids in that there is no region where medium inertia and high order reflections become negligible at the same time. This region appears for viscoelastic fluids at low frequencies and small bead-radius-to-bead-separation ratio. This is because for viscoelastic fluids, the equilibrium modulus g_e is zero ($g_e = 0$) and therefore each component of the dynamic modulus is $G' \sim \omega^2, G'' \sim \omega$ at the low-frequency terminal zone, so that $\Delta(\omega) \simeq \Lambda(\omega) \sim \omega^{1/2}$. On the other hand, for viscoelastic solids, the equilibrium modulus is finite ($g_e > 0$) and therefore $G' \sim \omega^0$ so $\Delta(\omega)$ is much larger than $\Lambda(\omega)$ at low frequencies.

The preceding analysis, which was carried out for a compressible viscoelastic solid, with a complex-valued, frequency dependent Poisson ratio, is an alternative to results previously presented by Levine and Lubensky [72] for two-fluid models. In two-fluid models at high frequencies the compressible network is dissipatively coupled to the incompressible fluid (solvent). Therefore, the longitudinal mode of the network

plays no role in the high-frequency bead dynamics. Moreover at large enough frequencies the fluid will carry the larger part of the stress in the material, while below some crossover frequency the network shear modulus is the dominant contributor to the mechanical properties of the two-fluid material. A simple calculation shows that this crossover frequency is on the order of 10^8 Hz [72], which is well above experimentally accessible frequencies, so that the network shear modulus is typically the principal contributor to the two-fluid shear modulus.

4.3 Two-point high-frequency compressible generalized Langevin Equation

In this section we write the equations of motion for the two probe beads of radius R and separated by a distance L embedded in a viscoelastic solid. The dynamics of micron-sized beads embedded in a viscoelastic solid are known to be described by a generalized Langevin Equation (GLE) [50, 45, 13],

$$\frac{d\boldsymbol{p}_{\mathrm{b}}(t)}{dt} = -\boldsymbol{H}_{\mathrm{e}} \cdot \delta\boldsymbol{r}_{\mathrm{b}}(t) - \int_{-\infty}^{t} \boldsymbol{\zeta}(t-t') \cdot \frac{\boldsymbol{p}_{\mathrm{b}}(t')}{m} dt' + \boldsymbol{f}_{\mathrm{B}}(t). \tag{4.13}$$

Where,

$$\delta\boldsymbol{r}_{\mathrm{b}} = \begin{pmatrix} \delta r_{\mathrm{b}(1)\perp} \\ \\ \delta r_{\mathrm{b}(1)\parallel} \\ \\ \delta r_{\mathrm{b}(2)\perp} \\ \\ \delta r_{\mathrm{b}(2)\parallel} \end{pmatrix} \tag{4.14}$$

is the bead displacement vector and $\boldsymbol{p}_{\mathrm{b}} = m\frac{d\delta\boldsymbol{r}_{\mathrm{b}}(t)}{dt}$ are the beads' momenta, with m the bead mass. The Brownian forces satisfy the fluctuation-dissipation theorem (FDT),

$$\langle \boldsymbol{f}_{\mathrm{B}}(t)\boldsymbol{f}_{\mathrm{B}}(t')\rangle_{\mathrm{eq}} = k_{\mathrm{B}}T\boldsymbol{\zeta}(t-t'). \tag{4.15}$$

If the fluctuations of the beads' positions are small compared to L the solutions to the linearized Cauchy's equation such as eq.(4.1) can be used to write a GLE with a bead-position-independent memory kernel. We can use eqs.(4.1) and (4.2) to write the components of the memory function tensor, $\boldsymbol{\zeta}(t) = \bar{\mathcal{F}}^{-1}\left\{\bar{\boldsymbol{\zeta}}[\omega]\right\}$ (where $\bar{\mathcal{F}}^{-1}\{\bar{f}[\omega]\}$ is the inverse one-sided Fourier transform),

$$\bar{\boldsymbol{\zeta}}[\omega] = \bar{\zeta}[\omega]\begin{pmatrix} \frac{1}{1-A_\perp(\omega)^2} & 0 & -\frac{A_\perp(\omega)}{1-A_\perp(\omega)^2} & 0 \\ 0 & \frac{1}{1-A_\parallel(\omega)^2} & 0 & -\frac{A_\parallel(\omega)}{1+A_\parallel(\omega)^2} \\ -\frac{A_\perp(\omega)}{1-A_\perp(\omega)^2} & 0 & \frac{1}{1-A_\perp(\omega)^2} & 0 \\ 0 & -\frac{A_\parallel(\omega)}{1-A_\parallel(\omega)^2} & 0 & \frac{1}{1+A_\parallel(\omega)^2} \end{pmatrix} - \frac{\boldsymbol{H}_\mathrm{e}}{i\omega} \quad (4.16)$$

Note that, although the two beads are correlated, the $\perp$ and $\parallel$ directions are decoupled. The expression for $A_\perp(\omega)$ and $A_\parallel(\omega)$, which include all reflections, medium inertia and compressibility where given in eqs.(4.8) and (4.7) respectively.

$\boldsymbol{H}_\mathrm{e}$ is the so-called frequency matrix involving only purely elastic elements. We have shown before that for viscoelastic solids there exists a frequency matrix $\boldsymbol{H}_\mathrm{e}$ outside of the memory function [50]. For a compressible viscoelastic solid the frequency matrix is given by,

$$\boldsymbol{H}_\mathrm{e} = H_\mathrm{e}\begin{pmatrix} \frac{1}{1-A_{\mathrm{e},\perp}^2} & 0 & -\frac{A_{\mathrm{e},\perp}}{1-A_{\mathrm{e},\perp}^2} & 0 \\ 0 & \frac{1}{1-A_{\mathrm{e},\parallel}^2} & 0 & -\frac{A_{\mathrm{e},\parallel}}{1+A_{\mathrm{e},\parallel}^2} \\ -\frac{A_{\mathrm{e},\perp}}{1-A_{\mathrm{e},\perp}^2} & 0 & \frac{1}{1-A_{\mathrm{e},\perp}^2} & 0 \\ 0 & -\frac{A_{\mathrm{e},\parallel}}{1-A_{\mathrm{e},\parallel}^2} & 0 & \frac{1}{1+A_{\mathrm{e},\parallel}^2} \end{pmatrix} \quad (4.17)$$

where

$$H_\mathrm{e} = \frac{24\pi R g_\mathrm{e}(\nu_\mathrm{e} - 1)}{6\nu_\mathrm{e} - 5} \quad (4.18)$$

and

$$A_{\mathrm{e},\parallel} = \frac{6Q(\nu_\mathrm{e}-1)}{6\nu_\mathrm{e}-5}, \qquad A_{\mathrm{e},\perp} = \frac{3Q(4\nu_\mathrm{e}-3)}{2(6\nu_\mathrm{e}-5)}. \tag{4.19}$$

Where $g_\mathrm{e} = G^*(\omega=0)$ and $\nu_\mathrm{e} = \nu^*(\omega=0)$. Eqs.(4.17)-(4.19) are obtained by solving the steady linearized Cauchy equation for two beads embedded in an infinite purely elastic medium and keeping only first-oder terms in Q.

For a homogeneous isotropic medium the mean-squared displacement tensor will be symmetric with four distinct components [18]. The diagonal component involving only autocorrelations of the first particle in the direction perpendicular to the line of centers is given by,

$$\langle \Delta\delta r^2_{\mathrm{b}}(t)\rangle_\perp \;:=\; 2\left(\langle \delta r_{\mathrm{b}(1)\perp}(0)^2\rangle - \langle \delta r_{\mathrm{b}(1)\perp}(t)\delta r_{\mathrm{b}(1))\perp}(0)\rangle\right), \tag{4.20}$$

with a similar definition for the mean-squared displacement (MSD) in the direction parallel to the line of centers. Similar definitions also hold for the second probe particle. The off-diagonal components of the mean-squared displacement tensor involve only cross-correlations, one of them in the direction perpendicular to the line of centers,

$$\langle \Delta\delta r^2_{\mathrm{b}(1,2)}(t)\rangle_\perp \;:=\; -2\langle \delta r_{\mathrm{b}(1)\perp}(t)\delta r_{\mathrm{b}(2))\perp}(0)\rangle \tag{4.21}$$

and an equivalent cross-mean-squared displacement (CMSD) in the direction perpendicular to the line of centers.

The following relationship between the one-sided Fourier transform of the mean-squared displacement in the direction perpendicular to the line of centers and the memory function tensor can be found by using the the FDT, eq.(4.15), and the solution of the GLE, eq.(4.13), in the frequency domain,

$$\langle \overline{\Delta\delta r^2_{\mathrm{b}}}[\omega]\rangle_\perp = \frac{2k_\mathrm{B}T\left(H_{\mathrm{e},1,1} - i\omega\left(mi\omega + \bar{\zeta}_{1,1}[\omega]\right)\right)}{i\omega\left[\left(H_{\mathrm{e},1,1} + i\omega\left(mi\omega + \bar{\zeta}_{1,1}[\omega]\right)\right)^2 - \left(H_{\mathrm{e},1,3} + i\omega\bar{\zeta}_{1,3}[\omega]\right)^2\right]}. \tag{4.22}$$

An equivalent relation can be written for the direction parallel to the line of centers with the replacements $\bar{\zeta}_{1,1}[\omega] \rightarrow \bar{\zeta}_{2,2}[\omega]$, $H_{\mathrm{e},1,1} \rightarrow H_{\mathrm{e},2,2}$ and $H_{\mathrm{e},1,3} \rightarrow H_{\mathrm{e},2,4}$. The following relation between the CMSD and the components of the memory tensor, can also be obtained from the solution of the GLE and the FDT in the frequency domain,

$$\langle\overline{\Delta\delta r^2_{\mathrm{b}(1,2)}}[\omega]\rangle_{\perp} = \frac{2k_{\mathrm{B}}T\left(H_{\mathrm{e},1,3} - i\omega\bar{\zeta}_{1,3}[\omega]\right)}{i\omega\left[\left(H_{\mathrm{e},1,1} + i\omega\left(mi\omega + \bar{\zeta}_{1,1}[\omega]\right)\right)^2 - \left(H_{\mathrm{e},1,3} + i\omega\bar{\zeta}_{1,3}[\omega]\right)^2\right]}. \quad (4.23)$$

Here again an equivalent equation can be written for the direction parallel to the line of centers with the replacements $\bar{\zeta}_{1,1}[\omega] \rightarrow \bar{\zeta}_{2,2}[\omega]$, $H_{\mathrm{e},1,1} \rightarrow H_{\mathrm{e},2,2}$ and $H_{\mathrm{e},1,3} \rightarrow H_{\mathrm{e},2,4}$.

Eqs.(4.22) and (4.23) and their equivalent equations in the direction parallel to the line of centers, used together with eq.(4.16) and definitions for the functions $A_{\perp}(\omega)$ and $A_{\parallel}(\omega)$, eqs. (4.8) and (4.7) relate observable two-bead statistics to linear viscoelastic properties (including compressibility) of the solid. These relations include bead and medium inertia as well as an infinite number of reflections.

If higher-order hydrodynamic reflections and medium and bead inertia are neglected the following simple relation between the Poisson ratio and the two-bead cross-correlations can be derived by taking the limits $m \rightarrow 0, \rho \rightarrow 0$ and only the first-order terms of a Taylor series expansion in Q of eqs. (4.22) and (4.23),

$$\nu^*(\omega) = 1 + \frac{\langle\overline{\Delta\delta r^2_{\mathrm{b}(1,2)}}[\omega]\rangle_{\parallel}}{4\left(\langle\overline{\Delta\delta r^2_{\mathrm{b}(1,2)}}[\omega]\rangle_{\perp} - \langle\overline{\Delta\delta r^2_{\mathrm{b}(1,2)}}[\omega]\rangle_{\parallel}\right)}. \quad (4.24)$$

Eq.(4.24) was originally presented by Levine and Lubensky [73] and has been used by Gardel et al. [30] and Pelletier et al. [99] to calculate the complex Poisson ratio of F-actin and actin composites. In Sections 4.4 and 4.5 we test the relations derived in this section for inferring the high-frequency compressibility of viscoelastic solids from two-bead cross-correlations. Additionally we illustrate the magnitude of the errors that can be introduced in the measured compressibility if eq.(4.24) is used to analyze two-bead cross-correlations obtained under experimental conditions where

medium inertia or higher-order reflections are expected to be important. We also evaluate, using our generalized Brownian dynamics (GBD) simulations [18] the possibility of using the two-point microrheology technique to elucidate the microstructural origins of enhanced compressibility in biopolymer composites [99].

4.4 Sensitivity of the two-point microrheology technique to medium compressibility

In this section we evaluate the sensitivity of the cross-correlations of bead positions to changes in the Poisson ratio of the medium. We consider both statics and dynamics of a time-dependent Poisson ratio. For the sample calculations that follow we consider a discrete relaxation spectrum, which gives the following form for the dynamic modulus of the medium

$$G^*(\omega) = g_e + \sum_{j=1}^{N} \frac{g_j \lambda_j i\omega}{1 + \lambda_j i\omega}. \tag{4.25}$$

To illustrate the effect of reflections and finite bead size on the solutions derived above, we consider the 4-mode relaxation spectrum, $\boldsymbol{H}^* = \{4, 3, 2, 1\}$ and $\boldsymbol{\lambda}^* = \{1, 3, 9, 27\}$ where $H_j := 6\pi R g_j$ and the asterisk indicates that they have been made dimensionless by using $\sqrt{k_B T / H_e}$ as the characteristic length scale, where $H_e = 6\pi R g_e$ is the incompressible H_e. The smallest relaxation time, $\lambda_1 = \min\{\lambda_j\}$ is used to make time dimensionless. For the following illustrations the density of the bead and the density of the medium are assumed to be the same, the dimensionless bead mass is set to $m^* = m/(\lambda_1^2 H_e) = 0.0001$. Therefore $\sqrt{m^*} = 0.01$ is the ratio between the smallest inertial time scale of the system and the shortest relaxation time of this material.

The complex Poisson ratio of a viscoelastic solid can also be spectrally decomposed as,

$$\nu^*(\omega) = \nu_e + \sum_{j=1}^{2N} \frac{\nu_j \theta_j i\omega}{1 + \theta_j i\omega} \tag{4.26}$$

where,

$$\nu_{\mathrm{e}} - \nu_{\mathrm{g}} = \sum_{j=1}^{2N} \nu_j \tag{4.27}$$

here $\nu_{\mathrm{e}} = \nu^*(\omega = 0)$ and $\nu_{\mathrm{g}} = \nu^*(\omega = \infty)$ are the equilibrium and glassy (or instantaneous) Poisson's ratios, respectively, and the θ_j are the delay times, while the ν_j are the associated lateral contraction ratios, *i.e.*, the strengths of the spectral lines that compose the discrete distribution of delay times [120].

The real part of the one-sided Fourier transform of the two-bead cross-correlations calculated using eq.(4.23) and its equivalent equation in the direction parallel to the line of centers of the beads is shown in Figure 4.2A. The Poisson ratios used to calculate these two-point cross-correlations are shown in Figure 4.2B, the black line corresponds to the incompressible solid, while the red lines correspond to the compressible solid. The upper line is the real part and the lower line is the imaginary part of the complex Poisson ratio. This particular compressible solid has a high compressibility at low frequencies ($\nu_{\mathrm{e}} = 0.1$) and becomes incompressible at higher frequencies ($\nu_{\mathrm{g}} = 0.5$).

Notice that the cross-correlations in the direction parallel to the line of centers are practically identical for the incompressible and compressible viscoelastic solid. The inset shows the only frequency region where a small difference can be observed. In data with noise, which will be the case in any situation of practical interest, this difference might be too small to be detected. When inertia and high order reflections are neglected from the calculations it can be shown analytically that the cross-correlations in the direction parallel to the line of centers are independent of the Poisson ratio [72]. Therefore the small difference that can be observed in the inset of Figure 4.2A between the cross-correlations in the direction parallel to the line of centers are entirely due to differences in the speed at which the hydrodynamic shear and longitudinal waves travel through the medium from one bead to the other. Since

the compressibility of the medium does not have an observable effect on the two-bead cross-correlations in the direction parallel to the line of centers this data can be used to extract the dynamic modulus of the material using the time-domain methods that we have previously described [16] for incompressible materials.

On the other hand in the direction perpendicular to the line of centers the cross-correlation for the beads embedded in the compressible solid are shifted upwards from the incompressible case. At high frequencies as the Poisson ratio of the compressible media approaches 0.5 the difference between the cross-correlations in the perpendicular direction decreases until it eventually vanishes completely as can be observed in Figure 4.2A. We show in Section 4.5 using GBD simulations that the vertical shift in the perpendicular direction to the line of centers caused by compressibility can be accurately detected in systems where microrheology is usually applied.

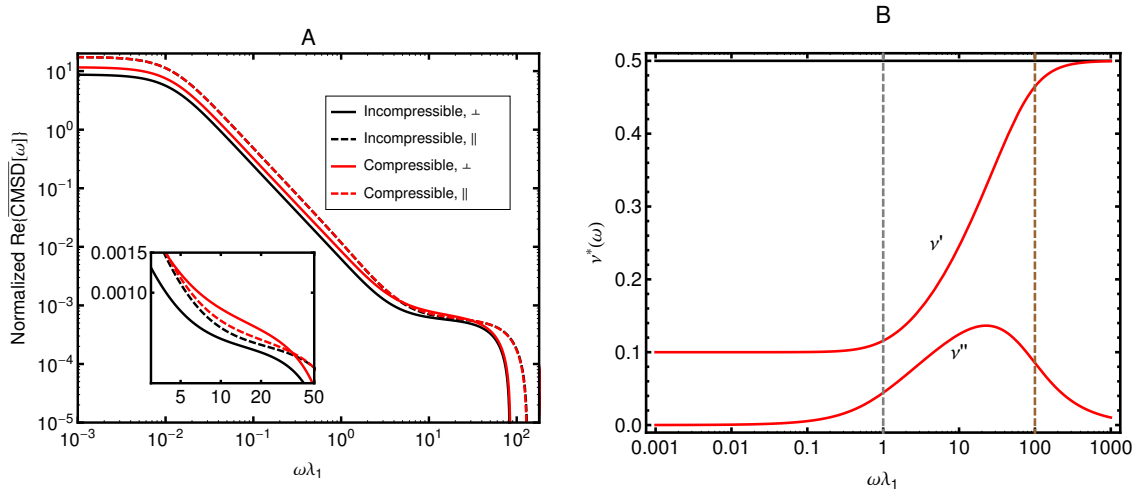

Figure 4.2. A: Real part of the one-sided Fourier transform of the two-bead cross-correlations (CMSD) for a 4-mode Maxwell solid as a function of frequency, eq.(4.23), normalized by $2k_BT/H_e$. The ratio of bead radius to bead separation, Q, was set to 0.2 for this figure. The black lines correspond to the cross-correlations for an incompressible viscoelastic solid while the red lines correspond to a compressible viscoelastic solid with Poisson ratio, eq. (4.26) , shown in part B (red line). Inset in part A: Zoom of the frequency range where the larger difference between the compressible and incompressible cross-correlations is observed.

Having established that changes in the compressibility of a viscoelastic solid may be detected in the direction perpendicular to the line of centers, we now consider sensitivity to changes in the dynamics of the Poisson ratio. Figure 4.3 shows the cross-correlations in the direction perpendicular to the line of centers for two beads embedded in compressible viscoelastic solids with the same glassy (ν_{g}) and equilibrium (ν_{e}) Poisson ratios, but with different distributions of delay times (θ_j). The differences in the dynamics of the Poisson ratio for the three different model solids are significant. The maximum in $\nu''(\omega)$ are about an order of magnitude of frequency apart. However the differences that can be observed in the two-point cross-correlations are very small. For most of the frequency range plotted in Figure 4.3A no differences can be detected between the cross-correlations corresponding to the three different solids. The only region where some effect of the dynamics of the Poisson ratio can be observed is shown in the inset of Figure 4.3A. The effect is too small to be detected in data with noise; moreover it occurs in a very narrow frequency range.

From the two-point cross-correlations in the direction perpendicular to the line of centers the equilibrium and instantaneous Poisson ratios can in principle be accurately determined, however it does not seem feasible to measure accurately the complete dynamics of the Poisson ratio using the two-point microrheology technique. In Section 4.5 we consider a specific application of the two point-microrheology technique; we do not however attempt to extract the dynamics of the Poisson ratio but rather evaluate, using GBD simulations and time-domain data analysis, how accurately a constant Poisson ratio can be extracted from the cross-correlations.

4.5 Application: Actin-Microtubule composite networks

Recently Pelletier et al. [99] used two-point passive microrheology to measure the Poisson ratio of F-actin and actin-microtubule composite networks. They found, in agreement with Gardel et al. [30], that pure F-actin is incompressible with $\nu = 1/2$.

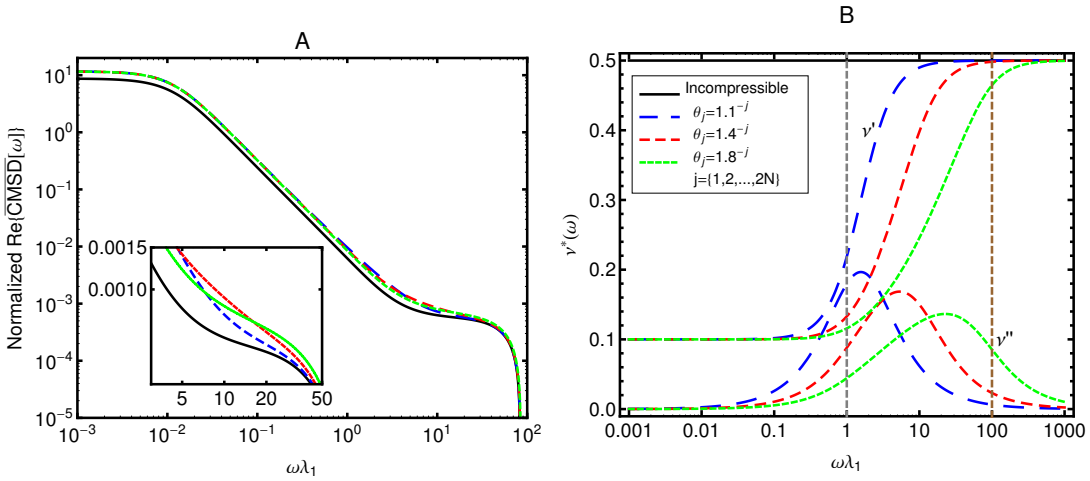

Figure 4.3. A: Real part of the one-sided Fourier transform of the two-bead cross-correlations (CMSD) in the direction perpendicular to the line of centers of the beads for a 4-mode Maxwell solid as a function of frequency, eq.(4.23), normalized by $2k_BT/H_e$. The bead radius to bead separation ratio, Q, was set to 0.2 in this calculations. Inset: Zoom of the frequency range where the larger difference between the compressible and incompressible cross-correlations is observed. B: The complex Poisson ratios, eq.(4.26), corresponding to the cross-correlations shown in part A. The black lines correspond to an incompressible solid and are given as reference. The dashed lines indicate the location of the shortest relaxation time (λ_1) and the characteristic inertial time ($\sqrt{M^*}$) for this systems.

By contrast, in the composite network, ν was found to be unambiguously less than 1/2 at longer times, and is closer to 0.3.

The different filament types influence each other through their viscoelastic responses. Actin filaments are a prototypical example of semiflexible polymers, and entangled, uncrosslinked actin filaments have been shown to follow the worm-like-chain model [30]. Microtubules are the stiffest element in cells. Their fluctuations, although much smaller than those of actin filaments, are important for deployment of polymerization forces and for the search and capture mechanism used to position the mitotic spindle. Microtubules have a persistence length of a few mm, and in solution might be expected to behave as rigid rods. Macroscopic linear rheology of microtubule solutions has shown an elastic plateau modulus of $\sim$ 1 Pa, with a weak

frequency dependence and no terminal relaxation over a frequency range extending as low as $\omega = 6.3 \times 10^{-3}$ rad/s [99].

In an attempt to interpret the experimental results reported by Pelletier et al. [99], Das and MacKintosh [20] developed a model for the mechanical response of a composite material consisting of rods in an elastic matrix using a mean-field approach and a dipole approximation for the rod-like inclusions. The elastic matrix under consideration is treated as an effective medium that is made of the bare elastic medium (*e.g.*, the F-Actin matrix) and a collection of rods (microtubules) embedded in it. Their approach is similar to what has been used to model aligned fiber-reinforced composites [21]. Consistent with the experiments of Pelletier et al. [99], they found that the addition of rigid rods can lead to enhanced compressibility of a nearly incompressible medium. Specifically, they found that for matrices characterized by Poisson's ratio $1/4 < \nu < 1/2$, the addition of rods reduces ν, while for $\nu < 1/4$, stiff rods increase ν. In this way, $\nu = 1/4$ can be thought of as a stable fixed point of such a composite.

We first summarize the main elements of the model proposed by Das and MacKintosh[20]. We then incorporate this model into our GBD simulations of two-bead microrheology with the purpose of evaluating the sensitivity of the two-bead microrheology technique to the changes in the compressibility of the actin network upon addition of microtubules. For an isotropic and homogeneous elastic compressible material with shear modulus G and Poisson ratio ν, the displacement field $\boldsymbol{u}$ at a position $\boldsymbol{r}$ in the medium due to a force $\boldsymbol{F}$ acting at a point $\boldsymbol{r}'$, is equal to $\boldsymbol{u}(\boldsymbol{r}) = \boldsymbol{\alpha}(\boldsymbol{r} - \boldsymbol{r}') \cdot \boldsymbol{F}(\boldsymbol{r}')$ where,

$$\boldsymbol{\alpha}(\boldsymbol{r}) = \frac{1}{8\pi G|\boldsymbol{r}|}\left[\boldsymbol{\delta}_{\boldsymbol{r}}\boldsymbol{\delta}_{\boldsymbol{r}}\left(1 - \frac{2\nu - 1}{2(\nu - 1)}\right) + \boldsymbol{\delta}\left(1 + \frac{2\nu - 1}{2(\nu - 1)}\right)\right], \tag{4.28}$$

where $\boldsymbol{\delta}_{\boldsymbol{r}}$ is the unit vector in the direction of $\boldsymbol{r}$, and $\boldsymbol{\delta}$ is the unit tensor. The change in the response function and Lamé coefficients upon addition of rods is calculated

as follows. Consider a single rod of length a embedded in the elastic medium. The presence of the rod represents a constraint on the displacement field induced by the applied force. For a force applied at the origin of the coordinate system, the net displacement of the ends of the rod with end-to-end vector a is given by,

$$\Delta \boldsymbol{u}(\boldsymbol{r}) = \boldsymbol{u}\left(\boldsymbol{r} + \boldsymbol{a}/2\right) - \boldsymbol{u}\left(\boldsymbol{r} - \boldsymbol{a}/2\right). \tag{4.29}$$

The constraint of an incompressible rod is approximated by a dipole at its center of mass. This induced (tensile) dipole is oriented along the rod and its strength is chosen so as to enforce a constant end-to-end distance of the rod: $G\pi a(\boldsymbol{a} \cdot \delta \boldsymbol{u})$. By keeping terms only leading order in $\boldsymbol{a}$, which is assumed to be smaller than all other length scales in the system, the resulting displacement field allows calculation of the change in the linear response functions. In the effective medium approach the change in response arises from a cloud of induced dipoles in the elastic continuum.

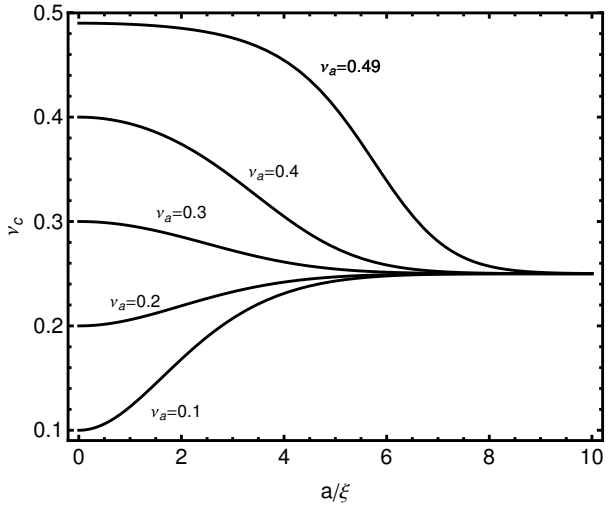

Figure 4.4. Real part of the Poisson ratio of a composite network (soft matrix with rigid rods) as a function of the ratio between the length of the rigid rods and the mesh size of the rod network. Each line corresponds to a different value of the Poisson ratio of the pure soft matrix.

The changes in the parallel and perpendicular response functions with the

addition of rods are:

$$\delta\alpha_{\parallel} = -\frac{\pi}{30} n a^3 \alpha_{\parallel} \tag{4.30}$$

and

$$\delta\alpha_{\perp} = \left[\frac{7 + 4\nu\,(4\nu - 5)}{8\,(\nu - 1)^2}\right] \alpha_{\perp}, \tag{4.31}$$

where n is the rod number density and an average has been taken over rod orientation. Therefore for a small increment dn in added rods, the following differential equation can be written for the change in the Poisson ratio, ν, upon addition of the rigid rods in the compressible elastic matrix

$$\frac{d\nu}{dn} = \frac{1}{60} a^3 \pi \left(1 - 6\nu + 8\nu^2\right). \tag{4.32}$$

By solving eq.(4.32) with initial condition $\nu(n = 0) = \nu_{\mathrm{a}}$, where ν_{a} is the Poisson ratio of the soft matrix (actin), we obtain an expression for the Poisson ration of the composite network (actin-microtubule)

$$\nu_{\mathrm{c}} = \frac{1 - e^{\frac{1}{30}\left(\frac{a}{\xi}\right)^2 \pi} - 4\nu_{\mathrm{a}} + 2\nu_{\mathrm{a}} e^{\frac{1}{30}\left(\frac{a}{\xi}\right)^2 \pi}}{2 - 4\nu_{\mathrm{a}} e^{\frac{1}{30}\left(\frac{a}{\xi}\right)^2 \pi} - 8\nu_{\mathrm{a}} + 8\nu_{\mathrm{a}} e^{\frac{1}{30}\left(\frac{a}{\xi}\right)^2 \pi}} \tag{4.33}$$

where, ξ is the mesh size of the microtubule network. The mesh size ξ is related to the rod density n by $1/\xi^2 = na$. The Poisson ratio of the composite network as a function of the ratio a/ξ is shown in Figure 4.4, for various values of the pure F-actin Poisson ratio. For soft matrices with Poisson ratio close to 0.5 the addition of the rigid rods (increasing a/ξ) causes an increase in the compressibility (or decrease in the Poisson ratio) of the composite network. On the other hand for highly compressible elastic matrices the addition of rigid rods causes an increase in the Poisson ratio on the composite network. In general, the model predicts a stable fixed point for the Poisson ratio at $\nu_{\mathrm{c}} = 1/4$.

To simulate the passive two-bead microrheology experiment in the actin and microtubules network we make use of eq. (4.33) with the Poisson ratio of the soft

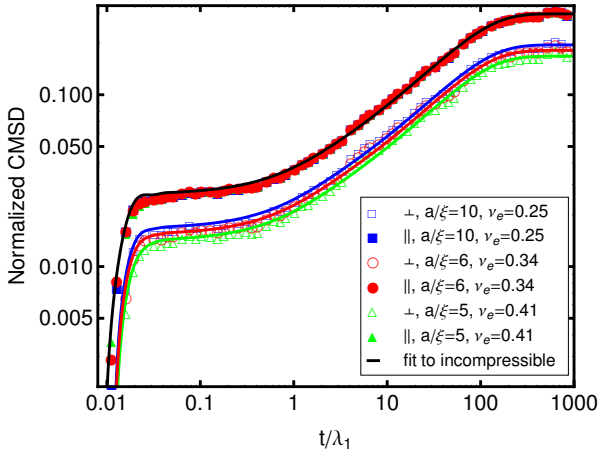

Figure 4.5. Two-bead cross-correlations, normalized by $2k_BT/H_e$, obtained using generalized Brownian dynamics simulations of the two-point passive microbead rheology experiment in F-actin and microtubule composites. Simulations where performed for different values of the radius to mesh-size ratio of microtubules, a/ξ, in the blend. The solid lines are fits of the inverse one-sided Fourier transform of eq.(4.23) to the generalized Brownian dynamics simulations results.

viscoelastic matrix, the F-actin, set to a value very close to $\nu_a \approx 0.5$. As explained in Section 4.4 here we consider only viscoelastic solids with a constant Poisson ratio. We performed GBD simulations [18] of the two-point passive microrheology of composite networks with different values of the a/ξ ratio. According to Figure 4.4 the compressibility of this nearly incompressible solid matrix will increase upon the addition of rigid rods (and increase the a/ξ ratio). The two-bead cross-correlations calculated from the simulations are shown in Figure 4.5. Notice that in the direction parallel to the line of centers all the data points collapse to a single curve. This is because, as was pointed in Section 4.4, the cross-correlations in this direction are not sensitive to changes in the speed at which the longitudinal waves travel through the medium. Therefore one can use the cross-correlations in the direction parallel to the line of centers to extract the dynamic modulus of the material as if analyzing the data of an incompressible medium. We do this using the time-domain data analysis strategy that we have previously proposed [16, 18]. The method involves fitting the CMSD in

the direction parallel to the line of centers (in the time domain), and then extracting the discrete relaxation spectrum of the medium from the fitted parameters. The line labeled as Input in Figure 4.6A shows the dynamic modulus that was used as input in the simulations. Output 1 illustrates the dynamic modulus that is obtained from analyzing the two-bead cross-correlations in the direction parallel to the line of centers as if they had been obtained from an incompressible medium. A very good agreement with the input dynamic modulus is obtained, as expected. The line labeled Output 2 in Figure 4.6A is the dynamic modulus obtained when the cross-correlations in the direction parallel to the line of centers are analyzed using the traditional inertialess generalized Stokes-Einstein relation (GSER), which does not account for inertia or high order hydrodynamic reflections (a detail discussion of why the traditional GSER fails in a situation such as the one considered here has been given in Chapter 3).

Once the dynamic modulus has been determined from the cross-correlations in the direction parallel to the line of centers, the Poisson ratio can be obtained by fitting a single extra parameter (in the case of a constant Poisson ratio) to the cross-correlations in the direction perpendicular to the line of centers. An approximation to the one-sided inverse Fourier transform [16] of eq.(4.23) is fitted to the time-domain cross-correlation in the direction perpendicular to the line of centers, using as fitting parameter the Poisson ratio of the viscoelastic solid. The solid lines in Figure 4.6B show $\nu'(\omega)$ obtained from the values of the ratio a/ξ used as inputs in the GBD simulations. We also calculate the Poisson ratios from the two-bead cross-correlations using eq.(4.24), which neglects inertia and high-order hydrodynamic interactions. Although this analysis correctly predicts a decrease in the Poisson ratio as the concentration of microtubules is increased, it can be observed that analyzing the cross-correlation data with this simplified equation leads to a frequency dependent Poisson ratio, even though the input Poisson ratio was constant. The simplified analysis works well in the lower frequency range but deviations from the input Poisson

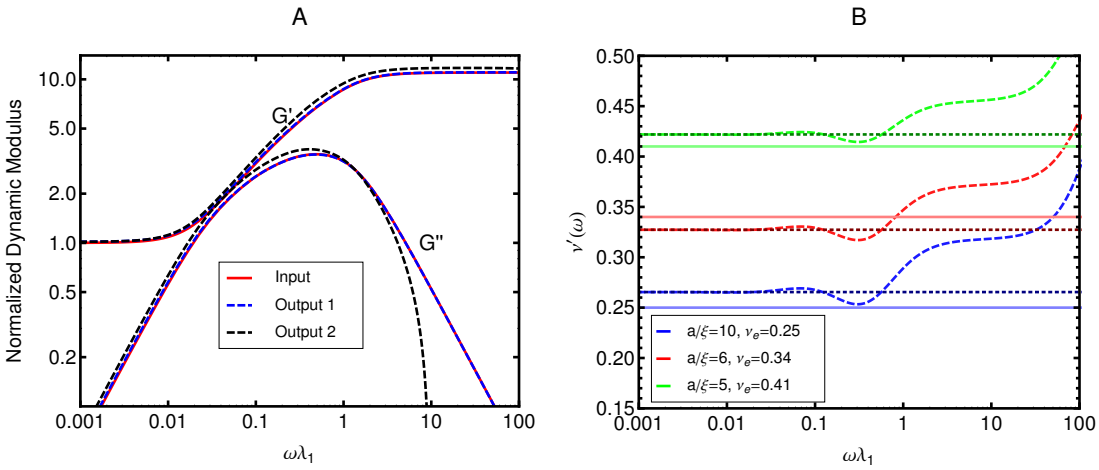

Figure 4.6. Monte-Carlo evaluation of the time-domain data analysis algorithms using the synthetic CMSD data generated with the BD simulations. A: Dynamic modulus, eq.(4.25) normalized by g_e, obtained from analyzing the cross-correlations in the direction parallel to the line of centers as if they came from an incompressible material. Output 1 was obtained with the data analysis algorithm that include inertia and infinite reflections, eq. (4.23). Output 2 was obtained with a data analysis algorithm that neglects inertia and accounts only for first order reflections. B: Real part of the complex Poisson ratio, eq.(4.26), obtained from analyzing the two-bead cross-correlations in the direction perpendicular to the line of centers. The solid (lighter) lines are the Poisson ratios used as input in the simulations, the dashed lines are the Poisson ratios obtained from analyzing the CMSD data using eq.(4.24), which neglects inertia and high order hydrodynamic reflections. The dotted (darker) lines are the Poisson ratios obtained by using the data analysis that accounts for inertia and all hydrodynamic interactions.

ratio start becoming significant at frequencies corresponding to the shortest relaxation time of the medium. According to this simplified analysis the material is compressible at low frequencies but becomes nearly incompressible at high frequencies. This is an important point since as we pointed out in Section 4.4 the sensitivity of the two-point microrheology technique to changes in the dynamics of the Poisson ratio is very low. This additional issue that can be introduced by not properly accounting for inertia and hydrodynamic reflections can make it even more challenging to obtain accurate compressibility measurements using microrheology techniques. Therefore compressibility measurements obtained using two-point microbead rheology may need

careful analysis in light of the dimensional analysis outlined in Section 4.2 to determine whether inertia and/or high order hydrodynamic reflections should be accounted for in the analysis. The dotted lines in Figure 4.6B show the Poisson ratios obtained by using the rigorous data analysis strategy based on eqs. (4.22) and (4.23). The small errors that can still be observed are due to the finite size of the ensemble used to calculate the cross-correlations, and can be reduced as much as desired by using more bead trajectories when calculating the ensemble averages on eqs. (4.22) and (4.23). With the proposed data analysis procedure the microstructural parameter a/ξ of the F-actin and microtubules composite can be estimated accurately using two-bead passive microrheology. Further more the analysis correctly reproduces the theoretical results presented in Figure 4.4, that is the increase in compressibility of the F-actin matrix as the concentration of microtubules is increased.

4.6 Conclusions

We have derived a generalized Stokes tensor for two hydrodynamically interacting beads embedded in a viscoelastic compressible solid. The tensors include the effects of medium inertia and consider an infinite number of reflections of the shear and longitudinal waves caused by the motion of the beads. A generalized Langevin equation for two hydrodynamically interacting beads embedded in a compressible viscoelastic solid was presented. Using the memory function tensor obtained from the generalized Stokes relation the GLE was solved in the frequency domain to obtain relations between the beads' auto- and cross-correlations and the components of the generalized Stokes tensor.

Using these new theoretical developments we have systematically evaluated the sensitivity of two-bead cross-correlations to changes in the static and dynamic properties of the complex Poisson ratio of a model viscoelastic material. We find that the sensitivity of the cross-correlation in the direction parallel to the line of centers of

the beads to the compressibility of the medium is very small. These effects which appear only at high frequencies, and are due to medium inertia, can be safely neglected in the data analysis. This means that the shear modulus can be inferred independently from the cross-correlations in the direction parallel to the line of centers even when inertia and higher-order hydrodynamic reflections are expected to have a relevant effect. This conclusion had already been reached with theoretical developments that neglect medium inertia and high order hydrodynamic reflections; here we show that it is still valid even when those effects are considered. On the other hand, the two-bead cross-correlations in the direction perpendicular to the line of centers show a detectable dependence on the compressibility of the material. A clearly distinguishable vertical shift can be detected in the cross-correlations obtained in a compressible medium with respect to those obtained in an incompressible one. However we have shown that the sensitivity of the cross-correlations in the direction perpendicular to the line of centers is practically undetectable to changes in the specific spectrum of delay times of the complex Poisson ratio. Therefore the passive two-point microrheology technique does not seem appropriate to accurately measure dynamic properties of the complex Poisson ratio.

Using generalized Brownian dynamics [16] and a microscopic model for biological composite networks [20] we simulated the two-bead microrheology experiment in F-actin and microtubules composites. We used the simulated two-bead cross-correlations to test data analysis formalisms for inferring microstructural properties of the composites. We find that commonly used data analysis which neglects inertia and higher-order hydrodynamic reflections will over predict Poisson ratios by 30 %. On the other hand the time-domain data analysis procedure [16, 18] that can be constructed using eq.(4.23) can successfully recover the input complex Poisson ratio of the F-actin and microtubules composite network in all the frequency range considered here. The traditional data analysis algorithm and the one that accounts for medium

inertia and high order reflections give comparable results at low frequencies, which indicates that medium inertia is the main cause for the failing of the simplified data analysis formalism.

There is a considerably large region of values for the radius-to-distance ratio and frequency, relevant to microbead rheology experiments, where the data analysis formalism that neglects medium inertia and higher-order reflections produces detectable errors in the dynamic modulus and the complex Poison ratio inferred from two-point cross-correlations. At high frequencies the wavelength of the shear and longitudinal waves propagating through the viscoelastic solid becomes small compared to the distance between the beads and therefore the assumption that stress propagates instantaneously becomes invalid. Additionally reflected waves can be important at low frequencies, where the penetration depth of the waves can become larger than the distance between the beads. In experiments a large separation between the probe beads can reduce the effect of higher-order reflections and allow for statistically relevant sampling of larger microstructures. However a large separation will increase the effects of medium inertia and reduce the signal-to-noise-ratio in the CMSD. These factors constrain the experimental conditions under which the two-point technique is applicable. As has been illustrated with the F-actin and microtubules composite networks, the data analysis formalism presented in this work significantly expands the region of distances between the beads and frequencies at which the dynamic modulus and the complex Poisson ratio can be accurately measured using two-point passive microrheology.

CHAPTER 5

A SINGLE-CHAIN MODEL FOR ACTIVE GELS I: ACTIVE DUMBBELL MODEL

This Chapter previously appeared in RSC Advances (The Royal Society of Chemistry) volume 4, issue 34, pages 17935-17949, year 2014.

5.1 Introduction

Active gels are networks of semiflexible polymer filaments driven by motor proteins that can convert chemical energy from the hydrolysis of adenosine triphosphate (ATP) to mechanical work and motion. Active gels are ubiquitous in living tissue—the cell cytoskeleton is an active gel composed of many different types of filaments and motors. Active gels play a central role in driving cell division and cell migration, [23, 118], and have also been successfully prepared *in vitro* to study their mechanical and rheological properties [117, 8, 91]. The semiflexible filaments that form active gels, such as actin and tubulin, are characterized by having a persistence length (length over which the tangent vectors to the contour of the filament remain correlated) that is much larger than the size of a monomer, and larger than the mesh size of the network, but typically smaller than the contour length of the filament. For instance, filamentous actin (F-actin) has persistence length of around 20 μm, while the mesh size of actin networks is estimated to be approximately 0.2 μm [85, 34, 115]. This sets them apart from flexible networks where the persistence length of the polymeric chains is much smaller than the mesh size of the networks formed by those chains. An important mechanical characteristic of semiflexible networks is that they exhibit significant strain hardening for modest strains. A tension of a few pN can increase the modulus of a semiflexible network by a factor of 100 [85, 34].

Molecular motors are proteins with a rigid, roughly cylindrical, backbone and clusters of binding heads on both ends that can attach to active sites along semiflexible

filaments [49, 46]. In the absence of ATP they act as passive cross-links between the semiflexible filaments. In the presence of ATP molecular motors can "walk" along the filaments. The direction in which motors move is determined by the filament structural polarity [127, 56]. A molecular motor starts walking when an ATP molecule attaches to a binding head domain of the motor protein, which causes it to detach from the filament. Using the chemical energy from the hydrolysis of ATP the detached motor head moves towards the next attachment site along the filament contour and reattaches, in a process known as the Lymn-Taylor cycle [81]. Each motor has at least two clusters of binding heads performing this same process. However, both of them do not necessarily detach at the same time. When the binding heads on one end of the motor are detached and moving towards the next attachment site, the heads on the other end can be attached to a different filament. This filament will feel an extensional or compressive force due to the motion of the motor. Therefore, in a network molecular motors can generate active, pair-wise interactions between filaments. The forces generated by the motors when they move along the filament are a function of the chemical potential difference between ATP and its hydrolysis products, which in itself is a function of the local concentration of ATP. *In-vivo* molecular motors operate far from equilibrium. In typical active gels found in living cells the difference in chemical potential between ATP and its hydrolysis products is on the order of $10k_{\mathrm{B}}T$ [55, 56]. Examples of molecular motors that have been extensively studied are myosin which moves along actin filaments; and kynesin and dynesin which move along microtubules.

Recent advances in experimental techniques have allowed the characterization of mechanical and rheological properties of active gels. These active polymeric networks have shown fundamental differences from their passive counterparts. The differences are not surprising given that these are materials in which molecular motors continuously convert chemical energy into mechanical work. Recent microrheology

experiments [8, 117, 91] on active gels have shown that the fluctuation-dissipation theorem (FDT) and the generalized Stokes-Einstein relation (GSER) are violated in active gels. The FDT is a central part of data analysis of passive microrheology experiments, where it is used to relate the position fluctuations of the probe bead to a frequency-dependent friction coefficient, from which, by using a generalized Stokes relation rheological properties can be extracted [51, 15, 108]. The violation of FDT is observed as a frequency-dependent discrepancy between the material response function obtained from active and passive microrheology experiments. In the active experiments an external force is applied to the probe bead and the material response function is calculated from the bead position signal [108]. In passive microrheology experiments, no external force is applied, and the material response function is calculated from the bead position autocorrelation function using the FDT [91]. Other microrheology experiments in active gels [91, 117] also indicate that the activity of molecular motors can produce significant strain hardening of the active networks. This is observed in the non-Gaussian statistics of the probe bead position or as an overall progressive increase in the magnitude of the modulus of the gel upon addition of ATP.

From the theoretical perspective, in the recent past a considerable amount of work has been devoted to deriving simple generalizations or extensions of the FDT for out-of-equilibrium systems, such as active gels [102, 10, 29]. In general, these extensions of FDT to out-of-equilibrium systems model the non-equilibrium forces as Brownian forces, but introduce an effective temperature [78, 79, 80, 97], which is higher than the real temperature and is meant to account for the larger magnitude of the non-equilibrium fluctuations. This kind of approach can not explain the observations in the microrheology experiments in active gels [91] since Brownian forces alone can not produce a frequency-dependent discrepancy between the material response obtained from the material's spontaneous stress fluctuations, and the mate-

rial response obtained by applying a small external perturbation and observing the material response. Other works [74, 43] have modeled the attachment/detachment dynamics of motor forces as a stochastic jump process. This approach has been successful in describing some of the features observed in the microrheology experiments of active gels, such as diffusive behavior of tracer beads at frequencies where storage modulus of the gel has plateau behavior. However these models assume that motors can be described as force dipoles inside a continuum, which is an assumption that can easily break down for semiflexible networks, where the mesh size is smaller than the persistence length of the filaments. They also assume that the motors do not interact through the strain field in the network and neglect strain hardening. Given the level of description of such models, removal of these assumptions is difficult; therefore more microscopic models are required to elucidate the specific effect that these physical features have on the rheology of active gels.

Another important mechanical feature of active gels that has been extensively studied experimentally, is their capacity of self-contraction and self-organization [71, 119, 23, 65, 63]. These mechanical features of active gels play a central role in cell division and motion. It has recently been shown that self-contraction in F-actin gels, is controlled by the buckling of individual filaments [71, 119]. This is known to be caused by the activity of myosin motors on F-actin filaments which support large tensions but buckle easily under piconewton compressive loads [23, 115]. Several works have used a continuum-mechanics level of description to model self-organization [64, 2] and rheology [79, 12, 33] of active gels and fluids. More microscopic models have described active gels using a master equation for interacting polar rods; Aranson and Tsimring [2] presented analytic and numerical results for rigid rods, later Head et al. [42] presented more detailed numerical simulations that account for filament semiflexibility. These models have been very successful in describing large scale phenomena such as the formation and dynamics of cytoskeletal patterns (eg.: asters, vortices).

However, the precise microscopic mechanisms underlying this process are still the subject of considerable experimental and theoretical investigation. Recently, a microscopic single-filament mean-field model to describe myosin-induced contraction of non-sarcomeric F-actin bundles was postulated by Lenz et al. [71]. In this work we use a similar description. However there are several issues in the level of description and mathematical formulation of Lenz et al. [71] that we discuss and reformulate here.

The main objective of this Chapter is to introduce a single-chain mean-field model for active gels. We present a level of description for active gels that has the minimum necessary components to predict mechanical and rheological features that have been observed in active gels. The general formulation of the model can account for many of the known microscopic characteristics of active gels. For example, motor concentration, the non-linear elasticity of semiflexible filaments, the dependence of motor attachment/detachment rates on the filament tension, and details about the motor-generated forces. However, in this introductory Chapter we make some assumptions that allow us to simplify the mathematics while still keeping most of the relevant physics in the model. Numerical simulations of more general formulations are postponed to Chapter 6. In Section 5.2 we give a detailed description of the model, and discuss the main assumptions, and parameters. In Section 5.3 we show that the active dumbbell model can predict the violation of the FDT observed in microrheology experiments of active gels. This is done by comparing the dynamic modulus of the gel obtained from the autocorrelation function of stress at the non-equilibrium steady state, with the modulus obtained from the stress response when a small perturbation is applied to the gel. In Section 5.4 we illustrate the use of the active dumbbell model to make predictions about the underlying mechanism of self-contraction in active F-actin bundles.

5.2 Description of the active dumbbell model

In this section we introduce a single-chain mean-field model for an active bundle. Active networks are formed by semiflexible filaments and molecular motors that form active cross-links between filaments (Figure 5.1A). In the presence of ATP, motors will go through detachment/attachment cycles [81] in which they detach from one of the filaments that they are linking and step forward (in a direction determined by the filament's structural polarity) therefore exerting a force on the other filament to which they remained attached. Our model follows a single probe filament (illustrated in gray in Figure 5.1A) and approximate its surroundings by an effective medium made of point-like motors that attach and detach from specific sites along the probe filament. The motors are assumed to form pair-wise interactions between filaments. When a motor is attached to the probe filament it is detached and steps forward on another filament in the mean-field and therefore pulls/pushes on the probe filament. The formulation of temporary network models provides a very useful mathematical and conceptual framework to model these dynamics [44, 54, 53]. In Figure 5.1B a probe filament is shown in more detail, each bead represents an active site along the filament where a motor can attach, and the springs represent the filament segments between this active sites. For the dumbbell version of the model (shown in Figure 5.1C) there are only two active sites per filament (at the ends) where motors attach. The motors create the type of pair-wise active interactions between the dumbbells described above. To model these interactions we use a mean-field approach, in which filaments have certain probabilities to undergo a transition from one attachment/detachment state into another depending on the state of the particular filament. The integer variable s is used to label the attachment/detachment state of the dumbbell.

We assume that before addition of ATP the distance between motors (acting

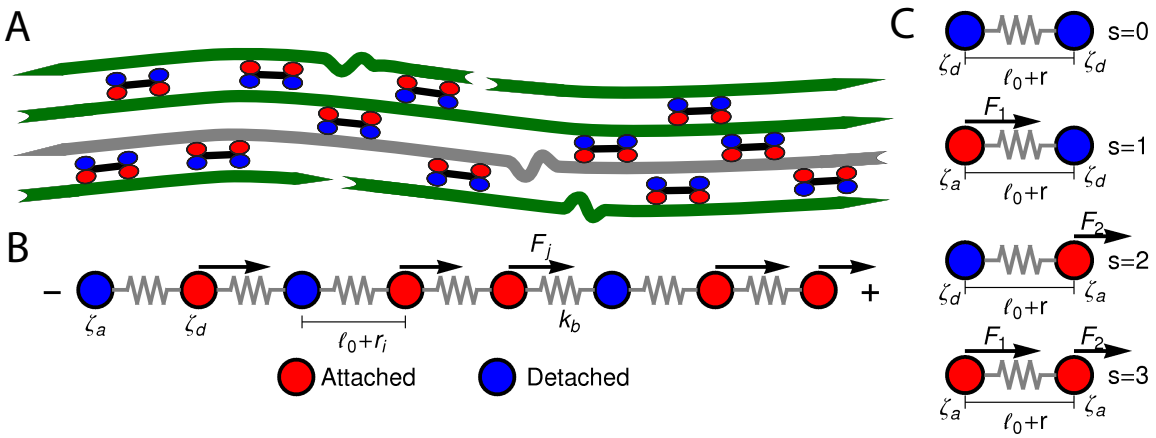

Figure 5.1. Sketch of the single-chain mean-field model for active gels. A: Active bundle formed by polar filaments and motors (which can move towards the barbed end of the filaments). Motors attach and detach from the filaments. After detaching from a given filament a motor will step forward in that filament and will exert a force on the other filament where it is still attached. The gray filament indicates a probe filament whose dynamics are followed by the model. B: The probe filament is represented by a bead-spring chain. Red beads represent attachment sites in the filament where a motor is attached, ζ_a is the friction coefficient of those beads. Blue beads represent sites in the filaments where no motor is attached ζ_d is the friction coefficient of those beads. ℓ_0 is the rest length of the filament before addition of ATP; r is the change in the end-to-end distance of the dumbbell due to motor activity. F_j is a motor-generated force acting on bead j. Motors generate a force on the filament only when attached. C: Sketch of the attachment/detachment states of a dumbbell version of the model. The attachment/detachment states model the interaction of the probe filament with the mean-field.

as passive cross-links) is given by ℓ_0. This is the rest length of the filament segment and therefore there is no tension on the filaments before addition of ATP. After addition of ATP the motors (cross-links) become active and start detaching from and reattaching to the beads. τ_d is the average time a motor spends attached to a bead before detaching from it, whereas the average time a motor spends detached before reattaching is given by the model parameter τ_a. Active gels can have, besides motors, permanent passive cross-links; however in the model presented here, all cross-links are allowed to become active, we do not consider permanent cross-links here. The force generated by a motor attached to bead j will be denoted F_j. Molecular motors can

only move in one direction along the filament, determined by the filament's polarity. In this single-chain description we introduce this asymmetry by making all the forces F_j, that the motors exert on the beads of a given dumbbell, have the same sign (either positive or negative). Another force acting on the filament is the viscous drag from the surrounding solvent (which is mainly water for these biological networks). The frictional force from the surrounding solvent is characterized by a friction coefficient. Motors are expected to increase the friction coefficient of the filament when attached to an active site. Therefore this friction coefficient is allowed to take two different values: ζ_a when attached, and $\zeta_d < \zeta_a$ if there is no motor attached to that bead. The change in the end-to-end length of the dumbbell due to the action of the motors is denoted r (see Figure 5.1). We emphasize that the strands (filament segments between motors) have non-zero rest length ℓ_0 and the motors generate a change r in this length. The strands do not collapse to zero length, their end-to-end lengths fluctuate around ℓ_0 due to motor activity.

The general physical picture of our model, that is, the single-chain description and the representation of semiflexible filaments as bead-spring chains are the same as in a previous model proposed by Lenz et al. [71]. As discussed in section 5.1, this model has been used by its authors to study buckling in non-sarcomeric actin bundles. However the level of description (state variables of the model) and mathematical formulation of our model does not follow the work of Lenz et al. [71]. Instead we use a mathematical formulation similar to the one used in temporary network models of associating polymer chains [44, 54, 53].

The following state variables (level of description) are used to construct the model of the active dumbbell $\Omega : \{s, F_1, F_2, r\}$. Now let $\psi(\Omega)$ be the probability density describing the probability of finding an active dumbbell in state s with a change in its end-to end distance r due to motor forces F_1 and F_2 at time t. The time

evolution for $\psi(\Omega)$ is given by the differential Chapman-Kolmogorov equation

$$\begin{aligned}\frac{\partial\psi(\hat{\omega},r;t)}{\partial t} &= \frac{\partial}{\partial r}\left\{\psi(\hat{\omega},r;t)\left[-\dot{\epsilon}(t)r + A(s)k_b r - \frac{(F_2-F_1)}{\zeta_a}\right]\right\} \\ &+ \sum_{s'=0}^{3}\int\int \mathbb{W}_{s,s'}(\hat{\omega}|\hat{\omega}')\psi(\hat{\omega}',r;t)dF_1'dF_2',\end{aligned} \tag{5.1}$$

where $\hat{\omega} : \{s, F_1, F_2\}$ is a subspace of Ω and $\epsilon(t)$ is an externally applied strain in the direction of filament alignment. On writing eq.(5.1) we have assumed that the semiflexible segment can be described as a Fraenkel spring with spring constant k_b . This assumption, although it is only expected to be valid for very small deformations (semiflexible filaments are known to strain harden under a tension of a few pN, which motors are known to generate [85, 34]) allows us to proceed analytically with the solution of the model. For a semiflexible filament segment MacKintosh et al. [82] derived a relation between the persistence and rest lengths of the semiflexible filament and its linear elastic response constant $k_b = \dfrac{3\pi^3 k_{\mathrm{B}} T \ell_p^2}{\ell_0^4}$, we use this relation throughout this Chapter. For F-actin filaments, the persistence length, ℓ_p, is around 10 μm, $\ell_0 \sim 1\mu$m, and therefore k_b is on the order of 1 μN/m.

The function $A(s)$, in eq.(5.1) gives the connectivity of the beads as a function of the motor-attachment state, s, and is defined as,

$$A(s) = \begin{cases} \frac{2}{\zeta_d} & \text{if} \quad s = 0 \\ \frac{1}{\zeta_d} + \frac{1}{\zeta_a} & \text{if} \quad s = 1 \text{ or } s = 2 \\ \frac{2}{\zeta_a} & \text{if} \quad s = 3 \end{cases} \tag{5.2}$$

where, as stated above, ζ_a is the friction coefficient of a bead when a motor is attached to it and ζ_d is the friction coefficient when there is no motor attached to it. For instance, several experimental measurements [119, 71] have shown that myosin II motors move along actin filaments at approximately $0.5 - 1$ μm/s, and they have an average stall force of 1 pN, therefore ζ_a is estimated to be around 1 $\mu\mathrm{N}\cdot\mathrm{s/m}$.

ζ_a is expected to be larger than ζ_d since the motor attachment heads increase the cross-sectional area of the actin filament when they attach to it. Additionally to τ_a and τ_d it is convenient to label two additional time scales of the model $\tau_{r,a} = \zeta_a/k_b$ and $\tau_{r,d} = \zeta_d/k_b$ which are local relaxation times of the filament when a motor is attached to it and when there is no motor attached to it respectively. For mysosin motors in actin gels τ_d is on the order of 200 ms while τ_a is usually between an order to two orders of magnitude smaller [71, 74]. Therefore in a typical active gel $\tau_a < \tau_d \leq \tau_{r,d} < \tau_{r,a}$ is expected.

The transition rate matrix $\mathbb{W}(\hat{\omega}'|\hat{\omega})$ in eq.(5.1) contains the transition rates between attachment/detachment states,

$$\mathbb{W}(\hat{\omega}'|\hat{\omega}) = \begin{pmatrix} * & \frac{\delta(F_1')\delta(F_2')}{\tau_d} & \frac{\delta(F_1')\delta(F_2')}{\tau_d} & 0 \\ \frac{p(F_1')\delta(F_2')}{\tau_a} & * & 0 & \frac{\delta(F_1')\delta(F_2')}{\tau_d} \\ \frac{\delta(F_1')p(F_2')}{\tau_a} & 0 & * & \frac{\delta(F_1')\delta(F_2')}{\tau_d} \\ 0 & \frac{\delta(F_1')p(F_2')}{\tau_a} & \frac{p(F_1')\delta(F_2')}{\tau_a} & * \end{pmatrix}. \tag{5.3}$$

For example, the second row of the first column gives the rate at which a dumbbell in state $s = 0$ jumps to state $s = 1$. The diagonal elements of the transition matrix are given by $\mathbb{W}_{s,s}(\hat{\omega}|\hat{\omega}) = -\sum_{s'(\neq s)=0}^{3} \mathbb{W}_{s',s}(\hat{\omega}'|\hat{\omega})$. The function $p(F)$ is the probability distribution from which a motor force is drawn every time a motor attaches to a bead. Motor force distributions have been measured experimentally in actin-myosin bundles [119, 71]. The first moment of this distribution is approximately $F_m = 1$pN, where F_m is usually referred to as the motor-stall force. The exact shape of these distributions can be incorporated into the model, however in this Chapter we will use simplifying assumptions about this distribution which will be discussed in Section 5.3. Note that we have assumed that the motor force distribution is time independent which is expected to be a good assumption as long as the kinetics of the

ATP $\rightarrow$ work reaction in the motors are much faster than any of the time scales in the model. We have also assumed that the τ_a and τ_d are independent of time and of the tension on the filament. This might be unrealistic since it has been shown that the tension on the filaments can affect attachment and detachment rates of the motors [93]. To summarize, we use a single-filament model of the active gel where binary active crosslinks with other filaments are accounted for by a mean-field of point-like motors that undergo transitions between attachment states determined by the phenomenological parameters τ_a, τ_d and $p(F)$.

Note that in the model presented here $p(F)$ is bead independent in contrast to the model by Lenz et al. [71]. In that model the transition rates do not depend on the motor force distribution but the motor force distribution depends on the position along the filament of the bead to which the motor is attached. Physically this assumption can be interpreted as the motors having spatial memory and being able to identify the particular position along the filament to which they are attaching. Presumably these assumptions are done to simplify the mathematics, however it leads to several issues in the solution and interpretation of the model predictions that have not been clearly resolved. We avoid such assumptions. Instead, $\boldsymbol{F}$ is kept as a stochastic state variable, $p(F)$ is the same far all motors, and the transition rates depend on this motor force distribution. In other words, our model exists at a more-detailed level of description than the model of Lenz et al. [71]. In Section 5.4 we will discuss the implications that these conceptual differences between the two models have in the explanation of the mechanisms underlying buckling and self-contraction in active gels.

In eq.(5.1) Brownian forces have not been included. To account for Brownian forces a term $A(s)k_{\mathrm{B}}T\dfrac{\partial\psi(\hat{\omega},r;t)}{\partial r}$ should be added inside the square bracket on the right hand side of eq.(5.1). Here we omit this term since it does not make any

difference for the proof-of-concept calculations presented here. In other words, the version of the model presented here represents an active limit, where the diffusive motion of the filaments due to thermal forces is negligible compared to the driven motion produced by motor activity. Since all terms of eq.(5.1) are linear, and motor and Brownian forces are in general uncorrelated [74, 43], a solution that includes Brownian forces will simply be the superposition of the solution presented here plus the well known solution for a passive dumbbell [9]. The passive part of the solution will not contribute to the active gel features we are investigating. For instance, it has been extensively shown that single-chain temporary network models that include Brownian forces, but not motor forces, satisfy the fluctuation dissipation theorem [53, 109].

It is common for active gels to contain permanent passive cross-links such as biotin or α-actinin in actomysosin networks. In those cases myosin contracts F-actin into dense foci around the permanent cross-links. Once contracted, these aggregates can undergo further coalescence with each other and may form structures such as asters or vortices. The present formulation of our single-chain mean-field model does not yet seem appropriate for describing that type of phenomena. Other descriptions such as multi-chain models [42] or coarser levels of description [64, 2] have been used to describe such observations. However other experiments [119, 94] have shown that local contraction can also occur in active gels containing motors alone. For instance sufficiently high density of myosin motors in the absence of passive cross-linkers has been shown to cause contractility in actomyosin bundles [119]. In these conditions, the length scale over which contraction occurs within the network is proportional to the F-actin length, consistent with poor network connectivity by myosin motors. Through the addition of passive cross-linkers the length of contraction is increased to macroscopic length scales [94, 60]. The model presented here is expected to describe well the dynamics of active gels that do not contain permanent passive cross-links or

sarcomeric organization.

In Sections 5.4 and 5.3 we show that the model described above presents some of the main mechanical and rheological characteristics observed in active gels. The predictions here are expected to be only qualitative since several strong assumptions have to be made to obtain analytic solutions of the model: i.) Aligned one-dimensional filaments, ii.) Filaments with only two attachment sites at its ends (dumbbells), iii.) Filaments modeled as Hookean springs, and iv.) Attachment/detachment rates independent of filament tension. There is experimental evidence indicating that often some of these assumptions break down in active gels, but the calculations presented here illustrate the fundamental elements that a single-chain model needs to describe the main mechanical and rheological characteristics of active gels. Removal of these assumptions is straightforward with this approach.

5.3 Dynamic Modulus of Active Gels

To test the validity of FDT in active gels, Mizuno et al. [91] compared the complex compliance of actin-mysoin networks measured with active and passive microrheology . In the active experiment they used optical tweezers to apply a small-amplitude oscillatory force to the bead. The complex compliance or the dynamic modulus of the medium can be calculated from the bead position signal [57]. In a passive microrheology experiment no external force is applied to the bead or a static harmonic trap is used to hold the bead near its equilibrium position. In this case the autocorrelation of the bead position is used to estimate the dynamic modulus using the FDT and a generalized Stokes relation [15, 51]. Before addition of ATP the complex compliance of the actin-myosin network obtained with the passive and active techniques were identical. In gels activated with ATP a frequency-dependent discrepancy between the complex compliance obtained from the passive and active experiments appears at frequencies below 10Hz. This discrepancy is due to a frequency-dependent increase

in the magnitude of the bead fluctuations observed in the passive microrheology experiment, in the actin-mysosin gels activated with ATP. These increased fluctuations have been linked to motor activity [43, 74, 68]. Since the FDT does not account for motor activity, the dynamic modulus calculated from the fluctuations using the FDT does not agree with the modulus obtained from the active experiment.

In this section, we perform calculations with the active dumbbell model that test the validity of FDT in active gels in a way similar to the microrheology experiments of Mizuno et al. [91]. We begin by calculating the relaxation modulus of the active gel from the autocorrelation function of stress at the non-equilibrium steady-state. In other words, we apply in an active gel the famous Green-Kubo formula which relates the autocorrelation function of stress with the relaxation modulus of a material [14]. In a second calculation we apply a small-amplitude oscillatory strain to the active gel and estimate the dynamic modulus from the observed stress. If the active dumbbell model satisfies the FDT the dynamic modulus obtained from those two calculations should be the same; if it does not, a time-dependent discrepancy should appear. Similar calculations are often performed for single-chain models of temporary networks, to demonstrate thermodynamic consistency (FDT compliance) [53, 109].

5.3.1 Dynamic modulus of active gels from a Green-Kubo Formula. For the derivation of the dynamic modulus we introduce the conditional probability $\psi_{\rm st}(\hat{\omega}, r; t|\hat{\omega}_0, r_0; 0)$ (where $\hat{\omega} : \{s, F_1, F_2\}$) that an active dumbbell at steady sate is in attachment state s with a change in its end-to end distance r due to motor forces F_1 and F_2 at time t when it had the initial conformation r_0 and the initial attachment state s_0 at $t = 0$. The time-evolution of $\psi_{\rm st}(\hat{\omega}, r; t|s_0, r_0; 0)$ obeys the

same evolution equation as eq.(5.1) for an arbitrary initial state (r_0, s_0),

$$\begin{aligned}\frac{\partial \psi_{\rm st}(\hat{\omega}, r; t|\hat{\omega}_0, r_0; 0)}{\partial t} &= \frac{\partial}{\partial r}\left\{\psi_{\rm st}(\hat{\omega}, r; t|\hat{\omega}_0, r_0, 0)\left[A(s)k_b r - \frac{(F_2 - F_1)}{\zeta_a}\right]\right\} \\ &+ \sum_{s'=0}^{3}\int\int \mathbb{W}_{s,s'}(\hat{\omega}|\hat{\omega}')\psi_{\rm st}(\hat{\omega}', r; t|\hat{\omega}_0, r_0; 0)dF_1' dF_2'.\end{aligned} \tag{5.4}$$

Where the initial condition for the probability distribution function is given by $\psi_{\rm st}(\omega, r; t = 0|\hat{\omega}_0, r_0; 0) = \delta(r - r_0)\delta_{s,s_0}$. The function $A(s)$ was defined in eq.(5.2) and the transition rate matrix $\mathbb{W}(\hat{\omega}|\hat{\omega}')$ in eq.(5.3), both in Section 5.2. Eq.(5.4) can be solved exactly using the same procedure outlined in Appendix B for eq.(5.1). If we make the motor force distribution a Dirac delta function centered around F_m, $p(F) = \delta(F - F_m)$, where F_m is a mean motor stall-force, all calculations can be performed analytically. At the end, the procedure reduces to solving a system of ordinary differential equations, eqs.(B.6a) and (B.6b), with initial conditions $\langle r\rangle_{\{s,\boldsymbol{F}\}}(t = 0) = \langle r\rangle_{\{0,s\}}$ and $\langle r^2\rangle_{\{s,\boldsymbol{F}\}}(t = 0) = \langle r^2\rangle_{\{0,s\}}$. The Green-Kubo formula requires the calculation of the autocorrelation function of stress at steady-state $\langle\sigma(0)\sigma(t)\rangle_{\rm st}$. Where σ, for this 1-dimensional system, is the normal stress in the direction of filament alignment. For a bead-spring single-chain model of a network, such as the one being considered, the macroscopic stress is related to the tension on the filaments by $\sigma = -n_c f r = n_c k_b r^2$, where $f = -k_b r$ is the tension on the filament and n_c is the number of filaments per unit volume [54, 9]. It is convenient to introduce the marginal probability density,

$$\phi_{\rm st}(s, r; t|s_0, r_0; 0) = \int_{-\infty}^{\infty}\int_{-\infty}^{\infty}\psi_{\rm st}(s, F_1, F_2, r; t|\hat{\omega}_0, r_0; 0)dF_1 dF_2 \tag{5.5}$$

Using eq.(5.5) the autocorrelation function of stress at steady state can be calculated as,

$$\begin{aligned}\langle\sigma(t)\sigma(0)\rangle_{\rm st} &= n_c^2 k_b^2 \sum_{s=1}^{3}\sum_{s_0=1}^{3}\int\int r^2 r_0^2 \phi_{\rm st}(s, r; t|s_0, r_0; 0)\phi_{\rm st}(s_0, r_0)dr_0 dr \\ &= n_c^2 k_b^2 \sum_{s=1}^{3}\sum_{s_0=1}^{3}\langle r(t)^2\rangle_s \langle r^2\rangle_{\{0,s_0\}}.\end{aligned} \tag{5.6}$$

Where $\phi_{\rm st}(s,r) = \lim_{t\to\infty}\phi(s,r;t|s_0,r_0;0)$. The expressions for the conditional second moments of r for a given attachment state s that appear in eq.(5.6) are given in Appendix B, eq.(B.9).

Using eq.(5.6) the non-equilibrium steady-state relaxation modulus of the active gel at the non-equilibrium steady-state can be expressed as,

$$G_{\rm GK}(t) = \frac{1}{n_c k_b \langle r^2\rangle_0}\langle\sigma(t)\sigma(0)\rangle_{\rm st} \tag{5.7}$$

where $\langle r^2\rangle_0 = \sum_{s=1}^{3}\langle r^2\rangle_{\{0,s\}}$.

The detailed procedure to obtain the full expression for the relaxation modulus is given in Appendix B. In the limit $\tau_{r,a}\to\tau_{r,d}$ when $\tau_a/\tau_d \ll 1$, simplified algebraic expressions can be obtained. Using eqs.(5.6) and (5.7) the following simplified expression for the relaxation modulus is obtained,

$$G_{\rm GK}(t) = \left(\frac{n_c F_m^2}{k_b}\right)\frac{1}{\tau_r}\left(\frac{1}{2}-\frac{\tau_a}{\tau_d}\right)\left[2\tau_d\left(2+\frac{\tau_r}{\tau_d}\right)e^{-\frac{2t}{\tau_r}} - \tau_d\left(4+\frac{\tau_r}{\tau_d}\right)e^{-\frac{4t}{\tau_r}}\right], \tag{5.8}$$

where $\tau_r = \zeta_a/k_b = \zeta_d/k_b$. A plot of this relaxation modulus for $\tau_a/\tau_d = 0.1$ and $\tau_r/\tau_d = 4$ is shown in Figure 5.6A. A distinctive feature of this relaxation modulus, which makes it different from typical relaxation moduli of passive networks, is that it has a maximum located at $t = \frac{\tau_r}{2}\log\left(\frac{4+\tau_{\rm r}/\tau_{\rm d}}{2+\tau_{\rm r}/\tau_{\rm d}}\right)$ with a magnitude given by $\frac{n_c F_m^2}{k_b}\frac{(1-2\tau_a/\tau_d)(2+\tau_r/\tau_d)}{2\tau_r/\tau_d(4+\tau_r/\tau_d)}$. As we show in Section 5.3.2 this feature is essential to the violation of FDT observed in active gels.

Also, by taking the one-sided Fourier transform of eq.(5.8), the non-equilibrium steady-state dynamic modulus of the active gel is obtained $G^*(\omega) = i\omega\bar{\mathcal{F}}\{G(t)\} = G'(\omega) + iG''(\omega)$,

$$G'_{\rm GK}(\omega) = \frac{n_c F_m^2}{k_b}\frac{(\tau_d-2\tau_a)\tau_r\omega^2(48\tau_d+28\tau_r+\tau_r^3\omega^2)}{2\tau_d(64+20\tau_r^2\omega^2+\tau_r^4\omega^4)}, \tag{5.9a}$$

$$G''_{\rm GK}(\omega) = \frac{n_c F_m^2}{k_b}\frac{8(\tau_d-2\tau_a)(4\tau_d+3\tau_r)\omega}{\tau_d(64+20\tau_r^2\omega^2+\tau_r^4\omega^4)}. \tag{5.9b}$$

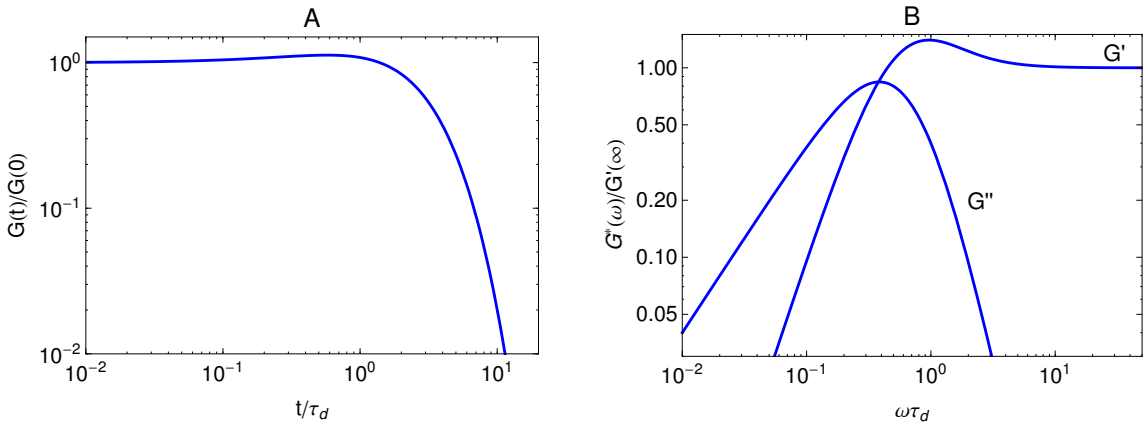

Figure 5.2. A: Non-equilibrium relaxation modulus for a gel formed by active dumbbells calculated from the autocorrelation function of stress at steady-state (Green-Kubo formula). B :Non-equilibrium dynamic modulus for a gel formed by active dumbbells calculated from the autocorrelation function of stress at steady-state (Green-Kubo formula). The parameter values used in these figures are $\tau_r = \zeta_a/k_b = \zeta_d/k_b = 4\tau_d$ and $\tau_a/\tau_d = 0.1$. It can be observed that a maximum appears in both $G(t)$ and $G'(\omega)$. This maximum is characteristic of active gels and does not appear in passive temporary networks.

Where $G'_{\mathrm{GK}}(\omega)$ is the storage modulus and $G''_{\mathrm{GK}}(\omega)$ is the loss modulus. Eq.(5.9) are valid in the limit $\tau_{r,a} \to \tau_{r,d}$ when $\tau_a/\tau_d \ll 1$. A plot of this dynamic modulus for $\tau_a/\tau_d = 0.1$ and $\tau_r/\tau_d = 4$ is shown in Figure 5.2B. Here, a maximum is also observed in $G'_{\mathrm{GK}}(\omega)$ which corresponds to the maximum in $G_{\mathrm{GK}}(t)$. Extrema do not occur in the relaxation or storage modulus of passive networks, and therefore this is a specific feature of active gels. The dynamic modulus of the active dumbbell gel also has features in common with the dynamic modulus of passive temporary networks, such as the high-frequency plateau in the storage modulus and the low frequency terminal zone in $G'(\omega)$ that goes as ω^2.

To further investigate how the shape of the dynamic modulus of the active network depends on the model parameters we performed calculations for different values of the ratios τ_a/τ_d and ζ_d/ζ_a. Figure 5.3A shows how the shape of the dynamic modulus depends on the ratio τ_a/τ_d for a constant value of τ_r/τ_d. It can be observed that as the values of τ_a/τ_d increase, $G''(\omega)$ and the maximum in $G'(\omega)$ decrease

slightly. In general, the shape of the dynamic modulus does not depend strongly on the ratio τ_a/τ_d. On the other hand, Figure 5.3B shows how the position of the maxima in $G'(\omega)$ and $G''(\omega)$ depends strongly on the ratio of friction coefficients ζ_a/ζ_d. This can be understood by considering that when ζ_d is much smaller than ζ_a local relaxation of the filament upon motor detachment is faster than tension build-up when the motor is attached. Therefore stress relaxation in the gel occurs at shorter time scales (higher frequencies).

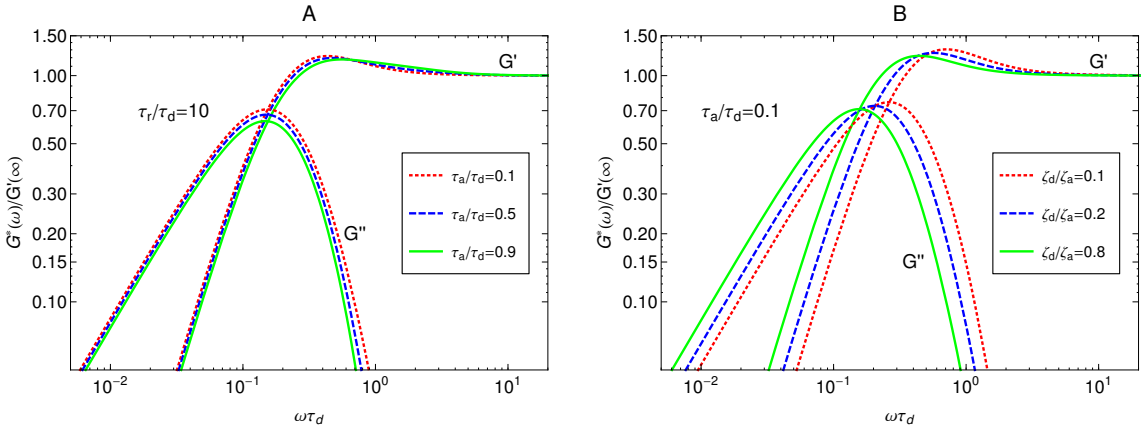

Figure 5.3. Non-equilibrium dynamic modulus for a gel formed by active dumbbells calculated from the autocorrelation function of stress at steady-state (Green-Kubo formula). A: Dependence on the ratio τ_a/τ_d for a constant $\tau_r/\tau_d = 10$ ratio. B: Dependence on the ratio ζ_d/ζ_a for a constant $\tau_a/\tau_d = 0.1$ ratio.

5.3.2 Dynamic modulus of active gels from a driven calculation. To show that the dumbbell model for active gels violates FDT in the way active gels do [91], we calculate the dynamic modulus observed in the stress response to an externally applied small-amplitude oscillatory strain. The calculation starts with eq.(5.1) with a small amplitude oscillatory strain applied to the bundle in the direction of filament alignment $\dot{\epsilon}(t) = \epsilon_0\omega \cos \omega t$. Where $\dot{\epsilon}$ is the strain rate, ϵ_0 is the strain amplitude and ω is the frequency. The detailed procedure to derive the dynamic modulus from this type of calculation and its general result are given in Appendix C. Moreover In the limit $\tau_{r,a} \to \tau_{r,d}$ when $\tau_a/\tau_d \ll 1$ the analytic expressions for G' and G'' can be

simplified to

$$G'_{\mathrm{D}}(\omega) = \frac{n_c F_m^2}{k_b} \frac{(\tau_d - 2\tau_a)\tau_r^2\omega^2(28 + \tau_r^2\omega^2)}{2\tau_d(64 + 20\tau_r^2\omega^2 + \tau_r^4\omega^4)}, \tag{5.10a}$$

$$G''_{\mathrm{D}}(\omega) = \frac{n_c F_m^2}{k_b} \frac{24(\tau_d - 2\tau_a)\tau_r\omega}{\tau_d(64 + 20\tau_r^2\omega^2 + \tau_r^4\omega^4)}. \tag{5.10b}$$

A plot of this dynamic modulus is shown in Figure 5.4A. This dynamic modulus presents features similar to those obtained from the Green-Kubo formula. However there is a frequency-dependent discrepancy between the two moduli discussed in the next subsection.

5.3.3 FDT in active gels. By comparing eq.(5.9) and eq.(5.10) it can now be established if the active dumbbell model exhibits violation of FDT observed in microrheology experiments of active gels. Figure 5.4A shows a comparison between the dynamic modulus of a typical actomyosin active gel obtained from the Green-Kubo formula, in Section 5.3.1, and the one obtained from the driven calculation, in Section 5.3.2. It can be observed that at high frequencies the two dynamic moduli are equal. In the limit $\tau_{r,a} \to \tau_{r,d}$ when $\tau_a/\tau_d \ll 1$, this high frequency plateau is given by $G'_{\mathrm{GK}}(\omega \to \infty) = G'_{\mathrm{D}}(\omega \to \infty) = \frac{n_c F_m^2}{2k_b}\left(1 - \frac{2\tau_a}{\tau_d}\right)$. At lower frequencies G^*_{GK} begins to grow faster than G^*_{D}. Then both the storage and loss moduli reach maxima. The maximum in G^*_{GK} is larger than in G^*_{D}. At lower frequencies, below the maximum, G'_{GK} and G'_{D} decrease as ω^2, while G''_{GK} and G''_{D} decrease as ω. The difference between G^*_{GK} and G^*_{D} persists as $\omega \to 0$.

Figure 5.5A shows the imaginary part of the complex compliance $J''(\omega) = 6\pi R\alpha''(\omega)$ of the actomyosin gel studied by Mizuno et al. [91]. Where $\alpha(\omega)$ is the complex compliance of the probe bead. In an active microrheology experiment the complex compliance is obtained from the relation $\langle \boldsymbol{r}_{\mathrm{b}}(\omega)\rangle = \alpha(\omega)\boldsymbol{f}^{\mathrm{trap}}$. Where $\boldsymbol{r}_{\mathrm{b}}(\omega)$ is the measured probe bead displacement and $\boldsymbol{f}^{\mathrm{trap}}$ is a small amplitude oscillatory

force, with frequency ω, applied with an optical trap. In the passive microrheology experiment the imaginary part of the complex compliance is obtained using the FDT, $\alpha''(\omega) = \frac{\omega}{6k_BT}C(\omega)$. Where $C(\omega) = \int_{-\infty}^{\infty}\langle \boldsymbol{r}_b(t)\cdot\boldsymbol{r}_b(0)\rangle e^{-i\omega t}dt$ is the autocorrelation function of the bead position. The complex compliance $J^*(\omega)$ is related to the dynamic modulus by $J^*(\omega)G^*(\omega) = 1$. The symbols are experimental data obtained using passive and active microrheology, while the lines are fits used to transform $J^*(\omega)$ to $G^*(\omega)$. The data were taken at steady state after addition of ATP to the actomyosin network. In Figure 5.5B the storage modulus obtained from the Green-Kubo calculation, eq.(5.9), and the one obtained from the driven calculation, eq.(5.10), are compared to the storage modulus of the actomyosin gel measured by active and passive microrheology by Mizuno et al. [91]. These experimental storage moduli are obtained from the fits to $J''(\omega)$ shown in figure 5.5A using standard procedures [6, 43, 83].

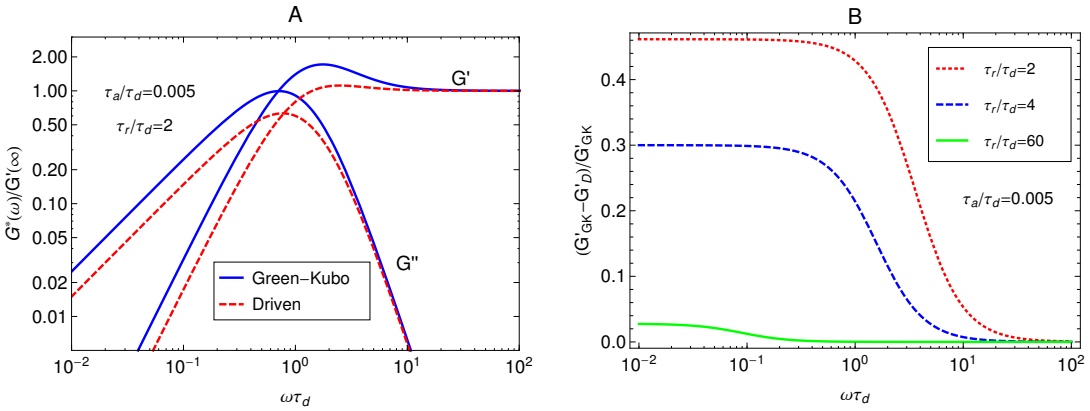

Figure 5.4. A : Comparison between the non-equilibrium dynamic modulus for an active gel calculated from, i) the autocorrelation function of stress at steady-state (Green-Kubo formula, eq.(5.9)), ii) the response to an external small-amplitude oscillatory strain, eq.(5.10). The parameter values used in these figures are $\tau_r = \zeta_a/k_b = \zeta_d/k_b = 2\tau_d$ and $\tau_a/\tau_d = 0.005$. B: Fluctuation-dissipation relation for the active dumbbell model, violation of FDT vanishes in the limit $\tau_r/\tau_d \to \infty$.

The frequency-dependent discrepancy between the response function of the active gel obtained from the driven and Green-Kubo calculations is in good qualitative agreement with the experimental observations of Mizuno et al. [91] in microrheology

experiments of actomysoin gels. For mysosin motors $\tau_d \sim 1 - 10$ s, if we make frequency dimensional using this τ_d in Figure 5.4A the discrepancy between G'_{GK} and G'_{D} appears around $10 - 50$ Hz which agrees in order of magnitude with the results of Mizuno et al. [91]. It is important to emphasize that the parameters τ_a and τ_d used for the prediction shown in Figure 5.5B were determined from other experiments [119, 71]. Only τ_r was fitted to the Mizuno et al. [91] data. The model predicts correctly the characteristic maximum observed in the $G'(\omega)$ obtained from the passive microrheology technique. However, the active dumbbell model can not predict, simultaneously, the frequency at which the the maximum occurs and the frequency where the discrepancy between the two moduli starts. This could be due to the very narrow relaxation spectrum of the dumbbell model in comparison with the real gel. Additional improvement in the prediction might be achieved by using a bead-spring chain with more beads, accounting for the polydispersity and non-linear elasticity of the actin filaments; these can increase the breadth of the relaxation spectrum of the gel. We note however that the predictions of the active dumbbell model are worst at lower frequencies, where the experimental observations indicates that $G'(\omega)$ goes to an elastic plateau, while the predictions continue to decay. However this discrepancy can be explained by the fact that the actomysoin gels prepared by Mizuno et al. [91] also contain biotin crosslinks, while the active dumbbell model does not contain permanent passive crosslinks, but only active crosslinks (motors).

By taking the ratio of eq.(5.9) and eq.(5.10) we can obtain the following relation for the active dumbbell model,

$$\frac{G'_{\mathrm{GK}}(\omega)}{G'_{\mathrm{D}}(\omega)} = 1 + \frac{48\tau_d}{28\tau_r + \tau_r^3\omega^2}. \tag{5.11}$$

This relation is valid for $\tau_a/\tau_d \ll 1$ and $\tau_r = \zeta_a/k_b = \zeta_d/k_b$. The second term on the right hand side of eq.(5.11) gives the deviation from the FDT. In the limit $\tau_r/\tau_d \to \infty$ this term vanishes and the FDT, $G'_{\mathrm{GK}}(\omega) = G'_{\mathrm{D}}(\omega)$, is recovered. A plot of this

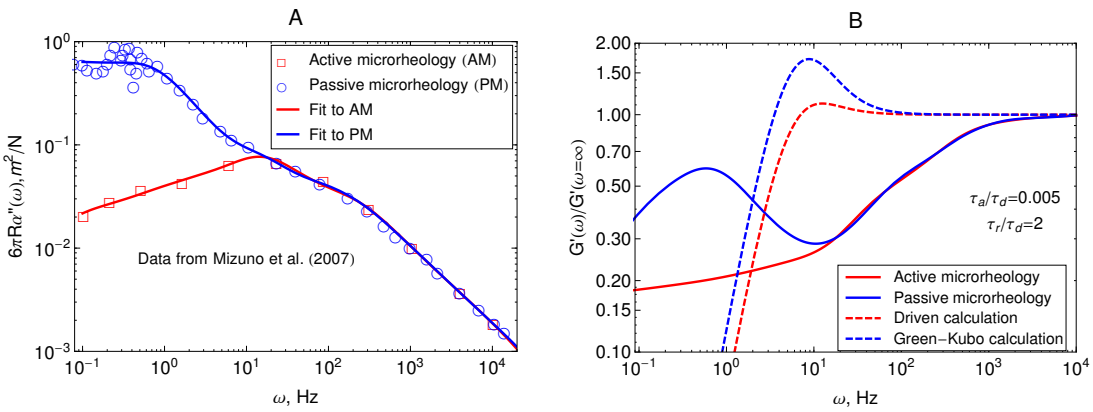

Figure 5.5. Predictions of the active dumbbell model of the dynamic modulus of active gels. A : Imaginary part of the creep compliance, $J''(\omega) = 6\pi R\alpha''(\omega)$, of an actomyosin gel measured using passive and active microrheology. The symbols are experimental results by Mizuno et al. [91] and the lines are fits used to convert J^* to G^*. B: Comparison of the storage moduli, $G'(\omega)$, predicted by the active dumbbell model with the storage moduli determined from the microrheology experiments of Mizuno et al. [91]. The parameter values used in these figures are typical for actomyosin gels, $\tau_r = \zeta_a/k_b = \zeta_d/k_b = 2\tau_d$ and $\tau_a/\tau_d = 0.005$.

relation, for different values of τ_r/τ_d, is shown in Figure 5.4B. Note that the deviation from the equilibrium FDT in eq.(5.11) is frequency-dependent and cannot, in general, be interpreted as an effective temperature. This result is in agreement with the conclusions of a recent and more general theoretical work by Ganguly and Chaudhuri [29] in which an extension of the FDT for active systems was derived. Eq.(5.11) is one of the main conclusions of this Chapter and in contrast to other models for active gels in which motor activity is accounted for by means of an effective temperature [78, 79, 80]. These latter works can not, in general, predict the correct frequency-dependent violation of the FDT due to the use of an effective temperature to model motor activity. Other works [74, 43] have used an attachment/detachment jump process to model motor dynamics. However those models were postulated on a continuum level of description, where motors are treated as force dipoles embedded within a continuum. In that picture each pole of the force dipole, representing the motor, is assumed to lie on a different filament. Those models have also been successful in

describing some of the observations in the microrheology of active gels.

The microrheology experiments of Mizuno et al. [91] can now be interpreted based on eq.(5.11). The frequency-dependent increase in the magnitude of the probe bead autocorrelation function in the passive microrheology of active gels is due to frequency-dependent stress fluctuations caused by motor activity. These fluctuations are therefore not related to the response function of the bead by the FDT. An additional, frequency-dependent term, as in eq.(5.11), is necessary to account for the magnitude and dynamics of motor activity. If such a modified FDT is used in the analysis of the passive microrheology data in active gels, it will account for frequency-dependent increase in the magnitude of the probe bead autocorrelation, yielding the same dynamic modulus obtained from the active technique. This conclusion agrees with previous works [74, 43] that have modeled the rheology of active gels on a continuum mechanics level of description but using a similar description of motor dynamics.

Other microrheology experiments in active gels [117, 91] have shown that motor-activity induces significant strain hardening of the semiflexible network. This can be observed in the statistics of bead displacements, which are Gaussian for non-active gels, but develop non-Gaussian tails when the gels are activated with ATP. The strain hardening is also observed as an overall increase in the magnitude of the dynamic modulus of the gel after addition of ATP. Since we have used a linear force law for the springs that represent the semiflexible filaments the current version of the model can not exhibit this feature. Non-linear spring force relations for semiflexible filaments [85, 98, 122] could be used to model the strain-hardening in active gels. Accounting for these physics has the potential of further improving the predictions presented in Figure 5.4B, which is explored in Chapter 6.

5.4 Buckling and contraction in active bundles

Recent experiments [71, 23] in actomyosin bundles without sarcomeric organization have shown that self-contraction, upon addition of ATP, is related to the buckling of individual F-actin filaments that form the bundle. In the experiments, individual bundles were observed and F-actin buckling was found coincident with contraction. Prior to ATP addition, compact bundles with aligned F-actin are observed. Upon ATP addition, the frequency of buckles increases rapidly during contraction, and then diminishes once contraction stops. These F-actin buckles are dynamic, with their amplitude, curvature, and location changing over time. Motor-induced buckling of actin filaments has been shown to be a ubiquitous process in the self-organization of the cellular cytoskeleton [23].

The main purpose of this Section is to compare our model and results to the other single-chain mean-field description of active gels available in the literature [71]. That model, as ours, treats the filaments as linear springs. However, as pointed in Section 5.2, there are several differences in the level of description and mathematical formulation of the two models. Here we discuss in more detail how these differences reflect in a specific observable of the model. Lenz et al. [71] specifically apply their model to study buckling and contraction in non-sarcomeric actomyosin bundles. Therefore using the model presented in Section 5.2 we calculate the fraction of buckled dumbbells, ϕ_B, as a function of time after addition of ATP in the absence of externally applied strain. Before addition of ATP the dumbbells have relaxed end-to-end length ℓ_0 . Upon addition of ATP Motor activity can change the end-to-end length of the dumbbells by an amount r. This change can cause compression ($r < 0$) or extension ($r > 0$) of the dumbbells. However F-actin filaments support large tensions but buckle easily under piconewton compressive loads [23, 115]. Therefore only dumbbells under compression ($r < 0$) buckle. A compressed dumbbell buckles when its tension $f = -k_b r$ reaches a buckling force threshold, F_B. An estimation of this force threshold can be obtained by treating the filaments as thin elastic cylinders

[115, 35] $F_B = \dfrac{k_{\rm B}T\ell_p}{\ell_0^2}$. For a typical F-actin filament, using the values presented in Section 5.2, $F_B \sim 0.1$ pN.

To proceed with the calculation of ϕ_B we set $\epsilon(t) \to 0$ in eq.(5.1) and introduce the marginal probability function $\phi(s, r, t)$,

$$\phi(s, r; t) = \int_{-\infty}^{\infty}\int_{-\infty}^{\infty} \psi(s, F_1, F_2, r; t) dF_1 dF_2 \tag{5.12}$$

To perform the integrals in eq.(5.12) we make use of the algebraic expressions for the conditional moments given in Appendix B. Here as in Section 5.3 we assume $p(F) = \delta(F - F_m)$. Using this $p(F)$ in eq.(B.1) and then putting the result into eq.(5.12) we can now take the integrals with respect to $\boldsymbol{F}$ to obtain:

$$\phi(s, r; t) \;\; = \;\; \frac{\delta_{s,0}}{4}\delta(r) + \sum_{s'=1}^{3} \frac{\delta_{s,s'}}{J_{s'}} \exp\left\{ -\frac{(r - \langle r\rangle_{s'})^2}{2(\langle r^2\rangle_{s'} - \langle r^2\rangle_{s'})} \right\}, \tag{5.13}$$

where the first and second conditional moments of r for a given s are given in Appendix B, eq. (B.9). And J is a normalization constant.

On average, filaments in motor-attachment state $s = 1$ (see Figure 5.1) undergo compression ($\langle r\rangle_{s=1} < 0$); filaments in motor-attachment state $s = 2$ experience, on average, the same magnitude of extension ($\langle r\rangle_{s=1} = -\langle r\rangle_{s=2}$). The end-to end distance of filaments in states $s = 0$ and $s = 3$ does not change, in average, due to motor activity ($\langle r\rangle_{s=3} = 0$). To find the fraction of buckled filaments eq.(5.13) is integrated over all the compressed filaments whose tension exceeds F_B and then summed over all the attachment states that is,

$$\phi_B(t) \;\; = \;\; \sum_{s=0}^{3} \int_{-\infty}^{-F_B/k_b} \phi(s, r; t) dr = \frac{1}{8}\sum_{s=1}^{3} \mathrm{erfc}\left\{ \frac{F_{\rm B} + k_b\langle r\rangle_s}{k_b\sqrt{2(\langle r^2\rangle_s - \langle r\rangle_s^2)}} \right\} \tag{5.14}$$

Eq.(5.14) gives the fraction of buckled filaments in the dumbbell as a function of time. Note that the first term on the right hand side of eq.(5.13) vanishes after performing the integral in eq.(5.14) since the end-to-end distance of the dumbbells on that attachment state does not change due to motor activity. In Figure (5.6A)

the fraction of buckled filaments is shown as a function of time, for different values of the ratio ζ_d/ζ_a. To make the calculations and plots shown here we make time dimensionless by τ_d and choose as characteristic length scale F_m/k_b. For these figure the ratio ζ_d/ζ_a is set to 0.1 and $\tau_{r,a}/\tau_d$ is set to 10. The ratio between the buckling force of the filaments, F_B, and the mean motor stall force F_m was set to 0.3, this value is inside the range observed experimentally in actomyosin networks [119, 71]. Upon addition of ATP at $t = 0$ there is a short lag time, after which the fraction of buckled filaments grows until reaching a steady state value that depends on the ratios ζ_a/ζ_d and τ_a/τ_d. The fraction of buckled filaments is never greater than 1/4, since this is the maximum fraction of filaments that can undergo compression due to motor activity. Since we have assumed $p(F) = \delta(F - F_m)$ the fraction of buckled filaments is expected to be smaller , for a given set of parameters, than in the real gel. A wider motor-force distribution will cause some filaments on attachment state $s = 3$ to also undergo compression. Qualitatively the shape of this curve coincides with the experimental observations of Lenz et al. [71]. Figure (5.6B) shows the steady state value of the fraction of buckled filaments as a function of the ratio τ_a/τ_d. It can be observed that for a given set of friction coefficients there is a critical values of the τ_a/τ_d at which buckling occurs. If, the detachment rate of the motors becomes comparable, or larger than the attachment rate then motor activity can not produce buckling of the semiflexible filaments. Here and through the rest of the Chapter it is useful to consider the limit $\tau_{r,a} \to \tau_{r,d}$ when $\tau_a/\tau_d \ll 1$, in this case the algebraic expressions simplify considerably. However, as mentioned in Section 5.2, in real systems $\tau_{r,a}$ is larger than $\tau_{r,d}$ therefore the expressions for this limit are presented only to illustrate the general features of the model, and do not represent a specific physical system. For instance, in this limit the expression for $\langle r \rangle_{s=1}$ at steady state simplifies to $\langle r(t = \infty) \rangle_{s=1} = \dfrac{F_m}{2k_b}\left(\frac{\tau_a}{\tau_d} - 1\right)$, and $\langle r^2(t = \infty) \rangle_{s=\{1,2,3\}} \to 0$. Therefore in this limit, the steady state does not depend on the friction coefficients and a filament buckles when

an effective motor force that accounts for the attachment/detachment, $\frac{F_m}{2}\left(1-\frac{\tau_a}{\tau_d}\right)$, is larger than the buckling force of the filament F_B.

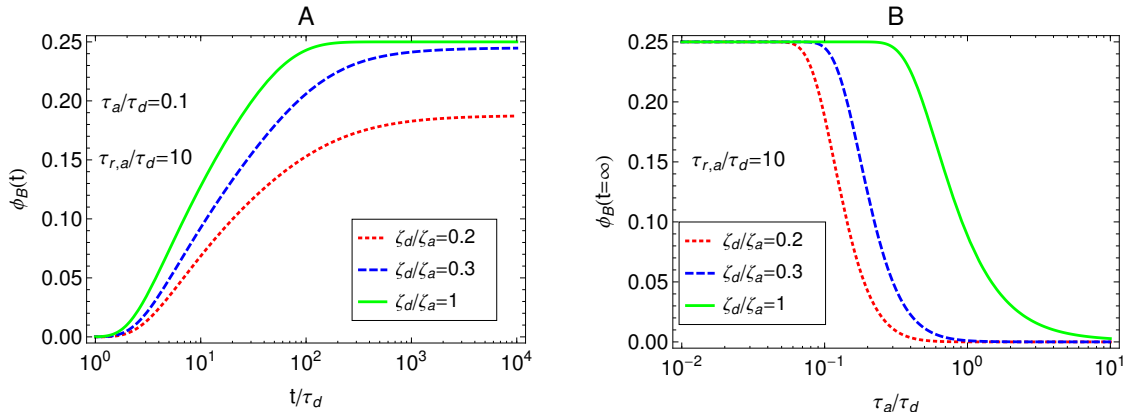

Figure 5.6. A: fraction of buckled filaments in a bundle, ϕ_B, as a function of time for different values of the ratio ζ_d/ζ_a. τ_a/τ_d was set to 0.1. B: Steady state fraction of buckled filaments as a function of τ_a/τ_d, for different values of the ratio ζ_d/ζ_a. For these plots $F_B/F_m = 0.3$ and $\tau_{r,a}/\tau_d$ was set to 10, where $\tau_{r,a} := \zeta_a/k_b$.

Some previous attempts have been made to use microscopic models to describe buckling of filaments in active bundles [71, 70], however, to our knowledge, this is the first time the dynamics of buckling formation have been calculated. This dumbbell version of our model is not sufficient to investigate the influence of motor concentration in the buckling dynamics. Lenz et al. [71] have investigated the effect of motor concentration and found that there is an optimum concentration of motors for contraction to occur. High concentrations of motors suppress buckling while very sparse motors can not generate it. We will investigate the effect of motor concentration using our model in Chapter 6. There is however a fundamental difference in how the model presented in this work and the model by Lenz et al. [71] explain the mechanisms that cause buckling and self-contraction in active bundles. In the model presented here buckling arises because a fraction of the filaments in the bundle exist in a motor attachment state where contraction is favored (eg.: state $s = 1$ for the dumbbell version). This is achieved by maintaining the motor forces as stochastic state variables

instead of pre-averaging eq.(5.1) over them. The filaments on attachment states that undergo contraction buckle when the tension in them reaches F_B. On the other hand in the model of Lenz et al. [71] buckling arises from the dependence of $p(F)$ on the position along the filament of the bead (active site) to which the motor attaches. In other words, in that model the underlying mechanism for buckling is postulated to be a spatial gradient of the motor stall forces.

5.5 Conclusions

We have introduced a single-chain mean-field model for active gels. The motors are assumed to create pair-wise active interactions between the filaments, which are taken into account by considering the probability for a motor to attach to (or detach from) the network active sites. We have postulated a minimum level of description that a single-chain mean-field model needs to reproduce the characteristic rheological and mechanical features of active gels. In the model presented here, the change in the end-to-end distance of the filaments, the attachment state of the filaments, and the motor-generated forces, are stochastic state variables that evolve according to a differential Chapman-Kolmogorov equation. The motor-generated forces are drawn from a stationary distribution of motor stall forces that can be measured experimentally [119, 71]. Most of the model parameters, which include attachment/detachment rates of motors, friction coefficients for filaments and motors, as well as parameters to characterized the elasticity of the semiflexible filaments, can be measured in independent experiments.

The general formulation of the model allows us to account for physics that are not available in models that have been postulated on coarser levels of description [74, 43, 71]. These physics include motor concentration in the gel, non-linear elasticity of the semiflexible filaments and attachment/detachment rates dependent on the local filament tension. However, to simplify the mathematics and with the aim of ob-

taining analytical results here we have made several assumptions. We have assumed that motors attach only at the ends of the filament, this means we have represented the filaments as dumbbells. This is expected to be a reasonable approximation only in the limit of very low motor concentration. We have also assumed that the semi-flexible filaments obey a linear elasticity law; again this is expected to be a reasonable assumption only in the limit of very low motor concentration where strain hardening is negligible. Additionally we have assumed that the attachment/detachment transition rates are independent of the local filament tension. In a Chapter 6 we present numerical results for a more general version of the model, where we examine the effect of relaxing some of the aforementioned assumptions.

We have shown that in its simplest form, the active dumbbell model, can qualitatively reproduce characteristic rheological and mechanical properties of active gels. For instance, the model can predict the buckling of individual filaments that is thought to be the underlying mechanism in the self-contraction of non-sarcomeric actin-mysoin bundles [71, 119]. We have calculated the dynamics of buckling formation and found that they are mostly determined by the ratio of the friction coefficients of the filament to that of the motors. In general, buckling occurs if the ratio of detachment/attachment rates is below a critical value that is determined by the buckling force of the filaments, the mean motor stall force and the friction coefficients of filaments and motors. The active dumbbell model can also predict the violation of the fluctuation-dissipation theorem observed in microrheology experiments in active gels [91]. We calculated and compared the dynamic modulus, of a network composed by active dumbbells, obtained from the autocorrelation function of stress at the non-equilibrium steady state and from the stress response after applying a small oscillatory strain. If the fluctuation-dissipation theorem were obeyed the two moduli would be equal [53, 109, 14]. We find that for the active dumbbell model there is a frequency-dependent discrepancy between the moduli obtained from the two different

methods. This discrepancy is in general determined by the attachment and detachment rates, as well as by the friction coefficients. When the ratio between the local relaxation time scale and the detachment time of the motors becomes very large, the FDT is recovered. In this limit, the dynamics of the system are completely dominated by the local relaxation of the filaments, and motor attachment/detachment dynamics have a negligible effect.

CHAPTER 6

THE ROLE OF FILAMENT LENGTH, FINITE-EXTENSIBILITY AND MOTOR FORCE STATISTICS IN STRESS RELAXATION AND BUCKLING MECHANISMS IN NON-SARCOMERIC ACTIVE GELS

6.1 Introduction

Active gels are networks of semiflexible polymer filaments driven by motor proteins that can convert chemical energy from the hydrolysis of adenosine triphosphate (ATP) to mechanical work and motion. Active gels perform essential functions in living tissue including motions, generation of forces and sensing of external forces. The cell cytoskeleton is an active gel composed of many different types of filaments and motors that performs most of the mechanical functions of cells. Moreover, active gels play a central role in driving cell division and cell motility [23, 118, 94]. Active gels have also been successfully prepared *in vitro* to study their mechanical and rheological properties [117, 8, 91].

In active gels, molecular motors assemble into clusters with a rigid, roughly cylindrical, backbone and groups of binding heads on both ends that can attach to active sites along semiflexible filaments [49, 46]. These clusters of motor proteins constitute the active component of active gels. In the absence of ATP motor clusters act as passive cross-links between the semiflexible filaments. In the presence of ATP molecular motors can walk along the filaments. The direction in which motors move is determined by the filament structural polarity [127, 56]. A molecular motor starts "walking" when an ATP molecule attaches to a binding head domain of the motor protein, which causes it to detach from the filament. Using the chemical energy from the hydrolysis of ATP the detached motor head moves towards the next attachment site along the filament contour and reattaches, in a process known as the Lymn-Taylor cycle [81]. Each motor has at least two clusters of binding heads performing this same process. However, both of them do not necessarily detach at the same time. When

the binding heads on one end of the motor are detached and moving towards the next attachment site, the heads on the other end can be attached to a different filament. This filament will feel a force due to the motion of the motor. Therefore, in a network molecular motors can generate active, pair-wise interactions between filaments.

The forces generated by the motors when they move along the filament are a function of the chemical potential difference between ATP and its hydrolysis products. *In-vivo* molecular motors operate far from equilibrium. In typical active gels found in living cells the difference in chemical potential between ATP and its hydrolysis products is on the order of $10k_{\mathrm{B}}T$ [55, 56]. Examples of molecular motors that have been extensively studied are myosin which moves along actin filaments; and kynesin and dynesin which move along microtubules. Each type of motor protein has particular characteristics that determine its function inside the cytoeskeleton. For instance the duty ratio of mysosin (ratio of attached to unattached time) increases with decreasing ATP concentration, when motor release induced by ATP binding becomes the rate-limiting step in the Lymn-Taylor cycle [81, 91]. Non-equilibrium motor activity appears when the motors switch from a non-processive mode, which cannot generate forces between filaments, to a processive tension-generating mode. In addition, the processing time of different myosin isoforms have different sensitivity to tension [93]. It has been recently shown that Myo1b is very sensitive to tension, where forces > 0.5 pN cause the motor to transform from a low-duty-ratio motor with attachment times < 1 s to a high-duty-ratio motor with attachment times > 50 s [111]. On the other hand Myo1c is far less sensitive to force than Myo1b enabling it to power motility over a range of forces.

The semiflexible filaments that form active gels, such as actin and tubulin, are characterized by having a persistence length (length over which the tangent vectors to the contour of the filament remain correlated) that is much larger than the size of

a monomer, and larger than the mesh size of the network, but typically smaller than the contour length of the filament. For instance, for filamentous actin (F-actin) the persistence length is around 10 μm, while the mesh size of actin networks is estimated to be approximately 1 μm. [85, 34, 115] This sets them apart from flexible networks where the persistence length of the polymeric chains is much smaller than the mesh size of the networks formed by those chains. An important mechanical characteristic of semiflexible networks is that they exhibit significant strain hardening for modest strains. A tension of a few pN can increase the modulus of a semiflexible network by a factor of 100 [85, 34]. This capacity of biological gels to stiffen as they are strained allows them to prevent large deformations that could threaten tissue integrity.

Recent advances in experimental techniques have allowed the characterization of mechanical and rheological properties of active gels. For instance an important mechanical feature of active gels that has been extensively studied experimentally, is their capacity of self-contraction and self-organization [71, 119, 23, 65, 63]. These mechanical features of active gels play a central role in cell division and motion. For instance, a widely studied active gel is the actin cortex, which is a disordered network of F-actin decorated with myosin II motors. Changes in cell shape, as required for migration and division, are mediated by the cell cortex, a thin shell of cross-linked F-actin bound to the inner layer of the plasma membrane. Myosin II motors drive contractility of the cortical actin network, enabling shape change and cytoplasmic flows underlying important physiological processes such as cell division, migration and tissue morphogenesis [94].

Several works have used a continuum-mechanics level of description to model self-organization [64, 2] and rheology [79, 12, 33] of active gels and fluids. More microscopic models have described active gels using a master equation for interacting polar rods; Aranson and Tsimring [2] presented analytic and numerical results for

rigid rods, later Head et al. [42] presented more detailed numerical simulations that account for filament semiflexibility. These models have been very successful in describing large scale phenomena such as the formation and dynamics of cytoskeletal patterns (eg.: asters, vortices). The latter work also investigated the effect of motor attachment/detachment rates on the predictions of the super-diffusive mass transport typical of active gels. However, the precise microscopic mechanisms underlying this process are still the subject of considerable experimental and theoretical investigation. Recently, a microscopic single-filament mean-field model to describe myosin-induced contraction of non-sarcomeric F-actin bundles was postulated by Lenz et al. [71]. In this work we use a similar description. However there are several issues in the level-of-description and mathematical formulation of Lenz et al. [71] which were discussed in Chapter 5.

Rheological experiments in active polymeric networks have revealed fundamental differences from their passive counterparts. Some of the differences are not surprising given that these are materials in which molecular motors continuously convert chemical energy into mechanical work. Recent microrheology experiments [8, 117, 91] on active gels have shown that the fluctuation-dissipation theorem (FDT) and the generalized Stokes-Einstein relation (GSER) are violated in active gels. The FDT is a central part of data analysis of passive microrheology experiments, where it is used to relate the position fluctuations of the probe bead to a frequency-dependent friction coefficient, from which, using a generalized Stokes relation rheological properties can be extracted [51, 15, 108]. The violation of FDT is observed as a frequency-dependent discrepancy between the material response function obtained from active and passive microrheology experiments. In the active experiments an external force is applied to the probe bead and the material response function is calculated from the bead position signal [108]. In passive microrheology experiments, no external force is applied, and the material response function is calculated from the bead position

autocorrelation function using the FDT [91]. Other microrheology experiments in active gels also indicate that the activity of molecular motors can produce significant strain hardening of the active networks. For instance non-Gaussian statistics of the probe bead position have been observed [117] in beads embedded in gels made to mimic the cytoskeleton. In other passive microrheology experiments a decrease in the overall magnitude of the the probe-bead power-spectral density and a slow-down of stress relaxation was observed after addition of ATP [91] to an actomyosin gel.

A considerable amount of work has been devoted to deriving simple generalizations or extensions of the FDT for out-of-equilibrium systems, such as active gels [102, 10, 29]. In general, these extensions of FDT to out-of-equilibrium systems model the non-equilibrium forces as Brownian forces, but introduce an effective temperature [78, 79, 80, 97], which is higher than the real temperature and is meant to account for the larger magnitude of the non-equilibrium fluctuations. This kind of approach can not explain the observations in the microrheology experiments in active gels [91] since Brownian forces alone can not produce a frequency-dependent discrepancy between the material response obtained from the material's spontaneous stress fluctuations, and the material response obtained by applying a small external perturbation and observing the material response. Other works [74, 43] have modeled the attachment/detachment dynamics of motor forces as a stochastic jump process. This approach has been successful in describing some of the features observed in the microrheology experiments of active gels, such as diffusive and superdiffusive behavior of tracer beads at frequencies where storage modulus of the gel has plateau behavior. However these models assume that the motors do not interact through the strain field in the network and neglect strain hardening. Given the level of description of such models, removal of these assumptions is difficult; therefore more microscopic models seem necessary to elucidate the specific effect that these physical features have on the rheology of active gels.

In Chapter 5 we introduced a single-chain mean-field model for active gels. We proposed a level of description with the minimum set of components necessary to predict mechanical and rheological features that have been observed in active gels. In that work we considered dumbbells, meaning that we had only two beads per filament. The filaments were modeled as Fraenkel springs, and the motor force distribution was made a Dirac delta function centered around a mean motor stall force. Those assumptions allowed us to obtain analytical expressions for several observables of the model, such as relaxation modulus and fraction of buckled filaments.

The main objective of this Chapter is to relax some of the assumptions of the model presented in Chapter 5. More specifically, we consider bead-spring chains with multiple beads, explore the effect of finite-extensibility of the filament segments and incorporate into the model motor force distributions that have been measured experimentally. In that form the model can no longer be solved analytically and we therefore use numerical simulations. In Section 6.2 we give a detailed description of the model, and discuss the main assumptions, and parameters. We generalize the proposed differential Chapman-Kolmogorov equation to the case of multiple beads and give the expressions for the finite-extensibility of the strands and the motor force distributions. We also discuss the numerical solution of the model and provide checks of the numerical algorithm used to solve the model against analytic solutions that can be obtained in special cases. In Section 6.3 we present predictions of the dynamic modulus of active gels using the active single-chain mean-filed model. The effect of multiple beads and finite extensibility of the strands in the relaxation spectrum of the active gel is discussed. We show that the the model can predict the violation of the FDT observed in microrheology experiments of active gels [91]. This is done by comparing the dynamic modulus of the gel obtained from the autocorrelation function of stress at the non-equilibrium steady state, with the modulus obtained from the stress response when a small perturbation is applied to the gel. In Section 6.4 we discuss

transport of filaments in an active gel using our model. We do this by following the mean-squared displacement of the probe filament center at the non-equilibrium steady-state. In Section 6.5 we illustrate the use of the model to describe the underlying mechanisms of self-contraction in active non-sarcomeric F-actin bundles. Here we specifically focus on the effect that the density of active crosslinks along the filament has on the fraction of buckled filaments and present predictions that show the relation between filament buckling and contraction of non-sarcomeric actomyosin bundles.

6.2 The active single-chain mean-field model

In this section we describe a single-chain mean-field model for an active bundle. Active networks are formed by semiflexible filaments and motor clusters (hereafter simply called motors) that form active cross-links between filaments (Figure 6.1A). For instance myosin II thick filaments, which cross-link actin, are $\sim 1.5\mu$m in length and contain $\sim$ 400 attachment heads [94]. In the presence of ATP, motors will go through detachment/attachment cycles [81] in which they detach from one filament and take nanometer-sized steps towards a direction determined by the filament's structural polarity, therefore exerting a force on the filament to which they remain attached. Our model follows a single probe filament (illustrated in gray in Figure 6.1B) and approximate its surroundings by an effective medium of motor clusters that attach and detach from specific sites along the probe filament. The motors are assumed to form pair-wise interactions between filaments. When a motor is attached to the probe filament it is detached and steps forward on another filament in the mean-field and therefore pulls/pushes on the probe filament. The formulation of temporary network models provides a very useful mathematical and conceptual framework to model this dynamics [44, 54, 53]. In Figure 6.1B a probe filament is shown in more detail, each bead represents a site along the filament where a motor can attach, and the springs represent the filament segments between this active sites. In this Chapter we

consider the case of multiple beads. The motors create the type of pair-wise active interactions between the bead-spring chains described above. To model these interactions we use a mean-field approach, in which filaments have certain probabilities to undergo a transition from one attachment/detachment state into another depending on the state of the particular filament.

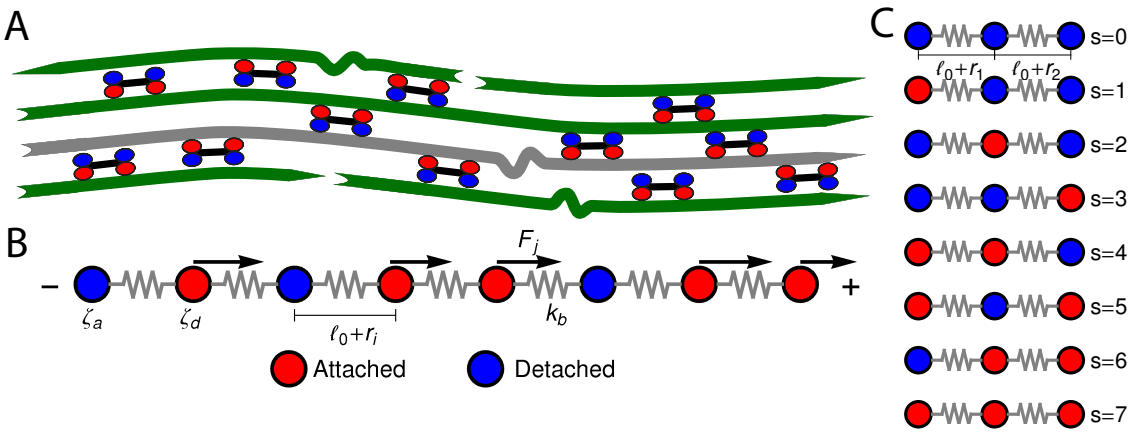

Figure 6.1. Sketch of the single-chain mean-field model for active gels. A: Active bundle formed by polar filaments and motors (which can move towards the barbed end of the filaments). Motors attach and detach from the filaments. After detaching from a given filament a motor will step forward in that filament and will exert a force on the other filament where it is still attached. The gray filament indicates a probe filament whose dynamics are followed by the model. B: The probe filament is represented by a bead-spring chain. Red beads represent attachment sites in the filament where a motor is attached, ζ_a is the friction coefficient of those beads. Blue beads represent sites in the filaments where no motor is attached ζ_d is the friction coefficient of those beads. ℓ_0 is the rest length of the strands before addition of ATP; r_i is the change in the end-to-end distance of a strand due to motor activity. F_j is a motor-generated force acting on bead j. Motors generate a force on the filament only when attached. C: Sketch of the attachment/detachment states of a three-bead version of the model ($N = 3$). The attachment/detachment states model the interaction of the probe filament with the mean field.

It is convenient to represent the attachment state by a single number s; by allocating number 0 to free beads and 1 to beads attached to a motor. In the following, the number 0 or 1 assigned to bead j on the chain in an attachment state is denoted by $n_j(s)$. By definition, s takes one of the values $0, 1, ..., 2^N (= s_{\max})$, where N is the

number of beads. For example, s is equal to 0 for a chain whose beads are all free (*i.e.*, $n_j(0) = 0$ for all j) and $s = s_{\max}$ for a chain whose all beads are attached (*i.e.*, $n_j(s_{\max}) = 1$ for all j). Figure 6.1 illustrates the labeling of the attachment states for a chain with three beads.

We assume that before addition of ATP the distance between non-processive motors (acting as passive cross-links) is given by ℓ_0. This is the rest length of the filament segments and therefore there is no tension in the filaments before addition of ATP. For instance, if an actin network is formed in the presence of high concentrations of myosin the resulting cross-link density is higher and ℓ_0 smaller than in the same network formed under lower concentrations. In typical actin networks prepared in-vitro ℓ_0 is on the order of 1μm [34, 115]. After addition of ATP the motors (cross-links) become active and start detaching from and reattaching to the beads. τ_d is the average time a motor spends attached to a bead before detaching from it, whereas the average time a motor spends detached before reattaching is given by the model parameter τ_a. The force generated by a motor attached to bead j will be denoted F_j. Molecular motors can only move in one direction along the filament, determined by the filament's polarity. Filaments are thus expected to move in the opposite direction. In this single-chain description we introduce this asymmetry by making all the forces F_j, that the motors exert on the beads of a given filament, have the same sign (either positive or negative). Another force acting on the filament is the viscous drag from the surrounding solvent (which is mainly water for biological networks). The frictional force from the surrounding solvent is characterized by a friction coefficient. Bulky motor cluster (*i.e.*: 1.5μm for myosin II thick filaments) increase the friction coefficient of the filament when attached to an active site. Therefore this friction coefficient is allowed to take two different values: ζ_a when attached, and $\zeta_d < \zeta_a$ if there is no motor attached to that bead. The change in the end-to-end length of a filament segment due to the action of the motors is denoted r_i.

The following state variables (level of description) are used to construct the model of the active dumbbell $\Omega : \{s, \boldsymbol{F}, \boldsymbol{r}\}$. Where $\boldsymbol{F} := \{F_1, F_2, F_j, ...F_N\}$ is a vector that contains the motor forces for all the beads and $\boldsymbol{r} := \{r_1, r_2, r_i, ...r_{N-1}\}$ is a vector that contains the change from the rest length in the end-to end distance of all the strands due to motor forces. Now let $\psi(\Omega)$ be the distribution function describing the probability of finding an active filament in state s with strands with a change in their end-to-end distance $\boldsymbol{r}$ due to motor forces $\boldsymbol{F}$ at time t. The time evolution for $\psi(\Omega)$ is given by the following differential Chapman-Kolmogorov equation:

$$\begin{aligned} \frac{\partial \psi(\hat{\omega}, \boldsymbol{r}; t)}{\partial t} &= \sum_{i,j=1}^{N-1} \frac{\partial}{\partial r_i} \Bigg\{ \psi(\hat{\omega}, \boldsymbol{r}; t) \Bigg[- \dot{\epsilon}(t) r_j + A_{i,j}(s) f(r_j) \\ &- \frac{(F_{j+1} - F_j)\, \delta_{i,j}}{\zeta_a} \Bigg] \Bigg\} + \sum_{s'=0}^{s_{\max}} \int \mathbb{W}_{s,s'}(\hat{\omega}|\hat{\omega}') \psi(\hat{\omega}', \boldsymbol{r}; t) d\boldsymbol{F} \end{aligned} \tag{6.1}$$

where $\hat{\omega} : \{s, \boldsymbol{F}\}$ is a subspace of Ω, $\epsilon(t)$ is an externally applied strain in the direction of filament alignment and $f(r_j)$ is the spring force. For linear springs $f(r_j) = -k_b r_j$. The linear spring constant for inextensible (ie.: fixed contour length ℓ_c) semiflexible filaments [82] is given by $k_b = \dfrac{3\pi^3 k_{\mathrm{B}} T \ell_p^2}{\ell_0^4}$. The rest length ℓ_0 is related to the contour length by $\ell_0 = \ell_c - \dfrac{\ell_0^2}{\pi \ell_p}$. For F-actin filaments, the persistence length, ℓ_p, is approximately 10 μm and $\ell_0 \sim 1\mu$m and therefore k_b is on the order of 1 μN/m. However approximating the filament segments (strands) as Fraenkel springs is only expected to be valid for very small deviations from the relaxed length ℓ_0. We discuss other, more accurate, expression for $f(r_j)$ below.

The matrix $A_{i,j}(s)$, in eq.(6.1) gives the connectivity of the beads as a function of the motor-attachment state, s, and is defined as,

$$A_{i,j}(s) = -a_i(s)\delta_{i,j-1} + [a_i(s) + b_i(s)]\delta_{i,j} - b_i(s)\delta_{i,j+1} \tag{6.2}$$

where $a_i(s)$ and $b_i(s)$ are given by,

$$\{a_i(s), b_i(s)\} = \begin{cases} \left\{\frac{1}{\zeta_a}, \frac{1}{\zeta_a}\right\} & \text{if} \quad \{n_i(s), n_{i+1}(s)\} = \{1,1\} \\ \left\{\frac{1}{\zeta_d}, \frac{1}{\zeta_a}\right\} & \text{if} \quad \{n_i(s), n_{i+1}(s)\} = \{0,1\} \\ \left\{\frac{1}{\zeta_a}, \frac{1}{\zeta_d}\right\} & \text{if} \quad \{n_i(s), n_{i+1}(s)\} = \{1,0\} \\ \left\{\frac{1}{\zeta_d}, \frac{1}{\zeta_d}\right\} & \text{if} \quad \{n_i(s), n_{i+1}(s)\} = \{0,0\}. \end{cases} \tag{6.3}$$

As stated above, ζ_a is the friction coefficient of a bead when a motor is attached to it and ζ_d is the friction coefficient when there is no motor attached to it. For instance, several experimental measurements [119, 71] have shown that myosin II motors move along actin filaments at approximately $0.5 - 1$ μm/s, they have an average stall force of 1 pN; therefore ζ_a is estimated to be around 1 $\mu\text{N}\cdot\text{s/m}$. ζ_a is expected to be larger than ζ_d since the motor attachment heads increase the cross-sectional area of the actin filament when they attach to it. Additionally to τ_a and τ_d it is convenient to label two additional time scales of the model $\tau_{r,a} = \zeta_a/k_b$ and $\tau_{r,d} = \zeta_d/k_b$ which are local relaxation times of the filament when a motor is attached to it and when there is no motor attached to it respectively. For myosin motors in actin gels τ_d is on the order of 100 ms while τ_a is usually between an order to two orders of magnitude smaller [71, 74]. Therefore in a typical active gel $\tau_a < \tau_d \leq \tau_{r,d} < \tau_{r,a}$ is expected.

In Chapter 5 we treated the strands between motors as linear springs to be able to obtain analytic solutions of the model. However semiflexible filaments are known to strain harden under a tension of a few pN, which motors are known to generate. The end-to-end, ℓ, versus tension, f, behavior of semi-flexible filaments has been the subject of extensive theoretical and experimental study during the last four decades [24, 85, 82, 122]. Given the importance of such relations to accurately model biological networks the elasticity of semiflexible filaments is still the object of ongo-

ing experimental and theoretical work. In bead-spring simulations an interpolation formula developed by Marko and Siggia [85] that approximates the force-extension curve of inextensible (ie.: fixed contour length ℓ_c) semiflexible filaments is commonly used [121, 122],

$$f(r) = -k_{\mathrm{WLC}} \left\{ r + \frac{\ell_c}{4(\ell_0/\ell_c + r/\ell_c - 1)^2} - \frac{\ell_c}{4(\ell_0/\ell_c - 1)} \right\}. \tag{6.4}$$

Where ℓ_0 is the rest length and r is the deviation from ℓ_0. The end-to-end length vs tension curve given by eq.(6.4) displays a linear regime for small tensions f and in the limit of strong stretching approaches ℓ_c with a characteristic saturation $\sim -f^{-1/2}$ (see Figure 6.2). Polymeric filaments that display this characteristic behavior are usually referred to as wormlike chains [24, 85, 82] (WLC). Note that since to linear order in r eq.(6.4) must match the behavior of the Fraenkel springs k_b and k_{WLC} are related by $\dfrac{k_{\mathrm{WLC}}}{k_b} = \dfrac{2(\ell_c - \ell_0)^3}{2(\ell_c - \ell_0)^3 + \ell_c^3}$.

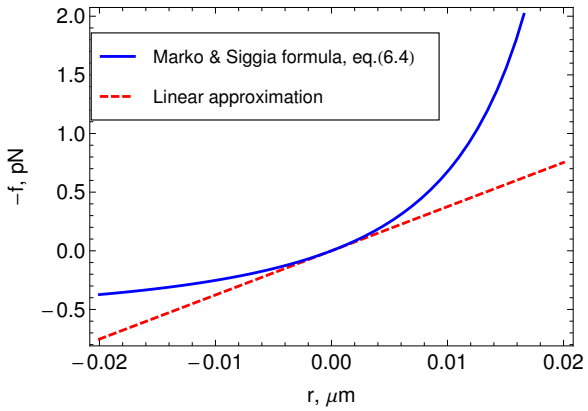

Figure 6.2. Relation between tension f and the deviation r from the rest-length ℓ_0 in a semiflexible filament as predicted by the wormlike chain model. The plot shows the linear approximation to it, and the Marko and Siggia [85] formula, eq.(6.4). The plot is made for values of the parameters typical of actin filaments in a network ℓ, $\ell_p = 10\mu$m $\ell_0 = 1\mu$m.

In our model, a filament of end-to-end length ℓ_f is constructed by connecting $N-1$ segments of rest length ℓ_0 through the connectivity matrix $\boldsymbol{A}(s)$. We assume a single value for ℓ_0. In real systems a distribution of ℓ_0 is expected, even if the strands

have the same ℓ_c. Initial cross-linking by non-processive motors of the thermally undulating filaments can create local pair-wise separations that differ from the zero-force end-to-end lengths of the filaments. Storm et al. [115] have performed a detailed analysis of ℓ_0 distributions and their effect in the mechanical response of semiflexible networks. We also assume that the tension in each segment as a function of r is given by eq. (6.4), or its linearized version. This assumption implies that the end-to-end length vs tension relation does not couple the strands (filament segments), the tension in each strand only depends in its own deviation from the relaxed length and not on the state of the other segments in the chain. However in the real WLC the tension in a particular strand depends on the orientation of the other segments in the chain.

A more accurate bead-spring chain discretization of the WLC would include bending potentials between the springs which introduce correlations between the strands' orientations. The approximation without bending potentials is expected to work best when the end-to-end length of the segment represented by a spring is larger than the persistence length of the filament [122]. More accurate bead-spring chain descriptions of semiflexible filaments include, in addition to finite extensibility of the strands, bending potentials between the springs. Recently a theoretical framework that allows one to systematically obtain coarse-grained models for semiflexible filaments was proposed [62]. This framework has been used to construct a bead-spring model for the WLC that incorporates quadratic penalties for stretch, shear, and bending deviations as well as coupling between the bend and shear degrees of freedom of the free energy of the chain [61]. That model allows for discretization at any segment length while still remaining accurate at shorter length-scale.

The transition rate matrix $\mathbb{W}(\hat{\omega}'|\hat{\omega})$ in eq.(6.1) contains the transition rates between attachment/detachment states. To construct $\mathbb{W}(\hat{\omega}'|\hat{\omega})$ a matrix $\mathbb{K}(l)$ of di-

mensions $2^l \times 2^l (l = 1, ..., N)$ is first generated by an iterative procedure:

$$\mathbb{K}(l) = \begin{pmatrix} \mathbb{K}(l-1) & \frac{1}{\tau_d} \prod_{i=1}^{N} \delta(F_i') \boldsymbol{\delta}(2^{l-1}) \\ \frac{p(F_l')}{\tau_a} \prod_{(i \neq l)=1}^{N} \delta(F_i') \boldsymbol{\delta}(2^{l-1}) & \mathbb{K}(l-1) \end{pmatrix}. \tag{6.5}$$

Where $\mathbb{K}(0) = 1$, $\delta(...)$ is the Dirac delta function and $\boldsymbol{\delta}(2^l)$ is an identity matrix of dimensions $2^l \times 2^l$. Then $\mathbb{W}(\hat{\omega}'|\hat{\omega})$ is defined in terms of $\mathbb{K}(l)$ as,

$$\mathbb{W}(\hat{\omega}'|\hat{\omega}) = \begin{cases} \mathbb{K}_{s',s}(N) & \text{if} \quad s' \neq s \\ -\sum_{s''(\neq s)=0}^{s_{\max}} \mathbb{K}_{s'',s}(N) & \text{if} \quad s = s'. \end{cases} \tag{6.6}$$

The block matrix at the upper-left or lower-right block element of $\mathbb{W}(\hat{\omega}'|\hat{\omega})$ represents the transition rate matrix of a chain having $N - 1$ beads, whereas the upper right and lower left elements stand for the detachment and attachment rates of motors in the Nth bead, respectively.

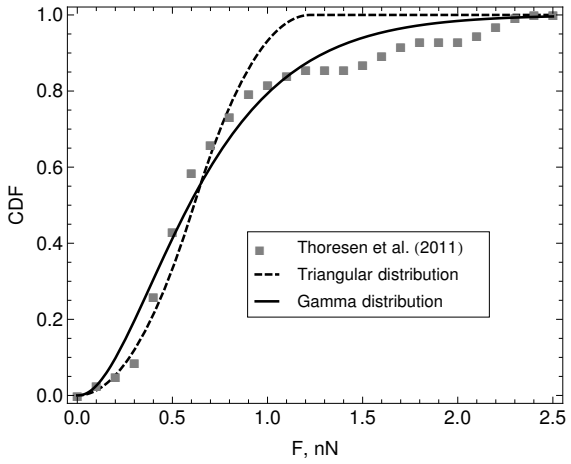

Figure 6.3. Cumulative distribution function (CDF) of myosin-generated forces in an actomyosin bundle. Symbols represent experimental data reported by Thoresen et al. [119]. The lines are fits to the cumulative distribution function of analytic probability distributions used to incorporate $p(F)$ in the model. From this distribution we find that the mean motor stall force for a myosin thick filament is approximately $F_m = 0.7$nN with standard-deviation given by $\delta F_m = 25$nN.

The function $p(F)$ is the probability density from which a motor force is drawn every time a motor attaches to a bead. In eq. (6.6) the subindex j indicates the

bead to which the motor attaches. Motor force distributions have been measured experimentally in actomyosin bundles [119, 71]. In Chapter 5 we assumed that the motor force distribution was given by a delta function centered around the mean-motor stall force that is $p(F) = \delta(F - F_m)$. where F_m is the mean motor-stall force. This assumption allowed us to proceed with the analytic solution of the model. However a more realistic shape of these motor force distributions can be incorporated into the model. Figure 6.3 shows the cumulative probability function of myosin motors in an actin bundle [119]. To incorporate this distribution in the model we fit the experimental data with either a triangular distribution (for fast, preliminary calculations) or with a Gamma distribution (for final, quantitative calculations). The first moment of this distribution is approximately $F_m = 0.7$nN and with standard-deviation, for the distribution shown in Figure 6.3 of approximately $\delta F_m = 0.25$nN. We assume that the motor force distribution is independent of time, or that it is stationary, this is expected to be a good assumption as long as the kinetics of the ATP $\rightarrow$ work reaction in the motors are much faster than any of the time scales in the model. To summarize, we use a single-filament model of the active gel where binary active crosslinks with other filaments are accounted for by a mean-field of motors that undergo transitions between attachment states determined by the phenomenological parameters τ_a, τ_d and $p(F)$ all found by independent experiments.

In this work a numerical algorithm derived from the proposed differential Chapman-Kolmogorov equation, eq.(6.1), is used to simulate an ensemble of filament trajectories [44] from which moments of the probability density $\psi(\Omega)$ can be calculated. In Chapter 5 we presented analytic solutions for a dumbbell (two beads) version of the model with several simplifying assumptions. Even for chains with more than two beads the numerical solutions can be checked against analytic solutions that can be obtained in specific cases. For instance, Figure 6.4A shows a comparison between the fraction of filaments in attachment state s (*i.e.*, $\int \psi(\Omega) d\boldsymbol{F} d\boldsymbol{r}$) obtained

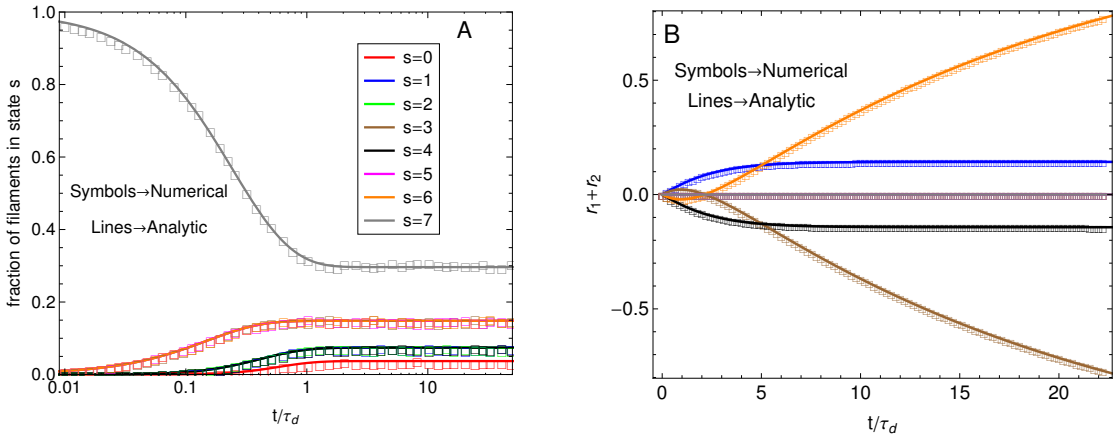

Figure 6.4. Check of the numerical algorithm used to solve the model against analytical solutions in particular cases. The procedure is illustrated for a filament with three beads (attachment states illustrated in Fig. 6.1C). A: Motor forces are turned off and the jump process between attachment states is checked against an analytic solution for the fraction of filaments in each attachment state. For the example shown the parameters were set to $\tau_a = 0.5$, $\tau_d = 1$. B: The jump process between attachment states is turned off and predefined values for the motor forces are specified. The numerical solution for $\sum_{i=1}^{N-1} r_i$ is checked against the analytic solution of the resulting deterministic equation for each attachment state. For the example shown the parameters were set to $\tau_{r,a} = 20$, $\tau_{r,d} = 2$, $\boldsymbol{F} = \{1, 2, 1\}$, $k_\mathrm{b} = 1$.

from a simulation where all motor forces are turned off and the analytic solution that is obtained for that particular case. The calculations were performed for the three-beads chain (attachment states illustrated in Figure 6.1C). Figure 6.4B shows a check of the numerical algorithm in the other case where analytic solutions are attainable. That is, when the jumps between attachment states are turned off and the motor forces for all beads are made equal to F_m. In that case the model reduces to a system of deterministic ordinary differential equations. The two calculations shown in Figure 6.4 confirm all terms in eq.(6.1) which is why these two particular checks were chosen. In general we find that to obtain convergence it is sufficient to set the value of the time step a factor of 10 times smaller than the smallest characteristic time scale of the system, taking relaxation times of the segments, attachment/detachment time scales into account.

Note that in the model presented here $p(F)$ is bead independent in contrast to the model by Lenz et al. [71]. In that model the motor force distribution depends on the position along the filament of the bead to which the motor is attached. In other words in that model the underlying mechanism for buckling is postulated to be a spatial gradient of the motor stall forces. Physically this assumption can be interpreted as the motors having spatial memory and being able to identify the particular position along the filament to which they are attaching. Presumably this pre-averaging and its related assumptions are done to simplify the mathematics; however this leads to several issues in the solution and interpretation of the model predictions that have not been clearly resolved. We do not make such assumptions. Instead $\boldsymbol{F}$ is kept as a stochastic state variable, $p(F)$ is the same for all motors, and the transition rates depend on this motor force distribution. In other words, our model exists at a more detailed level of description than the model of Lenz et al. [71]. In Section 6.5 we will discuss the implications that these conceptual differences between the two models have in the explanation of the mechanisms underlying buckling and self-contraction in active gels. In Sections 6.3, 6.4 we use the active single-chain mean-field model to describe some of the rheological and mass transport properties that have been observed in active gels.

6.3 Dynamic Modulus of Active Gels

6.3.1 Introduction. To test the validity of FDT in active gels, Mizuno et al. [91] compared the complex compliance of actin-myosin networks measured with active and passive microrheology. In the active experiment they used an optical trap to apply a small-amplitude oscillatory force to the bead, $\boldsymbol{f}^{\text{trap}} = A\cos\,\omega t\;\boldsymbol{\delta}_x$, where A is the amplitude, ω is the frequency and $\boldsymbol{\delta}_x$ is the unit vector in the direction of the applied force. The complex compliance, $\alpha(\omega)$, is obtained form the relation $\langle \boldsymbol{r}_{\text{b}}(\omega)\rangle = \alpha(\omega)\boldsymbol{f}^{\text{trap}}$. Where $\boldsymbol{r}_{\text{b}}(\omega)$ is the measured probe bead position, which can

also be written as $\langle \boldsymbol{r}_{\rm b}(\omega)\rangle = A\left[\alpha'(\omega)\cos\,\omega t + \alpha''(\omega)\sin\,\omega t\right]\boldsymbol{\delta}_x$. Where $\alpha'(\omega)$ characterizes the elastic response of the medium, in phase with the applied force, and $\alpha''(\omega)$ characterizes the viscous response, out of phase with the applied force. In a passive microrheology experiment no external force is applied to the bead or a static harmonic trap is used to hold the bead near its equilibrium position and the imaginary part of $\alpha(\omega)$ is obtained using the FDT, $\alpha''(\omega) = \dfrac{\omega}{6k_{\rm B}T}C(\omega)$. Where $C(\omega) = \int_{-\infty}^{\infty}\langle \boldsymbol{r}_{\rm b}(t)\cdot\boldsymbol{r}_{\rm b}(0)\rangle e^{-i\omega t}dt$ is the autocorrelation function of the bead position [15, 51]. Before addition of ATP the complex compliance of the actin-myosin network obtained with the passive and active techniques were identical. In gels activated with ATP a frequency-dependent discrepancy between the complex compliance obtained from the passive and active experiments appears at frequencies below 10Hz. This discrepancy is due to a frequency-dependent increase in the magnitude of the bead fluctuations observed in the passive microrheology experiment, in the actin-mysosin gels activated with ATP. These increased fluctuations have been linked to motor activity [43, 74, 68]. Since the FDT does not account for motor activity, the complex compliance calculated from these fluctuations using the FDT does not agree with the complex compliance obtained from the active experiment.

Figure 6.5A shows the imaginary part of the complex compliance $J''(\omega) = 6\pi R\alpha''(\omega)$ of the actomyosin gel studied by Mizuno et al. [91]. The complex compliance, $J^*(\omega)$, is related to the dynamic modulus, $G^*(\omega)$, by $J^*(\omega)G^*(\omega) = 1$. The symbols are experimental data obtained using passive and active microrheology, while the lines are fits used to transform $J^*(\omega)$ to $G^*(\omega)$. The data were taken at steady state after addition of ATP to the actomyosin network. Part B of Figure 6.5 shows the dynamic modulus obtained from the fits to $J''(\omega)$ shown in figure 6.5A using standard procedures [6, 43, 83]. The red lines represent the dynamic modulus obtained from the active microrheology experiment, where an external strain or force was applied using optical tweezers. The blue lines represent the modulus obtained from the

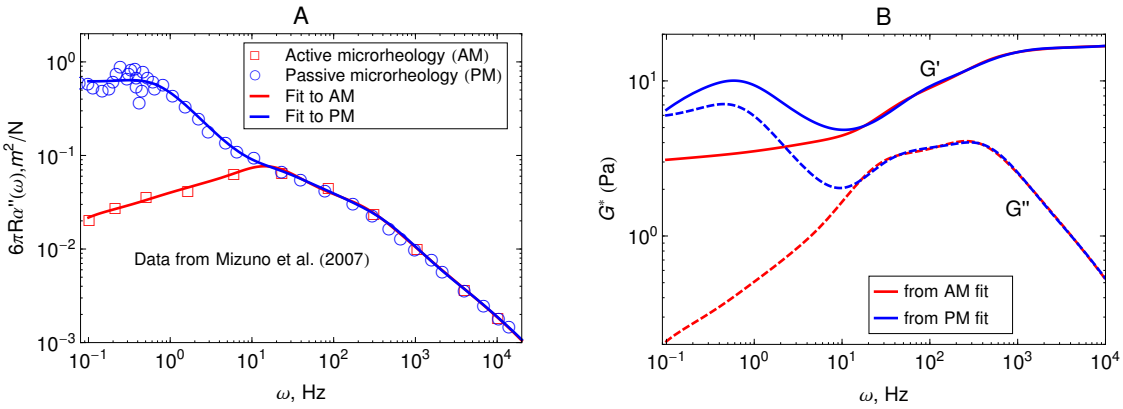

Figure 6.5. A : Imaginary part of the creep compliance, $J''(\omega) = 6\pi R\alpha''(\omega)$, of an actomyosin gel measured using passive and active microrheology. The symbols are experimental results by Mizuno et al. [91] and the lines are fits used to convert J^* to G^*. B: Dynamic modulus obtained from the creep compliance shown in part A.

passive microrheology technique without applying any external strain or force.

In this section, we perform calculations with the active single-chain mean-field model that test the validity of FDT in active gels in a way similar to the microrheology experiments of Mizuno et al. [91]. We begin by calculating the relaxation modulus of the active gel from the autocorrelation function of stress at the non-equilibrium steady-state. That is, we apply the Green-Kubo formula, that relates the autocorrelation function of stress with the relaxation modulus of a material [14], to the active gel. In a second calculation we apply a small step-strain to the active gel and estimate the dynamic modulus from the stress relaxation curve. If the active single-chain mean-field model satisfies the FDT the dynamic modulus obtained from those two calculations should be the same, if it does not, a frequency-dependent discrepancy should appear. Similar calculations are often performed for single-chain models of not-active networks, to demonstrate FDT compliance [53, 109].

Other microrheology experiments in active gels [117, 91] have shown that motor-activity induces significant strain hardening of the semiflexible network. Mizuno

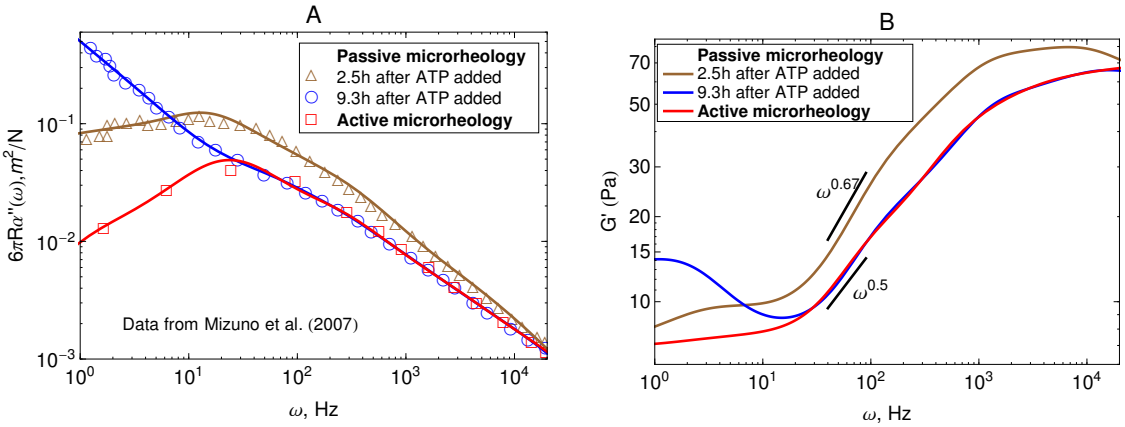

Figure 6.6. Strain hardening of the active gel due to motor activity with initial 3.5 mM ATP concentration. The response function is reduced after the myosin motors switch from a nonprocessive mode to a processive tension-generating mode at approximately 2.5 hours after addition of ATP. A : Imaginary part of the creep compliance, $J''(\omega) = 6\pi R\alpha''(\omega)$, of an actomyosin gel measured using passive microrheology. The symbols are experimental results by Mizuno et al. [91] and the lines are fits used to convert J^* to G^*. B: Storage modulus obtained from the creep compliance shown in part A.

et al. [91] observed this effect in the power-spectral density of the probe bead in passive microrheology experiments. Their experimental results are shown in Figure 6.6A. As can be observed the overall magnitude of the response function starts to decrease after the myosin motors switch from a nonprocessive mode to a processive tension-generating mode at approximately 2.5 hours after addition of ATP. The strain hardening can also be observed in the storage modulus obtained from this passive microrheology experiments shown in Figure 6.6B. The stiffening of the filaments generated by the motors causes an overall decrease in the magnitude of stress fluctuations and therefore a decrease in the storage modulus obtained from passive microrheology experiments. A broadening in the relaxation spectrum of the gel which causes a slow-down in stress relaxation at frequencies around 10^2Hz is also observed. For instance, the storage modulus obtained from passive microrheology goes from a $\omega^{0.67}$ behavior to $\omega^{0.5}$ when myosin motors become processive.

6.3.2 Dynamic modulus of active gels from a Green-Kubo Formula. For

the derivation of the dynamic modulus we introduce the conditional probability $\psi_{\rm st}(\hat{\omega}, \boldsymbol{r}; t|\hat{\omega}_0, \boldsymbol{r}_0; 0)$ (where $\hat{\omega} : \{s, \boldsymbol{F}\}$) that an active filament at steady state is in attachment state s with strands that have a change in their end-to end distance $\boldsymbol{r}$ due to motor forces $\boldsymbol{F}$ at time t when it had the initial conformation $\boldsymbol{r}_0$ and the initial attachment state s_0 at $t = 0$. The time-evolution of $\psi_{\rm st}(\hat{\omega}, \boldsymbol{r}; t|s_0, \boldsymbol{r}_0; 0)$ obeys the same evolution equation as $\psi_{\rm st}(\hat{\omega}, \boldsymbol{r}; t)$: that is eq.(6.1), with initial condition given by $\psi_{\rm st}(\omega, \boldsymbol{r}; t = 0|\hat{\omega}_0, \boldsymbol{r}_0; 0) = \delta(\boldsymbol{r} - \boldsymbol{r}_0)\delta_{s,s_0}$.

To obtain the relaxation modulus in a way similar to what is done in passive microrheology experiments, we use the Green-Kubo formula. This formula relates the relaxation modulus, $G(t)$, of a material to the autocorrelation function of stress at equilibrium (see Appendix for derivation). We apply it at a non-equilibrium steady state without modification, in the same way the FDT is applied for the analysis of passive microrheology data in active gels. This requires the calculation of the autocorrelation function of stress at steady-state $\langle\sigma(0)\sigma(t)\rangle_{\rm st}$. Where σ is the normal stress in the direction of filament alignment in the bundle. For the mean-field single-chain model, such as the one under consideration, the macroscopic stress is related to the tension on the filaments by $\sigma = -n_c \sum_{i=1}^{N-1} f_i r_i$ where f_i is the tension on the filament and n_c is the number of filaments per unit volume [54, 9, 44]. For the calculations with linear springs σ simplifies to $n_c k_b \sum_{i=1}^{N-1} r_i^2$, whereas for WLC springs the tension f_i is given by eq.(6.4). With these, the non-equilibrium steady-state relaxation modulus of the active gel is obtained from,

$$G_{\rm GK}(t) = \frac{1}{n_c k_{\rm B} T} \langle\sigma(t)\sigma(0)\rangle_{\rm st} . \tag{6.7}$$

The Green-Kubo simulations start with an ensemble of filaments in which for all the filaments the beads have motors attached to them, and all the strands are relaxed ($r_i = 0$ for all i) we let the ensemble of filaments reach steady state before calculating $\langle\sigma(t)\sigma(0)\rangle_{\rm st}$ on the fly using the photon correlation spectroscopy algorithm [27, 84].

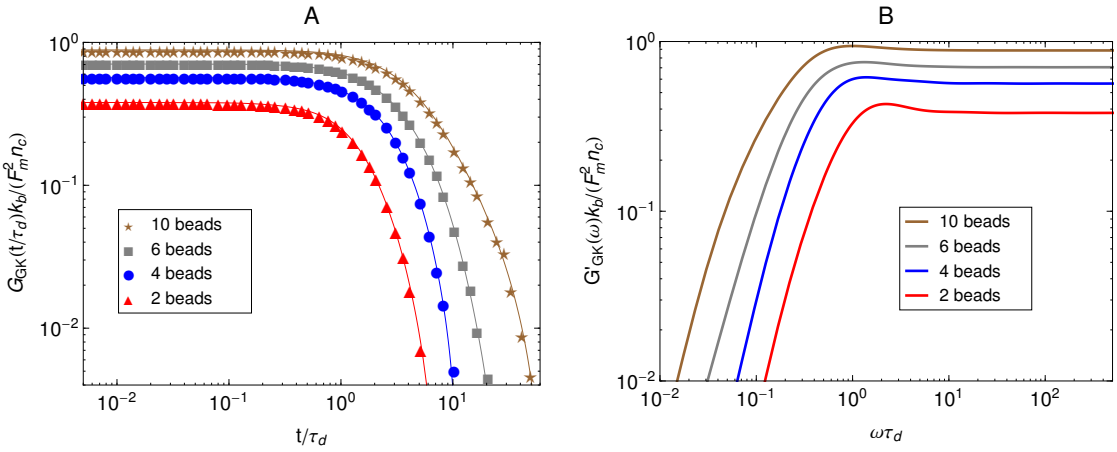

Figure 6.7. Effect of the number of beads for a fixed strand rest length, ℓ_0, on the stress relaxation behavior of the the active single-chain mean-field model with linear springs observed in a Green-Kubo simulation. Model parameters used were $\tau_a/\tau_d = 0.005$, $\tau_{r,a}/\tau_d = 2$, $\zeta_d/\zeta_a = 0.1$, and the Gamma motor force distribution shown in Figure 6.3. A: Relaxation modulus, symbols are simulation results and lines are fits used to transfer the information to the frequency domain. B: Storage modulus obtained from the fits in part A.

The relaxation modulus of the active single-chain mean-field model obtained from Green-Kubo simulations is shown in Figure 6.7A. Where the symbols represent simulation results and the lines are fits used to carry the information to the frequency domain [6, 7]. By taking the one-sided Fourier transform of the relaxation modulus the non-equilibrium steady-state dynamic modulus of the active gel is obtained $G^*(\omega) = i\omega\bar{\mathcal{F}}\{G(t)\} = G'(\omega) + iG''(\omega)$. Where $\bar{\mathcal{F}}\{G(t)\} := \int_0^\infty G(t)e^{-i\omega t}dt$ is the one-sided Fourier transform; $G'_{\mathrm{GK}}(\omega)$ is the storage modulus and $G''_{\mathrm{GK}}(\omega)$ is the loss modulus. The storage modulus of the active bundle as predicted by our model is shown in Figure 6.7B. A distinctive feature of this storage modulus is that it has a maximum. Extrema do not occur in the relaxation or storage modulus of passive networks, and therefore this is a specific feature of active gels. As we show in Section 6.3.3 this feature is essential to the violation of FDT observed in active gels. The storage modulus of the active single-chain mean-field model also has features in common with the storage modulus of passive temporary networks, such as the high frequency

plateau in the storage modulus and the low frequency terminal zone in $G'_{\mathrm{GK}}(\omega)$ that goes as ω^2.

In Chapter 5 we discussed how the shape of the dynamic modulus of the active network depends on the model parameters τ_a, τ_d and ζ_d, ζ_a. In general, we observe that as the values of τ_a/τ_d increase, $G''_{\mathrm{GK}}(\omega)$ and the maximum in $G'_{\mathrm{GK}}(\omega)$ decrease slightly. The shape of the dynamic modulus does not depend strongly on the ratio τ_a/τ_d. On the other hand the position of the maxima in $G'_{\mathrm{GK}}(\omega)$ and $G''_{\mathrm{GK}}(\omega)$ strongly depends on the ratio of friction coefficients ζ_a/ζ_d. When ζ_d is much smaller than ζ_a local relaxation of the filament upon motor detachment is faster than tension build-up when the motor is attached. Therefore stress relaxation in the gel occurs at shorter time scales (higher frequencies). Here we will focus on what changes when we relax some of the assumptions made in Chapter 5.

First we consider the effect of the density of motor clusters in the dynamic modulus of active gels. In experiments the number of motors per filament is commonly used as a control parameter to study the effect of motor activity in the mechanical properties of active gels [94, 119, 60]. For instance, rheological measurements in actomyosin gels [60] have shown that varying the myosin concentration at fixed actin filament length has the same effect on the magnitude of the storage modulus of an actomyosin gel as varying the average actin filament length (with the capping protein gelsolin) for fixed myosin concentration. Therefore it has been suggested that the number of myosin thick filaments per actin filament is the relevant control parameter to study the effect of motors on the dynamic modulus of actomyosin gels. In the active single-chain mean-field model the number of motors per filament can be controlled by changing the number of beads, N, for a fixed rest length of the strands, ℓ_0 and a fixed τ_a/τ_d ratio. Which is equivalent to varying the total rest length of the filaments, $\ell_f = (N-1)\ell_0$, for a fixed motor concentration. The average number density of active

cross-links, at steady-state, is given by $n_c N\tau_d/(\tau_a + \tau_d)$. Where n_c is the number of filaments per unit volume and $\tau_d/(\tau_a + \tau_d)$ is the fraction of attached motors. If the motors are operating under strong attachment or high duty ratios, $\tau_a \ll \tau_d$, such as the case under consideration, the average number density of active cross-links is approximately $n_c N$.

The effect of increasing the number of motors per filament in the relaxation modulus of the active single-chain mean-field model is shown in Figure 6.7A. We find that the magnitude of the relaxation modulus increases with increasing number of motors per filament. This tendency agrees with what is observed experimentally in actomyosin gels [60]. In real systems however entanglements between myosin filaments contribute significantly to the modulus, especially in concentrated gels formed by long filaments [60]. The results obtained with the single-chain mean-field model are also consistent with theoretical calculations in temporary networks formed by associating polymers [54, 53], where the magnitude of the storage modulus also increases with increasing number of stickers per chain. Another effect of increasing the density of active cross-links is that the spectrum of relaxation times becomes broader making the longest relaxation time larger. The shape of the characteristic peak in $G'_{\mathrm{GK}}(\omega)$ also changes as the number of motors per filament is increased as can be observed in Figure 6.7B. The peak is narrow and relatively high compared to the plateau for low motor densities. It becomes wider and relatively lower for larger motor densities, as τ_d and the longest relaxation time become more separated.

We previously considered only a linear version of our model, in which the strands were modeled by Fraenkel springs. However as has been shown in microrheology experiments on actomyosin gels [91] (Figure 6.6) molecular motors can cause strain hardening of the active gel. Therefore here we check for the effect of finite extensibility of the strands in the relaxation modulus observed in the Green-Kubo

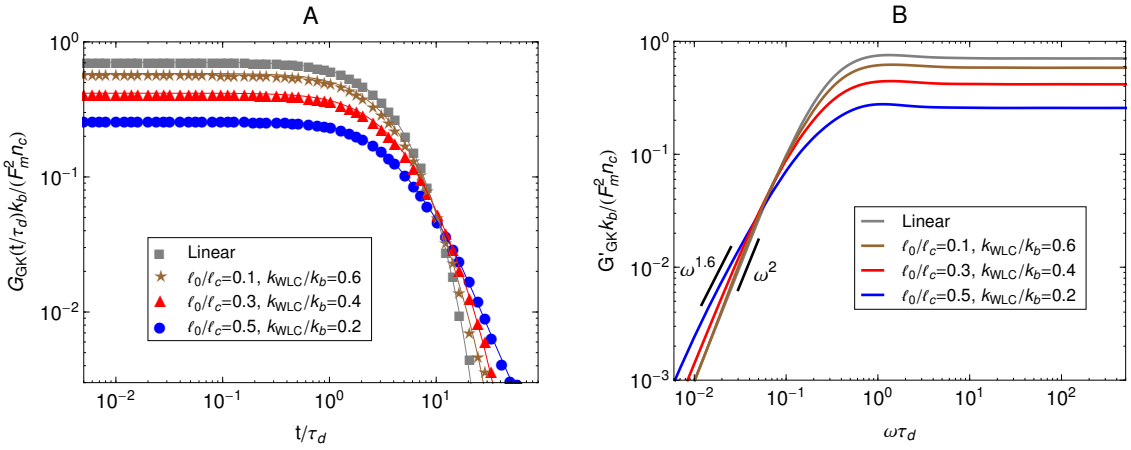

Figure 6.8. Effect of strand stiffness on the stress relaxation behavior of the active single-chain mean-field model observed in a Green-Kubo simulation. Strands for which the ratio ℓ_0/ℓ_c is large can be thought as being more prestressed than strands for which the ratio ℓ_0/ℓ_c is small. Model parameters used were $\tau_a/\tau_d = 0.005$, $N = 6$, $\tau_{r,a}/\tau_d = 2$, $\zeta_d/\zeta_a = 0.1$, and the Gamma motor force distribution shown in Figure 6.3. Results shown are for a chain with six beads. k_{WLC} for eq.(6.4) was chosen such that the small tension behavior matches the linear spring. A: Relaxation modulus, symbols are simulation results and lines are fits used to transfer the information to the frequency domain. B: Storage modulus obtained from the fits in part A.

simulations. To perform a calculation similar to the experiments of Mizuno et al. [91] we vary the initial stiffness of the strands by changing the ratio between the rest length of the strands, ℓ_0, and their contour length, ℓ_c. Strands for which ℓ_0 is closer to ℓ_c can be thought of as being initially stiffer than strands for which the ratio ℓ_0/ℓ_c is small. Figure 6.8A shows the effect of finite-extensibility on the relaxation modulus obtained from Green-Kubo simulations. As the strands are made stiffer by making the ratio ℓ_0/ℓ_c larger there is an overall decrease in the magnitude of the relaxation modulus obtained from Green-Kubo simulations. The result for a chain with linear springs (*i.e.*, $\ell_0/\ell_c \to 0$) is shown as reference. The parameter k_{WLC} for the non-linear springs is chosen such that their small-tension behavior matches the linear spring behavior. In addition to the overall decrease in magnitude, there is also a decrease in the slope of the relaxation modulus at long times, which means that

the breadth of the spectrum of relaxation times of the active gel becomes larger as the strands are made stiffer. Figure 6.8B shows the storage modulus obtained from the one-sided Fourier transform of the relaxation modulus shown in Figure 6.8A. The same effects observed in the relaxation modulus can be seen here. For the linear springs the low-frequency behavior in $G'_{\mathrm{GK}}(\omega)$ is the ω^2 typical of a terminal zone. On the other hand, at the same frequencies, the $G'_{\mathrm{GK}}(\omega)$ of the gel with the stiffer WLC springs considered displays a $\omega^{1.6}$ behavior and the terminal zone can not be observed in the calculated frequency window. This again indicates that the stiffer strands increase the breadth of the relaxation spectrum of the gel. These theoretical results agree qualitatively with the experimental observations of Mizuno et al. [91] shown in Figure 6.6. Where stiffer filaments were also observed to produce a broader relaxation spectrum and an overall decrease in the modulus obtained from passive microrheology experiments in actomyosin gels.

Other passive microrheology experiments in active gels have also shown that motor activity induces significant strain hardening of the semiflexible network. For instance, Stuhrmann et al. [117] observed the statistics of the displacements of a tracer bead embedded in an *in vitro* cytoskeleton and found that the distribution of the bead position fluctuations becomes narrower with time due to motor activity. Moreover the statistics develop non-Gaussian tails when the gels are activated with ATP. These observations have been attributed to the stiffening of the semiflexible filaments due to motor activity. The effect of molecular motors and strand semi-flexibility in the non-equilibrium statistics of the active single-chain mean-field model are shown in Figure 6.9. The change in the total end-to-end length of the filaments, $\sum_{i=1}^{N-1} r_i$, is plotted in Figure 6.9A and the non-equilibrium statistics of the total tension are shown in Figure 6.9B. As the filaments are made stiffer by increasing the ratio ℓ_0/ℓ_c these distributions become narrower (*i.e.*, smaller variance). It can also be observed in the insets of Figure 6.9 that the absolute residuals between the distributions obtained from

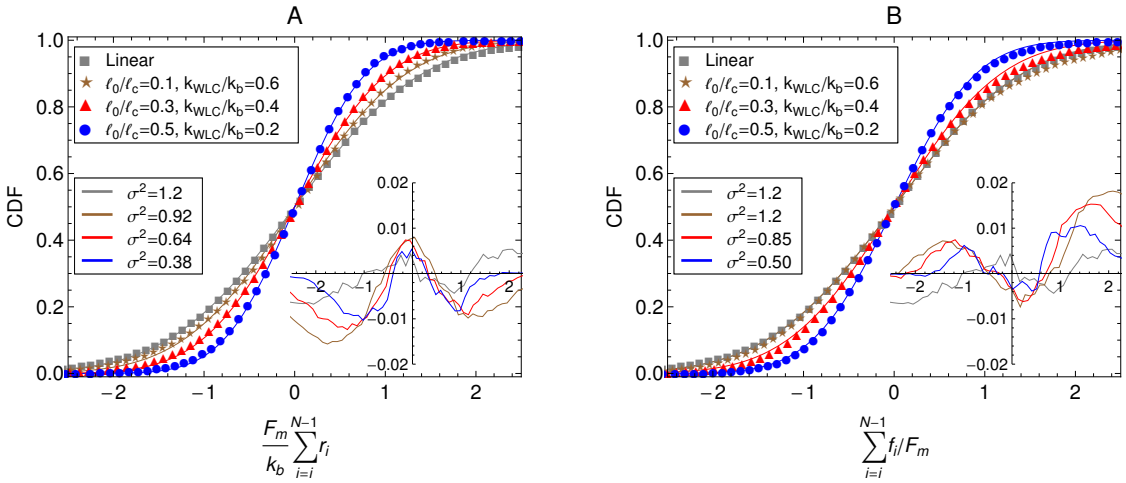

Figure 6.9. Effect of the strand stiffness on the non-equilibrium steady state statistics of the active single-chain mean-field model. A: Cumulative density function (CDF) of the change in the end-to-end length of the filaments due to motor activity. B: CDF of the the total tension on filaments due to motor activity. Model parameters used were $\tau_a/\tau_d = 0.005$, $N = 6$, $\tau_{r,a}/\tau_d = 2$, $\zeta_d/\zeta_a = 0.1$, and the Gamma motor force distribution shown in Figure 6.3. Results shown are for a chain with six beads. k_{WLC} for eq.(6.4) was chosen such that the small tension behavior matches the linear spring. Symbols are simulation results, the lines are fits to Gaussian CDFs. The lower legend shows the second moments of the fitted Gaussian curves and the insets show the absolute residuals between these fits and the simulation results.

the simulation and their best Gaussian fits are larger for the WLC filaments. This indicates that the molecular motors are indeed extending/compressing the filaments beyond the linear regime of the tension-extension relation. This explains why a tracer bead embedded in an active gel "feels" a non-harmonic potential. Note that there is a slight asymmetry in the absolute residuals between the distributions obtained from the simulation and their best Gaussian fit, this is due to the asymmetric character of the WLC tension-extension relation, eq.(6.4), where tension rises steeply for extensions but remains relatively flat for compressions. In real systems filaments actually buckle for small compressions, which leads to contraction of the entire gel. Buckling and contraction in active gels is discussed in Section 6.5.

6.3.3 Dynamic modulus of active gels from a small step-strain calculation.

To show that the active single-chain mean-field model violates FDT in the way active gels do [91], we calculate the dynamic modulus observed in the stress response to an externally applied small step-strain in the direction of filament orientation. We simulate an ensemble of chains with dynamics given by eq.(6.1), starting from an initial condition in which all the strands are relaxed ($r_i = 0$ for all i) we let the ensemble of chains reach steady state before applying a small uniform step strain, ϵ, at $t = t_{\rm st}$. We assume that on the time scale of interest for which $G(t)$ is calculated the step-strain applied at the boundaries propagates instantaneously through the system. Therefore $r_i(t = t_{\rm st}+) = r_i(t = t_{\rm st}-) + \epsilon_0 r_i(t = t_{\rm st}-)$ for $i = 1, 2, 3, ..., N-1$, where ϵ_0 is the strain magnitude. Then the relaxation of stress back to its steady state value is followed. In this externally driven calculation the relaxation modulus is given by $G_{\rm D} = \dfrac{\langle\sigma(t)\rangle_{\rm st}}{\epsilon_0}$. The subscript D indicates that the modulus is obtained from an externally driven experiment (externally applied force or strain). To obtain the plots shown here we average over an ensemble of 3000 filaments.

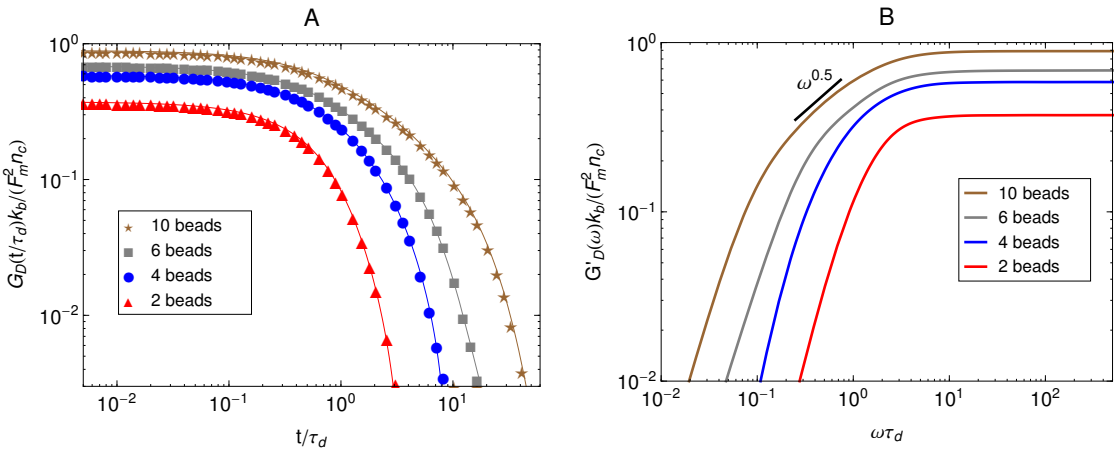

Figure 6.10. Effect of the number of beads for a fixed strand rest length, ℓ_0, on the stress relaxation behavior of the active single-chain mean-field model with linear springs observed in a step-strain calculation. Model parameters used were $\tau_a/\tau_d = 0.005$, $\tau_{r,a}/\tau_d = 2$, $\zeta_d/\zeta_a = 0.1$, and the motor force distribution shown in Figure 6.3. A: Relaxation modulus, symbols are simulation results and lines are fits used to transfer the information to the frequency domain. B: Storage modulus obtained from the fits in part A.

A plot of the relaxation modulus of the active single-chain mean-field model obtained from the step-strain calculation is shown in Figure 6.10A. Similar to what is observed in the Green-Kubo calculations the overall magnitude of the relaxation modulus increases with increasing density of motors, which is controlled by varying the number of beads, N, for a fixed rest length of the strands, ℓ_0 and a fixed τ_a/τ_d ratio. Also, the breadth of the relaxation spectrum for the gel increases with increasing number of motors per filament. The storage moduli corresponding to the relaxation moduli shown in Figure 6.10A are plotted in Figure 6.10B. These results show a trend similar to what is observed in the rheological experiments of Koenderink et al. [60] in actomyosin gels, who find that $G'(\omega)$ can be tuned over two orders of magnitude by controlling the number of myosin motors per actin filament. With increasing N, a behavior that goes as $\sim \omega^{0.5}$ appears at intermediate frequencies in the storage modulus obtained from the step-strain calculations. This viscoelastic relaxation behavior is of the Rouse type and does not appear in G'_{GK} because in that case the characteristic peak appears instead. This type of relaxation behavior is also observed experimentally in the dynamic modulus of actomyosin gels measured using active microrheology (see Figure 6.6). In the active single-chain mean-field model the Rouse behavior originates from the attachment/detachment of motors. However it does not become visible until the longest relaxation time becomes significantly larger and separated from τ_d. This type of low-frequency Rouse mode also appears in temporary networks formed by associating polymers [54, 53], where it is called associative Rouse behavior, to distinguish it from another Rouse behavior observed at high frequencies in those type of systems. The frequency-dependent discrepancy between the modulus obtained from the Gree-Kubo formula and the one obtained from the step-strain calculation that appears at frequencies around $1/\tau_d$ indicates a violation of the FDT.

6.3.4 FDT in active gels. By comparing the moduli obtained from the Green-

Kubo simulations, shown in Figure 6.7, with the moduli obtained from the step-strain simulations, shown in Figure 6.10, it can now be checked if the active single-chain mean-field model describes the frequency-dependent violation of FDT observed in the microrheology of active gels. Figure 6.11A shows a comparison between the relaxation modulus for a ten-bead chain with linear springs obtained from the Green-Kubo formula and the one obtained from the step-strain calculation. It can be observed that at high frequencies the two dynamic moduli are equal. At intermediate frequencies G'_{GK} grows towards a maximum while G'_{D} exhibits a Rouse relaxation behavior $\sim \omega^{0.5}$. Both G''_{GK} and G''_{D} exhibit maxima but the maximum in G''_{GK} is larger than in G''_{D}. At lower frequencies, below the maximum, G'_{GK} and G'_{D} decrease as ω^2, while G''_{GK} and G''_{D} decrease as ω. The difference between G^*_{GK} and G^*_{D} persists as $\omega \to 0$.

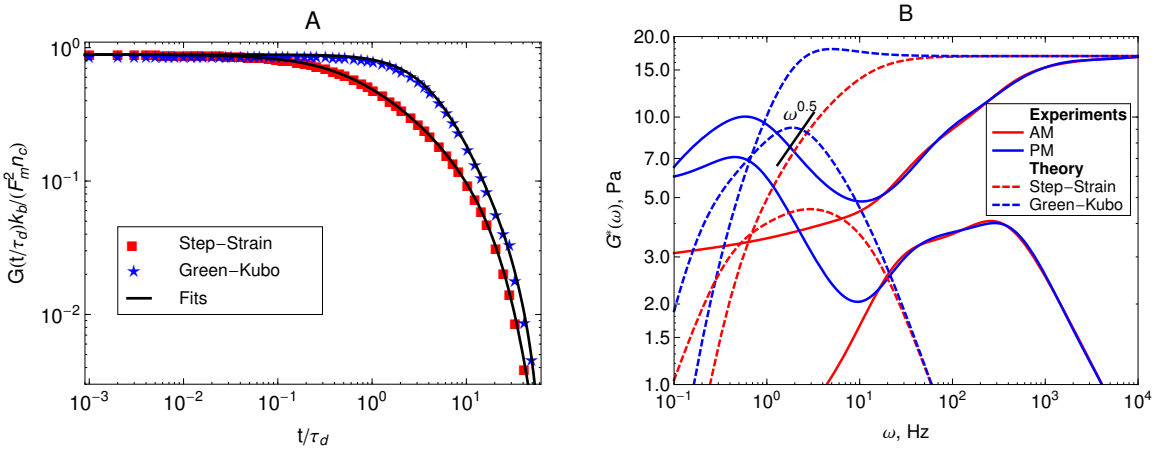

Figure 6.11. Predictions of the active dumbbell model of the dynamic modulus of active gels. A: Comparison between modulus obtained from the Green-Kubo simulations and the modulus obtained from a step-strain simulation for a 10-beads chain. B : Comparison of the dynamic modulus, $G^*(\omega)$, predicted by the active single-chain mean-field model with the dynamic modulus determined from the passive (PM) and active (AM) microrheology experiments of Mizuno et al. [91]. The parameter values used in these figures are $\ell_0 = 1\mu$m, $\tau_a = 1$ms, $\tau_d = 200$ms, $\zeta_a = 0.8\mu\mathrm{N}\cdot\mathrm{s/m}$, $\zeta_d = 0.08\mu\mathrm{N}\cdot\mathrm{s/m}$, $N = 10$, $n_c = 2.3\times10^{13}$filaments/m^3 and the motor force distribution shown in Figure 6.3. The parameter, ζ_a is fitted to the experimental data to match the time scale at which the moduli determined from passive and active microrheology start to diverge.

Figure 6.11B presents a comparison between the dynamic moduli obtained

from our theory and the microrheology experiments of Mizuno et al. [91] in actomyosin gels. The frequency-dependent discrepancy between the response function of the active gel obtained from the step-strain and Green-Kubo calculations is in good qualitative agreement with the experimental observations of Mizuno et al. [91] in microrheology experiments in actomyosin gels. We emphasize that the parameters τ_a, τ_d, F_m and k_b used for the prediction shown in Figure 6.7B were determined from other experiments [119, 71]. Only ζ_a and ζ_d were fitted to the data of Mizuno et al. [91].The model describes the characteristic maximum observed in the $G'(\omega)$ obtained from the passive microrheology technique, which causes G'_{GK} to be larger than G'_{D} at low frequencies. The frequency-dependent increase in the magnitude of the probe bead autocorrelation function observed in the passive microrheology of active gels is caused by the frequency-dependent stress fluctuations caused by motor activity. These fluctuations are therefore not related to the response function of the bead by the FDT. An additional, frequency-dependent term, is necessary to account for the magnitude and dynamics of motor activity. If such a modified FDT is used in the analysis of the passive microrheology data in active gels, it will account for a frequency-dependent increase in the magnitude of the probe bead autocorrelation, yielding the same dynamic modulus obtained from the active technique [74, 43].

The predictions shown in Figure 6.11B are an improvement with respect to the ones presented in Chapter 5, given the wider relaxation spectrum achieved by increasing the number of beads in the filaments from two beads to ten beads. However, there is still some discrepancy between the model predictions and the experimental results. In the data, significant stress relaxation is occurring at frequencies between 10^1 to 10^3 Hz while in the model predictions most of the relaxation occurs at frequencies below 10^1 Hz. This could be due to a high polydispersity in the total lengths of actin filaments that form the gel, which can further increase the breadth of the relaxation spectrum of the gel. Accounting for polydispersity in the filament lengths

is possible and straight forward to implement in the single-chain mean-field approach [58]. However this will require experimental characterization of the molecular-weight distribution of actin filaments from which the active gel is formed. Accounting for dispersion [115] in the rest length of the strands, ℓ_0, may also improve the predictions by increasing the breadth of the relaxation spectrum. However the model predictions are worst at the lower frequencies, where the experimental observations indicate that $G'_{\mathrm{D}}(\omega)$ goes to an elastic plateau, while the predictions present a terminal zone. The model also predicts a time scale for the the maximum in $G'_{\mathrm{GK}}(\omega)$ that is about ten times shorter than the one observed experimentally. The two latter discrepancies are related to the fact that the actomyosin gels prepared by Mizuno et al. [91] also contain biotin cross-links, while our model does not contain permanent passive cross-links, but only active cross-links (motors). When passive cross-linkers such as biotin or α-actinin are present in an actomyosin gel myosin contracts F-actin into dense foci around the passive cross-links. Once contracted, these aggregates can undergo further coalescence and may form larger length-scale structures such as asters or vortices [60]. This in turn introduces longer time scales and length scales relevant for the dynamics of the active gel. The proposed single-chain mean-field framework does not yet seem appropriate for modeling those physics. Other descriptions such as multi-chain models [42] or coarser levels of description [64, 2] have been used to describe such phenomena.

The deviation from the equilibrium FDT predicted by our model is additive and frequency-dependent and cannot, in general, be interpreted as an effective temperature. This result is in agreement with the conclusions of a recent and more general theoretical work by Ganguly and Chaudhuri [29] in which an extension of the FDT for active systems was derived. In contrast to other models for active gels in which motor activity is accounted for by means of an effective temperature [78, 79, 80]. These latter works can not, in general, predict the correct frequency-dependent violation of

the FDT due to the use of an effective temperature to model motor activity. Other works [74, 43] have used an attachment/detachment jump process to model motor dynamics. However those models were postulated in a continuum level of description, where motors are treated as force dipoles embedded within a continuum. Those models have also been successful in describing some of the observations in the microrheology of active gels. However given their level of description, including physics such as finite extensibility of the network strands or realistic motor force distributions can be difficult.

6.4 Super-diffusive mass transport

The "diffusion" of tracer beads or labeled filaments inside active gels has been extensively studied both experimentally and theoretically [74, 43, 68, 105]. In experiments, the mass transport of probe beads or filaments in active gels often exhibits super-diffusive behavior [68, 105]. This is different from passive networks where the mass transport of probe beads often exhibits sub-diffusive behavior due to the viscoelasticity of the medium. Head et al. [42] investigated the mass-transport of filaments in active gels using a multi-chain model. Their model also accounts for the elasticity of the filaments and for motor attachment/detachment dynamics. They find that filament translational motion ranges from diffusive to super-diffusive, depending on the ratio of attachment/detachment rates of the motors. And becomes sub-diffusive when motor forces are turned off.

In our model mass transport can be quantified by the mean-squared displacement of the probe filament center, $\langle \Delta R_c^2(t) \rangle_{\text{st}}$. Figure 6.12 shows $\langle \Delta R_c^2(t) \rangle_{\text{st}}$ obtained from simulations of the active single-chain mean-field model for different values of the ratio of detachment and attachment rates. It can be observed that filament transport has behavior that ranges from diffusive $\langle \Delta R_c^2(t) \rangle_{\text{st}} \sim t$ to super-diffusive $\langle \Delta R_c^2(t) \rangle_{\text{st}} \sim t^{\alpha}$ with α as large as 2. It can be observed that for gels with weak motor

attachment, large τ_a/τ_d ratio, filament translational motion of the filaments has two well-defined regions. At time scales shorter than $\tau_{r,a}$ the mean-squared displacement of filament centers goes roughly as t^2 which is the characteristic ballistic behavior expected from a filament being pulled by motors. While for time scales larger than $\tau_{r,a}$ the behavior becomes diffusive. Note that we have not included Brownian forces in eq.(6.1) and therefore the apparent diffusive behavior that is observed in $\langle \Delta R_c^2(t) \rangle_{\rm st}$ at long times for large τ_a/τ_d ratios is not due to thermal motion of the filaments. In these weak attachment scenarios significant local relaxation occurs in the strands between motor attachment events. This causes the motion of the filament centers to become slower, since the filament has time to significantly retract between motor attachment events.

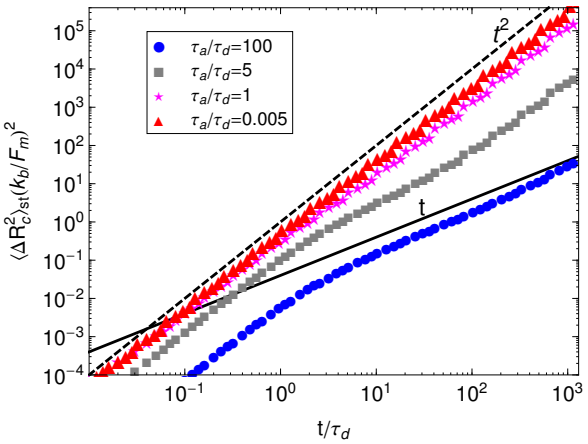

Figure 6.12. Mean-squared displacement of the probe filament center, $\langle \Delta R_c^2(t) \rangle_{\rm st}$, of 3-beads filaments for different values of the ratio between detachment and attachment rates. For this simulations $\tau_{r,a}/\tau_d = 2$ and $\zeta_a/\zeta_d = 0.1$, we use the Gamma motor force distribution shown in Figure 6.3. The lines are given as reference for diffusive $\langle \Delta R_c^2(t) \rangle_{\rm st} \sim t$ and super-diffusive behavior $\langle \Delta R_c^2(t) \rangle_{\rm st} \sim t^\alpha$, $\alpha > 0$.

In the strong motor attachment regime, achieved by making the ratio τ_a/τ_d smaller the two regions in $\langle \Delta R_c^2(t) \rangle_{\rm st}$ become less well-defined. For strong motor attachment the mean-squared displacement of filament centers deviates only slightly from the t^2 behavior at long times. This is because in the strong attachment scenario almost no relaxation of the strands occurs between attachment events. This means

that for the strong motor attachment mass-transport is mostly dominated by motor dynamics. The filament's and motor size (*i.e.*: friction coefficients) have a negligible effect in $\langle \Delta R_c^2(t) \rangle_{\rm st}$ in the strong motor attachment regime. These observations agree with what is observed in the simulations of Head et al. [42] who also find that in the strong motor attachment regime only slight deviations from super-diffusive behavior are observed in $\langle \Delta R_c^2(t) \rangle_{\rm st}$. As discussed above, in the low and intermediate motor attachment regimes, they also observe sub-diffusion of the filaments at short time scales related to non-processive motors acting as passive cross-links which generate viscoelasticity of the aggregate structures that retards filament motion [41]. Since our model does not account for permanent passive cross-links we do not observe this sub-diffusive behavior in the filaments' motion.

6.5 Buckling and contraction in active bundles

Recent experiments [94, 71, 23] in actomyosin bundles without sarcomeric organization have shown that self-contraction, upon addition of ATP, is related to the buckling of individual F-actin filaments that form the bundle. In the experiments, individual bundles were observed and F-actin buckling was found coincident with contraction. Prior to ATP addition, compact bundles with aligned F-actin are observed. Upon ATP addition, the frequency of buckles increases rapidly during contraction, and then diminishes once contraction stops. These F-actin buckles are dynamic, with their amplitude, curvature, and location changing over time. Motor-induced buckling of actin filaments has been shown to be a ubiquitous process in the self-organization of the cellular cytoskeleton [23].

The main purpose of this Section is to expand the results presented in Chapter 5 by presenting more quantitative predictions of the buckling dynamics observed in active bundles. We also compare our model and results to the other single-chain mean-field description of active gels available in the literature [71]. As pointed out in

Section 6.2, there are several differences in the level of description and mathematical formulation of the two models. Here we discuss in more detail how these differences reflect in a specific observable of the model. Using the model presented in Section 6.2 we calculate the fraction of buckled filament segments, ϕ_B, as a function of time after addition of ATP in the absence of externally applied strain. Before addition of ATP all the myosin motors are attached (as passive cross-links) and the strands between them have relaxed end-to-end length ℓ_0. Therefore a filament has total rest length $\ell_f = (N-1)\ell_0$, where N is the number of myosin cross-links along the filament (beads). Upon addition of ATP motor activity can change the end-to-end length of the strands by an amount r. This change can cause compression ($r < 0$) or extension ($r > 0$) of the strands. However F-actin filaments support large tensions but buckle easily under piconewton compressive loads [23, 115]. Therefore only strands under compression ($r < 0$) buckle. A compressed strand buckles when its tension $f = -k_b r$ reaches a buckling force threshold, F_B. An estimation of this force threshold can be obtained by treating the filaments as thin elastic cylinders [115, 35] $F_B = \dfrac{k_{\mathrm{B}} T \ell_p}{\ell_0^2}$. For a typical F-actin filament, using the values presented in Section 6.2, $F_B \sim 0.1$ pN. We simulate an ensemble of filaments and keep track of the number of strands that buckle in each filament. We then average over the ensemble of filaments and divide by the total number of strands in the filament to obtain ϕ_B.

In Chapter 5 we presented buckling predictions with the dumbbell version of the model ($N = 2$). The analytic results presented there revealed that in our model buckling arises because a fraction of the filaments in the bundle exist in a motor attachment state where contraction is favored. This is achieved by maintaining the motor forces as stochastic state variables instead of pre-averaging eq.(6.1) over them. The filaments on attachment states that undergo contraction buckle when the tension in them reaches F_B. However the model presented in Chapter 5 did not allow us to make quantitative predictions of the buckling dynamics. Since the dumbbell version

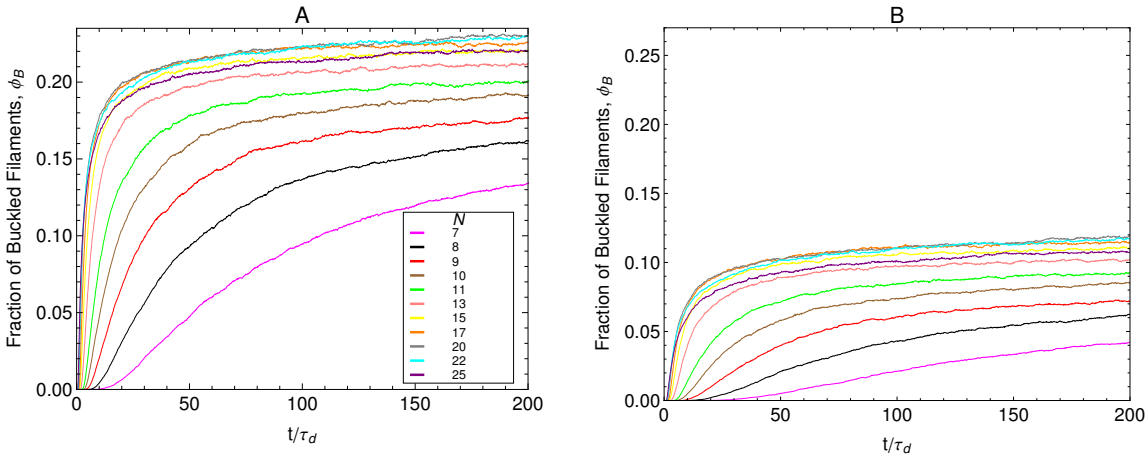

Figure 6.13. Fraction of buckled filaments, ϕ_B for different number of beads along the filaments. Where N is the number of beads and the total rest length of the filaments is given by $\ell_f = (N-1)\ell_0$. With ℓ_0 the rest length of the strands between beads. Simulations were performed with linear springs, with τ_a/τ_d set to 0.1 and $\zeta_d/\zeta_a = 0.1$. Since $k_b \sim \frac{k_B T \ell_p^2}{\ell_0^4}$ and $F_B \sim \frac{k_B T \ell_p}{\ell_0^2}$ we make $\tau_{r,a}/\tau_d = (\frac{32}{N-1})^4$ and $F_B/F_m = (\frac{N-1}{70})^2$. In part A: $\delta F_m/F_m = 0.5$. And in part B: $\delta F_m/F_m = 0.3$.

had only two beads along the filament, which is not the most accurate representation of real systems. Additionally in Chapter 5 we assumed $p(F) = \delta(F - F_m)$ and therefore the fraction filament compression was possible only in one of the attachment states of the dumbbell. Here we consider the case of N beads in a filament of total rest length ℓ_f, and use a motor force distribution as the one shown in Figure 6.3. In Figure 6.13 the effect that the number of beads has on the fraction of buckled filaments is shown. In general, the fraction of buckled filaments increases with the number of beads until reaching a maximum. After this maximum the fraction of buckled filaments sharply decreases with increasing number of beads. The fraction of buckled filaments also depends strongly on the width of the motor force distribution. For the case with a wider motor force distribution shown in Figure 6.13A compression of filaments in a given attachment state is more likely to occur and this results in more buckling. The fraction of buckled filaments is reduced significantly when the width of the motor force distribution is reduced from $\delta F_m/F_m = 0.5$ to $\delta F_m/F_m = 0.3$ as can be observed

in Figure 6.13B.

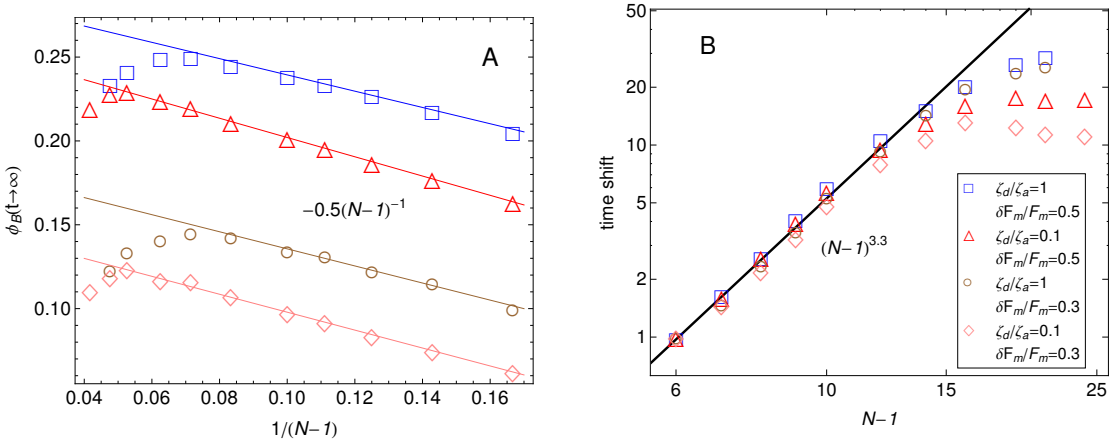

Figure 6.14. Effect of the number of beads N, width of the motor for distribution, δF_m, and ratio of detached to attached friction coefficients, ζ_a/ζ_d, on the fraction of buckled filaments. Simulations were performed with linear springs, with τ_a/τ_d set to 0.1. The total rest length of the filaments ℓ_f is held fixed, then the length of the strands is $\ell_0 = \ell_f/(N-1)$. Since $k_b \sim \frac{k_B T \ell_p^2}{\ell_0^4}$ and $F_B \sim \frac{k_B T \ell_p}{\ell_0^2}$ we make $\tau_{r,a}/\tau_d = (\frac{32}{N-1})^4$ and $F_B/F_m = (\frac{N-1}{70})^2$. A: Steady state value of the fraction of buckled filaments. B: Time shift required to collapse the different curves of ϕ_B such as the ones shown in Figure 6.13 to a single master curve.

We showed previously with the analytic solutions obtained in Chapter 5 that the steady state value of the fraction of buckled filaments depends strongly on the ratios ζ_a/ζ_d and τ_a/τ_d. For a given set of friction coefficients there is a critical values of the τ_a/τ_d at which buckling occurs. If, the detachment rate of the motors becomes comparable to, or larger than the attachment rate then motor activity can not produce buckling of the filaments. Figure 6.14 shows a more systematic exploration of the parameter space of the model with regards to buckling predictions. Note that we consider only the strong-attachment case (*i.e.*: $\tau_a/\tau_d < 1$) since this is the relevant case for the actomyosin bundles to which we compare our predictions. In Figure 6.14A the effect of the density of beads along the filaments is shown. It can be observed that independently of the width of the motor force distribution and the ratio of friction coefficients the steady-state fraction of buckled filaments goes as $-\frac{1}{2}(N-1)^{-1}$ until

it reaches a maximum around $N = 17$. For the number of beads larger than the location of this maximum, ϕ_B decreases in a way that also appears to be independent of the width of the motor force distribution and the ratio of friction coefficients. For the part of these curves that lies on the right side of the maximum the observed behavior can be interpreted as being due to the increase in the number of attachment states where compression of strands occurs caused by the higher density of active cross-links. However increasing the number of beads for a constant filament length ℓ_f also makes the strands between beads shorter (*i.e.*: $\ell_0 = \ell_f/(N-1)$) and therefore stiffer since $k_b \sim \frac{k_B T \ell_p^2}{\ell_0^4}$. When the curves in Figure 6.14A reach their maxima it is because the latter effect becomes predominant over the former effect. This indicates that there exists a critical value for the number of beads in the filament for which buckling is maximized. For values of N larger than this critical value the stiffening of the strands dominates and ϕ_B drops sharply. In that regime the translational motion of the filaments is expected to be more relevant than the buckling dynamics. In Figure 6.14B it can be observed that for values of N below the location of the maximum observed in Figure 6.14B the curves of ϕ_B vs t can be collapsed into a single master curve. The time shift factor goes with the number of beads in the filament as $(N-1)^{3.3}$ and is independent of δF_m and ζ_d/ζ_a. For values of N larger than the critical value the buckling dynamics appear to be independent of the number of beads along the filament. This again indicates that below a critical number of beads (around $N = 17$), increasing the density of active cross-links along the filament can increase how fast contraction occurs in non-sarcomeric bundles, while for N larger than that critical value contraction dynamics are dominated by the stiffness of the strands and increasing the density of active cross-links has no effect.

Figure 6.15 shows a comparison between the fraction of buckled filaments predicted by the active single-chain mean-field model and contraction data for a non-sarcomeric actomyosin bundle reported by Lenz et al. [71]. The friction coefficients

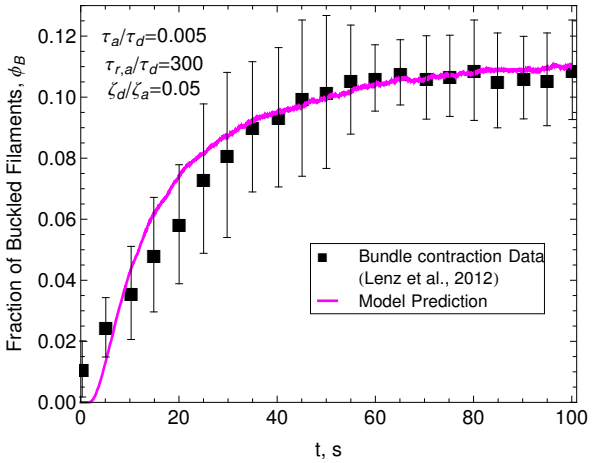

Figure 6.15. Fraction of buckled filaments, ϕ_B, in a active bundle after addition of ATP as predicted by the active single-chain mean-field model. Predictions are compared to the contraction data of an actomyosin bundle reported by Lenz et al. [71]. $\ell_0 = 1\mu$m, $\tau_a = 1$ms, $\tau_d = 200$ms, $\zeta_a = 121\mu\text{N}\cdot\text{s/m}$, $\zeta_d = 6.1\mu\text{N}\cdot\text{s/m}$, $N = 10$, and the motor force distribution shown in Figure 6.3. The only parameters fitted to the contraction data are the friction coefficients.

(e.i.: ζ_a and ζ_d) were used to fit the prediction to the data. The other parameters are known from independent measurements and were reported by Lenz et al. [71]. The values for the friction coefficients obtained from fitting the bundle contraction data are significantly larger than the ones obtained from the fits to the microrheology data of Mizuno et al. [91]. Although both experiments used actomyosin gels there were differences in their composition and ATP concentration. Moreover the gels prepared by Mizuno et al. [91] also contained biotin—a passive cross-linker. The contour length of actin between myosin motors and the size of the myosin motor clusters can vary significantly depending on gel composition and preparation, which may explain the discrepancy in friction coefficients obtained from different experiments. The role of filament buckling as a mechanism in non-sarcomeric actomysosin bundle contraction has been observed experimentally [94, 71]. Network contraction has been observed to correspond exactly with the extent of individual F-actin shortening via buckling. Moreover in experiments [119] it is observed that for low myosin density ($N \leq 2$)

bundle structure is weak and dissociation occurs upon addition of ATP. Intermediate myosin densities ($N = 2 - 4$) allow enough cross-linking within the bundles to maintain network integrity upon ATP addition, but contraction is not observed. For higher myosin densities ($N > 4$) myosin-generated forces lead to filament buckling and bundle contraction. We note that in its present form the active single-chain mean-field model can only describe contraction in active bundles containing myosin and actin alone. In these conditions, the length scale over which contraction occurs within the network is proportional to the F-actin length, consistent with poor network connectivity by myosin motors. Through the addition of permanent passive cross-linkers such as α-actinin the length of contraction can be increased to macroscopic length scales. This leads to the formation of structures such as asters and vortices that form due to clustering of actin filaments around the permanent cross-links.

Some previous attempts have also been made to use microscopic models to describe buckling of filaments in nonsarcomeric active bundles [71, 70], however, to our knowledge, this is the first attempt to quantitatively describe the dynamics of buckling formation. For instance Lenz et al. [71] proposed a single-chain bead-spring model to explain their bundle contraction data. They also investigated the effect of density of active crossinks and found that there is a value for which for contraction is maximized. They found that strong active cross-linking suppress buckling while filaments with very sparse motors do not buckle. Our results are apparently in agreement with their theoretical results. As discussed in Section 6.2 we assumed a single value for ℓ_0—in real systems a distribution of ℓ_0 is expected. Lenz et al. [71] studied the effect of a distribution of ℓ_0 by arbitrarily assuming a uniform distribution and found that it does not have a qualitative effect in their model predictions. However there is a fundamental difference on how the model presented in this work and the model by Lenz et al. [71] explain the mechanisms that cause buckling and self-contraction in active bundles as was discussed in Section 6.2. In the model presented here buckling

arises because a fraction of the filaments in the bundle exist in a motor attachment state where contraction is favored. In the model of Lenz et al. [71] buckling arises due to a spatial gradient of the motor stall forces.

6.6 Conclusions

We presented a single-chain mean-field mathematical model for active gels that can describe several experimental observations. For instance, our model describes the dynamic modulus and the frequency-dependent violation of the fluctuation-dissipation theorem observed in active gels. It also describes the super-diffusion of filaments and the contraction mechanisms in non-sarcomeric active bundles. The model allows accounting for physics that are not available in models that have been postulated on coarser levels of description [74, 43, 71]. Recently microscopic multi-chain models for describing the dynamics of active gels have also been proposed [42, 41]. However for realistic chain lengths and densities the numerical simulation of those models is notoriously expensive. This makes observables such as the relaxation modulus difficult to calculate for time-scales of practical interest. Here we have proposed a more coarse grained level of description that overcomes those limitations by using a mean-field approach. Although our framework can not yet account for the large length scale physics that arise when permanent cross-links are present, it provides important insight into the role of molecular motors in the mechanical properties of active gels.

In Chapter 5 we made several assumptions to simplify the mathematics and with the aim of obtaining analytical results. In this Chapter we discussed numerical simulations results for a more general version of the model and examined the effect of relaxing some of the aforementioned assumptions. We implemented experimentally measured motor force distributions into the model, generalized the differential Chapman-Kolmogorov equation to bead-spring chains made of multiple beads and examined the effect of finite extensibility of the filament segments. This allowed a

more quantitative description of the role of molecular motors in the rheology and mechanical properties of active gels. For instance, we presented quantitative agreement of the predictions of buckling dynamics in non-sarcomeric actomyosin bundles with the contraction data of Lenz et al. [71]. We were also able to look at the effect of density of active cross-links along the filaments and find that there is a fairly universal density for which buckling is maximized. This universality arises from the competing effects of increased motor activity and strand stiffening as the density of active cross-links along the filament is increased.

By increasing the length of the filaments we were also able to increase the breadth of the relaxation spectrum of the gel which improved the agreement of the dynamic modulus predictions with the data of Mizuno et al. [91]. The effect of finite extensibility of the filament strands on the dynamic modulus obtained from the Green-Kubo formula was also found to be in agreement with the passive microrheology experiments of Mizuno et al. [91]. The strain hardening of the filaments causes an overall decrease in the response function observed in passive microrheology experiments as well as a slowdown of the stress relaxation processes in the gel. This is observed in our simulations as a decrease in the slope of the terminal zone of the storage modulus obtained from the Green-Kubo simulations. We also calculated the mass transport of filaments in the active gel using our model. We found that the mean-squared displacement of filament centers has a behavior that varies from diffusive to super-diffusive depending on the motor attachment and detachment rates. These results are in agreement with experimental results [68, 105] as well a observations in multi-chain simulations [42].

By removing some assumptions we obtained certain improvement in the quality of the predictions of the active single-chain mean-field model for active gels. However, fully quantitative predictions will require a more accurate bead-spring description of

the semiflexible filaments which includes, additionally to finite-extensibility, bending potentials between the springs [61]. Polydispersity in the molecular weight of the filaments is also expected to be important in biological networks and could have a big impact in the quality of the predictions. This will require characterization of the molecular weight distribution of the filaments forming the gel. Including specific details about the motor protein used to prepare the gel might also be necessary to have a fully quantitative description of the rheology of active gels. For instance, different myosin isoforms have been shown to have different sensitivity to tension [93]. Including all these additional physics in the framework of our model is straightforward. However we note that this will introduce additional parameters into the model that must be determined either from experiments or independent theories.

CHAPTER 7

CONCLUSIONS

We have developed an alternative time-domain data analysis strategy for one-bead microrheology that extends the applicability of the time-domain methods to include medium inertia effects and linear and non-linear particle traps. Our approach was to adapt traditional BD simulation algorithms to the simulation of the Generalized Langevin equation (GLE). Analogous to the common practice of BD simulations of Langevin equations we have made use of the inertia-less GLE to make the simulation of the non-linear GLEs more computationally efficient. By making use of the photon correlation spectroscopy algorithm (PCS), our methodology has been made especially suitable and efficient for the analysis of data with a broad distribution of timescales spanning from high frequency inertial effects to purely elastic responses (over six decades of frequency).

We have derived a generalized Stokes tensor for two hydrodynamically interacting beads embedded in a viscoelastic incompressibe fluids and compressible solids. The tensors include the effects of medium inertia and consider an infinite number of reflections of the shear and longitudinal waves caused by the motion of the beads. To derive a time-domain data analysis strategy for inferring high-frequency linear viscoelastic properties from two-point cross correlations, we have proposed rational function approximations for the components of the memory function tensor. The approximations allow one to perform efficiently the inverse one-sided Fourier transform of the expressions obtained for the MSD and CMSD from solutions of the GLE in the frequency domain. The rational approximation of the memory function tensor was also used to construct generalized Brownian dynamics (BD) simulations of the two-point passive microrheology experiment. Using these new theoretical developments we have systematically evaluated the sensitivity of two-bead cross-correlations

to changes in the static and dynamic properties of the dynamic modulus and the complex Poisson ratio of a model viscoelastic material. We find that the sensitivity of the cross-correlation in the direction parallel to the line of centers of the beads to the compressibility of the medium is very small. These effects which appear only at high frequencies, and are due to medium inertia, can be safely neglected in the data analysis. This means that the dynamic shear modulus can be inferred independently from the cross-correlations in the direction parallel to the line of centers even when inertia and high order hydrodynamic reflections are expected to have a relevant effect. On the other hand, the two-bead cross-correlations in the direction perpendicular to the line of centers show a detectable dependence on the compressibility of the material. However the sensitivity of the cross-correlations in the direction perpendicular to the line of centers is practically undetectable to changes in the specific spectrum of delay times of the complex Poisson ratio.

Using the generalized Brownian dynamics and a microscopic model for biological composite networks we simulated the two-bead microrheology experiment in F-actin and microtubules composites. We used the simulated two-bead cross-correlations to test data analysis formalisms for inferring microstructural properties of the biological composites. We find that commonly used data analysis which neglects inertia and high order hydrodynamic reflections will predict Poisson ratios close to 0.5 at high frequencies when actually the microstructural parameters used as input in the simulation give smaller Poisson ratios. This case study with the F-actin and microtubules composite networks, shows that the data analysis formalism presented in this work significantly expands the region of distances between the beads and frequencies at which the dynamic modulus and the complex Poisson ratio can be accurately measured using two-point passive microrheology.

We have also introduced a single-chain mean-field mathematical model for ac-

tive gels that can describe several experimental observations. Moreover the model allows accounting for physics that are not available in models that have been postulated on coarser levels of description. For instance, the active single-chain mean-field model describes the frequency-dependent violation of the fluctuation-dissipation theorem observed in active gels. It can also describe the motor-induced strain hardening and the the super-diffusion of filaments ubiquitous in active gels. Additionally the model provides new insight into buckling as a contraction mechanism in non-sarcomeric active bundles. Recently microscopic multi-chain models for describing the dynamics of active gels have also been proposed. However for realistic chain lengths and densities the numerical simulation of those models is notoriously expensive. This makes observables such as the relaxation modulus difficult to calculate for time-scales of practical interest. The more coarse-grained level of description proposed here overcomes those limitations by using a mean-field approach.

The active single-chain mean-field model can not yet account for the large length-scale physics that arise in active gels when permanent passive cross-links are present. For this reason the predictions of the dynamic modulus of active gels are only qualitative and the formation of large scale structures such as asters and vortices can not yet be described. A fully quantitative description of active gels in the single-chain mean-field framework will require accounting for permanent passive cross-links. It will also require a more accurate bead-spring model of the semiflexible filaments which includes, additionally to finite-extensibility, bending potentials between the springs. Polydispersity in the molecular weight of the filaments is also expected to be important in biological networks and could have a considerable impact in the quality of the predictions. Including details about the specific motor protein used to prepare the gel might also be necessary to achieve a more quantitative description of the rheology of active gels.

APPENDIX A
DERIVATION OF TWO-POINT HYDRODYNAMIC INTERACTION SCALAR FUNCTIONS

Here we show the detailed derivation of the two-point hydrodynamic interaction scalar functions $A_\perp$ and $A_\parallel$, eqs.(4.7) and eqs.(4.8) respectively.

A.1 Introduction

We begin with the equation of motion for a compressible elastic solid

$$\rho\frac{\partial^2\boldsymbol{u}(\boldsymbol{r},t)}{\partial t^2} = G\nabla^2\boldsymbol{u}(\boldsymbol{r},t) + (G+\lambda)\nabla(\nabla\cdot\boldsymbol{u}(\boldsymbol{r},t)) + \boldsymbol{f}(\boldsymbol{r},t). \tag{A.1}$$

where $\boldsymbol{u}(\boldsymbol{r},t)$ is the displacement and $\boldsymbol{f}(\boldsymbol{r},t)$ is an external applied force field, G is the elastic modulus, K is the bulk modulus and $\lambda = K - \frac{2}{3}G$ is the first Lamé coefficient. The derivation is illustrated for a purely elastic solid, but in the frequency domain the results are equivalent for a viscoelastic solid according to the correspondence principle. The force is applied at the particle 1 located at the origin $\boldsymbol{r} = 0$. We assume that it is given as the point force, that is,

$$\boldsymbol{f}(\boldsymbol{r},t) = \frac{\delta(|\boldsymbol{r}|)}{4\pi r^2}\boldsymbol{F}(t) \tag{A.2}$$

where $\boldsymbol{F}(t)$ is the time-dependent part of the force. We seek to calculate the displacement field $\boldsymbol{u}$ at $\boldsymbol{r}$ where the particle 2 is located. The coefficient of the force field and the displacement field gives the mutual compliance.

By taking the Fourier transform for $\boldsymbol{r}$ and t, eq.(A.1) becomes

$$-\rho\omega^2\boldsymbol{u}(\boldsymbol{k},\omega) = -Gk^2\boldsymbol{u}(\boldsymbol{k},\omega) - (G+\lambda)\boldsymbol{k}\boldsymbol{k}\cdot\boldsymbol{u}(\boldsymbol{k},\omega) + \boldsymbol{f}(\boldsymbol{k},\omega), \tag{A.3}$$

or, equivalently,

$$\Big[\big[(2G+\lambda)k^2 - \rho\omega^2\big]\boldsymbol{\delta}_{\boldsymbol{k}}\boldsymbol{\delta}_{\boldsymbol{k}} + (Gk^2 - \rho\omega^2)(\boldsymbol{\delta} - \boldsymbol{\delta}_{\boldsymbol{k}}\boldsymbol{\delta}_{\boldsymbol{k}})\Big]\cdot\boldsymbol{u}(\boldsymbol{k},\omega) = \boldsymbol{f}(\boldsymbol{k},\omega). \tag{A.4}$$

Therefore, the displacement field in the $(\boldsymbol{k},\omega)$-domain is written as

$$\boldsymbol{u}(\boldsymbol{k},\omega) = \left[\frac{\boldsymbol{\delta}_{\boldsymbol{k}}\boldsymbol{\delta}_{\boldsymbol{k}}}{(2G+\lambda)k^2 - \rho\omega^2} + \frac{\boldsymbol{\delta} - \boldsymbol{\delta}_{\boldsymbol{k}}\boldsymbol{\delta}_{\boldsymbol{k}}}{Gk^2 - \rho\omega^2}\right]\cdot\boldsymbol{f}(\boldsymbol{k},\omega). \tag{A.5}$$

The force field eq.(A.2) is written in the $(\boldsymbol{k}, \omega)$-domain as

$$\boldsymbol{f}(\boldsymbol{k}, \omega) = \boldsymbol{F}(\omega). \tag{A.6}$$

By putting this into eq.(A.5) and by taking the inverse Fourier transform for $\boldsymbol{k}$, we have

$$\boldsymbol{u}(\boldsymbol{r}, \omega) = \boldsymbol{H}(\boldsymbol{r}) \cdot \boldsymbol{F}(\omega) \tag{A.7}$$

where $\boldsymbol{H}$ is the Oseen tensor defined by

$$\boldsymbol{H}(\boldsymbol{r}) = \frac{1}{(2\pi)^3} \int d^3\boldsymbol{k}\ e^{i\boldsymbol{k}\cdot\boldsymbol{r}} \left[\frac{\boldsymbol{\delta}_{\boldsymbol{k}}\boldsymbol{\delta}_{\boldsymbol{k}}}{(2G+\lambda)k^2 - \rho\omega^2} + \frac{\boldsymbol{\delta} - \boldsymbol{\delta}_{\boldsymbol{k}}\boldsymbol{\delta}_{\boldsymbol{k}}}{Gk^2 - \rho\omega^2} \right]. \tag{A.8}$$

Note that $\boldsymbol{\delta}_{\boldsymbol{k}}$ is the unit vector in the direction of $\boldsymbol{k}$, and $\boldsymbol{\delta}$ is the identity matrix.

A.2 Oseen tensor

Since $\boldsymbol{H}(\boldsymbol{r})$ depends on the vector $\boldsymbol{r}$ only, it can be written in terms of the scalars $A_\perp$ and $A_\parallel$ and unit vector $\boldsymbol{\delta}_{\boldsymbol{r}}$ parallel to $\boldsymbol{r}$ as

$$\boldsymbol{H}(\boldsymbol{r}) = A_\perp \boldsymbol{\delta} + \left(A_\parallel - A_\perp\right) \boldsymbol{\delta}_{\boldsymbol{r}}\boldsymbol{\delta}_{\boldsymbol{r}}. \tag{A.9}$$

Therefore the scalars $A_\perp$ and $A_\parallel$ are determined from the two equations:

$$\mathrm{Tr}\left\{\boldsymbol{H}\right\} = 2A_\perp + A_\parallel, \tag{A.10}$$

$$\boldsymbol{\delta}_{\boldsymbol{r}} \cdot \boldsymbol{H} \cdot \boldsymbol{\delta}_{\boldsymbol{r}} = A_\parallel. \tag{A.11}$$

By putting eq.(A.8), the left sides can also written as

$$\begin{aligned} \mathrm{Tr}\left\{\boldsymbol{H}\right\} &= \frac{1}{(2\pi)^3} \int d^3\boldsymbol{k}\ e^{i\boldsymbol{k}\cdot\boldsymbol{r}} \left[\frac{1}{(2G+\lambda)k^2 - \rho\omega^2} + \frac{2}{Gk^2 - \rho\omega^2} \right] \\ &= \frac{f(k_l)}{2G+\lambda} + \frac{2f(k_\mathrm{t})}{G}, \end{aligned} \tag{A.12}$$

$$\begin{aligned} \boldsymbol{\delta}_{\boldsymbol{r}} \cdot \boldsymbol{H} \cdot \boldsymbol{\delta}_{\boldsymbol{r}} &= \frac{1}{(2\pi)^3} \int d^3\boldsymbol{k}\ e^{i\boldsymbol{k}\cdot\boldsymbol{r}} \left[\frac{(\boldsymbol{\delta}_{\boldsymbol{k}} \cdot \boldsymbol{\delta}_{\boldsymbol{r}})^2}{(2G+\lambda)k^2 - \rho\omega^2} + \frac{1 - (\boldsymbol{\delta}_{\boldsymbol{k}} \cdot \boldsymbol{\delta}_{\boldsymbol{r}})^2}{Gk^2 - \rho\omega^2} \right] \\ &= \frac{g(k_l)}{2G+\lambda} + \frac{f(k_\mathrm{t}) - g(k_\mathrm{t})}{G} \end{aligned} \tag{A.13}$$

where we have defined

$$f(x) := \frac{1}{(2\pi)^3}\int d^3\boldsymbol{k}\ e^{i\boldsymbol{k}\cdot\boldsymbol{r}}\frac{1}{k^2-x^2}, \tag{A.14}$$

$$g(x) := \frac{1}{(2\pi)^3}\int d^3\boldsymbol{k}\ e^{i\boldsymbol{k}\cdot\boldsymbol{r}}\frac{(\boldsymbol{\delta_k}\cdot\boldsymbol{\delta_r})^2}{k^2-x^2} \tag{A.15}$$

By solving eqs.(A.10-A.13) for $A_\parallel$ and $A_\perp$, we have

$$A_\perp = \frac{f(k_l)-g(k_l)}{2(2G+\lambda)} + \frac{f(k_\mathrm{t})+g(k_\mathrm{t})}{2G}, \tag{A.16}$$

$$A_\parallel - A_\perp = -\frac{f(k_l)-3g(k_l)}{2(2G+\lambda)} + \frac{f(k_\mathrm{t})-3g(k_\mathrm{t})}{2G}.. \tag{A.17}$$

Where $f(x)$ and $g(x)$ are given by:

$$f(x) = \frac{2\pi}{(2\pi)^3}\int_0^\infty \frac{dk\ k^2}{k^2-x^2}\int_{-1}^1 dz\ e^{ikrz} = \frac{e^{-ixr}}{4\pi r}, \tag{A.18}$$

$$\begin{aligned} g(x) &= \frac{2\pi}{(2\pi)^3}\int_0^\infty \frac{dk\ k^2z^2}{k^2-x^2}\int_{-1}^1 dz\ e^{ikrz} \\ &= \frac{1}{4\pi r}\left[\frac{2}{ixr}e^{-ixr} + e^{-ixr} - \frac{2}{(ixr)^2}(1-e^{-ixr})\right]. \end{aligned} \tag{A.19}$$

APPENDIX B

ANALYTIC SOLUTION OF THE ACTIVE DUMBBELL MODEL

To solve eq.(5.1) analytically we begin by postulating a general form for the solution,

$$\begin{aligned}\psi(\Omega;t) &= \delta_{s,0}\delta(F_1)\delta(F_2)\tilde{\psi}(s=0,r;t|\boldsymbol{F}) + \delta_{s,1}p(F_1)\delta(F_2)\tilde{\psi}(s=1,r;t|\boldsymbol{F}) \\ &+ \delta_{s,2}\delta(F_1)p(F_2)\tilde{\psi}(s=2,r;t|\boldsymbol{F}) + \delta_{s,3}p(F_1)p(F_2)\tilde{\psi}(s=3,r;t|\boldsymbol{F})\end{aligned} \tag{B.1}$$

where $\boldsymbol{F} = \{F_1, F_2\}$. By putting eq.(B.1) in eq.(5.1) it can be shown that this probability density function satisfies eq.(5.1) with $\tilde{\psi}(r,s;t|\boldsymbol{F})$, a conditional probability distribution for a given set of motor forces $\{F_1, F_2\}$, that evolves according to,

$$\begin{aligned}\frac{\partial\tilde{\psi}(s,r;t|\boldsymbol{F})}{\partial t} &= \frac{\partial}{\partial r}\left\{\tilde{\psi}(s,r;t|\boldsymbol{F})\left[-\dot{\epsilon}(t)r + A(s)k_b r - \frac{F(s)}{\zeta_a}\right]\right\} \\ &+ \sum_{s'=0}^{3}\tilde{\mathbb{W}}(s|s')\tilde{\psi}(s',r;t|\boldsymbol{F}).\end{aligned} \tag{B.2}$$

Where the function $F(s)$ is given by,

$$F(s) = \begin{cases} 0 & \text{if} \quad s=0 \\ -F_1 & \text{if} \quad s=1 \\ F_2 & \text{if} \quad s=2 \\ F_2 - F_1 & \text{if} \quad s=3 \end{cases} \tag{B.3}$$

The transition rate matrix, $\tilde{\mathbb{W}}(s'|s)$, that appears in eq.(B.2) whose elements give the transition rate at which a dumbbell that is in state s jumps to state s' is defined as,

$$\tilde{\mathbb{W}}(s'|s) = \begin{pmatrix} * & \frac{1}{\tau_d} & \frac{1}{\tau_d} & 0 \\ \frac{1}{\tau_a} & * & 0 & \frac{1}{\tau_d} \\ \frac{1}{\tau_a} & 0 & * & \frac{1}{\tau_d} \\ 0 & \frac{1}{\tau_a} & \frac{1}{\tau_a} & * \end{pmatrix}, \tag{B.4}$$

with diagonal elements given by $\tilde{\mathbb{W}}(s|s) = -\sum_{s'(\neq s)=0}^{3}\tilde{\mathbb{W}}(s'|s)$.

Now that the $\boldsymbol{F}$ dependence has been "factored-out" from $\tilde{\psi}(r,s;t|\boldsymbol{F})$, it is straightforward to obtain a solution from eq.(B.2). Since the equation is linear, the solution is a Gaussian distribution for r given by,

$$\tilde{\psi}(r,s;t|\boldsymbol{F}) = \frac{1}{J}\exp\left\{-\frac{\left(r-\langle r\rangle_{\{s,\boldsymbol{F}\}}\right)^2}{2\left(\langle r^2\rangle_{\{s,\boldsymbol{F}\}}-\langle r\rangle^2_{\{s,\boldsymbol{F}\}}\right)}\right\}, \tag{B.5}$$

where J is the normalization factor and $\langle r\rangle_{\{s,\boldsymbol{F}\}} := \int r\tilde{\psi}(r,s;t|\boldsymbol{F})dr$ and $\langle r^2\rangle_{\{s,\boldsymbol{F}\}} := \int r^2\tilde{\psi}(r,s;t|\boldsymbol{F})dr$ are the first and second conditional moments of r for a given s and $\boldsymbol{F}$. The evolution equations for these conditional moments can be derived from eq.(5.4) by multiplying both sides by r and r^2, respectively. Integrating over r gives,

$$\frac{d}{dt}\langle r\rangle_{\{s,\boldsymbol{F}\}} = \dot{\epsilon}(t)\langle r\rangle_{\{s,\boldsymbol{F}\}} - k_bA(s)\langle r\rangle_{\{s,\boldsymbol{F}\}} + \frac{F(s)}{\zeta_a} + \sum_{s'=0}^{3}\tilde{\mathbb{W}}(s'|s)\langle r\rangle_{\{s',\boldsymbol{F}\}}, \tag{B.6a}$$

$$\begin{aligned}\frac{d}{dt}\langle r^2\rangle_{\{s,\boldsymbol{F}\}} &= 2\dot{\epsilon}(t)\langle r^2\rangle_{\{s,\boldsymbol{F}\}} - 2k_bA(s)\langle r^2\rangle_{\{s,\boldsymbol{F}\}} + \frac{2F(s)}{\zeta_a}\langle r\rangle_{\{s,\boldsymbol{F}\}} \\ &+ \sum_{s'=0}^{3}\tilde{\mathbb{W}}(s'|s)\langle r^2\rangle_{\{s',\boldsymbol{F}\}}.\end{aligned} \tag{B.6b}$$

For a given set of initial conditions this system of coupled ordinary differential equations (eight equations, for the dumbbell version of the model) is solved for $\langle r\rangle_{\{s,\boldsymbol{F}\}}$ and $\langle r^2\rangle_{\{s,\boldsymbol{F}\}}$. These moments can, in general, be expressed as

$$\langle r\rangle_{\{s,\boldsymbol{F}\}} = a_1\left(s,t,X,\langle r\rangle_{\{0,s\}}\right)F_1 + a_2\left(s,t,X,\langle r\rangle_{\{0,s\}}\right)F_2, \tag{B.7}$$

$$\begin{aligned}\langle r^2\rangle_{\{s,\boldsymbol{F}\}} &= b_1\left(s,t,X,\langle r\rangle_{\{0,s\}},\langle r^2\rangle_{\{0,s\}}\right)F_1^2 \\ &+ b_2\left(s,t,X,\langle r\rangle_{\{0,s\}},\langle r^2\rangle_{\{0,s\}}\right)F_1F_2 \\ &+ b_3\left(s,t,X,\langle r\rangle_{\{0,s\}},\langle r^2\rangle_{\{0,s\}}\right)F_2^2.\end{aligned} \tag{B.8}$$

Where $X:\{k_b,\tau_d,\tau_a,\zeta_d,\zeta_a\}$ are model parameters; and $\langle r\rangle_{\{0,s\}}$ and $\langle r^2\rangle_{\{0,s\}}$ are initial conditions for the first and second conditional moments of r for a given s, respectively.

In general, the specific expressions for a_1, a_2, b_1, b_2 and b_3 as a function t and s are calculated by solving eqs.(B.6a) and (B.6b) after specifying values for k_b, τ_d, τ_a, ζ_d, ζ_a, $\langle r \rangle_{\{0,s\}}$ and $\langle r^2 \rangle_{\{0,s\}}$.

Once specific expressions for $\langle r \rangle_{\{s,\boldsymbol{F}\}}$ and $\langle r^2 \rangle_{\{s,\boldsymbol{F}\}}$ are obtained the probability density function of active dumbbell conformations can be obtained by putting back these moments into eq.(B.5), and then inserting the result into eq.(B.1).

A distribution of motor forces, $p(F)$ must be specified before making further calculations with the model. For $p(F) = \delta(F - F_m)$ the conditional second moments of r for a given attachment state s that can be calculated analytically and are given by

$$\langle r \rangle_{s=1} = a_1(s=1)F_m, \quad \langle r \rangle_{s=2} = a_1(s=2)F_m, \tag{B.9a}$$
$$\langle r \rangle_{s=3} = [a_1(s=3) + a_2(s=3)]F_m;$$

$$\langle r^2 \rangle_{s=1} = b_1(s=1)F_m^2, \quad \langle r^2 \rangle_{s=2} = b_1(s=2)F_m^2, \tag{B.9b}$$
$$\langle r^2 \rangle_{s=3} = [b_1(s=3) + b_2(s=3) + b_3(s=3)]F_m^2.$$

And are therefore completely determined by the solution of eqs.(B.6a) and (B.6b)

APPENDIX C

DYNAMIC MODULUS FROM DRIVEN CALCULATION

To calculate the dynamic modulus of the active gel observed in a driven experiment a small amplitude oscillatory strain is applied to the bundle in the direction of filament alignment $\dot{\epsilon}(t) = \epsilon_0\omega \cos \omega t$. We need to calculate the macroscopic stress in the active gel that results from such a deformation. For a single-chain bead-spring model this is given by,

$$\sigma = n_c k_b \langle r^2 \rangle = n_c k_b \sum_{s=1}^{3} \int_{-\infty}^{\infty} r^2 \phi(s, r; t) dr. \tag{C.1}$$

Where $\phi(s, r, t)$ is the marginal probability density defined in eq.(5.12). In the long-time limit the conditional moments $\langle r \rangle_{\{s,\boldsymbol{F}\}}$ and $\langle r^2 \rangle_{\{s,\boldsymbol{F}\}}$, which are required to calculate $\phi(s, r, t)$ have the form:

$$\langle r \rangle_{\{s,\boldsymbol{F}\}} = g_1(s, \omega) \sin \omega t + h_1(s, \omega) \cos \omega t \tag{C.2a}$$

$$\langle r^2 \rangle_{\{s,\boldsymbol{F}\}} = g_2(s, \omega) \sin \omega t + h_2(s, \omega) \cos \omega t \tag{C.2b}$$

The coefficients g_1 and g_2 are associated with the material response that is in phase with the applied strain, while h_1 and h_2 are associated with the material response that is out of phase with the applied strain. By putting eqs. (C.2a) and (C.2b) in eqs. (B.6a) and (B.6b) a set of equations for g_1, g_2, h_1 and h_2 is obtained:

$$-\epsilon_0\omega \langle r \rangle_{\{0,s\}} + \omega g_1(s, \omega) + k_b A(s) h_1(s, \omega) = \sum_{s'=0}^{3} \tilde{\mathbb{W}}(s'|s) h_1(s, \omega) \tag{C.3a}$$

$$k_b A(s) g_{1,s}(\omega) - \omega h_1(s, \omega) = \sum_{s'=0}^{3} \tilde{\mathbb{W}}(s'|s) g_1(s, \omega) \tag{C.3b}$$

$$\begin{aligned} - \quad & \epsilon_0\omega \langle r^2 \rangle_{\{0,s\}} + \omega g_2(s, \omega) + 2k_b A(s) h_2(s, \omega) \\ + \quad & \frac{2F(s)}{\zeta_a} h_1(s, \omega) = \sum_{s'=0}^{3} \tilde{\mathbb{W}}(s'|s) h_2(s, \omega) \end{aligned} \tag{C.3c}$$

$$2k_b A(s) g_2(s, \omega) - \omega h_{2,s} + \frac{2F(s)}{\zeta_a} g_1(s, \omega) = \sum_{s'=0}^{3} \tilde{\mathbb{W}}(s'|s) g_1(s, \omega) \tag{C.3d}$$

Where $\langle r\rangle_{\{0,s\}}$ and $\langle r^2\rangle_{\{0,s\}}$ are the non-equilibrium steady-state values for the first and second conditional moments, respectively; and the transition matrix $\tilde{\mathbb{W}}(s'|s)$ was defined in eq.(B.4). For the active dumbbell model this yields a system of 16 coupled linear equations. In general the solutions for g_1 can be written as a function of $\boldsymbol{F}$ as:

$$g_1 = a_{1,1}(s,\omega,X,\langle r\rangle_{\{0,s\}})F_1 + a_{1,2}(s,\omega,X,\langle r\rangle_{\{0,s\}})F_2 \tag{C.4}$$

where $X : \{k_b, \tau_d, \tau_a, \zeta_d, \zeta_a\}$ are model parameters. An equivalent equation can be written for h_1. Note that the first subindex in the $a_{i,j}$ coefficients indicates whether the coefficient is used to express the solution for g or h; and the second subindex indicates if the coefficients multiply either F_1 or F_2. For g_2 the solutions can be expressed as,

$$\begin{aligned} g_2 &= b_{1,1}(s,\omega,X,\langle r\rangle_{\{0,s\}},\langle r^2\rangle_{\{0,s\}})F_1^2 + b_{1,2}(s,\omega,X,\langle r\rangle_{\{0,s\}},\langle r^2\rangle_{\{0,s\}})F_1F_2 \\ &+ b_{1,3}(s,\omega,X,\langle r\rangle_{\{0,s\}},\langle r^2\rangle_{\{0,s\}})F_2^2. \end{aligned} \tag{C.5}$$

And an equivalent definition for h_2. As in Section 5.3.1 we specify a motor force distribution $p(F_j) = \delta(F_j - F_m)$ with this $\phi(s,r,t)$ can be written as in eq.(5.13) but with conditional moments of r for a given s are given by,

$$\begin{aligned} \langle r\rangle_{s=1} &= a_{1,1}(s=1)F_m\sin\,\omega t + a_{2,1}(s=2)F_m\cos\,\omega t, \\ \langle r\rangle_{s=2} &= a_{1,2}(s=2)F_m\sin\,\omega t + a_{2,2}(s=2)\;F_m\cos\,\omega t, \\ \langle r\rangle_{s=3} &= \sum_{i=1}^{2} a_{1,i}(s=3)F_m\sin\,\omega t + \sum_{i=1}^{2} a_{2,i}(s=3)\;F_m\cos\,\omega t; \end{aligned} \tag{C.6a}$$

$$\begin{aligned} \langle r^2\rangle_{s=1} &= b_{1,1}(s=1)F_m^2\sin\,\omega t + b_{2,1}(s=2)F_m^2\cos\,\omega t, \\ \langle r^2\rangle_{s=2} &= b_{1,3}(s=2)F_m^2\sin\,\omega t + b_{2,3}(s=2)\;F_m^2\cos\,\omega t, \\ \langle r^2\rangle_{s=3} &= \sum_{i=1}^{3} b_{1,i}(s=3)F_m^2\sin\,\omega t + \sum_{i=1}^{3} b_{2,i}(s=3)\;F_m^2\cos\,\omega t. \end{aligned} \tag{C.6b}$$

The dynamic modulus of the gel, observed in the driven or active experiment, can now be calculated by using eqs.(C.1) and (C.6) and the relation $\sigma =$

$\epsilon_0 \left[G'(\omega)\text{sin } \omega t + G''(\omega)\text{cos } \omega t\right]$. This gives in general,

$$G'_{\mathrm{D}}(\omega) = n_c k_b F_m^2 \left[b_{1,1}(s=1) + b_{1,3}(s=2) + \sum_{i=1}^{3} b_{1,i}(s=3) \right] \tag{C.7a}$$

$$G''_{\mathrm{D}}(\omega) = n_c k_b F_m^2 \left[b_{2,1}(s=1) + b_{2,3}(s=2) + \sum_{i=1}^{3} b_{2,i}(s=3) \right]. \tag{C.7b}$$

APPENDIX D

GREEN-KUBO FORMULA

Consider a physical system described by the set of state variables Ω, which may be deterministic (eg., position and momentum) or coarse-grained variables. Now let $\psi(\Omega;t)$ be the probability density describing the probability that the system is in state Ω at time t. The time evolution for $\psi(\Omega;t)$ is given by

$$\frac{\partial\psi(\Omega;t)}{\partial t} = \mathcal{L}_{\text{eq}}\psi(\Omega;t). \tag{D.1}$$

The linear operator $\mathcal{L}_{\text{eq}}$ may be the Liouville operator for atoms, or an infinitesimal generator for a Fokker-Planck or differential Chapman-Kolmogorov equation. Formally, we can write the solution of eq.(D.1) as $\psi(\Omega;t) = e^{\mathcal{L}_{\text{eq}}t}\psi(\Omega;0)$. The equilibrium probability density $\psi_{\text{eq}}(\Omega)$ is

$$\psi_{\text{eq}}(\Omega) = \frac{e^{-\beta\mathcal{H}(\Omega)}}{\int e^{-\beta\mathcal{H}(\Omega)}d\Omega} \tag{D.2}$$

where $\beta = \frac{1}{k_{\text{B}}T}$, and $\mathcal{H}(\Omega)$ is the Hamiltonian for an atomistic level of description or the free energy for a single-chain level of description.

Now consider that the system is in an initial equilibrium state denoted by Ω_0. At $t = 0$ a small step-strain of magnitude ϵ_0 is applied to the system. The subset of Ω that is changed by the external perturbation is denoted by $\boldsymbol{x}$. The microscopic stress, $\hat{\boldsymbol{\tau}}(\boldsymbol{x})$ can be written in terms of $\mathcal{H}(\Omega)$ using a virtual work argument [114], $\hat{\boldsymbol{\tau}}(\boldsymbol{x}) = \boldsymbol{x}\dfrac{\partial\mathcal{H}(\Omega)}{\partial\boldsymbol{x}}$.

At this point it is useful to introduce the marginal probability density $\phi(\boldsymbol{x};t) = \int\psi(\Omega;t)d\hat{\boldsymbol{x}}$ where $\hat{\boldsymbol{x}}$ is the subset of Ω not contained in $\boldsymbol{x}$. Then $\phi(\boldsymbol{x};t)$ for $t = 0+$ is given by,

$$\phi_+(\boldsymbol{x};t) = \int\delta(\boldsymbol{x} - [\boldsymbol{\delta}+\boldsymbol{\gamma}]\cdot\boldsymbol{x}_0)\psi_{\text{eq}}(\Omega_0)d\Omega_0 \tag{D.3}$$

where $\boldsymbol{\delta}$ is the identity tensor and $\boldsymbol{\gamma}$ is the deformation tensor, which, for example in

step shear is given by,

$$\boldsymbol{\gamma} = \begin{pmatrix} 0 & \epsilon_0 & 0 \\ 0 & 0 & 0 \\ 0 & 0 & 0 \end{pmatrix}. \tag{D.4}$$

We assume that the step-strain, applied at the boundaries, propagates instantaneously through the system, on the time scale of interest for which $G(t)$ is calculated. Eq.(D.3) can be written in terms of $\mathcal{H}(\Omega)$ by making use of eq.(D.2)

$$\begin{aligned} \phi_+(\boldsymbol{x};t) &= \frac{e^{-\beta\mathcal{H}(\{[\boldsymbol{\delta}-\boldsymbol{\gamma}]\cdot\boldsymbol{x},\hat{\boldsymbol{x}}\})}}{\int e^{-\beta\mathcal{H}(\{[\boldsymbol{\delta}-\boldsymbol{\gamma}]\cdot\boldsymbol{x},\hat{\boldsymbol{x}}\})}d\Omega} \\ &\approx \frac{e^{-\beta\mathcal{H}(\Omega)}\left[1+\beta\frac{\partial\mathcal{H}(\Omega)}{\partial\boldsymbol{x}}\cdot\boldsymbol{\gamma}\cdot\boldsymbol{x}\right]}{\int e^{-\beta\mathcal{H}(\Omega)}\left[1+\beta\frac{\partial\mathcal{H}(\Omega)}{\partial\boldsymbol{x}}\cdot\boldsymbol{\gamma}\cdot\boldsymbol{x}\right]d\Omega} \\ &= \frac{e^{-\beta\mathcal{H}(\Omega)}\left[1+\beta\hat{\boldsymbol{\tau}}:\boldsymbol{\gamma}\right]}{\int e^{-\beta\mathcal{H}(\Omega)}d\Omega\left[1+\beta\boldsymbol{\gamma}:\langle\hat{\boldsymbol{\tau}}\rangle_{\rm eq}\right]} \\ &\approx \psi_{\rm eq}(\Omega)\left[1+\beta\boldsymbol{\gamma}:(\hat{\boldsymbol{\tau}}(\boldsymbol{x})-\langle\hat{\boldsymbol{\tau}}\rangle_{\rm eq})\right]. \end{aligned} \tag{D.5}$$

Where in the second and fourth lines we have taken only first-order terms in the Taylor series expansion with respect to $\boldsymbol{\gamma}$, since we are considering the response to a small perturbation. In the third line we used the definition of microscopic stress, $\hat{\boldsymbol{\tau}}(\boldsymbol{x})$ given above.

The macroscopic stress that is observed after applying the step strain, $t \geq 0$, is

$$\begin{aligned} \boldsymbol{\tau}(t) &= n_c\langle\hat{\boldsymbol{\tau}}(\boldsymbol{x})\rangle \\ &= n_c\int\hat{\boldsymbol{\tau}}(\boldsymbol{x})\phi(\boldsymbol{x};t)d\boldsymbol{x} \\ &= n_c\int\hat{\boldsymbol{\tau}}(\boldsymbol{x})e^{\mathcal{L}_{\rm eq}t}\psi_+(\Omega;t=0+)d\hat{\boldsymbol{x}}d\boldsymbol{x} \\ &= \langle\hat{\boldsymbol{\tau}}\rangle_{\rm eq}-\beta n_c\left[\langle\hat{\boldsymbol{\tau}}\rangle_{\rm eq}\langle\hat{\boldsymbol{\tau}}\rangle_{\rm eq}-\langle\hat{\boldsymbol{\tau}}(0)\hat{\boldsymbol{\tau}}(t)\rangle_{\rm eq}\right]:\boldsymbol{\gamma}. \end{aligned} \tag{D.6}$$

Where n_c is the number of chains per unit volume for a coarse-grained object or $1/V$ for atomistic or multi-chain descriptions, and V is the volume of the sample. We used eq.(D.5) and stationarity $\langle\hat{\boldsymbol{\tau}}\rangle_{\rm eq}$=$\langle\hat{\boldsymbol{\tau}}(0)\rangle_{\rm eq}$= $\langle\hat{\boldsymbol{\tau}}(t)\rangle_{\rm eq}$ to obtain the last line. The relaxation modulus is obtained from,

$$\begin{aligned}\boldsymbol{\gamma}G(t) = \boldsymbol{\tau}(t) - \langle\boldsymbol{\tau}\rangle_{\rm eq} &= \frac{\beta}{n_c}\left[\langle\boldsymbol{\tau}(0)\boldsymbol{\tau}(t)\rangle_{\rm eq} - \langle\boldsymbol{\tau}\rangle_{\rm eq}\langle\boldsymbol{\tau}\rangle_{\rm eq}\right] : \boldsymbol{\gamma} \\ &= \frac{\beta}{n_c}\langle\left[\boldsymbol{\tau}(0) - \langle\boldsymbol{\tau}\rangle_{\rm eq}\right]\left[\boldsymbol{\tau}(t) - \langle\boldsymbol{\tau}\rangle_{\rm eq}\right]\rangle_{\rm eq} : \boldsymbol{\gamma}.\end{aligned} \tag{D.7}$$

Where we used $\boldsymbol{\tau} = n_c\hat{\boldsymbol{\tau}}$ and eq.(D.6) to obtain the first line. By defining $\delta\boldsymbol{\tau}(t) = \boldsymbol{\tau}(t) - \langle\boldsymbol{\tau}\rangle_{\rm eq}$ we obtain the Green-Kubo formula for stress,

$$\boldsymbol{\gamma}G(t) = \delta\boldsymbol{\tau}(t) = \frac{\beta}{n_c}\langle\delta\boldsymbol{\tau}(t)\delta\boldsymbol{\tau}(0)\rangle_{\rm eq} : \boldsymbol{\gamma}. \tag{D.8}$$

In Chapter 6 we consider the case of a bundle of filaments aligned in the z direction to which a step-strain of magnitude ϵ_0 is applied in the direction of filament orientation. Therefore $\boldsymbol{\gamma}_{zz} = \epsilon_0$, and all the other components of $\boldsymbol{\gamma}$ are set equal to zero. The fluctuations of the zz component of stress, $\sigma(t) = \delta\boldsymbol{\tau}_{zz}(t)$, are followed.

BIBLIOGRAPHY

[1] K. M. Addas, C. F. Schmidt, and J. X. Tang. Microrheology of solutions of semiflexible biopolymer filaments using laser, tweezers interferometry. *Physical Review E*, 70:021503, 2004.

[2] I. S. Aranson and L. S. Tsimring. Pattern formation of microtubules and motors: inelastic interaction of polar rods. *Physical Review E*, 71(5):050901, 2005.

[3] A. M. Ardekani and R. H. Rangel. Unsteady motion of two solid spheres in Stokes flow. *Physics of Fluids*, 18:103306, 2006.

[4] G. K. Batchelor. Brownian diffusion of particles with hydrodynamic interaction. *Journal of Fluid Mechanics*, 74:1–29, 1976.

[5] M. Baumgaertel, A. Schausberger, and H. H. Winter. The relaxation of polymers with linear flexible chains of uniform length. *Rheologica Acta*, 29:400–408, 1990.

[6] M. Baumgaertel and H. H. Winter. Determination of discrete relaxation and retardation time spectra from dynamic mechanical data. *Rheologica Acta*, 28:511–519, 1989.

[7] M. Baumgaertel and H. H. Winter. Interrelation between continuous and discrete relaxation time spectra. *Journal of Non-Newtonian Fluid Mechanics*, 44:15–36, 1992.

[8] O. J. N. Bertrand, D. K. Fygenson, and O. A. Saleh. Active, motor-driven mechanics in a DNA gel. *Proceedings of the National Academy of Sciences*, 109(43):17342–17347, 2012.

[9] R. B. Bird, C. F. Curtiss, R. C. Armstrong, and O. Hassager. *Dynamics of Polymeric Liquids, 2 Volume Set*. Wiley-Interscience, 1996.

[10] P. Bohec, F. Gallet, C. Maes, S. Safaverdi, P. Visco, and F. van Wijland. Probing active forces via a fluctuation-dissipation relation: Application to living cells. *EPL (Europhysics Letters)*, 102(5):50005, 2013.

[11] J. F. Brady and G. Bossis. Stokesian dynamics. *Annual Review of Fluid Mechanics*, 20:111–57, 1988.

[12] M. E. Cates, S. M. Fielding, D. Marenduzzo, E. Orlandini, and J. M. Yeomans. Shearing active gels close to the isotropic-nematic transition. *Phys. Rev. Lett.*, 101:068102, Aug 2008.

[13] P. M. Chaikin and T. Lubensky. *Principles of condensed matter physics*. Cambridge University Press, Cambridge, UK, 1 edition, 1994.

[14] D. Chandler. *Introduction to modern statistical mechanics*, volume 1. Oxford University Press, 1987.

[15] A. Córdoba, T. Indei, and J. D. Schieber. The effects of compressibility, hydrodynamic interaction and inertia on two-point, passive microrheology of viscoelastic materials. *Soft Matter*, 9(13):3521–3534, 2013.

[16] A. Córdoba, T. Indei, and J.D. Schieber. Elimination of inertia from a generalized Langevin equation: Applications to microbead rheology modeling and data analysis. *Journal of Rheology*, 56:185, 2012. The prefactors in the right side of eqs. (2) and (9b) were printed as 2 but should have been 1. In eqs.(4) and (8) the prefactors in the right side were printed as 2 but should should have been 2π. The prefactors in front of η_0, ζ_0 and μ_0 in eqs. (13), (14), (16) and (29) were printed as 2 but should should have been 1. These were misprints, and do not affect any of the results presented in the paper.

[17] A. Córdoba, J. D. Schieber, and T. Indei. A single-chain model for active gels I: Active dumbbell model. *RSC Advances*, 4:17935–17949, 2014.

[18] A. Córdoba, J.D. Schieber, and T. Indei. The effects of hydrodynamic interaction and inertia in determining the high-frequency dynamic modulus of a viscoelastic fluid with two-point passive microrheology. *Physics of Fluids*, 24:073103, 2012.

[19] J. C. Crocker, M. T. Valentine, E. R. Weeks, T. Gisler, P. D. Kaplan, A.G. Yodh, and D.A. Weitz. Two-point microrheology of inhomogeneous soft materials. *Physical Review Leters*, 85:888, 2000.

[20] M. Das and F. C. MacKintosh. Poisson's ratio in composite elastic media with rigid rods. *Physical Review Letters*, 105:138102, 2010.

[21] V. F. Pasa Dutra, S. Maghous, A. Campos Filho, and A. R. Pacheco. A micromechanical approach to elastic and viscoelastic properties of fiber reinforced concrete. *Cement and Concrete Research*, 40(3):460 – 472, 2010.

[22] M. M. Dygas, B. J. Matkowsky, and Z. Schuss. A singular perturbation approach to non-markovian escape problems. *SIAM Journal on Applied Mathematics*, 46:265–298, 1986.

[23] M. S. e Silva, M. Depken, B. Stuhrmann, M. Korsten, F. C. MacKintosh, and G. H. Koenderink. Active multistage coarsening of actin networks driven by myosin motors. *Proceedings of the National Academy of Sciences*, 108(23):9408–9413, 2011.

[24] M. Fixman and J. Kovac. Polymer conformational statistics. III. modified gaussian models of stiff chains. *The Journal of Chemical Physics*, 58:1564, 1973.

[25] D. A. Fletcher and P.L. Geissler. Active biological materials. *Annual Review of Physical Chemistry*, 60:469, 2009.

[26] D. R. Foss and J. F. Brady. Structure, diffusion and rheology of brownian suspensions by stokesian dynamics simulation. *Journal of Fluid Mechanics*, 2000.

[27] D. Frenkel and B. Smit. *Understanding molecular simulation: from algorithms to applications*. Academic press, 2 edition, 2001.

[28] J. Fricks, L. Yao, T. C. Elston, and M. G. Forest. Time-domain methods for diffusive transport in soft matter. *SIAM Journal on Applied Mathematics*, 69:1277–1308, 2009.

[29] C. Ganguly and D. Chaudhuri. Stochastic thermodynamics of active brownian particles. *Physical Review E*, 88(3):032102, 2013.

[30] M. L. Gardel, M. T. Valentine, J. C. Crocker, A. R. Bausch, and D. A. Weitz. Microrheology of entangled f-actin solutions. *Physical Review Letters*, 91:158302, 2003.

[31] C. W. Gardiner. *Stochastic Process, A handbook for the natural and social sciences*. Springer, New York, 1 edition, 1985.

[32] C. W. Gardiner. *Stochastic Process, A handbook for the natural and social sciences*. Springer, New York, 4 edition, 2009.

[33] L. Giomi, T. B. Liverpool, and M. C. Marchetti. Sheared active fluids: Thickening, thinning, and vanishing viscosity. *Phys. Rev. E*, 81:051908, May 2010.

[34] F. Gittes and F. C. MacKintosh. Dynamic shear modulus of a semiflexible polymer network. *Physical Review E*, 58(2):1241–1244, 1998.

[35] F. Gittes, B. Mickey, J. Nettleton, and J. Howard. Flexural rigidity of microtubules and actin filaments measured from thermal fluctuations in shape. *The Journal of Cell Biology*, 120(4):923–934, 1993.

[36] F. Gittes and C. F. Schmidt. Interference model for back-focal-plane displacement detection in optical tweezer. *Optics Letters*, 23:7–9, 1998.

[37] P. S. Grassia, E. J. Hinch, and L. C. Nitsche. Computer simulations of brownian motion of complex systems. *Journal of Fluid Mechanics*, 282:373, 1995.

[38] G. N. Greaves, A. L. Greer, R. S. Lakes, and T. Rouxel. Poisson's ratio and modern materials. *Nature Materials*, 10:823–837, November 2011.

[39] J. Happel and H. Brenner. *Low Reynolds number hydrodynamics*. Martinus Nijhoff Publishers, 2 edition, 1986.

[40] J. F. Hart, E. W. Cheney, C. L. Lawson, H. J. Maehly, C. K. Mesztenyi, J. R. Rice, H. G. Thacher, and C.Witzgall. *Computer Approximations*. Wiley, New York, 1 edition, 1968.

[41] D. A. Head, W. J. Briels, and G. Gompper. Nonequilibrium structure and dynamics in a microscopic model of thin-film active gels. *Phys. Rev. E*, 89:032705, Mar 2014.

[42] D. A. Head, G. Gompper, and W. J. Briels. Microscopic basis for pattern formation and anomalous transport in two-dimensional active gels. *Soft Matter*, 7(7):3116–3126, 2011.

[43] D. A. Head and D. Mizuno. Nonlocal fluctuation correlations in active gels. *Physical Review E*, 81(4):041910, 2010.

[44] J. G. Hérnandez Cifre, T. H. Barenbrug, J. D. Schieber, and B. H. A. A. Van den Brule. Brownian dynamics simulation of reversible polymer networks under shear using a non-interacting dumbbell model. *Journal of Non-Newtonian Fluid Mechanics*, 113(2):73–96, 2003.

[45] W. Hess and R. Klein. Generalized hydrodynamics of systems of brownian particles. *Advances in Physics*, 32:173–283, 1983.

[46] T. L. Hill, E. Eisenberg, Y. D. Chen, and R. J. Podolsky. Some self-consistent two-state sliding filament models of muscle contraction. *Biophysical journal*, 15(4):335–372, 1975.

[47] E. J. Hinch. Brownian motion with stiff bonds and rigid constraints. *Journal of Fluid Mechanics*, 271:219, 1994.

[48] C. Hohenegger and M. G. Forest. Two-bead microrheology: Modeling protocols. *Physical Review E*, 78:031501, 2008.

[49] A F Huxley. Muscular contraction. *The Journal of physiology*, 243(1):1, 1974.

[50] T. Indei, J. D. Schieber, and A. Córdoba. Competing effects of inertia and particle diffusion in viscoelastic materials, and their ramifications for passive microrheology. *Physical Review E*, 85:041504, 2012.

[51] T. Indei, J. D. Schieber, and A. Córdoba. Competing effects of particle and medium inertia on particle diffusion in viscoelastic materials, and their ramifications for passive microrheology. *Physical Review E*, 85(4):041504, 2012.

[52] T. Indei, J. D. Schieber, A. Córdoba, and E. Pilyugina. On treating inertia in passive microbead rheology. *Physical Review E*, 0:0, 2012.

[53] T. Indei, J. D. Schieber, and J. Takimoto. Effects of fluctuations of cross-linking points on viscoelastic properties of associating polymer networks. *Rheologica acta*, 51(11-12):1021–1039, 2012.

[54] T. Indei and J. Takimoto. Linear viscoelastic properties of transient networks formed by associating polymers with multiple stickers. *The Journal of Chemical Physics*, 133:194902, 2010.

[55] F. Jülicher, A. Ajdari, and J. Prost. Modeling molecular motors. *Reviews of Modern Physics*, 69(4):1269, 1997.

[56] F. Jülicher and J. Prost. Cooperative molecular motors. *Physical Review Letters*, 75(13):2618–2621, 1995.

[57] M. Karim, S. C Kohale, T. Indei, J. D. Schieber, and R. Khare. Determination of viscoelastic properties by analysis of probe-particle motion in molecular simulations. *Physical Review E*, 86(5):051501, 2012.

[58] R. N. Khaliullin and J. D. Schieber. Application of the slip-link model to bidisperse systems. *Macromolecules*, 43(14):6202–6212, 2010.

[59] Y. Kimura. Microrheology of soft mattter. *Journal of the Physical Society of Japan*, 78:041005, 2009.

[60] G. H. Koenderink, Z. Dogic, F. Nakamura, P. M. Bendix, F. C. MacKintosh, J. H. Hartwig, T. P. Stossel, and D. A. Weitz. An active biopolymer network controlled by molecular motors. *Proceedings of the National Academy of Sciences*, 106(36):15192–15197, 2009.

[61] E. F. Koslover and A. J. Spakowitz. Discretizing elastic chains for coarse-grained polymer models. *Soft Matter*, 9(29):7016–7027, 2013.

[62] E. F. Koslover and A. J. Spakowitz. Systematic coarse-graining of microscale polymer models as effective elastic chains. *Macromolecules*, 46(5):2003–2014, 2013.

[63] K. Kruse, JF Joanny, F. Jülicher, J. Prost, and K. Sekimoto. Asters, vortices, and rotating spirals in active gels of polar filaments. *Physical Review Letters*, 92(7):78101, 2004.

[64] K. Kruse and F. Jülicher. Self-organization and mechanical properties of active filament bundles. *Physical Review E*, 67(5):051913, 2003.

[65] K. Kruse and K. Sekimoto. Growth of fingerlike protrusions driven by molecular motors. *Physical Review E*, 66(3):031904, 2002.

[66] G. J. Kynch. The slow motion of two spheres through a viscous fluid. *Journal of Fluid Mechanics*, 5:193–208, 1959.

[67] L. D. Landau and E. M. Lifshitz. *Fluid mechanics*. Butterworth-Heinemann, UK, 2 edition, 1987.

[68] A. W. C. Lau, B. D. Hoffman, A. Davies, J. C. Crocker, and T. C. Lubensky. Microrheology, stress fluctuations, and active behavior of living cells. *Physical Review Letters*, 91(19):198101, 2003.

[69] E. H. Lee. Stress analysis in visco-elastic bodies. *Quarterly of Applied Mathematics*, 13:183–190, 1955.

[70] M. Lenz, M. L. Gardel, and A. R. Dinner. Requirements for contractility in disordered cytoskeletal bundles. *New Journal of Physics*, 14(3):033037, 2012.

[71] M. Lenz, T. Thoresen, M. L. Gardel, and A. R. Dinner. Contractile units in disordered actomyosin bundles arise from F-actin buckling. *Physical Review Letters*, 108(23):238107, 2012.

[72] A. J. Levine and T. C. Lubensky. Response function of a sphere in a viscoelastic two-fluid medium. *Physical Review E*, 63:041510, 2001.

[73] A. J. Levine and T. C. Lubensky. Two-point microrheology and electrostatic analogy. *Physical Review E*, 65:011501, 2001.

[74] A. J. Levine and F. C. MacKintosh. The mechanics and fluctuation spectrum of active gels. *The Journal of Physical Chemistry B*, 113(12):3820–3830, 2009.

[75] T. Li, S. Kheifets, D. Medellin, and M.G. Raizen. Measurement of the instantaneous velocity of a brownian particle. *Science*, 328:1673, 2010.

[76] A. E. Likhtman, S. K. Sukumaran, and J. Ramirez. Linear viscoelasticity from molecular dynamics simulation of entangles polymers. *Macromolecules*, 40:6748–6757, 2007.

[77] T. B. Liverpool and F. C. MacKintosh. Inertial effects in the response of viscous and viscoelastic fluids. *Physical Review Letters*, 95:208–303, 2005.

[78] T. B. Liverpool, A. C. Maggs, and A. Ajdari. Viscoelasticity of solutions of motile polymers. *Physical Review Letters*, 86(18):4171–4174, 2001.

[79] T. B. Liverpool and M. C. Marchetti. Rheology of active filament solutions. *Phys. Rev. Lett.*, 97:268101, Dec 2006.

[80] T. B. Liverpool and M. C. Marchetti. Bridging the microscopic and the hydrodynamic in active filament solutions. *EPL (Europhysics Letters)*, 69(5):846, 2007.

[81] R. W. Lymn and E. W. Taylor. Mechanism of adenosine triphosphate hydrolysis by actomyosin. *Biochemistry*, 10(25):4617–4624, 1971.

[82] F. C. MacKintosh, J. Käs, and P. A. Janmey. Elasticity of semiflexible biopolymer networks. *Physical Review Letters*, 75(24):4425–4428, 1995.

[83] F. C. MacKintosh and A. J. Levine. Nonequilibrium mechanics and dynamics of motor-activated gels. *Physical Review Letters*, 100(1):18104, 2008.

[84] D. Magatti and F. Ferri. Fast multi-tau real-time software correlator for dynamic light scattering. *Applied Optics*, 40:4011–4021, 2001.

[85] J. F. Marko and E. D. Siggia. Stretching DNA. *Macromolecules*, 28(26):8759–8770, 1995.

[86] T. G. Mason, K. Ganesan, J. H. van Zanten, D. Wirtz, and S. C Kuo. Particle tracking microrheology of complex fluids. *Physical Review Letters*, 79:3282–3285, 1997.

[87] T. G. Mason and D. A. Weitz. Optical measurements of frequency-dependent linear viscoelastic moduli of complex fluids. *Physical Review Letters*, 74:1250–1253, 1995.

[88] P. Mazur and W. van Saarloos. Many-sphere hydrodynamic interactions and mobilities in a suspension. *Physica A*, 115:21–57, 1982.

[89] S. A. McKinley, L. Yao, and M. G. Forest. Transient anomalous diffusion of tracer particles in soft matter. *Journal of Rheology*, 53:1487–1506, 2009.

[90] H. Metiu, D.W. Oxtoby, and K.F. Freed. Hydrodynamic theory for vibrational relaxation of liquids. *Physical Review A*, 15:361, 1977.

[91] D. Mizuno, C. Tardin, C. F. Schmidt, and F. C. MacKintosh. Nonequilibrium mechanics of active cytoskeletal networks. *Science*, 315(5810):370–373, 2007.

[92] H. Mori. A continued-fraction representation of the time-correlation functions. *Progress in Theoretical Physics*, 34:399–416, 1965.

[93] K. I. Morozov and L. M. Pismen. Strain dependence of cytoskeleton elasticity. *Soft Matter*, 8(35):9193–9199, 2012.

[94] M. P. Murrell and M. L. Gardel. F-actin buckling coordinates contractility and severing in a biomimetic actomyosin cortex. *Proceedings of the National Academy of Sciences*, 109(51):20820–20825, 2012.

[95] K. C. Neuman and S. M. Block. Optical trapping. *Review of Scientific Instruments*, 75:2787–2809, 2004.

[96] H. C. Öttinger. *Stochastic processes in polymeric fluids: tools and examples for developing simulation algorithms*. Springer, Berlin, Germany, 1 edition, 1996.

[97] J. Palacci, C. Cottin-Bizonne, C. Ybert, and L. Bocquet. Sedimentation and effective temperature of active colloidal suspensions. *Physical Review Letters*, 105(8):088304, 2010.

[98] M. Pasquali, V. Shankar, and D. C. Morse. Viscoelasticity of dilute solutions of semiflexible polymers. *Phys. Rev. E*, 64:020802, Jul 2001.

[99] V. Pelletier, N. Gal, P. Fournier, and M. L. Kilfoil. Microrheology of microtubule solutions and actin-microtubule composite networks. *Physical Review Letters*, 102:188303, 2009.

[100] G. Pesce, G. Volpe, A. Chiara De Luca, G. Rusciano, and Giovanni Volpe. Quantitative assessment of non-conservative radiation forces in an optical trap. *Europhysics Letters*, 86:38002, 2009.

[101] W. H. Press, B. P. Flannery, S. A. Teukolsky, and W. T. Vetterling. *Numerical recipes: the art of scientific computing*. Cambridge University Press, Cambridge, 1 edition, 1986.

[102] J. Prost, J.-F. Joanny, and J. M. R. Parrondo. Generalized fluctuation-dissipation theorem for steady-state systems. *Phys. Rev. Lett.*, 103:090601, Aug 2009.

[103] Y. Roichman, B. sun, J. Amato-Grill, and D. G. Grier. Optical forces arising from phase gradients. *Physical Review Letters*, 100:013602, 2008.

[104] Y. Roichman, B. Sun, A. Stolarski, and D.G. Grier. Influence of nonconservative optical forces on the dynamics of optical trapped colloidal spheres: The fountain of probability. *Physical Review Letters*, 101:128301, 2008.

[105] T. Sanchez, D. T. N. Chen, S. J. DeCamp, M. Heymann, and Z. Dogic. Spontaneous motion in hierarchically assembled active matter. *Nature*, 491(7424):431–434, 2012.

[106] T. Savin and P. S. Doyle. Static and dynamic errors in particle tracking microrheology. *Biophysical Journal*, 88:623–638, 2005.

[107] H. M. Schaink, J. J. M. Slot, R. J. J. Jongschaap, and J. Mellema. The rheology of systems containing rigid spheres suspended in both viscous and viscoelastic media, studied by stokesian dynamics simulations. *Journal of Rheology*, 44:473–498, 2000.

[108] J. D. Schieber, A. Córdoba, and T. Indei. The analytic solution of Stokes for time-dependent creeping flow around a sphere: application to linear viscoelasticity as an ingredient for the Generalized Stokes-Einstein relation and microrheology analysis. *Journal of Non-Newtonian Fluid Mechanics*, 200(0):3 – 8, 2013.

[109] J. D. Schieber and K. Horio. Fluctuation in entanglement positions via elastic slip-links. *The Journal of Chemical Physics*, 132:074905, 2010.

[110] B. Schnurr, F. Gittes, F. C. MacKintosh, and C. F. Schmidt. Determining microscopic viscoelasticity in flexible and semiflexible polymer networks from thermal fluctuations. *Macromolecules*, 30:7781–7792, 1997.

[111] H. Shuman, M. J. Greenberg, A. Zwolak, T. Lin, C. V. Sindelar, R. Dominguez, and E. M. Ostap. A vertebrate myosin-I structure reveals unique insights into myosin mechanochemical tuning. *Proceedings of the National Academy of Sciences*, page 201321022, 2014.

[112] T. M. Squires and T. G. Mason. Fluid mechanics of microrheology. *Annual Review of Fluid Mechanics*, 42:413, 2010.

[113] L. Starrs and P. Bartlett. Colloidal dynamics in polymer solutions: Optical two-point microrheology, measurements. *Faraday Discussions*, 123:323–334, 2003.

[114] R. J. A. Steenbakkers and J. D. Schieber. Derivation of free energy expressions for tube models from coarse-grained slip-link models. *The Journal of chemical physics*, 137(3):034901, 2012.

[115] C. Storm, J. J. Pastore, F. C. MacKintosh, T. C. Lubensky, and P. A. Janmey. Nonlinear elasticity in biological gels. *Nature*, 435(7039):191–194, 2005.

[116] C. Storm, J. J. Pastore, F. C. MacKintosh, T.C. Lubensky, and P.A. Janmey. Nonlinear elasticity in biological gels. *Nature*, 435:191, 2005.

[117] B. Stuhrmann, M. S. e Silva, M. Depken, F. C. MacKintosh, and G. H. Koenderink. Nonequilibrium fluctuations of a remodeling in vitro cytoskeleton. *Physical Review E*, 86(2):020901, 2012.

[118] T. Surrey, F. Nédélec, S. Leibler, and E. Karsenti. Physical properties determining self-organization of motors and microtubules. *Science*, 292(5519):1167–1171, 2001.

[119] T. Thoresen, M. Lenz, and M. L. Gardel. Reconstitution of contractile actomyosin bundles. *Biophysical journal*, 100(11):2698–2705, 2011.

[120] N. W. Tschoegl, Wolfgang G. Knauss, and Igor Emri. Poisson's ratio in linear viscoelasticity a critical review. *Mechanics of Time-Dependent Materials*, 6:3–51, 2002. 10.1023/A:1014411503170.

[121] P. T. Underhill and P. S. Doyle. On the coarse-graining of polymers into bead-spring chains. *Journal of non-newtonian fluid mechanics*, 122(1):3–31, 2004.

[122] P. T. Underhill and P. S. Doyle. Alternative spring force law for bead-spring chain models of the worm-like chain. *Journal of Rheology*, 50:513, 2006.

[123] W. van Saarloos and P. Mazur. Many-sphere hydrodynamic interactions and mobilities in a suspension. ii. mobilities at finite frequencies. *Physica A*, 120:77–102, 1983.

[124] J. H. van Zanten and K. P. Rufener. Brownian motion in a single relaxation time maxwell fluid. *Physical Review E*, 62:5389–5396, 2000.

[125] N. Willenbacher, C. Oelschlaeger, M. Schopferer, P. Fischer, F. Cardinaux, and F. Scheffold. Broad bandwidth optical and mechanical rheometry of wormlike micelles solutions. *Physical Review Letters*, 99:068302, 2007.

[126] K. Xu, M. G. Forest, and I. Klapper. On the correspondence between creeping flows of viscous and viscoelastic fluids. *Journal of Non-Newtonian Fluid Mechanics*, 145:150–172, 2007.

[127] A. Yamada and T. Wakabayashi. Movement of actin away from the center of reconstituted rabbit myosin filament is slower than in the opposite direction. *Biophysical journal*, 64(2):565–569, 1993.

[128] S. Yamada, D. Wirtz, and S. C. Kuo. Mechanics of living cells measured by laser tracking microrheology. *Biophysical Journal*, 78:1736–1747, 2000.

[129] R. Zwanzig and M. Bixon. Hydrodynamic theory of the velocity correlation function. *Physical Review A*, 2:2005–2012, 1970.